

© 2009

Michael Romanelli

ALL RIGHTS RESERVED

MOLECULAR LANTHANIDE FLUORIDES:
PHOTOLUMINESCENCE FROM NOVEL
ARCHITECTURES

By

MICHAEL DENNIS ROMANELLI

A Dissertation submitted to the
Graduate School-New Brunswick
Rutgers, The State University of New Jersey

in partial fulfillment of the requirements

for the degree of

Doctor of Philosophy

Graduate Program in Chemistry & Chemical Biology

written under the direction of

Professor John G. Brennan

and approved by

New Brunswick, New Jersey

January 2010

ABSTRACT OF THE DISSERTATION

Molecular Lanthanide Fluorides: Highly Luminescent Materials From Novel Architectures

by MICHAEL ROMANELLI

Dissertation Director:

Professor John G. Brennan

Novel molecular lanthanide (Ln) species have been prepared that showcase not only their exceptional optical properties but also deviations from the “typical” reaction/product schemes realized over the past few decades. Ln chalcogenolates $[(L)_xLn(SC_6F_5)_3]$ and $(L)_xLn(SeC_6F_5)_3$; (Ln = Pr, Nd, Sm, Er, or Yb; L = pyr, DME, or THF); x = 3 or 4] have been prepared and their optical and structural properties are discussed. The photoluminescence quantum efficiency (QE), radiative decay, and effective bandwidth for the $^4F_{11/2} \rightarrow ^4I_{9/2}$ transition of $Nd(SC_6F_5)_3(DME)_3$ were found to be 9%, 1.39ms, and 59nm, respectively. At the time, this was one of the highest reported quantum efficiencies for a molecular Nd species.

Ligand, metal radii, and neutral donor molecule have been found to influence the physical and optical properties of these species. By changing any one of these variables, vastly different products can arise; for example, 7-coordinate $[Nd(SC_6F_5)_3(THF)_3]_2$ with bridging thiolates, 7-coordinate $Nd(SeC_6F_5)_3(THF)_3$, and 8-coordinate $Nd(SC_6F_5)_3(DME)_2$, have all been successfully isolated. Using the same ligand and neutral donor with Er gives 6-coordinate $Er(SeC_6F_5)_3(THF)_3$, a near perfect octahedral

geometry with a significant structural trans influence. DFT calculations indicate that the trans influence in these bond lengths result from covalent Ln-E interactions. Cluster compounds $\text{DME}_3\text{Yb}_4\text{F}_2\text{O}(\text{OCH}_2\text{CH}_2\text{OCH}_3)_2(\text{SeSe})(\text{SC}_6\text{F}_5)_4 \cdot \text{DME}$ and $(\text{pyr})_{24}\text{Ln}_{28}\text{F}_{68}(\text{SePh})_{16}$ (Ln = Ce, Nd, Pr) have been prepared by C-F bond activation and direct fluoride source (NH_4F), respectively. At 41%, the $^4\text{F}_{11/2} \rightarrow ^4\text{I}_{9/2}$ transition of $(\text{pyr})_{24}\text{Nd}_{28}\text{F}_{68}(\text{SePh})_{16}$ is the highest QE to date for any molecular Nd species.

$(\text{pyr})_x\text{M}(\text{SeC}_6\text{F}_5)_2$ (M = Zn, Cd, Hg and x = 0 or 2) were synthesized by reductive cleavage of $\text{F}_5\text{C}_6\text{SeSeC}_6\text{F}_5$ by the respective metals. Both the Zn and Cd species have tetrahedral coordination environments. The Hg analog has a near linear, modulated structure, with no coordinated pyridine ligands. These molecular II-VI semiconductor precursors melt between 115 and 175°C and when heated to 650°C under reduced pressures, give crystalline MSe (M = Zn, Cd, Hg) products.

Acknowledgements:

To my advisor, Professor John Brennan; bask in the glory of the wins, I never made it easy or played soft, and I'm sure you wanted it that way. Thank you for the last 5 years of wisdom, guidance, and for answering even the simplest of questions without hesitation (or laughter). Thank you for allowing me to develop my own ideas, even the many that only looked good on paper. Your patience and understanding are unparalleled, especially in those tension producing times experienced throughout the attainment of a Ph.D. You are truly a man to look up to in both personal and professional ways, and I hope to someday be able to hold a candle to your distinguished career in chemistry.

To all the members of the Brennan group and the Rutgers chemistry community, I give thanks. To my committee members, Drs. Goldman, Potenza, and Riman; thank you for your support throughout my career at Rutgers. Whether it was sitting in on my formal research proposals or chatting about chemistry/life, you've all helped me get to this point, and you have my sincerest gratitude. Santanu and Lu, thank you for showing me the ropes of rare earth chemistry, and helping me figure out how to successfully navigate the glovebox. Our chemistry is unique and without your help, the nuances of our techniques would have been hard to master. To Kieran and Joe, thanks for the laughs and the workouts. If there were ever a school for the advancement of random knowledge, you two would be the founders. There are far too many people in this department (faculty, student, and staff alike) to thank individually for all their contributions to my research. Be it research related, administrative, or personal, there was always someone around to help. Tom, whether it's one sentence or a paragraph, words can't describe my appreciation for all that you've done. While it takes a lifetime to master, you've taught

me more about crystallography than I would have ever learned from books, and in the process you have become a true friend. Ajith, thank you for your dedication to this project, and spending so much of your time not only performing the spectroscopy, or analyzing the data, but for taking the time to explain it all solely for my benefit.

To my family, thank you for your continual support throughout *all* the years it took me to get to this point. Mom and Dad, I know the path was full of obstacles but we made it. Thank you for always believing in me and giving me the opportunity to make it this far. You are the best parents a son could wish for and I only hope I've made you as proud to be my parents as I am to be your son. Amanda and Chris, Stacey and Jim: Thanks for your "interest" in what I do. I'm sure my long winded answers were more than you bargained for from a casual question, but you all always seemed intrigued in what I was doing and excited to hear of my latest developments. When I was finally finished with my ramblings (usually when I noticed the glossy eyes and robotic nods), you always had a party, games, or a drink ready as a distraction. To my wife Alyson...I love you. Your patience and understanding are unwavering, and your love breathtaking. You are an inspiration in all that you do, and you add a spark to life that I never knew existed, but would have been lost without. Frank, what can I say...thanks for the spider webs.

Table of Contents

Title Page.....	i
Abstract.....	ii-iii
Acknowledgements.....	iv-v
Table of Contents.....	vi-vii
List of Tables.....	viii-ix
List of Figures.....	x-xv
List of Abbreviations.....	xvi
Introduction.....	1-10
Chapter 1. Fluorinated Derivatives of Lanthanide Chalcogenolate Complexes	
1.1 Introduction.....	11-22
1.2 Lanthanide Thiolates: Synthesis, Structure, and Discussion.....	23-28
1.3 Lanthanide Selenolates: Synthesis, Structure, and Discussion.....	28-47
1.4 Photoluminescence.....	48-64
1.5 Conclusions.....	64-65
References.....	66-68
Chapter 2. Lanthanide Fluoride Clusters From C-F Bond Cleavage: An Introduction to Novel Molecular Species Containing Ln-F Bonds	
2.1 Introduction.....	69-71
2.2 DME ₃ Yb ₄ F ₂ O(OCH ₂ CH ₂ OCH ₃) ₂ (SeSe)(SC ₆ F ₅) ₄ •DME: Synthesis, Structure, and Discussion.....	71-79
2.3 Conclusions.....	80

References.....	81
Chapter 3. Nanosized Molecular Rare-Earth Fluoride Clusters: $(\text{pyr})_{24}\text{Ln}_{28}\text{F}_{68}(\text{SePh})_{16}$	
(Ln = Nd, Pr)	
3.1 Introduction.....	82-83
3.2 $(\text{pyr})_{24}\text{Ln}_{28}\text{F}_{68}(\text{SePh})_{16}$ (Ln = Nd, Pr) : Synthesis, and Structure	83-94
3.3 $(\text{pyr})_{24}\text{Nd}_{28}\text{F}_{68}(\text{SePh})_{16}$: Photoluminescence.....	94-97
3.4 $[(\text{pyr})_{24}\text{Ce}_{28}\text{F}_{68}(\text{SePh})_{16}]^{3+} [\text{Ce}_3(\text{SePh})_{10}]^{1-}_3$: Synthesis, and Structure....	98-110
3.5 Conclusions.....	111
References.....	112-115
Chapter 4. Molecular Precursors to II-VI Semiconductors: $(\text{pyr})_x\text{M}(\text{SeC}_6\text{F}_5)_2$ (M = Zn,	
Cd with x = 2; M = Hg with x = 0)	
4.1 Introduction.....	116-117
4.2 $(\text{pyr})_2\text{M}(\text{SeC}_6\text{F}_5)_2$ (M = Zn, Cd) : Synthesis and Structure.....	117-127
4.3 3D+1 Modulated $\text{Hg}(\text{SeC}_6\text{F}_5)_2$: Synthesis and Structure.....	128-133
4.4 Thermolysis Reactions.....	133-135
4.5 Conclusions.....	135-136
References.....	137-139
Experimental.....	140-165
Vita.....	166

List of Tables

Table 1. Crystal data and structure refinement for $(\text{DME})_2\text{Nd}(\text{SC}_6\text{F}_5)_3$. (Page 24)

Table 2. Bond Lengths (\AA) and Angles ($^\circ$) for $(\text{DME})_2\text{Nd}(\text{SC}_6\text{F}_5)_3$. Note the long Ln-F dative bond (highlighted in red). (Page 25)

Table 3. Crystal data and structure refinement for $[(\text{THF})_3\text{Nd}(\text{SC}_6\text{F}_5)_3]_2$. (Page 26)

Table 4. Bond Lengths (\AA) and Angles ($^\circ$) for $[(\text{THF})_3\text{Nd}(\text{SC}_6\text{F}_5)_3]_2$. Note the long Ln-F dative bond (highlighted in red). (Page 27)

Table 5. Bond Lengths (\AA) and Angles ($^\circ$) for $(\text{THF})_3\text{Nd}(\text{SeC}_6\text{F}_5)_3$. Note the long Ln-F dative bond (highlighted in red). (Page 30)

Table 6. Bond Lengths (\AA) and Angles ($^\circ$) for $(\text{THF})_3\text{Sm}(\text{SeC}_6\text{F}_5)_3$. Note the Ln-F dative bond (highlighted in red). (Page 33)

Table 7. Bond Lengths (\AA) and Angles ($^\circ$) for $(\text{THF})_3\text{Er}(\text{SeC}_6\text{F}_5)_3$. (Page 38)

Table 8. Summary of Ln-ligand bond lengths (\AA) in mer-octahedral LnX_3Y_3 Coordination Compounds. (Page 40)

Table 9. Comparison of Computed (DFT) and Experimental (X-Ray) Metal-Ligand Bond Lengths (\AA) for $(\text{THF})_3\text{Yb}(\text{SC}_6\text{F}_5)_3$ and $(\text{THF})_3\text{Er}(\text{SeC}_6\text{F}_5)_3$. (Page 42)

Table 10. Bond Lengths (\AA) and Angles ($^\circ$) for $(\text{pyr})_4\text{Yb}(\text{SeC}_6\text{F}_5)_3$. (Page 44)

Table 11. Crystal data and structure refinement for $\text{DME}_3\text{Yb}_4\text{F}_2\text{O}(\text{OCH}_2\text{CH}_2\text{OCH}_3)_2(\text{SeSe})(\text{SC}_6\text{F}_5)_4 \cdot \text{DME}$. (Page 73)

Table 12. Bond Lengths (\AA) and Angles ($^\circ$) for $\text{DME}_3\text{Yb}_4\text{F}_2\text{O}(\text{OCH}_2\text{CH}_2\text{OCH}_3)_2(\text{SeSe})(\text{SC}_6\text{F}_5)_4 \cdot \text{DME}$. (Page 73)

Table 13. Fluorescence Decay Time ($^4F_{3/2} \rightarrow ^4I_{11/2}$) and the Phonon Frequencies of Some Reported Laser Hosts. (Page 83)

Table 14. Crystal data and structure refinement for $(\text{pyr})_{24}\text{Ln}_{28}\text{F}_{68}(\text{SePh})_{16}$ (Ln = Nd, Pr). (Page 87)

Table 15. Important Bond Length Ranges (\AA) for $(\text{pyr})_{24}\text{Ln}_{28}\text{F}_{68}(\text{SePh})_{16}$ (Ln = Nd, Pr). (Page 87)

Table 16. Crystal data and structure refinement for $\{[(\text{py})(\text{NH}_4)]^+[(\text{pyr})\text{Ce}(\text{NH}_3)_2(\text{SePh})_4]^- \}_2$. (Page 103)

Table 17. Bond lengths (\AA) and angles ($^\circ$) for $\{[(\text{pyr})(\text{NH}_4)]^+[(\text{py})\text{Ce}(\text{NH}_3)_2(\text{SePh})_4]^- \}_2$ (Page 103)

Table 18. Highest intensity, low angle diffraction lines for Ce_{28} and Ce dimer (Page 111)

Table 19. Crystal data and structure refinement for $(\text{pyr})_2\text{Zn}(\text{SeC}_6\text{F}_5)_2$ (Page 116)

Table 20. Bond Lengths (\AA) and Angles ($^\circ$) for $(\text{pyr})_2\text{Zn}(\text{SeC}_6\text{F}_5)_2$ (Page 117)

Table 21. Crystal data and structure refinement for $(\text{pyr})_2\text{Cd}(\text{SeC}_6\text{F}_5)_2$ (Page 121)

Table 22. Bond Lengths (\AA) and Angles ($^\circ$) for $(\text{pyr})_2\text{Cd}(\text{SeC}_6\text{F}_5)_2$ (Page 121)

Table 23. Crystal data and structure refinement for $[(\text{pyr})\text{Cd}(\text{SeC}_6\text{F}_5)_2]_2$ (Page 125)

Table 24. Bond Lengths (\AA) and Angles ($^\circ$) for $[(\text{pyr})\text{Cd}(\text{SeC}_6\text{F}_5)_2]_2$ (Page 125)

Table 25. C-Hg-C Bond Angles ($^\circ$) for molecules Hg1 – Hg9 (Page 132)

Table 26. Se-Hg-Se Bond Angles ($^\circ$) for molecules Hg1 – Hg9 (Page 134)

Table 27. Comparison between key features of $\text{Hg}(\text{SeC}_6\text{F}_5)_2$ and $\text{Hg}(\text{SePh})_2$ (Page 138)

Table 28. Observed Emission Bands and Their Measured and Calculated Radiative Properties for (a) Nd8 and (b) Nd1 Compounds (Page 140)

List of Illustrations

Fig 1. Ground state shell structure of Lanthanum showing the radially contracted and shielded 4f shell. (Page 32)

Fig 2. Energy level diagram for Ce-Yb. Arrows indicate characteristic radiative emission transitions (μm). (Page 4)

Fig 3. Representation of $\text{Yb}(\text{C}_5\text{Me}_5)_2(\text{S}_2\text{CNet}_2)$, showing early Ln-E architectures. (Page 11)

Fig 4. $(\text{pyr})_4\text{Yb}(\text{EPh})_2$ showing the utility of less bulky EPh groups in the synthesis of novel Ln-E complexes. (Page 12)

Fig 5. Fluorinated pdd-D ligand used by Hasegawa for improved rare earth optical properties. (Page 18)

Fig 6. Electronic transitions for two nonradiative relaxation pathways: Cross relaxation and excitation migration. (Page 19)

Fig 7. Energy transfer pathway from the rare earth excited state to resonant phonon energy levels of nearby organic functionalities. (Page 20)

Fig 8. Schematic representation of the vibrational quenching of the $^4\text{F}_{3/2}$ emission in Nd^{3+} by the vibrational modes of C-H bonds. (Page 21)

Fig 9. Improved Nd^{3+} emission by C-H substitution with C-F and C-D bonds of hfa-D ligand. (Page 22)

Fig 10. ORTEP of $(\text{DME})_2\text{Nd}(\text{SC}_6\text{F}_5)_3$ with thermal ellipsoids drawn at 50% probability level. (Page 24)

Fig 11. ORTEP of $[(\text{THF})_3\text{Nd}(\text{SC}_6\text{F}_5)_3]_2$ with thermal ellipsoids drawn at 50% probability level. (Page 26)

Fig 12. ORTEP of $(\text{THF})_3\text{Nd}(\text{SeC}_6\text{F}_5)_3$ with thermal ellipsoids drawn at 50% probability level. (Page 31)

Fig 13. ORTEP of $(\text{THF})_3\text{Sm}(\text{SeC}_6\text{F}_5)_3$ with thermal ellipsoids drawn at 50% probability level. (Page 33)

Fig 14. ORTEP of $(\text{THF})_3\text{Er}(\text{SeC}_6\text{F}_5)_3$ with thermal ellipsoids drawn at 50% probability level. (Page 35)

Fig 15. ORTEP of the four asymmetric $(\text{THF})_3\text{Er}(\text{SeC}_6\text{F}_5)_3$ molecules in the unit cell with thermal ellipsoids drawn at 50% probability level. (Page 36)

Fig 16. ORTEP of $(\text{pyr})_4\text{Yb}(\text{SeC}_6\text{F}_5)_3$ with thermal ellipsoids drawn at 50% probability level. (Page 45)

Fig 17. ORTEP of $(\text{pyr})_4\text{Yb}(\text{SC}_6\text{F}_5)_3$ for comparison with $(\text{py})_4\text{Yb}(\text{SeC}_6\text{F}_5)_3$, again with thermal ellipsoids drawn at 50% probability level. (Page 46)

Fig 18. Emission spectra of $(\text{DME})_2\text{Nd}(\text{SC}_6\text{F}_5)_3$ and $[(\text{THF})_3\text{Nd}(\text{SC}_6\text{F}_5)_3]_2$. (Page 49)

Fig 19. Emission decay curves of $(\text{DME})_2\text{Nd}(\text{SC}_6\text{F}_5)_3$ and $[(\text{THF})_3\text{Nd}(\text{SC}_6\text{F}_5)_3]_2$ for the $^4\text{F}_{3/2} \rightarrow ^4\text{I}_{11/2}$ transition. Inset is data derived from MC fitting model. (Page 50)

Fig 20. Emission decay curves of $(\text{DME})_2\text{Nd}(\text{SC}_6\text{F}_5)_3$ and $[(\text{THF})_3\text{Nd}(\text{SC}_6\text{F}_5)_3]_2$ for the $^4\text{F}_{3/2} \rightarrow ^4\text{I}_{13/2}$ transition. Inset is data derived from MC fitting model. (Page 51)

Fig 21. (a) Absorption spectrum for 0.0058M $(\text{THF})_8\text{Nd}_8\text{O}_2\text{Se}_2(\text{SePh})_{16}$ in THF. The inset shows the deconvolution of the absorption band at 871 nm. (b) Absorption spectrum for 0.0058M $(\text{DME})_2\text{Nd}(\text{SC}_6\text{F}_5)_3$ in DME. Labeled transitions arise from the $^4\text{I}_{9/2} \text{Nd}^{3+}$ ground state. (Page 54)

Fig 22. Observed emission bands located at 927, 1078, 1360, and 1843 nm for (THF)₈Nd₈O₂Se₂(SePh)₁₆ and 897, 1071, 1347, and 1824 nm for (DME)₂Nd(SC₆F₅)₃. (Page 61)

Fig 23. Fluorescence decay of the $^4F_{3/2} \rightarrow ^4I_{11/2}$ transition of Nd³⁺ in (THF)₈Nd₈O₂Se₂(SePh)₁₆ (circles) and the corresponding MC fit assuming a dipole-dipole interaction. The upper curve (Triangle) is the radiative decay corresponding to a decay time of 1187 μs. (Page 62)

Fig 24. Partially Labeled DME₃Yb₄F₂O(OCH₂CH₂OCH₃)₂(SeSe)(SC₆F₅)₄•DME with thermal ellipsoids drawn at 50% probability. (Page 72)

Fig 25. Core Structure: DME₃Yb₄F₂O(OCH₂CH₂OCH₃)₂(SeSe)(SC₆F₅)₄•DME with thermal ellipsoids drawn at 50% probability. (Page 75)

Fig 26. Core Structure: DME₃Yb₄F₂O(OCH₂CH₂OCH₃)₂(SeSe)(SC₆F₅)₄•DME with thermal ellipsoids drawn at 50% probability, rotated 90° with respect to Fig 25. (Page 76)

Fig 27. μ₂-oxo ligand from DME oxygen abstraction producing WSCl₄:WOSCl/DME. (Page 78)

Fig 28. Ln ion mediated C-F bond activation mechanism for C₆H₅F. (Page 79)

Fig 30. ORTEP of (pyr)₂₄Ln₂₈F₆₈(SePh)₁₆ (Ln = Nd, Pr). All protons have been removed for clarity, and thermal ellipsoids have been drawn at 10% for ease of visualization. (Page 86)

Fig 31. POV-Ray diagram of the fluoride cluster (pyr)₂₄Ln₂₈F₆₈(SePh)₁₆, with green Ln, red F, blue N (from pyr), yellow Se (from SePh), and with the C and H atoms removed for clarity. (Pages 89-90)

- Fig 32.** Depiction of different states of disorder about pyridine and selenolate ligands in $(\text{pyr})_{24}\text{Ln}_{28}\text{F}_{68}(\text{SePh})_{16}$. (Page 91)
- Fig 33.** Unit cell packing of $(\text{pyr})_{24}\text{Ln}_{28}\text{F}_{68}(\text{SePh})_{16}$ in I-42m. (Page 92)
- Fig 34.** Calculated Connolly surface showing the solvent excluded volume for a pyridine molecule. (Page 94)
- Fig 35.** Representation of lattice solvent disorder in $(\text{pyr})_{24}\text{Ln}_{28}\text{F}_{68}(\text{SePh})_{16}$. (Page 95)
- Fig 36.** Top: Absorption spectrum of $(\text{pyr})_{24}\text{Nd}_{28}\text{F}_{68}(\text{SePh})_{16}$; Bottom: Emission spectrum of $(\text{pyr})_{24}\text{Nd}_{28}\text{F}_{68}(\text{SePh})_{16}$ pumped with 800 nm light. (Page 97)
- Fig 37.** Top: Measured decay curve for the ${}^4\text{F}_{3/2} \rightarrow {}^4\text{I}_{11/2}$ transition; Bottom: spectroscopic details for $(\text{pyr})_{24}\text{Nd}_{28}\text{F}_{68}(\text{SePh})_{16}$, where $\Delta\lambda_{\text{eff}}$ = effective band width at FWHM, τ_{rad} = calculated radiative lifetime, and τ_{fl} = measured radiative lifetime. (Page 98)
- Fig 38.** Representation of disordered trimers found in $[(\text{pyr})_{24}\text{Ce}_{28}\text{F}_{68}(\text{SePh})_{16}]^{3+}[\text{Ce}_3(\text{SePh})_{10}]^{1-}_3$. (Page 100)
- Fig 39.** ORTEP of $\{[(\text{pyr})(\text{NH}_4)]^+[(\text{pyr})\text{Ce}(\text{NH}_3)_2(\text{SePh})_4]^- \}_2$, with thermal ellipsoids drawn at 50% probability level. (Page 102)
- Fig 40.** Simulated powder patterns for Ce_{28} and Ce dimer. (Page 106)
- Fig 41.** Ce_{28} Cluster : Simulated powder pattern for $50^\circ > 2\theta > 0^\circ$. (Page 107)
- Fig 42.** Ce Dimer: Simulated powder pattern for $50^\circ > 2\theta > 0^\circ$. (Page 108)
- Fig 43.** Ce_{28} Cluster : Low angle simulated powder pattern for $20^\circ > 2\theta > 0^\circ$. (Page 109)
- Fig 44.** Ce Dimer : Low angle simulated powder pattern for $20^\circ > 2\theta > 0^\circ$. (Page 109)
- Fig 45.** Experimental powder pattern of isolated crystalline powder from Ce_{28} reaction. (Page 111)

Fig 46. ORTEP of $(\text{pyr})_2\text{Zn}(\text{SeC}_6\text{F}_5)_2$ with thermal ellipsoids drawn at 50% probability level. Hydrogen atoms have been removed for clarity. (Page 118)

Fig 47. ORTEP of $(\text{pyr})_2\text{Zn}(\text{SeC}_6\text{F}_5)_2$ unit cell packing with thermal ellipsoids drawn at 50% probability. Protons and carbon atoms of pyridine molecules, as well as fluorine atoms have been removed for clarity. (Page 119)

Fig 48. ORTEP of $(\text{pyr})_2\text{Cd}(\text{SeC}_6\text{F}_5)_2$ with thermal ellipsoids drawn at 50% probability level. Hydrogen atoms have been removed for clarity. (Page 120)

Fig 49. ORTEP of $(\text{pyr})_2\text{Cd}(\text{SeC}_6\text{F}_5)_2$ unit cell with thermal ellipsoids drawn at 50% probability level. Hydrogen atoms have been removed for clarity. (Page 122)

Fig 50. ORTEP of $[(\text{pyr})\text{Cd}(\text{SeC}_6\text{F}_5)_2]_2$ unit cell with thermal ellipsoids drawn at 50% probability level. Hydrogen atoms have been removed for clarity. (Page 124)

Fig 51. Top: ORTEP of $\text{Hg}(\text{SeC}_6\text{F}_5)_2$ oriented with the Se-C bond in the plane of the paper. Bottom: ORTEP of $\text{Hg}(\text{SeC}_6\text{F}_5)_2$ oriented with the Se-C bond orthogonal to the plane of the paper. Both have thermal ellipsoids drawn at 50% probability. (Page 127)

Fig 52. ORTEP of modulated $\text{Hg}(\text{SeC}_6\text{F}_5)_2$ super cell viewed perpendicular to the 100, 010, and 001 direction (respectively, from top to bottom). (Page 129)

Fig 53. II-VI precursor thermolysis reaction temperature profile. (Page 132)

Fig 54. (a) Experimental energy transfer function of the $^4\text{F}_{3/2} \rightarrow ^4\text{I}_{11/2}$ decay of Nd^{3+} in $(\text{THF})_8\text{Nd}_8\text{O}_2\text{Se}_2(\text{SePh})_{16}$. The two slopes on the temporal window show the evolution of energy transfer from dipole–dipole (DD) to a migration process at a later time. (b)

Experimental energy transfer function of the $^4\text{F}_{3/2} \rightarrow ^4\text{I}_{11/2}$ decay of Nd^{3+} in $(\text{DME})_2\text{Nd}(\text{SC}_6\text{F}_5)_3$. The slope, $s = 3/10$, shows the predominance of a quadrupole–quadrupole interaction-mediated energy transfer process. (Page 142-143)

- Fig 55.** Schematic representation of cross relaxation and excitation migration mechanisms quenching Nd^{3+} fluorescence. (Page 148)
- Fig 56.** Schematic representation of the vibrational quenching of the $^4\text{F}_{3/2}$ emission in Nd^{3+} by the vibrational modes of C–H and O–H functional groups. (Page 150)
- Fig 57.** Visible absorption spectrum for $(\text{THF})_3\text{Er}(\text{SeC}_6\text{F}_5)_3$. (Page 156)
- Fig 58.** Visible absorption spectrum for $(\text{THF})_3\text{Nd}(\text{SeC}_6\text{F}_5)_3$. (Page 158)
- Fig 59.** Wire frame illustration of isolated $[(\text{CH}_3)_4\text{N}]^+[\text{SeC}_6\text{H}_5]^-$. (Page 159)
- Fig 60.** ORTEP of $[(\text{THF})_{10}\text{Nd}_6\text{O}_2(\text{Se})_4(\text{SeC}_6\text{F}_5)_6][\text{Hg}(\text{SeC}_6\text{F}_5)_2]_2 \cdot 2\text{THF}$. (Page 160)
- Fig 61.** ORTEP of $[(\text{THF})_4\text{Nd}_3(\text{SePh})_9]_n \cdot 2.5\text{THF}$. Thermal ellipsoids drawn at 50% probability. (Page 161)
- Fig 62.** ORTEP of $[(\text{THF})_4\text{Nd}_3(\text{SePh})_9]_n \cdot 2.5\text{THF}$ unit cell packing. (Page 162)
- Fig 63.** Comparison of calculated powder pattern of $(\text{pyr})_{24}\text{Pr}_{28}\text{F}_{68}(\text{SePh})_{16} \cdot 26(\text{C}_5\text{H}_5\text{N})$ with experimental powder pattern of $(\text{pyr})_{24}\text{La}_{28}\text{F}_{68}(\text{SePh})_{16} \cdot 26(\text{C}_5\text{H}_5\text{N})$. (Page 163)

List of Abbreviations

Ln, general designation for any of the 14 lanthanide atoms or ions from La-Yb.

L, neutral donor ligand (i.e. Pyridine, 1,2-Dimethoxyethane, Tetrahydrofuran)

Pyr or py, Pyridine

DME, 1,2-Dimethoxyethane

THF, Tetrahydrofuran

M, any transition or main group metal

CCDC, *Cambridge Crystallographic Data Centre*

E, any of the chalcogen atoms, i.e., S, Se, Te

QE, Quantum Efficiency

PL, Photoluminescence

Introduction:

The history of the lanthanides is not relatively old when one considers that just under a century ago, due to problems of separation, there were still claimed to be 100s of elements in the lanthanide series. It wasn't until 1913 that Moseley *et al.* used X-ray spectroscopy to prove that only 14 elements resided in the 4f series. It wasn't until just 50 years ago that enough progress was made in lanthanide chemistry to make these rare earth metals technologically important. In an address to the British Association in 1887, Sir William Crooks, an English chemist and physicist stated, "These elements (rare earths) perplex us in our researches, baffle us in our speculations, and haunt us in our dreams. They stretch like an unknown sea before us - mocking, mystifying and murmuring strange revelations and possibilities". This delayed progress of rare earth chemistry was undoubtedly due to the lack of techniques available to separate the metals from their respective ores, and the fact that their chemistry was quite unlike that of the transition metals. Research with these elements has continually grown, but there still exists two conflicting schools of thought on the matter, and in fact many scientists throughout the decades had begun to declare the chemistry of the lanthanides predictable and boring. This became such a common trend that in a 1971 chemistry text book written by G.C. Pimentel and R.D. Spratley it was stated, "Lanthanum has only one important oxidation state in aqueous solution, the 3^+ state. With few exceptions, this tells the whole boring story about the other 14 Lanthanides."¹ As it turns out these conflicting viewpoints have both proven to be true, and it is because of the lanthanides' predictability *and* uniqueness that interest in the lanthanides continues to grow.

At the heart of the lanthanides' "uniqueness" is the nature of their atomic structure. In most cases the ionic radii of the lanthanide ion and the coordinating ions can be added such that predictable ionic bond distances can be calculated by radii summation. Ionic radii have been calculated by R.D. Shannon² and are specific for each atom type, charge, and coordination number. Traversing the 4f series, the lanthanide ionic radii decrease predictably in size, and this phenomenon is known as the "lanthanide contraction". Small differences in solubility and complexation of the 14 lanthanides can be attributed to this size effect and correlations between metal radii and structural features of isolable complexes can be made.

With the exception of the latter part of the actinide series, no elements save the lanthanides, have shielded valence orbitals. The 4f valence shell of a lanthanide ion is radially contracted such that it is shielded from its surroundings by filled radially extended $5s^2$ and $5p^6$ orbitals (Fig. 1). This one fact alone is a major contributor to many of the fundamental physical and chemical properties of the lanthanides. Lanthanide bonding is characteristically ionic as the filled $5s^2$ and $5p^6$ orbitals inhibit overlap of the valence 4f orbital with the bonding orbitals of coordinating ligands, and as a result the lanthanide ion is experienced as a sphere of positive charge by coordinating ions.

The nature of the optical properties of the lanthanides is also due in part to this shielding effect. Emission bands are relatively narrow, and show little change from crystal field effects. Within the lanthanide series each metal ion has a discrete set of energy levels available for absorption and emission of photons. This gives a wide range of accessible wavelengths for various optical processes (Fig. 2).

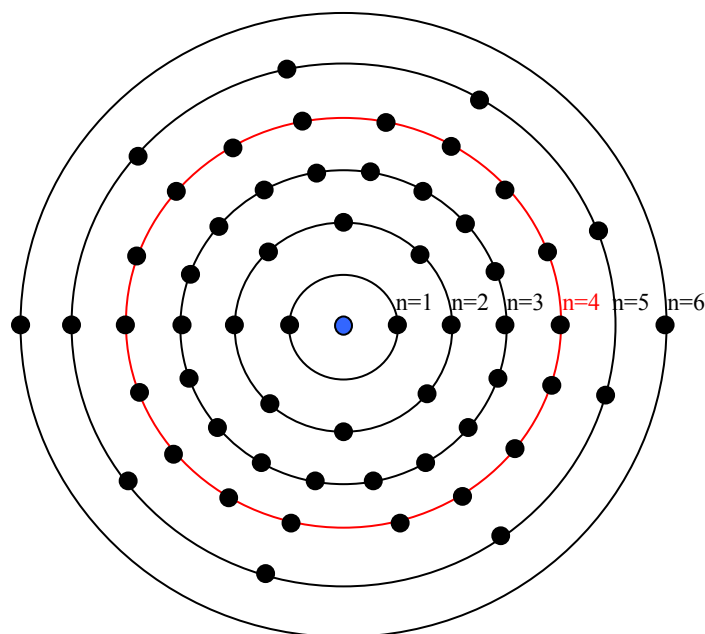


Fig 1. Ground state shell structure of Lanthanum showing the radially contracted and shielded 4f shell (highlighted in red).

Another effect valence orbital shielding has on bonding is that the coordination environment in lanthanide complexes is largely non-directional and determined by ligand requirements not by the bonding requirements (orbital overlap, orientation, and phase) normally seen in covalent models. With poor orbital overlap, steric effects dominate the bonding in lanthanide molecules, and electrostatic interactions are the main driving force behind complex formation. As a result, coordination numbers are often high with 6-8 coordinate species being common, and an increasingly large number of reports with coordination numbers greater than 10 are found in the literature.³⁻¹³

Fig 2. Energy level diagram for Ce-Yb. Arrows indicate characteristic radiative emission transitions (μm).

The shielding of the 4f orbitals also contributes to other fundamental characteristics of the lanthanides. It has been well known that throughout the series the different lanthanide metals share a common principle oxidation state of 3^+ when ionized, and only a few metals have traditionally adopted a Ln^{2+} (Eu, Sm, and Yb) or Ln^{4+} (Ce, Pr) oxidation state. More recently the number of lanthanide metals able to form isolable species where the metal is in a 2^+ oxidation state has doubled. Work by Bochkarev and Evans has led to the successful synthesis of redox active lanthanide molecules containing divalent Tm, Dy, and Nd ions.^{14,15} These molecules exhibit similar reduction capabilities compared to the already established Eu^{2+} , Sm^{2+} , and Yb^{2+} complexes. This remarkable discovery illustrates that the chemistry of the lanthanides is anything but predictable since oxidation states were believed to be one of the most well understood properties of lanthanide ions since the early 1900s.

Our starting point to better understand the nature of molecular rare earth chemistry began by exploring the fringes of what has been deemed “typical” lanthanide chemistry; the bonding of lanthanides to chalcogens ($\text{E} = \text{S}, \text{Se}, \text{Te}$). Reactions producing molecular species containing Ln-E bonds have received increasing attention over the past decade as the apparent hard/soft mismatch is inherently intriguing. The highly ionic nature of the small electropositive “hard” Ln ions in conventional lanthanide molecules contrasts with the relatively “soft” covalent nature of the chalcogens, making the nature of the lanthanide chalcogen bonding scheme unclear. While a purely ionic bonding model of lanthanide complexes is valid in most cases, and ionic bond summations predict a largely ionic bonding scheme, some degree of directional bonding in Ln-E complexes has been proposed. These observations imply that there is of some degree of covalent

character in these molecules. Further research into these novel Ln-E molecules will better our fundamental understanding of the bonding scheme between lanthanides and chalcogens. Ln-E molecules are also of interest because they may be suitable precursors for the incorporation of lanthanide ions in new optical materials. The Ln-E bonding scheme could also prove to be a stepping stone for the preparation of altogether novel lanthanide species. Through careful design, new Ln-E species have the potential to show improved optical properties in highly luminescent lanthanide materials.

From a technological perspective, it was only in the 1960s that rare earth containing species were first used in technological applications. Europium was doped into an yttrium oxysulfide host, and the resulting phosphor replaced the standard weakly emitting red phosphor (which had to compete with stronger intensity green and blue phosphors) in televisions.¹⁶ It wasn't until 1964 that J.E. Geusic *et al.* at Bell Labs created the widely used Nd:YAG laser. The Nd:YAG laser has become one of the principle lasers used in a variety of applications, from materials processing (drilling and spot welding), in military uses including range finders and target designators, to scientific research such as pumping tunable visible light lasers, and mass spectroscopy.¹⁷

Lanthanide chemistry is becoming increasingly important and the need for new lanthanide materials is seen by looking at today's technological advances in optics and telecommunications. In the early 2000's we began to see lanthanide research reaching new heights, with constant advances in optical and telecommunication materials fueling the research effort. For example, optical fibers used in telecommunication systems are doped with Erbium for signal amplification, and erbium-doped waveguide amplifiers show improved optical gain.¹⁸ Europium and Cerium doped solid-state materials are also

being used to convert UV and blue light into white light for new high efficiency lighting applications.¹⁹

One commonality between the above devices is that they all rely on solid-state lanthanide sources. This puts a serious limitation on the utility of such species in new materials, and applications requiring soluble lanthanide sources. Solid-state lanthanide materials are extremely insoluble in apolar environments, making the incorporation of these light emitting ions into novel host environments such as polymers or quality thin films impractical. The realization of materials having strong emission intensities and lifetimes that are able to be incorporated into these matrices would advance such areas as optical fibers, large area displays, organic LEDs, and open the door for a new era of optical technology. There exists a need for the discovery of lanthanide complexes that can rival solid-state materials with respect to certain key optical properties, and can also be used for applications where soluble lanthanide sources are needed. Interest in molecular lanthanide ion complexes has grown considerably since the realization that such complexes could be utilized as light conversion molecular devices (LCMDs).²⁰ Efficient LCMDs may be used in luminescent probes, fluorescent lighting, electroluminescent devices, and even antireflection coatings for solar cells.²¹

The main focus of the research in this area, and the topic of this thesis, is the preparation of lanthanide complexes with organic based ligands that have physical properties not available to solid-state materials being used today. The organization of this thesis will be a progression from smaller more easily understood monomers and dimers to larger more complex species. The successful isolation of the largest nano-scale molecular lanthanide species to date (of its kind) will be discussed. The structural

relationships between reaction variables will be discussed and the progression of structural vs. optical properties that arise in the prepared Ln-E species will be detailed.

References

- ¹ Pimentel, G.C., Sprately R.D, *Understanding Chemistry*, Holden-Day Inc., San Francisco, **1971**.
- ² Shannon, R.D. Revised Effective Ionic Radii and Systematic Studies of Interatomic Distances in Halides and Chalcogenides. *Acta Cryst* **1976**, *A32*, 751.
- ³ Schumann, H., Herrmann, K., Muehle, S. H., Dechert, S. Organometallic compounds of the lanthanides. 168. Lanthanidocene complexes containing sulfur-functionalized cyclopentadienyl ligands. *Zeitschrift fuer Anorganische und Allgemeine Chemie* **2003**, *629*, 1184.
- ⁴ Wang, S., Li, H., Xie, Z. A Novel Full-Sandwich Lanthanacarborane Complex Bearing an η^7 -Carboranyl Ligand, $\{[\eta^7\text{Me}_2\text{Si}(\text{C}_1_3\text{H}_9)(\text{C}_2\text{B}_{10}\text{H}_{11})]_2\text{Yb}(\text{III})\}_2\text{Yb}(\text{II})\} \{\text{Na}_8(\text{THF})_{20}\}$. *Organometallics* **2001**, *20*, 3842.
- ⁵ Watson, P.L., Tulip, T.H., Williams, I. Defluorination of perfluoroolefins by divalent lanthanoid reagents: activating carbon-fluorine bonds. *Organometallics* **1990**, *9*, 1999.
- ⁶ Shinomoto, R., Zalkin, A., Edelstein, N.M. Preparation of some Lewis base adducts of tris(methyltrihydroborato)holmium and -ytterbium and crystal structures of tris(methyltrihydroborato)ytterbium(III) diethyl etherate and tris(methyltrihydroborato)holmium(III) bis(pyridine). *Inorganica Chimica Acta* **1987**, *139*, 97.
- ⁷ Hosmane, N.S., Wang, Y., Zhang, H., Oki, A.R., Maguire, J.A., Waldhoer, E., Kaim, W., Binder, H., Kremer, R.K. A Systematic Synthetic Approach to a Novel, Mixed 2,3-C₂B₄- and 2,4-C₂B₄-Erbium(III) Carborane Bent-Sandwich Complex. *Organometallics* **1995**, *14*, 1101.
- ⁸ Wang, S., Wang, Y., Cheung, M., Chan, H., Xie, Z. Substituents effect on molecular structures of 13-vertex closo-metallacarboranes of rare earths. Synthesis and structural characterization of metallacarboranes bearing nido- and arachno-carborane ligands. *Tetrahedron* **2003**, *59*, 10373.
- ⁹ Berube, C.D., Yazdanbakhsh, M., Gambarotta, S., Yap, G.P.A. Serendipitous Isolation of the First Example of a Mixed-Valence Samarium Tripyrrole Complex. *Organometallics* **2003**, *22*, 3742.
- ¹⁰ Bunzli, J.C.G., Klein, B., Chapuis, G., Schenk, K.J. Crystal structure and emission spectrum of the undecacoordinate complex tris(nitrato)-1,4,7,10,13-pentaoxacyclopentadecaneeuropium(III). *Inorganic Chemistry* **1982**, *21*, 808.

-
- ¹¹ Hou, Z., Koizumi, T., Nishiura, M., Wakatsuki, Y. Lanthanide(II) Complexes Bearing Linked Cyclopentadienyl-Anilido Ligands: Synthesis, Structures, and One-Electron-Transfer and Ethylene Polymerization Reactions. *Organometallics* **2001**, 20, 3323.
- ¹² Qian, C., Nie, W., Sun, J. Synthesis of diphenylmethylene bridged fluorenyl cyclopentadienyl lanthanocene complexes with C_s symmetry and crystal structures of the ate complexes $[Li(thf)_4][LnCl_2\{(C_{13}H_8)CPh_2(C_5H_4)\}]$ and $[Li(thf)_4][Ln(BH_4)_2\{(C_{13}H_8)CPh_2(C_5H_4)\}]$ ($Ln = Nd$ or La). *Journal of the Chemical Society, Dalton Transactions: Inorganic Chemistry* **1999**, 18, 3283.
- ¹³ Evans, W.J., Johnston, M.A., Clark, R.D., Ziller, J.W. Variability of (ring centroid)-Ln-(ring centroid) angles in the mixed ligand C_5Me_5/C_8H_8 complexes $(C_5Me_5)Ln(C_8H_8)$ and $[(C_5Me_5)Yb(THF)](\mu-\eta^8:\eta^8-C_8H_8)[Yb(C_5Me_5)]$. *Journal of the Chemical Society Dalton Transactions* **2000**, 10, 1609.
- ¹⁴ Evans, W.J. The Importance of Questioning Scientific Assumptions: Some Lessons from f Element Chemistry. *Inorg. Chem.* **2007**, 46, 3435.
- ¹⁵ Bochkarev, M. N., Fedushkin, I. L., Fagin, A. A., Petrovskaya, T.W., Ziller, J. W., Broomhall-Dillard, R. N. R., Evans, W. J. *Angew. Chem., Int. Ed. Engl.* **1997**, 36, 133.
- ¹⁶ Lutz, D. The quietly expanding rare earth market. *The Industrial Physicist* **1996**, 2, 28.
- ¹⁷ "Lasers in Chemistry" (http://www.lasalle.edu/academ/chem/laser_web/index.htm), accessed 1/15/05).
- ¹⁸ Strohhöfer C., Polman A. Absorption and emission spectroscopy in Er^{3+} - Yb^{3+} doped aluminum oxide waveguides. *Optical Materials* **2003**, 21, 705.
- ¹⁹ Park, W.J., Song, Y.H., Moon, J.W., Jang, D.S., Yoon, D.H. From Blue-Purple to Red-Emitting Phosphors, $A_{2-x}B_xP_2O_7$: Eu^{2+} , Mn^{2+} (A and B = Alkaline-Earth Metal) under Near-UV Pumped White LED Applications. *Journal of the Electrochemical Society* **2009**, 156, J148.
- ²⁰ Lehn J.-M., Perspectives in Supramolecular Chemistry - From Molecular Recognition towards Molecular Information Processing and Self-Organization. *Angew. Chem. Int. Ed. Engl.* **1990**, 29, 1304.
- ²¹ de Sa' G.F., Malta O.L. Spectroscopic properties and design of highly luminescent lanthanide coordination complexes. *Coordination Chemistry Reviews* **2000**, 196, 165.

Chapter 1. Fluorinated Derivatives of Lanthanide Chalcogenolate Complexes

1.1 Introduction

It was originally believed that sterically demanding, highly electronegative ligands such as pentamethyl cyclopentadienyl(Cp*) were needed to synthesize molecules with Ln-E bonds. By effectively blocking solvent molecules and oxygen containing ligands from the metal center, the Ln-E bond was stabilized. In 1981, Tilley *et al.* synthesized an early example of a Ln-E molecule, $\text{Yb}(\text{Cp}^*)_2(\text{S}_2\text{CNEt}_2)$, containing a Ln-S bond using the bulky ligand approach for stabilization of the product (Fig. 3).¹ Similarly, in 1988 Berg *et al.* used the bulky ligand approach to prepare $[(\text{Cp}^*)_2\text{Yb}]_2[\mu_2\text{E}]$ (E is S, Se, Te) by the reaction of $(\text{Cp}^*)_2\text{Yb}$ with Ph_3PS , As_2S_3 , COS , Ph_3PSe , elemental Se, $n\text{-Bu}_3\text{PTe}$ or elemental Te to give the bridging chalcogenido complexes.²



Fig 3. Representation of $\text{Yb}(\text{Cp}^*)_2(\text{S}_2\text{CNEt}_2)$, showing early Ln-E architectures.

More recent advances in lanthanide chalcogenolate chemistry have led to the development of new methodologies for the synthesis of stable Ln-E complexes without the need for sterically bulky ligand species. Novel Ln-E complexes are now being synthesized using novel chalcogenolate ligands (EPh, E = S, Se, Te), and the formation of such stable species as $(\text{pyr})_4\text{Yb}(\text{EPh})_2$ ³ has been realized (Fig. 4).

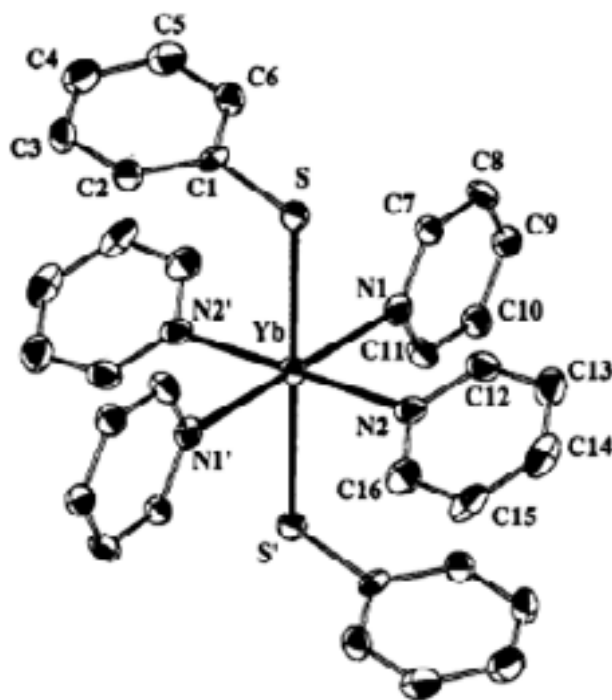
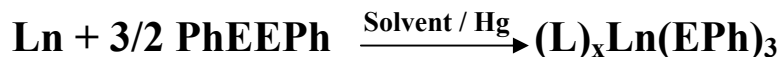


Fig 4. $(\text{pyr})_4\text{Yb}(\text{EPh})_2$ showing the utility of less bulky EPh groups in the synthesis of novel Ln-E complexes.

A variety of new Ln-E molecules and clusters have now been synthesized by the general reaction of lanthanide metals with diaryldichalcogen (PhEPh) starting materials in a variety of Lewis base solvents according to the general scheme:



where L = solvent (pyridine, DME, or THF) and catalytic amounts of mercury were added. Mercury is able to catalyze the reaction in two ways. The mercury can insert itself into the E-E bond, thus activating the bond and reducing the PhEPh. Through transmetallation, the lanthanide metal is then oxidized and reduction of the mercury occurs. The mercury can also activate the Ln by forming an amalgam with the Ln metal that activates the metal for insertion into the E-E bond of the PhEPh. An inclusive series of Ln-E molecules has been synthesized, with differing structural characteristics due to systematic variation of the metal, ligand, and solvent. This new approach to stabilize the Ln-E bond has proven successful for the preparation of molecular lanthanide species with unique physical and chemical properties.

The multitudinous number of novel Ln-E containing species now prepared in this way reveals a correlation between the reaction variables with the structural features of the resultant product. It was found that by varying the metal, chalcogen, or neutral donor, products with vastly different structural features arose. The isolation of these species proved useful, not only to better understand the chemistry from a theoretical perspective, but also for the design and isolation of larger, more complex species. In a study by Lee *et*

al., it was found that for benzenethiolates in pyridine, changing the Ln metal shows marked effects on the resultant structure. Three species, $(\text{pyr})_3\text{Yb}(\text{SPh})_3$, $[(\text{pyr})_4\text{Ho}(\text{SPh})_3]_2$, and $[(\text{pyr})_3\text{Sm}(\text{SPh})_3]_4$ were isolated, showing a striking change in nuclearity upon increasing the ionic radii of the metal.⁴ Increasing the ionic radius of the metal allows the E-Ph ligands to more easily bridge metal centers. By changing the chalcogenolate ligand, benzeneselenolate complexes were isolated using THF as the donor solvent. Late metals (Ho, Er, Tm) crystallized as $(\text{THF})_3\text{Ln}(\text{SePh})_3$ monomers, while larger metals (Pr, Nd, Sm) gave rise to 1D coordination polymers, $[(\text{THF})_4\text{Ln}_3(\text{SePh})_9]_n$. In $(\text{pyr})_4\text{Yb}(\text{SePh})_2$ and $(\text{pyr})_5\text{Yb}(\text{TePh})_2$, the longer Ln-E bond decreases the steric repulsions between the phenyl and pyridine rings allowing for the coordination of an additional neutral donor in $(\text{pyr})_5\text{Yb}(\text{TePh})_2$. Choice of neutral donor also has significant effects on the resultant structure as evidenced by $[(\text{THF})_4\text{Sm}_3(\text{SePh})_9]_n$ and $[(\text{pyr})_3\text{Sm}(\text{SePh})_3]_2$, where the more basic pyridine is able to effectively compete for coordination about the metal center and terminate the oligomerization of the product. While substitution of the group attached to the chalcogen only weakly (when at all) alters the isolated EPh structure, the groups studied were only chosen to impart “bulkiness” around the coordination sphere. 2,4,6-substituted aryl and $\text{Si}(\text{SiR}_3)_3$ based chalcogenolate complexes were also compared, all of which possess similar electronic environments with respect to the chalcogen (i.e. little change of electron density about the chalcogen), and have little to no bonding affinity to the metal itself other than through the chalcogen. It would benefit these studies to prepare species where functional groups attached to the chalcogen have an electron withdrawing nature and/or have an affinity for the metal center.

The impetus for the work described herein is twofold. Firstly, we wanted to better our understanding of structure/property relationships between Ln-E species. Secondly, we wanted to use this knowledge to prepare larger, more complex species with improved optical properties. Initial research in this area was in the synthesis of fluorinated analogs to hydrocarbon Ln-E complexes. Isolation of fluorinated derivatives of the $(L)_x\text{Ln}(\text{EPh})_y$ molecules has brought about novel Ln-EC₆F₅ based complexes that show novel chemical and physical properties. These fluorinated species also have new structural features not found in the hydrocarbon analogs. By the addition of fluorine atoms, electron density is essentially drawn away from the chalcogen and into the aromatic ring, resulting in stabilization of the negative charge about the chalcogen. There also exists a stronger electrostatic interaction between the highly electronegative fluorine atom with the electropositive lanthanide metal that is not readily seen in hydrocarbon analogs. Because steric considerations vary little between fluorinated and non fluorinated species, interpretations based on changing the electronic environment about the ligand can be made. Following similar reactions used for the preparation of the hydrocarbon analogs, and having commercially available pentafluorobenzenethiol, Melman prepared the first fluorinated lanthanide chalcogenolate complexes, $(L)_x\text{Ln}(\text{SC}_6\text{F}_5)_y$ (L = THF for Ce, Ho, Sm, Eu, and Er; L = py for Sm, Yb; L = DME for Er).⁵

It has become clear from these initial studies that substantial structural changes can be attributed to a change in the electronic properties of the ligands. There is an increased propensity for π - π stacking of the arene rings that changes both the inter and intra molecular structures compared to the hydrocarbon analogs. The greatest structural effects however, are the presence of dative Ln-F interactions increasing the coordination

number of the resultant Ln-E complex. These dative interactions are usually weak, as evidenced by their longer than predicted metal-F bond lengths.

For the fluorinated derivatives of lanthanide thiolates, a decrease in nuclearity can best be seen by comparing fluorinated Sm thiolate molecules with non fluorinated Sm molecules. In the hydrocarbon analog, the THF species forms a 1D polymer and the pyridine adduct forms a tetramer (the more strongly donating pyridine effectively competes for coordination to the metal center, thus arresting polymerization). For the analogous fluorinated species, the THF adduct forms a dimer and the pyridine adduct forms a monomer. The reason for this reduction in nuclearity using either solvent is two part; First, the fluorine atom withdraws electron density from the chalcogen, making it less basic. This reduces the chalcogen's ability to bridge metal centers. Second, the fluorine atom has the ability to saturate the primary coordination sphere by effectively competing for access to the metal center. Depending on the metal and solvent used, this dative interaction can be eliminated, as seen in seven coordinate $(\text{pyr})_4\text{Yb}(\text{SC}_6\text{F}_5)_3$.

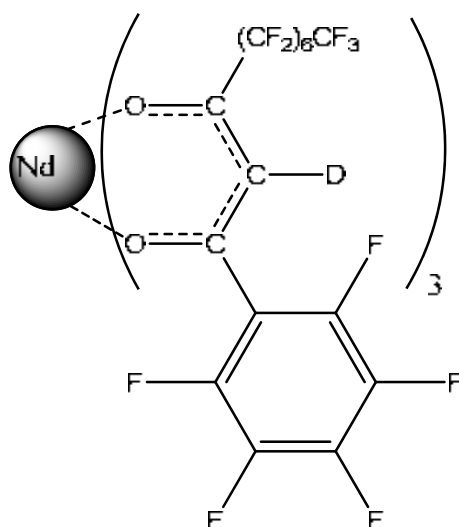
In addition to expanding our fundamental knowledge of Ln-E complexes, new fluorinated derivatives have the potential to show enhanced optical properties. Initial observations of physical crystal decomposition and x-ray diffraction data show $(\text{L})_x\text{Ln}(\text{SC}_6\text{F}_5)_y$ compounds being more air stable than their hydrocarbon analogs. This is presumably due to the inductive stabilization of the negative charge around the anion by the fluoride substituents. The creation of dative interactions between the lanthanide cation and the electronegative fluorine atom also creates stability through chelate effects. Fluorinated compounds are also substantially more soluble in polar solvents due in part to the polarization of electron density away from the E reducing the formation of oligomeric

products. The increased solubility of these new Ln-E complexes could allow for the incorporation of photoluminescent lanthanide ions into new host matrixes, namely organic polymers. Applications utilizing such soluble lanthanide sources include optical fiber coatings and planar waveguides. For lanthanide sources to be used in real devices, emission intensity and lifetime (radiative decay) optimization is essential in order to rival current solid-state Ln sources.

Common to both solid-state and molecular lanthanide sources is the nature of their optical properties. The luminescence of lanthanide ions is often from forbidden f-f electronic transitions (Laporte selection rules, i.e. $\Delta l = 0$ is forbidden). This is advantageous because emission lifetimes stemming from these transitions can be relatively long (in the micro to millisecond range). A less desirable consequence, however, is that direct excitation of a forbidden f-f transition is hindered because of the ions poor ability to absorb energy. For molecular species, poor energy absorption by the Ln ion can be improved by utilizing the “antenna effect”. This effect is essentially the attachment of a chromophore based ligand to the metal ion. The chromophore acts like an antenna in that it will absorb higher energy light and transfer this energy to the metal ion. Hasegawa *et al.* showed improved Nd(III) photoluminescence by using a pentafluorophenyl group as a chromophore (Fig 5).⁶

The singlet excited state of these fluorinated aromatic rings goes to the triplet state through intersystem crossing, and through resonance of the lowest triplet state with that of the excited levels of Nd(III) ions, improved Nd(III) emission was observed. The chromophore was excited at 359nm where Nd(III) has no absorption, showing strong

photosensitization of Nd(III) by the chromophore. While this method shows promise, it still relies on high energy excitation sources rather than direct photon absorption by the



Nd(pdd-D)₃:tris(4,4,5,5,6,6,7,7,8,8,9,9,10,10-pentadecafluoro-1-pentafluorophenyl-1,3-decanedionate)neodymium(III)

Fig 5. Fluorinated ligand used by Hasegawa for improved Nd radiative emission.

metal ion itself. Using high energy excitation sources is disadvantageous because of energy requirements and because there is an increased likelihood of non-radiative emission processes whenever there is a large energy difference between absorption and emission bands.

Another method employed to increase the emission properties of organo-lanthanide complexes is to reduce key competitive relaxation processes that can quench radiative emission of the absorbed energy. In addition to concentration quenching mechanisms such as cross relaxation and excitation migration (Fig 6), resonant phonon

energy transfer (Fig 7) appears to be one of the most detrimental non-radiative emission pathways available to these systems.

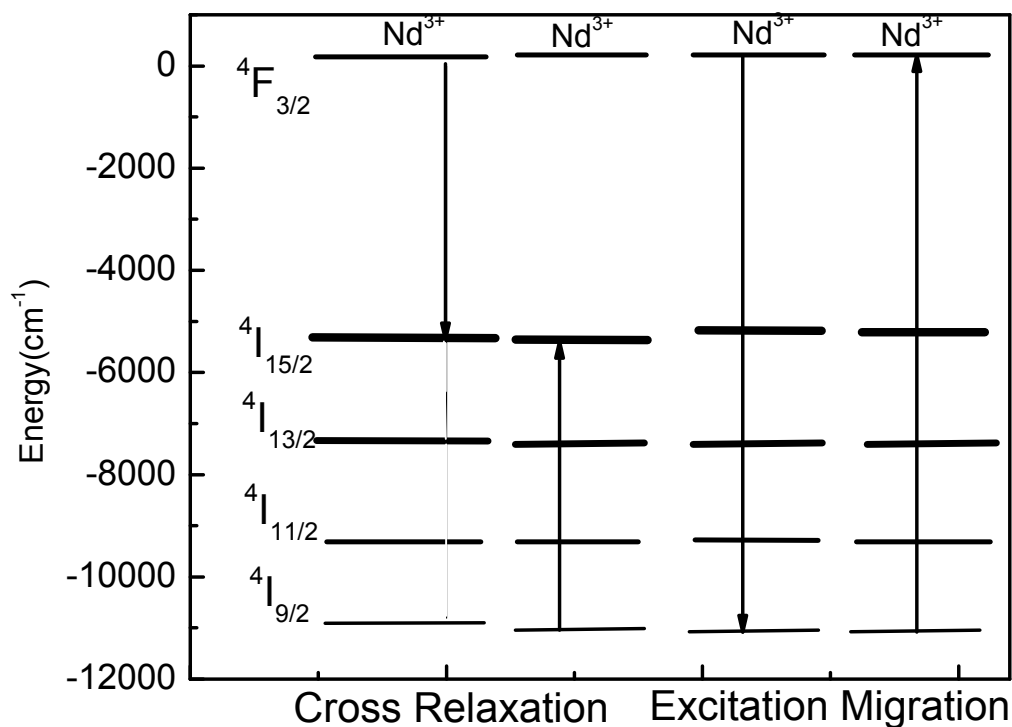


Fig 6. Electronic transitions for two nonradiative relaxation pathways: Cross relaxation and excitation migration.

With increasing control over the structural features of Ln-E species, we should also have a greater degree of control over these processes. Given the organic nature of the ligands surrounding the metal ion, it is clear that a high energy phonon environment around the metal ion can exist. High energy phonon environments having vibrational relaxation energies that match radiative transition energies of the metal ion can quench

emission intensities. This non-radiative process is caused specifically by vibronic coupling of the $v = 2$ vibrational states of C-H bonds (Fig 8) with the emission energy of the lanthanide ion. For example, the four near-IR radiative transitions of Nd^{3+} originate from the $^4\text{F}_{3/2}$ state, and the energy gap for the $^4\text{F}_{3/2} \rightarrow ^4\text{I}_{15/2}$ transition is at $\sim 5400\text{cm}^{-1}$ ($\sim 1.8\mu\text{m}$). This matches well with the 2nd order vibrational energy of C-H bonds, which is 5900cm^{-1} .

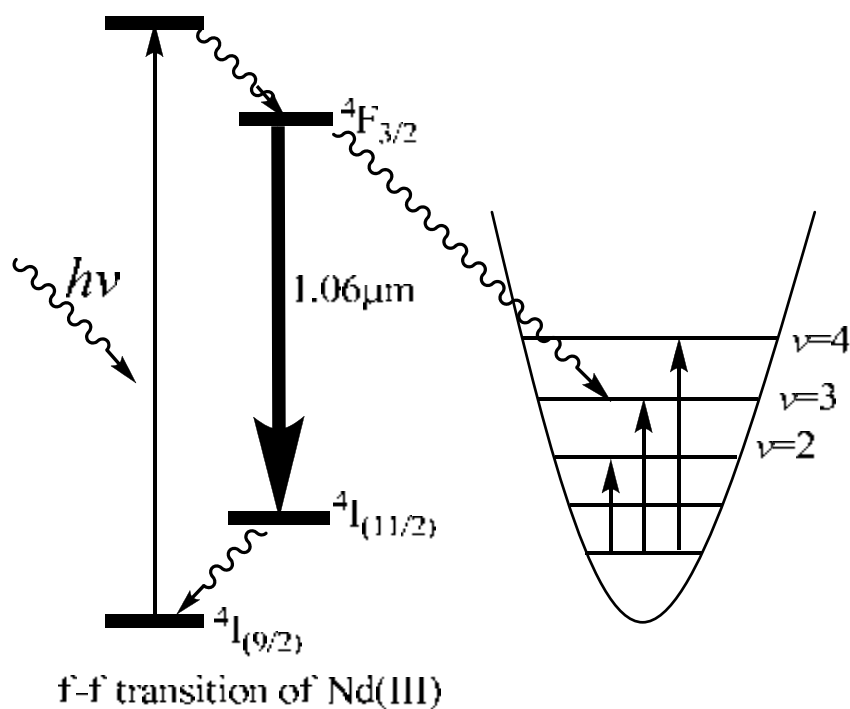


Fig 7. Energy transfer pathway from the rare earth excited state to resonant phonon energy levels of nearby organic functionalities.

Minimizing the C-H bonds around the Nd^{3+} ion will decrease these non-radiative decay pathways, and the corresponding emission intensities will be stronger. This can be accomplished by introducing ligands and solvents containing C-F or C-D functionalities which would require higher order vibrational overtones to effectively match the emission energies of the rare earth ion. While second order C-H vibrations match the Nd^{3+} ion's radiative transitions, only sixth (C-F) and third (C-D) order overtones match the Nd^{3+} ion's radiative emission energies. The sixth overtone for a C-F stretching vibration is 5400 cm^{-1} and the third overtone for a C-D vibration is 6300 cm^{-1} .

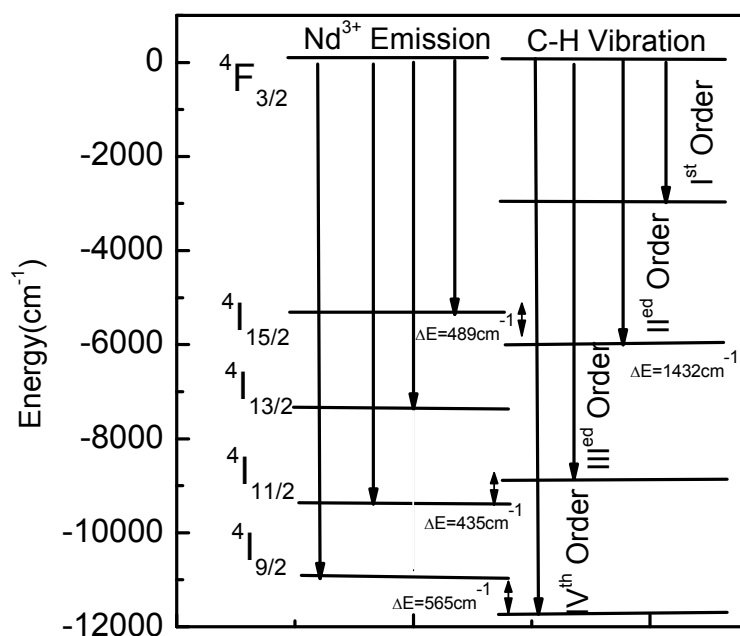


Fig 8. Schematic representation of the vibrational quenching of the $4F_{3/2}$ emission in Nd^{3+} by the vibrational modes of C-H bonds.

In an early report showing improved radiative emission by controlling vibrational coupling, Hasegawa *et al.* first observed effective luminescence for Nd^{3+} ions in organic

solvents by eliminating C-H and O-H groups around the Ln ion and using deuterated solvents. In this study, quantum efficiencies of 0.1% (methanol-d₄) and 0.6% (DMF-d₇) were measured, and lifetimes up to 6.30 μs for the $^4F_{3/2} \rightarrow ^4I_{11/2}$ transition in Nd(hfa-D)₃⁷ (Fig. 9) were measured by substituting C-H groups with C-F and C-D functionalities.

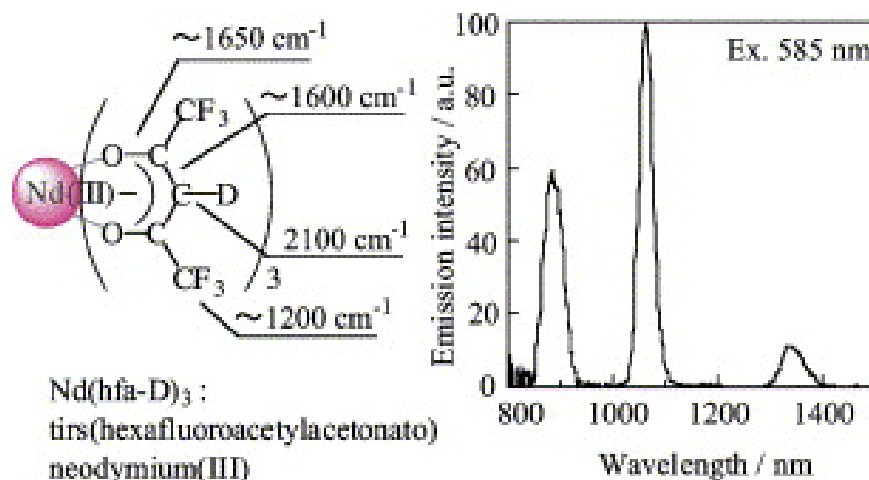


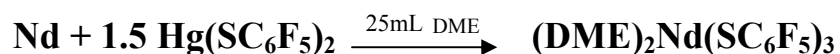
Fig 9. Improved Nd³⁺ emission by C-H substitution with C-F and C-D bonds of hfa-D ligand.

While this is a clear indication that the local environment around the photo active metal center is key to developing increasingly efficient luminescent species, the low quantum efficiencies seen for these systems is an issue that must be addressed. Following in this chapter is a detailed discussion of our initial efforts to prepare luminescent rare earth species and of our progress in correlating structure with chemical, physical, and optical properties.

1.2 Lanthanide Thiolates: Synthesis and Structure

The starting point for this endeavor was the successful synthesis of novel trivalent lanthanide compounds with fluorinated thiolate ligands. Lanthanide perfluorochalcogenolate molecules, $(\text{DME})_2\text{Nd}(\text{SC}_6\text{F}_5)_3$ (**1**) and $[(\text{THF})_3\text{Nd}(\text{SC}_6\text{F}_5)_3]_2$ (**2**) were initially prepared. Because both of these molecules have low vibrational energy environments (reduction of C-H groups), they have the potential to show increased photoluminescence QE and radiative lifetimes. Furthermore, varying on only the neutral donor used, we are able to study structure/property relationships. Nd was chosen because of its technologically important NIR emission bands.

The reaction schemes are straightforward, and produce high quality single crystals in good yield. The synthesis of (**1**) is described by the following reaction scheme involving the oxidation of elemental neodymium by $\text{Hg}(\text{SC}_6\text{F}_5)_2$.



$(\text{DME})_2\text{Nd}(\text{SC}_6\text{F}_5)_3$ (Fig. 10) is a single seven coordinate neodymium atom coordinated to two chelating DME molecules. There is a 2.88\AA dative interaction between F15 and Nd1 which is consistent with literature reports of similar structures,⁶ as well as π - π stacking of the S1 and S2 aryl groups. Important crystallographic details, bond distances and angles can be seen in Tables 1 & 2.

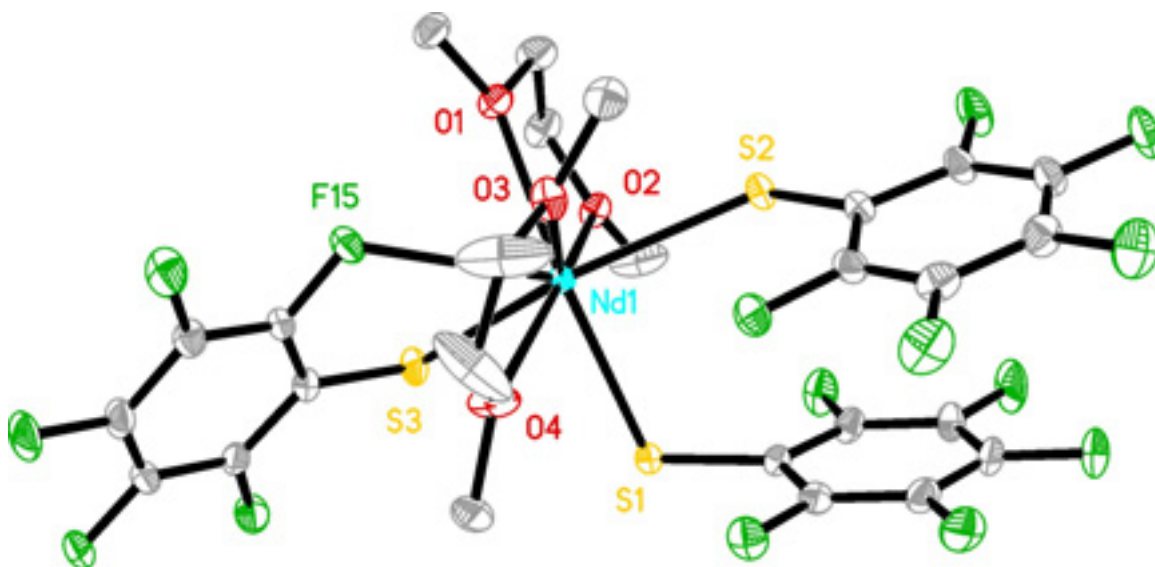


Fig 10. ORTEP of $(\text{DME})_2\text{Nd}(\text{SC}_6\text{F}_5)_3$ with thermal ellipsoids drawn at 50% probability level.

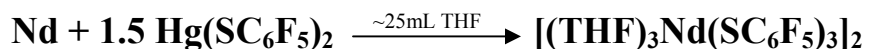
Table 1. Crystal data and structure refinement for $(\text{DME})_2\text{Nd}(\text{SC}_6\text{F}_5)_3$

Empirical formula	C ₂₆ H ₂₀ F ₁₅ Nd O ₄ S ₃	
Formula weight	921.84 g/mol	
Temperature	100(2) K	
Wavelength	0.71073 Å	
Crystal system	Triclinic	
Space group	P $\bar{1}$	
Unit cell dimensions	$a = 8.5954(5)$ Å	$\alpha = 71.244(1)^\circ$.
	$b = 12.7731(7)$ Å	$\beta = 84.394(1)^\circ$.
	$c = 15.2844(9)$ Å	$\gamma = 88.361(1)^\circ$.
Volume	$1581.35(16)$ Å ³	
Z	2	
Density (calculated)	1.936 Mg/m ³	
Final R indices [$I > 2\sigma(I)$]	R1 = 0.0316, wR2 = 0.0737	

Table 2. Bond Lengths (Å) for (DME)₂Nd(SC₆F₅)₃. Note the long Ln-F dative bond (highlighted in red).

Nd(1)-O(3)	2.4628(17)	Nd(1)-O(2)	2.5040(17)
Nd(1)-O(4)	2.5063(18)	Nd(1)-O(1)	2.5379(18)
Nd(1)-S(3)	2.8398(6)	Nd(1)-S(1)	2.8402(6)
Nd(1)-S(2)	2.8444(6)	Nd(1)-F(15)	2.8813(15)

The analogous THF adduct (**2**) was synthesized by the same reaction scheme as above only using THF as the Lewis base solvent:



This molecule crystallizes as a dimer, and consists of two seven coordinate neodymium ions, each coordinated to three terminal THF molecules, two terminal perfluorobenzenethiolates, and bridged by two μ_2 -perfluorobenzenethiolate ligands (Fig. 11). Also present are two dative $\sim 2.72\text{\AA}$ Nd-F interactions and π - π stacking of the S1', S2, and S3 aryl groups. Important crystallographic details, bond distances and angles can be seen in Tables 3 & 4.

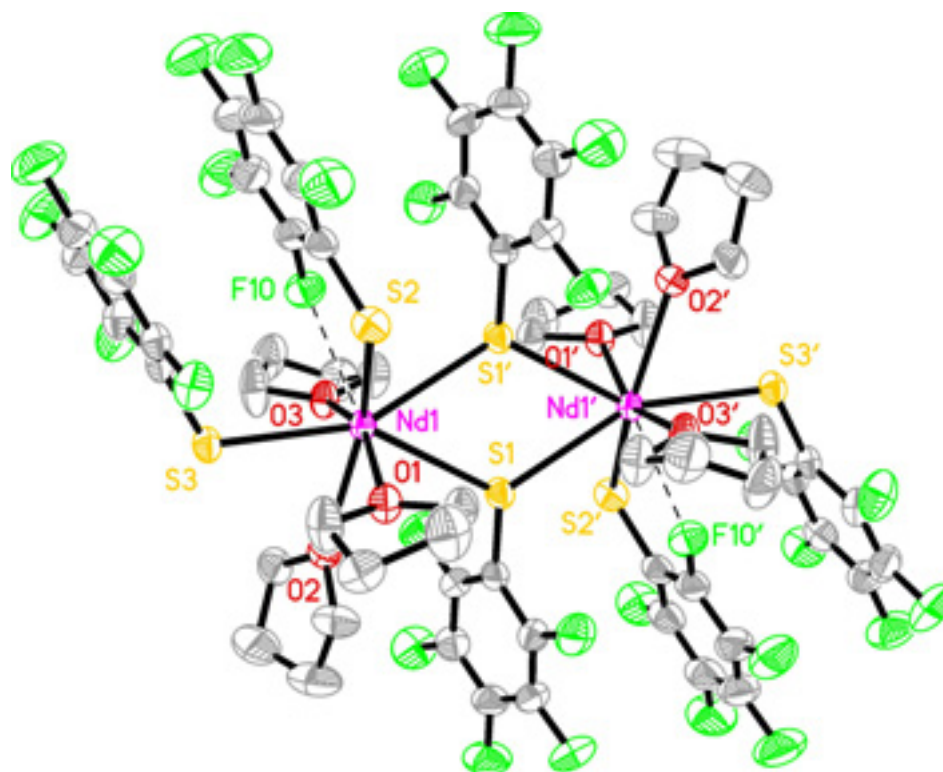


Fig 11. ORTEP of $[(\text{THF})_3\text{Nd}(\text{SC}_6\text{F}_5)_3]_2$ with thermal ellipsoids drawn at 50% probability level.

Table 3. Crystal data and structure refinement for $[(\text{THF})_3\text{Nd}(\text{SC}_6\text{F}_5)_3]_2$

Empirical formula	C ₃₀ H ₂₄ F ₁₅ Nd O ₃ S ₃	
Formula weight	957.91	
Temperature	100K	
Wavelength	0.71073 Å	
Crystal system	Triclinic	
Space group	P $\bar{1}$	
Unit cell dimensions	$a = 11.0533(6)$ Å	$\alpha = 71.5410(1)^\circ$
	$b = 12.4574(7)$ Å	$\beta = 76.4560(1)^\circ$
	$c = 13.2140(7)$ Å	$\gamma = 84.8030(1)^\circ$
Volume	$1677.63(16)$ Å ³	
Z	2	
Density (calculated)	1.896 Mg/m ³	
Final R indices $[I > 2\sigma(I)]$	R1 = 0.0222, wR2 = 0.0575	

Table 4. Bond Lengths (Å) and Angles (°) for [(THF)₃Nd(SC₆F₅)₃]₂. Note the long Ln-F dative bond (highlighted in red).

Nd(1)-O(3A)	2.4792(12)	Nd(1)-O(1A)	2.4862(12)
Nd(1)-O(2)	2.5346(12)	Nd(1)-F(10)	2.7223(12)
Nd(1)-S(3)	2.8301(4)	Nd(1)-S(2)	2.8358(5)
Nd(1)-S(1)	2.9815(4)		

To help elucidate structure/property relationships in these systems, it was advantageous to continue studying the structures of novel Ln-E species. Both **(1)** and **(2)** were synthesized using neodymium as the metal ion and SC₆F₅⁻ as the ligand, only differing in the neutral donor solvent used in the reaction. Because of the monodentate bonding of THF molecules, saturation of the primary coordination sphere is accomplished by bridging of the thiolate ligands across metal centers, which leads to the dimeric product. While there are three THF M-O bonds in the coordination sphere of [(THF)₃Nd(SC₆F₅)₃]₂ there are only two, less polar, chelating DME molecules coordinated to the metal ion in (DME)₂Nd(SC₆F₅)₃. Because of its bidentate bonding, DME saturates the coordination sphere with 4 M-O bonds. Furthermore, the chelating effect of the DME stabilizes the formation of the monomeric structure rather than larger oligomeric products. This has been seen before with similar species, i.e. in (DME)₂Er(SC₆F₅)₃. Unlike seven coordinate (DME)₂Er(SC₆F₅)₃ however, the larger Nd ionic radii also enables the formation of a Nd-F dative interaction, giving rise to an eight coordinate species.

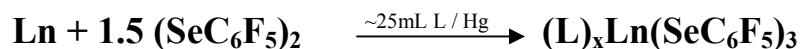
In the present study, dative fluorine interactions can be seen in both species with Nd-F dative bonds of 2.72 Å (THF), and 2.88 Å (DME). The shorter Nd-F dative bond length in the THF compound can be explained by there being less ligand-ligand repulsion from the absence of chelating DME molecules around the Nd ion. In $(\text{DME})_2\text{Nd}(\text{SC}_6\text{F}_5)_3$ there are 4 oxygen atoms bound to the metal ion. This sterically hinders the formation of an Nd-F bond, and increases the electron density around the metal ion. Evident in $[(\text{THF})_3\text{Nd}(\text{SC}_6\text{F}_5)_3]_2$ is π - π stacking of the phenyl rings of the S(2) and S(3) aryl groups.

Structural elucidation of these novel lanthanide fluorothiolates was useful for studying previous bonding/structure theories. Structural features of $[(\text{THF})_3\text{Nd}(\text{SC}_6\text{F}_5)_3]_2$ and $(\text{DME})_2\text{Nd}(\text{SC}_6\text{F}_5)_3$ add to our knowledge of structure/property relationships in Ln-E compounds. More interesting is the detailed comparison of the optical properties for these two molecules given in the photoluminescence section of this chapter, where we begin to see how we can control tuning of photoluminescence properties by systematically changing structural features.

1.3 Lanthanide Selenolates: Synthesis and Structure

The lack of commercially available selenolate derivatives has precluded the facile synthesis of analogous $(\text{L})_x\text{Ln}(\text{SeC}_6\text{F}_5)_y$ species. Our current understanding of the effect that substituting metal, ligand, solvent, or even heteroatoms has on resultant structural features, has led to the systematic synthesis and design of increasingly complex and interesting lanthanide species.^{3-6,7,13} Detailed here is our work on the synthesis of novel Ln-E complexes with fluorinated selenolate ligands, and the unique structural properties that arise.

$(L)_xLn(SeC_6F_5)_3$ ($L = THF, pyr$; $Ln = Nd, Sm, Er, Yb$) were synthesized according to the general scheme:



Unlike the lanthanide perfluorothiolate species prepared by transmetallation reactions between Ln metal with $Hg(SC_6F_5)_2$, lanthanide perfluoroselenolates are prepared by the direct reduction of the fluorinated diaryldiselenide with the rare earth metal. The withdrawal of electron density away from the chalcogen weakens the E-E bond in the starting material, stabilizes the anion, and facilitates the direct insertion of the lanthanide metal.

Representative of an early metal lanthanide perfluoroselenolate, $(THF)_3Nd(SeC_6F_5)_3$ (**3**) is isolated as a seven coordinate distorted pentagonal bipyramidal monomer (Fig 12), and crystallizes in the triclinic $P\bar{1}$ space group. The primary coordination sphere consists of three terminally bound THF molecules arranged in pseudo merihedral fashion. In a plane nearly perpendicular to the plane passing through the three oxygen atoms of the bound THF molecules, there are three Nd-Se bonds of the selenolate anions. Additionally, a $\sim 2.65 \text{ \AA}$ Nd-F dative interaction is present and lies within the plane of the Nd-Se bonds (Important bond angles and distances are given in Table 5). Both the fluorination of the anions as well as replacing the sulfur atom with the less basic selenium atom have marked effects on the resultant molecular structure. The most significant influence on structure arises by changing the chalcogen atom bound to the metal. In dimeric $[(THF)_3Nd(SC_6F_5)_3]_2$, the more basic thiolate is able to effectively

bridge metal centers, in contrast to $(\text{THF})_3\text{Nd}(\text{SeC}_6\text{F}_5)_3$, where the reduction in electron donating ability of the selenium atom results in only terminal bonding. Also, π - π stacking of the aryl groups is absent in $(\text{THF})_3\text{Nd}(\text{SeC}_6\text{F}_5)_3$, likely because the Nd-Se-C-F connectivity has more rotational freedom, allowing the fluorine atom to form a dative interaction with the metal ion. The preference to form this dative interaction between the electropositive metal and electronegative fluorine precludes the weaker π - π stacking found in the thiolate analog.

Table 5. Bond Lengths (Å) for $(\text{THF})_3\text{Nd}(\text{SeC}_6\text{F}_5)_3$. Note the Ln-F dative bond (highlighted in red).

Nd(1)-O(2)	2.407(2)	Nd(1)-O(3)	2.4121(19)
Nd(1)-O(1)	2.4851(19)	Nd(1)-Se(1)	2.8923(4)
Nd(1)-Se(3)	2.9283(3)	Nd(1)-Se(2)	2.9677(3)
Nd(1)-F(10)	2.6494(16)		

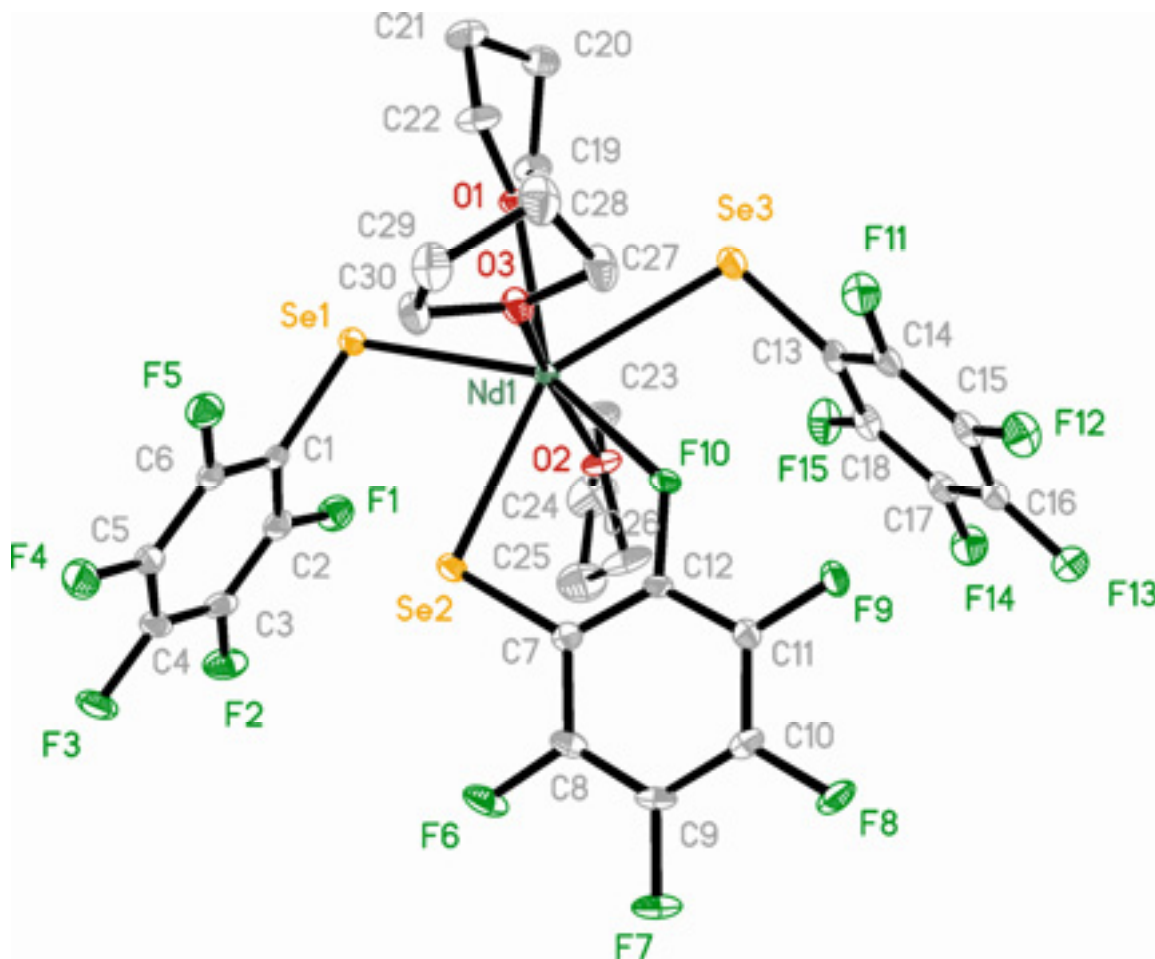


Fig 12. ORTEP of $(\text{THF})_3\text{Nd}(\text{SeC}_6\text{F}_5)_3$ with thermal ellipsoids drawn at 50% probability level.

Fluorination of the aryl group also affects the resultant structure, as seen by comparing $(\text{THF})_3\text{Nd}(\text{SeC}_6\text{F}_5)_3$ with $[(\text{THF})_4\text{Nd}_3(\text{SePh})_9]_n$.⁵ In addition to selenium's reduced basicity relative to sulfur, fluoride induced reduction of selenium's electron donating ability further decreases the chalcogen's ability to bridge metal centers. Additionally, the Nd-F interaction in $(\text{THF})_3\text{Nd}(\text{SeC}_6\text{F}_5)_3$ saturates the primary coordination sphere, whereas in $[(\text{THF})_4\text{Nd}_3(\text{SePh})_9]_n$, the absence of Nd-F interactions favors bridging of the chalcogen atoms. It is also interesting to note that in the

fluorinated selenolate species, steric crowding allows for only a seven coordinate metal, while the hydrocarbon analog there are eight coordinate Nd atoms.

As expected, $(\text{THF})_3\text{Sm}(\text{SeC}_6\text{F}_5)_3$ (**4**) (Fig. 13) is isostructural with $(\text{THF})_3\text{Nd}(\text{SeC}_6\text{F}_5)_3$, with the two species differing only in an overall contraction of bond lengths to the smaller Sm ion (Table 6). This trademark effect of the lanthanides can clearly be seen when comparing the average M-Se bonds of the two species, 2.89(3)Å (Sm) vs. 2.92(3)Å (Nd). As calculated by R.D. Shannon,⁸ there is only a 0.025Å difference between the radii of the two 6-coordinate metals. A closer look at the structures reveals directional bonding at the primary coordination sphere. Specifically, one can see a merihedral configuration in which the THF molecules lie in one plane, and the SePh lie in another nearly perpendicular plane. O(1) and O(3) are nearly trans to one another, having a O(1)—Sm(1)—O(3) angle of 164.14°. Almost 90° away, O(2) lays trans to the bidentate selenolate bound to the metal through both Se(1) and F(1). While this geometry is distorted by the inclusion of the M-F dative interaction, the electronic effects of the F and Se can be seen by a lengthening of the Sm-O bond trans to the M-Se/M-F bonds (Sm-O(2)). The cis Sm-O bonds are 2.376Å (O(3)) and 2.381Å (O(1)), while the Sm-O(2) bond is 2.462Å. The same can be seen for the Nd—O(1) bond trans to the M-Se/M-F bonds. Synthesis of true mer-octahedral complexes should provide a better model to quantitatively analyze these systems from a fundamental perspective.

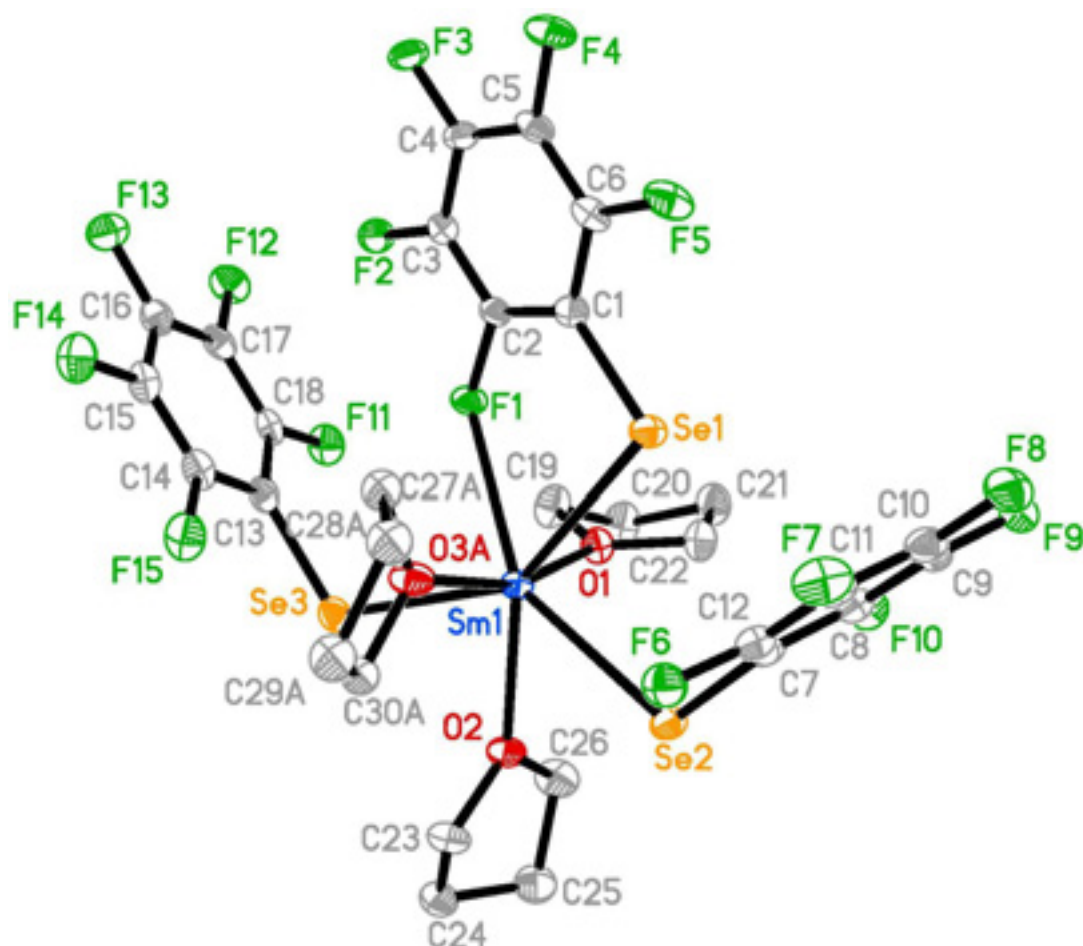


Fig 13. ORTEP of $(\text{THF})_3\text{Sm}(\text{SeC}_6\text{F}_5)_3$ with thermal ellipsoids drawn at 50% probability level.

Table 6. Bond Lengths (\AA) for $(\text{THF})_3\text{Sm}(\text{SeC}_6\text{F}_5)_3$. Note the Ln-F dative bond (highlighted in red).

Sm(1)-O(2)	2.462(2)	Sm(1)-O(3)	2.376(2)
Sm(1)-O(1)	2.381(2)	Sm(1)-Se(1)	2.9347(4)
Sm(1)-Se(3)	2.8995(4)	Sm(1)-Se(2)	2.8648(4)
Sm(1)-F(1)	2.6274(18)		

$(\text{THF})_3\text{Sm}(\text{SeC}_6\text{F}_5)_3$ illustrates the effects fluorination has on the resultant Ln-E structure. While the THF adduct of the SeC_6H_5 species has not yet been isolated, past results let us believe that it would be similar to the 1D neodymium polymer, $[(\text{THF})_4\text{Nd}_3(\text{SeC}_6\text{H}_5)_9]_n$. The fluorinated thiolate, $[(\text{THF})_2\text{Sm}(\text{SC}_6\text{F}_5)_3]_2$, *has* been synthesized however, and lets us extend our study as we traverse the lanthanide series.¹⁰ As with the fluorinated selenolates, both the Nd and Sm fluorinated thiolates have the same structural features. The decreased bridging capacity of the selenolate coupled with its decreased basicity due to fluorination of the phenyl group, gives rise to the monomeric species, $(\text{THF})_3\text{Sm}(\text{SeC}_6\text{F}_5)_3$. Unlike the Nd complexes, the smaller ionic radii of Sm allows only two THF molecules per metal in $[(\text{THF})_2\text{Sm}(\text{SC}_6\text{F}_5)_3]_2$. The reduced crowding around the primary coordination sphere allows for two Sm-F dative interactions, whereas the Nd fluorinated thiolate has three THF molecules per metal, and only one Nd-F interaction per metal. Additionally, while $(\text{THF})_3\text{Nd}(\text{SeC}_6\text{F}_5)_3$ has shorter Nd-F interactions than does $[(\text{THF})_3\text{Nd}(\text{SC}_6\text{F}_5)_3]_2$, one of the Sm-F interactions (2.582 Å) in $[(\text{THF})_2\text{Sm}(\text{SC}_6\text{F}_5)_3]_2$ is actually shorter than the 2.627 Å Sm-F interaction in the $(\text{THF})_3\text{Sm}(\text{SeC}_6\text{F}_5)_3$ monomer. This is likely due to the reduction in steric crowding around the metal center from the coordination of one less THF molecule. This allows one of the SC_6F_5 ligands more space to approach the metal center.

Traversing the lanthanide series further, $(\text{THF})_3\text{Er}(\text{SeC}_6\text{F}_5)_3$ (**5**) is the first representative of a late group lanthanide perfluoroselenolate (Fig. 14).

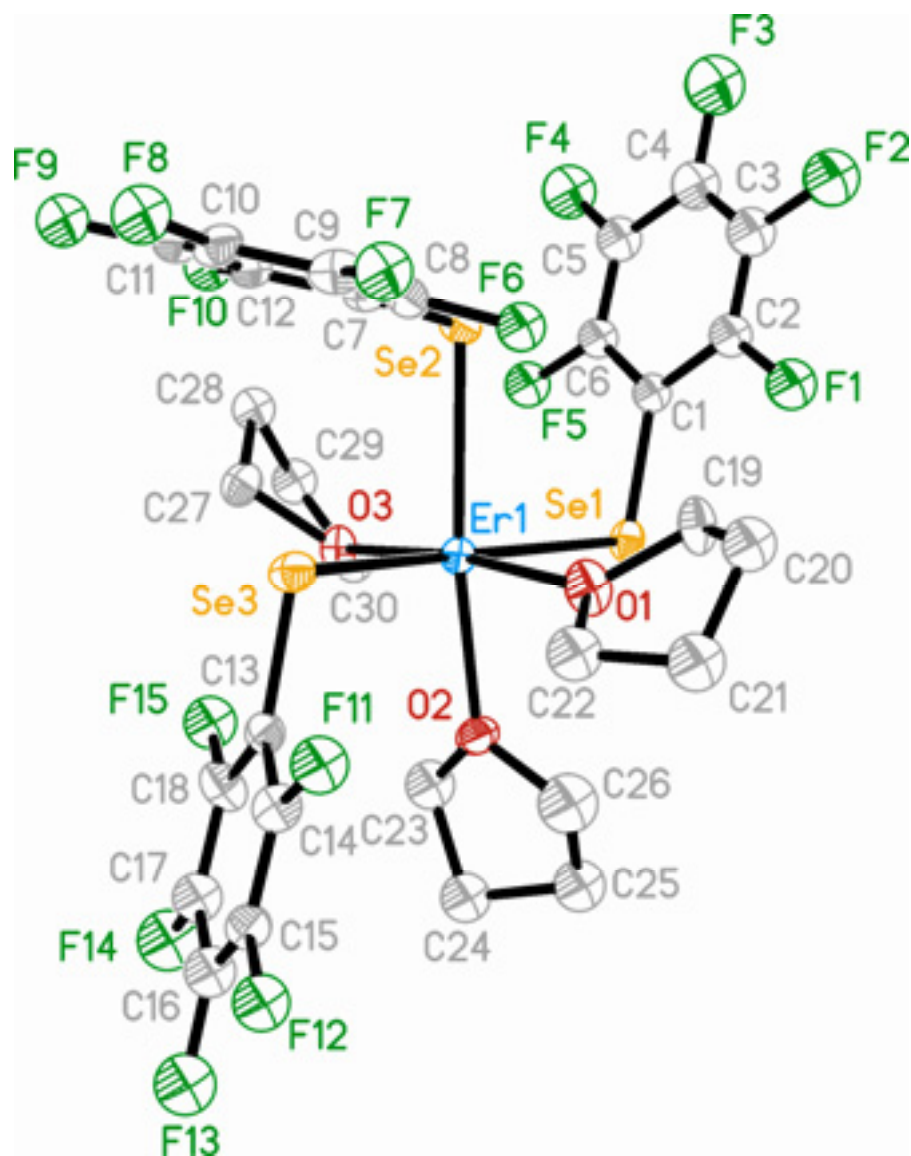


Fig 14. ORTEP of (THF)₃Er(SeC₆F₅)₃ with thermal ellipsoids drawn at 50% probability level.

This compound is isolated as a six coordinate Er species arranged in a mer-octahedral fashion. The first of several structural attributes that set this molecule apart

from the early metals is that it crystallizes in the higher symmetry monoclinic $P2_1$ space group. The isolated molecule is unique in that it contains four molecules in the asymmetric unit (Fig. 15).

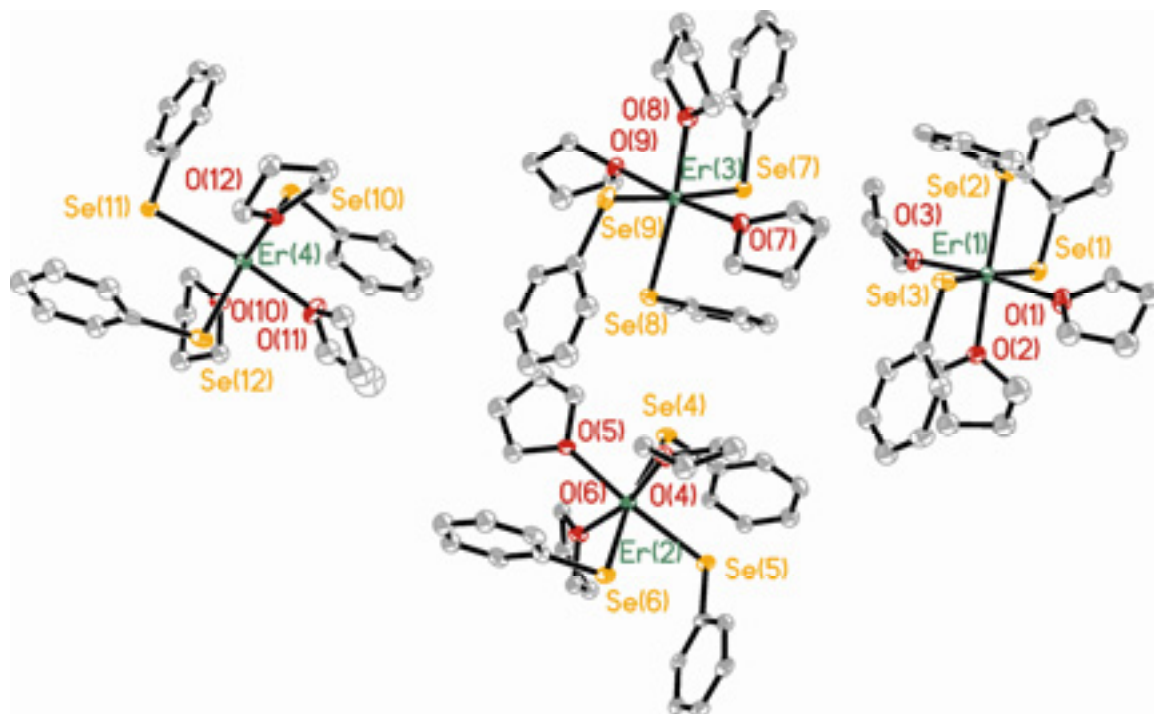


Fig 15. ORTEP of the four asymmetric $(\text{THF})_3\text{Er}(\text{SeC}_6\text{F}_5)_3$ molecules in the unit cell with thermal ellipsoids drawn at 50% probability level.

The four molecules are different because of variations in metal-ligand bond orientations. Being terminally bound, the three THF ligands have rotational freedom about the Ln-O bond vector, with little consideration for steric effects. This gives rise to

unique Er-THF bond and torsion angles for the four molecules. Further contributing to the asymmetry among the four molecules, the Er-Se and Se-C bond features are heavily constrained by steric crowding, and efficient packing within the unit cell to minimize intramolecular repulsions is a dominant driving force that can affect resultant structures. Er-Se-C bond angles range from 97.3 to 105.3° across all molecules, and there is up to 5.6° variability within one molecule. Er-Se-C-C torsion angles also vary throughout the molecules, illustrating the flexibility of the selenolates as they respond to ligand-ligand repulsions.

The reduction in the ionic radius of Er compared to Sm increases crowding around the metal center such that dative Er-F interactions are no longer present in this system. Unlike the analogous Nd and Sm molecules, the closest Er-F interaction ($\sim 3.66\text{\AA}$) is over an angstrom longer, even given the reduction in the ionic radii of Er. Details of the above features (Ln-F interaction, mer-octahedral geometry, asymmetry) can be seen by looking at the crystallographic data for this molecule. Deviations from ideality or comparisons with other species can also be made. Table 7 shows bond length differences between all four molecules and bond angle differences within one molecule. For the four asymmetric molecules, intermolecular differences in Er-O and Er-Se bonds illustrate their asymmetry, while intramolecular bond angles show mer-octahedral geometry for all four molecules.

Table 7. Selected Bond Lengths (Å) and Angles (°) for (THF)₃Er(SeC₆F₅)₃.

Er1-O3	2.291(5)	Er1-O1	2.306(6)	Er1-O2	2.323(5)
Er1-Se2	2.8046(8)	Er1-Se1	2.830(8)	Er1-Se3	2.855(9)
Er2-O6	2.282(5)	Er2-O4	2.303(5)	Er2-O5	2.312(5)
Er2-Se5	2.8109(8)	Er2-Se6	2.8438(8)	Er2-Se4	2.8446(8)
Er3-O7	2.310(5)	Er3-O8	2.318(6)	Er3-O9	2.327(5)
Er3-Se8	2.8045(8)	Er3-Se9	2.8227(8)	Er3-Se7	2.8269(8)
Er4-O12	2.304(5)	Er4-O10	2.304(5)	Er4-O11	2.328(5)
Er4-Se11	2.8022(8)	Er4-Se12	2.8272(8)	Er4-Se10	2.8333(8)
O3-Er1-O1	172.9(2)	O3-Er1-O2	85.2(2)	O1-Er1-O2	87.9(2)
O3-Er1-Se2	90.58(14)	O1-Er1-Se2	96.47(17)	O2-Er1-Se2	167.01(15)
O3-Er1-Se1	91.11(13)	O1-Er1-Se1	89.11(15)	O2-Er1-Se1	79.84(15)
Se2-Er1-Se1	87.96(2)	O3-Er1-Se3	96.06(13)	O1-Er1-Se3	83.83(15)
O2-Er1-Se3	101.15(15)	Se2-Er1-Se3	91.51(2)	Se1-Er1-Se3	172.82(3)

We continue to see the marked effect fluorinated selenolate ligands impart on these lanthanide chalcogenolate systems by comparing (THF)₃Er(SC₆F₅)₃,⁷ (THF)₃Er(SeC₆F₅)₃, and (THF)₃Er(SeC₆H₅)₃.⁵ All three of these molecules are isolated as monomeric species because of the small ionic radius of the Er metal. Changing from S to Se, as well as going from a hydrocarbon to a fluorinated phenyl ring affects the ability of dative interactions to occur. With Er, dative Er-F bonds only exist in the seven coordinate thiolate species, leaving (THF)₃Er(SeC₆F₅)₃ as a six coordinate mer-octahedral complex. This contrasts with (THF)₃Er(SeC₆H₅)₃, which is isolated as a fac-octahedral molecule. The lack of π - π interactions, as well as the mer configuration in (THF)₃Er(SeC₆F₅)₃, are likely due to the packing requirements of the four asymmetric molecules in the unit cell. While π - π stacking is favorable in that it imparts stability within a molecule, intermolecular packing in the unit cell is a dominant structural driving

force. The fluorinated rings in this system point towards the vicinity of smaller THF molecules rather than aligning with other perfluorophenyl rings, leading to efficient packing of the molecules in the unit cell. It should be noted that while π - π stacking is not present, weaker intermolecular T-stacking is present between fluorine atoms on certain phenyl groups with the aromatic rings from other molecules.

This molecule allows for a quantitative analysis of covalent contributions to the bonding schemes of these systems. As mentioned earlier, bonding in lanthanide chemistry is predictably (and historically) ionic in nature with metal-ligand bond lengths almost always equal to the summation of ionic radii, and bonding in lanthanide structures rarely shows directionality. Reports of deviations from these “norms” have been scarcely mentioned in the past, with only a few more recent examples showing some degree of directionality in the bonding of lanthanide species,¹⁰⁻¹⁷ however these reports have yet to clearly describe the nature of the bonding in non-classical bonding complexes.

We first noticed that there appeared to be a structural trans-influence in a mer-octahedral thiolate coordination compound, (py)₃Yb(SPh)₃, over a decade ago. Yb-S bonds trans to SPh were significantly longer than the Yb-S bond trans to the neutral pyridine donors. Similar non-classical Ln-ligand bond lengths are also formed in related compounds (Table 8). Interpretations of these apparent structural trans influences have been limited due to the difficulty of comparing compounds because outside influences, rather than orbital overlap and intermolecular electronic effects, may also be influencing the length of the Ln-ligand bond.

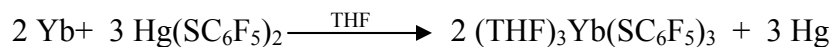
Table 8. Summary of Ln-ligand bond lengths (Å) in mer-octahedral LnX_3Y_3

<u>Coordination Compounds</u>			
LnX_3Y_3 Compound	Ln-X trans to X	Ln-X trans to Y	Δ_{x-y}^*
$(\text{THF})_3\text{YbCl}_3$ ¹⁷	2.530(3), $\overline{2.533(3)}$	2.513(4)	0.018
$(\text{THF})_3\text{YbBr}_3$ ¹⁸	2.708(1), 2.708(1)	2.665(1)	0.043
$(\text{py})_3\text{Yb}(\text{SPh})_3$ ¹⁹	2.682(3), 2.650(2)	2.609(4)	0.057
$(\text{py})_2(\text{THF})_1\text{Sm}(\text{SR})_3$ ²⁰	2.749(3), 2.751(3)	2.720(3)	0.030
LnX_3Y_3 Compound	Ln-X trans to X	Ln-X trans to Y	Δ_{x-y}^*
$(\text{THF})_3\text{Ln}(\text{OC}_6\text{F}_5)_3$ ²¹	2.111(2), 2.111(2)	2.084(2)	0.027
$(\text{THF})_3\text{Ln}(\text{SC}_6\text{F}_5)_3$	2.678(2), 2.680(2)	2.642(2)	0.039
$(\text{THF})_3\text{Er}(\text{SeC}_6\text{F}_5)_3$	2.830(8), 2.835(9)	2.8046(8)	0.028
$(\text{DME})\text{Yb}(\text{SePh})_4^-$ ²²	2.807(2), 2.776(2)	2.769(2), 2.793(2)	0.011

While the above structural trans influences illustrate the presence of directional bonding between the Ln and ligand, quantitative examinations of lanthanide systems with clearly defined covalent characteristics are relatively scarce. Such a study would be important to better define the fundamental nature of the lanthanide-ligand bond.

Having four unique mer-octahedral molecules in the asymmetric unit, $(\text{THF})_3\text{Er}(\text{SeC}_6\text{F}_5)_3$ is an ideal model for DFT calculations. Being structurally similar, $(\text{THF})_3\text{Yb}(\text{SC}_6\text{F}_5)_3$ (**6**) is also well suited for DFT analysis to confirm the presence of structural trans effects and covalent contributions to the Ln-ligand bond.

(THF)₃Yb(SC₆F₅)₃ was prepared by transmetallation reactions of elemental Yb with Hg(SC₆F₅)₂ according to:²³



In both (THF)₃Er(SeC₆F₅)₃ and (THF)₃Yb(SC₆F₅)₃, Ln-E bonds trans to anionic EPh are significantly longer than Ln-E bonds trans to neutral THF. A similar pattern is also noted for the Ln-O bonds, with the Ln-O bond for the THF ligands trans to EPh being significantly longer than the Ln-O bonds trans to neutral THF.

Geometry optimizations of (THF)₃Yb(SC₆F₅)₃ and (THF)₃Er(SeC₆F₅)₃ species were performed by Karsten Krogh-Jespersen²⁴ using DFT (see Computational Details in the experimental section) based upon the experimentally determined X-ray crystal structure of (THF)₃Er(SeC₆F₅)₃, which was used to correctly model the coordination geometry of the complex. Optimized M-L bond lengths were computed for (THF)₃Yb(SC₆F₅)₃ and (THF)₃Er(SeC₆F₅)₃, and found to be systematically larger than the observed values determined by single crystal XRD (Table 9). Overall, the discrepancy is only 0.05 Å, and no significant changes in overall structure conformation occur as a result. The computed Ln-O bond length when O(THF) is trans to anionic E deviates more strongly (ca. 0.11 Å) from the observed value. Defining $\Delta_{\text{Ln-E}}$ as the difference between the average of the two Ln-E bond lengths when trans to anionic E with the Ln-E bond length when trans to THF, we compute $\Delta_{\text{Yb-S}}$ to be -0.047 Å and $\Delta_{\text{Er-Se}}$ to be -0.041 Å. Experimental values were found to be -0.037 Å and -0.029 Å, respectively. The asymmetry is thus larger, both experimentally and computed, when E = S than when E =

Se, by about 0.006 Å. However, the asymmetry in Ln-O distances from the computations is more than twice as large as observed, e.g. $\Delta_{\text{Yb-O}} = \Delta_{\text{Er-O}} = 0.074$ Å as compared with the experimental values of 0.033 Å and 0.030 Å, respectively.

Table 9. Comparison of Computed (DFT) and Experimental (X-Ray) Metal-Ligand Bond Lengths [Å] for (THF)₃Yb(SC₆F₅)₃ and (THF)₃Er(SeC₆F₅)₃.

	<u>DFT</u>	<u>X-Ray</u>
Yb(1)-O(1)	2.331	2.271
Yb(1)-O(2)	2.411	2.308
Yb(1)-O(3)	2.344	2.280
Yb(1)-S(1)	2.727	2.678
Yb(1)-S(2)	2.681	2.642
Yb(1)-S(3)	2.729	2.680
$\Delta_{\text{Yb-O}}^{\text{c}}$	0.074	0.033
$\Delta_{\text{Yb-S}}^{\text{c}}$	-0.047	-0.037
	<u>DFT</u>	<u>X-Ray</u>
Er(4)-O(12)	2.368	2.304
Er(4)-O(11)	2.443	2.337
Er(4)-O(10)	2.370	2.310
Er(4)-Se(12)	2.876	2.828
Er(4)-Se(11)	2.843	2.802
Er(4)-Se(10)	2.892	2.833
$\Delta_{\text{Er-O}}^{\text{c}}$	0.074	0.030
$\Delta_{\text{Er-Se}}^{\text{c}}$	-0.041	-0.029

DFT calculations of $(\text{THF})_3\text{Yb}(\text{SC}_6\text{F}_5)_3$ and $(\text{THF})_3\text{Er}(\text{SeC}_6\text{F}_5)_3$ quantify previously seen trends in Ln-E bond lengths that illustrate structural trans effects in these species. This effect indicates that there are covalent contributions in Ln-E systems.

Bonds between Ln and the neutral donors also tend to follow the same bond length distribution patterns, with bonds trans to anions longer than bonds trans to neutral donors. In $(\text{THF})_3\text{Yb}(\text{SC}_6\text{F}_5)_3$, the Yb-O bonds trans to O are 2.271 and 2.280 Å, and the Yb-O trans to S is significantly longer, at 2.308 Å. A similar pattern is noted for the four independent molecules in $(\text{THF})_3\text{Er}(\text{SeC}_6\text{F}_5)_3$, but the differences change significantly within the independent molecules. Fluorination of the arene group increases the length of the Ln-Se bond and decreases the length of the trans Er-O(THF) bond, by the polarizing influence of the electronegative fluorides lessening the charge density at Se. This increase in Er-Se bond length can be seen by comparing the Er-Se bond lengths of $(\text{THF})_3\text{Er}(\text{SeC}_6\text{H}_5)_3$ with those of $(\text{THF})_3\text{Er}(\text{SeC}_6\text{F}_5)_3$. The average Er-Se bond length in the fac-octahedral selenolate $(\text{THF})_3\text{Er}(\text{SeC}_6\text{H}_5)_3$, is significantly shorter (2.7766(6) Å) than the average of the four crystallographically unique Er-Se bonds trans to THF in $(\text{THF})_3\text{Er}(\text{SeC}_6\text{F}_5)_3$, (2.805(3) Å). Following the same trend seen for the Ln-E bond lengths, the average Er-O(THF) bonds trans to SeC_6F_5 in $(\text{THF})_3\text{Er}(\text{SeC}_6\text{F}_5)_3$ (2.321(7) Å) are significantly shorter than the three crystallographically equivalent Er-O(THF) bonds in *fac*-($\text{THF})_3\text{Er}(\text{SeC}_6\text{H}_5)_3$ (2.347(3) Å).

To finish the series, $(\text{py})_4\text{Yb}(\text{SeC}_6\text{F}_5)_3$ was also synthesized (Fig. 16) by the direct reduction of the $\text{F}_5\text{C}_6\text{SeSeC}_6\text{F}_5$ with Yb metal. Of the series, $(\text{py})_4\text{Yb}(\text{SeC}_6\text{F}_5)_3$ not only has the smallest metal radii, but also employs a different Lewis base solvent to show that the generality of these reactions is equivalent to previous thiolate and selenolate

methodologies. As with the Nd and Sm analogs, this molecule crystallizes in the triclinic spacegroup $P\bar{1}$. The coordination of an additional pyridine molecule was expected, as this trend has been observed in the past for similar Ln species.^{5,7} The basicity of pyridine allows it to more effectively compete for access to the metal center, disrupting both Yb-F interactions and the formation of an octahedral Yb complex, such as $(\text{THF})_3\text{Yb}(\text{SeC}_6\text{F}_5)_3$. $(\text{py})_4\text{Yb}(\text{SeC}_6\text{F}_5)_3$ is isolated as a seven coordinate molecule having no Yb-F interaction. This increase in coordination number upon using pyridine in place of THF or DME is supported by past species, for example $(\text{py})_4\text{Sm}(\text{SeC}_6\text{F}_5)_3$, which is an eight coordinate monomer. Table 10 shows significant bond lengths and angles for $(\text{py})_4\text{Yb}(\text{SeC}_6\text{F}_5)_3$. There are five equatorial bonds (in orange below) which are all between 64.36° and 78.84° , with ideal pentagonal bipyramidal angles being 72° . The two axial ligands have average bond angles of 89.40° (N1) and 90.57° (N3) with respect to the ligands lying in the plane of the pentagon. While not ideal, this complex has features of a pentagonal bipyramidal structure.

Table 10. Bond Lengths (Å) and Angles ($^\circ$) for $(\text{pyr})_4\text{Yb}(\text{SeC}_6\text{F}_5)_3$

Yb1-N2	2.419(6)	Yb1-N3	2.450(6)	Yb1-N1	2.456(6)
Yb1-N4	2.457(6)	Yb1-Se1	2.8672(8)	Yb1-Se2	2.8880(9)
Yb1-Se3	2.8888(8)				
N2-Yb1-N3	92.1(2)	N2-Yb1-N1	88.4(2)	N3-Yb1-N4	89.7(2)
N1-Yb1-N4	89.8(2)	N3-Yb1-Se1	91.26(15)	N1-Yb1-Se1	88.37(14)
N2-Yb1-N4	141.1(2)	N2-Yb1-Se1	153.77(15)	N4-Yb1-Se1	64.91(13)
N2-Yb1-Se2	78.84(14)	N3-Yb1-Se2	89.92(15)	N1-Yb1-Se2	90.33(15)
N4-Yb1-Se2	140.06(14)	Se1-Yb1-Se2	75.17(2)	N2-Yb1-Se3	76.76(14)
N3-Yb1-Se3	89.83(15)	N1-Yb1-Se3	90.13(15)	N4-Yb1-Se3	64.37(13)
Se1-Yb1-Se3	129.26(2)	Se2-Yb1-Se3	155.57(2)		

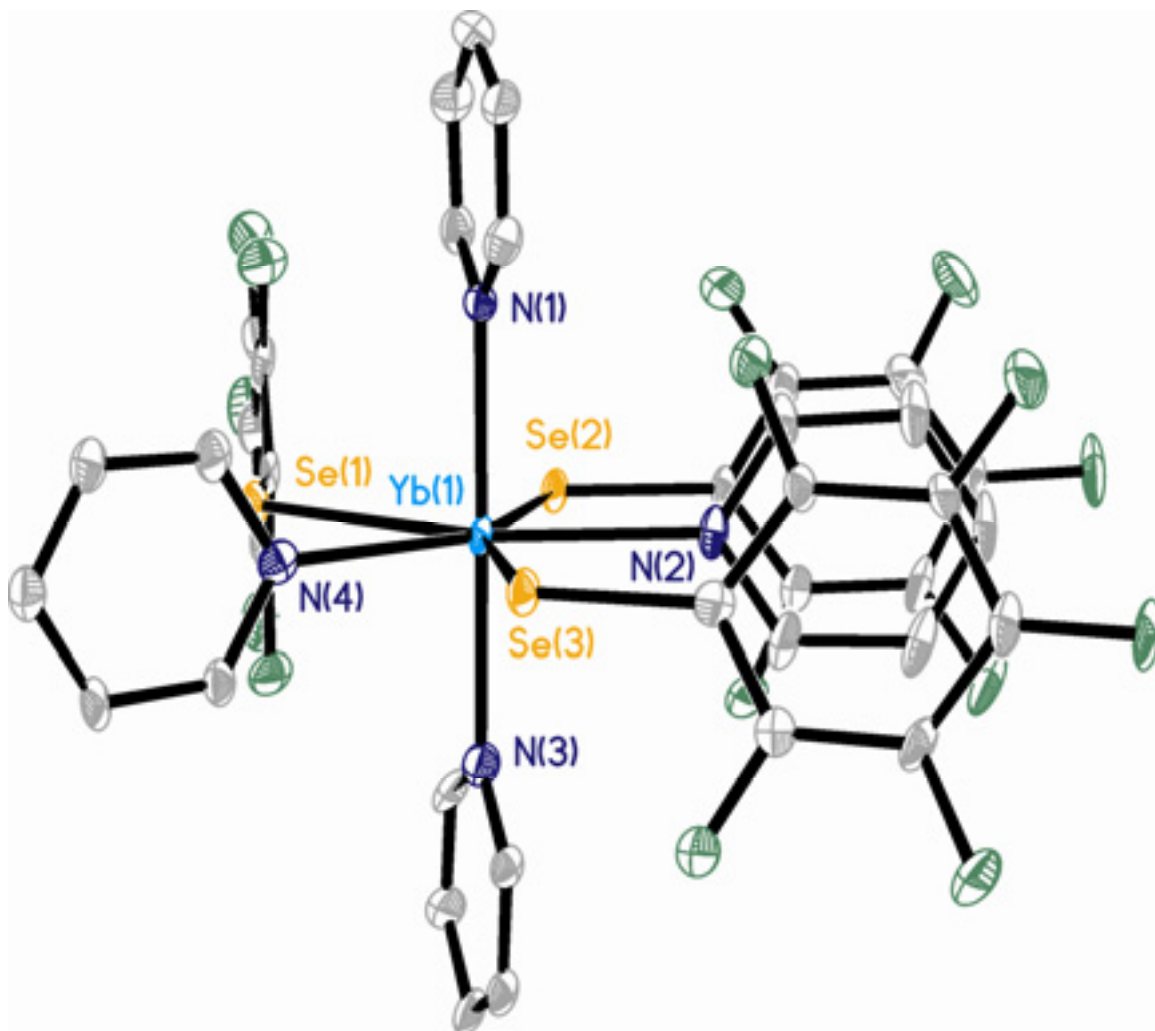


Fig. 16 ORTEP of $(\text{py})_4\text{Yb}(\text{SeC}_6\text{F}_5)_3$ with thermal ellipsoids drawn at 50% probability level.

A striking structural feature of $(\text{pyr})_4\text{Yb}(\text{SeC}_6\text{F}_5)_3$ is the triple π - π stacking between the Se(2) and Se(3) selenolates, and the sandwiched N(2) pyridine. This feature is also seen in $(\text{pyr})_4\text{Yb}(\text{SC}_6\text{F}_5)_3$ ⁷ (Fig 17, shown with the pentagonal symmetry in the plane of the paper), which is a nearly isostructural seven coordinate species. However similar these two systems are, differing synthetic procedures led to distinct differences. In our product there is only one lattice pyridine present, where there exists an additional lattice THF for the thiolate species. Furthermore, upon close observation of the ligand connectivity around the two species, significant differences are noticed.

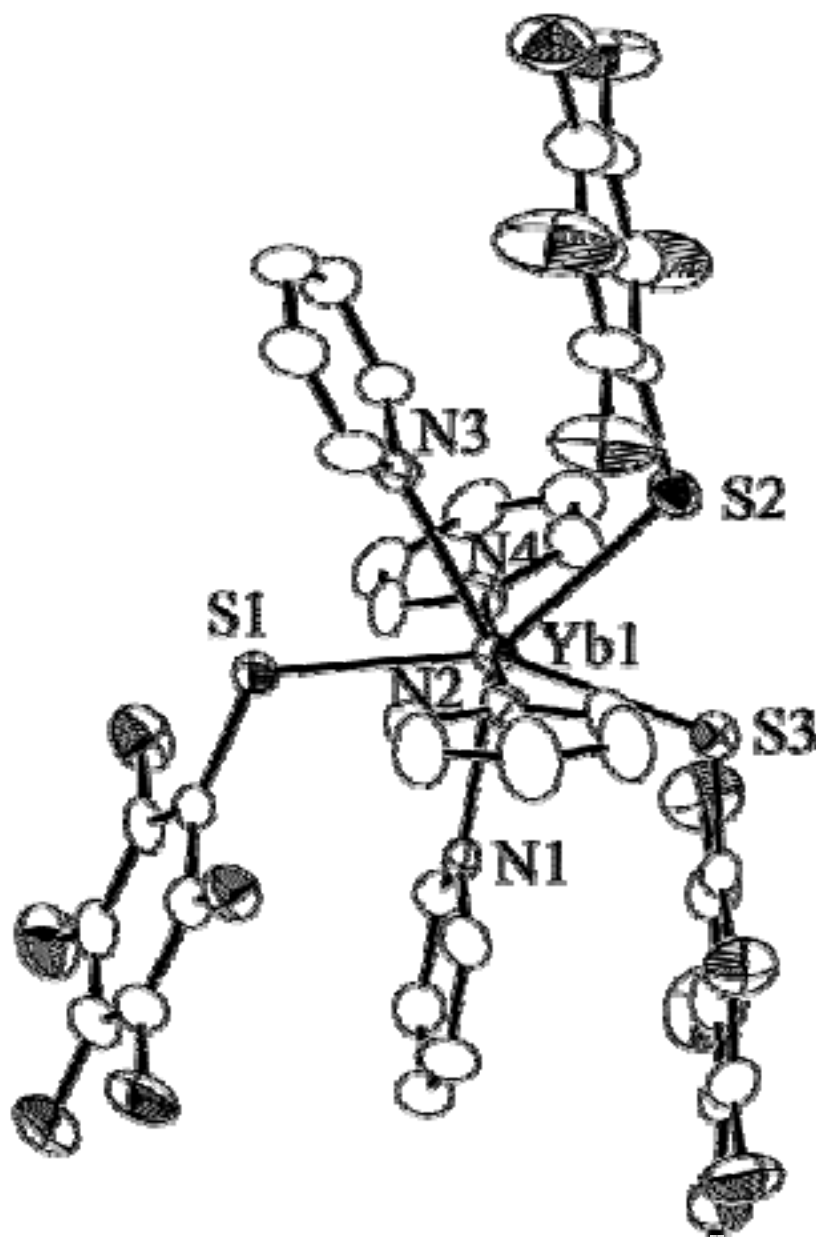


Fig. 17 ORTEP of $(\text{py})_4\text{Yb}(\text{SC}_6\text{F}_5)_3$ for comparison to $(\text{py})_4\text{Yb}(\text{SeC}_6\text{F}_5)_3$, again with thermal ellipsoids drawn at 50% probability level.

With both species having pentagonal bipyramidal geometry, the three chalcogenolates in equatorial positions, and the “sandwich” arrangement of π - π stacking, the difference lies in the third (non-sandwiching) chalcogenolate ligand. In the thiolate species, the non- π - π stacking thiolate (S2) is 65.5° (S2-Yb1-S3 angle) from its nearest thiolate (S3), likely resulting from the additional π - π stacking between it and the equatorial pyridine (N3). In $(\text{pyr})_4\text{Yb}(\text{SeC}_6\text{F}_5)_3$, however, this angle is 75.5° (Se1-Yb1-Se2 angle), likely resulting from the repulsive forces imposed upon it from “piggybacking” the Se(2) selenolate rather than forming π - π interactions with the N(4) pyridine. While one might attribute this structural difference to the change in chalcogen, it more likely arises from the efficient packing of the crystalline solid. Remembering that lattice solvents have a certain degree of disorder and “freedom” while residing in the voids of the lattice, having the additional lattice THF spaces the Yb molecules further apart. Because of this, the Yb molecules are arranged in such a way that the positioning of the thiolates around the molecule is less hindered by intermolecular crowding. In the selenolate species, having only one lattice pyridine per molecule, the molecules pack much more tightly, and in order to minimize repulsive forces, the selenolates must be arranged in the “piggyback” fashion described above. This adds a new dimension to the design of future molecules, as we can more clearly see that lattice solvents are also important variables that can affect the resultant structures of rare earth species, and ultimately many of their related properties.

1.4 Photoluminescence Studies

We began by looking for enhanced emission from soluble lanthanide molecules, and $(\text{DME})_2\text{Nd}(\text{SC}_6\text{F}_5)_3$ and $[(\text{THF})_3\text{Nd}(\text{SC}_6\text{F}_5)_3]_2$ were chosen as starting points. While both Er^{3+} or Tm^{3+} are also suitable ions for these studies, we chose neodymium containing targets because of the strong $1.07\mu\text{m}$ and $1.3\mu\text{m}$ emissions utilized in telecommunication technologies. As mentioned previously, for optimum emission quantum efficiencies, the minimization of emission quenching vibrational groups is a requirement. $(\text{DME})_2\text{Nd}(\text{SC}_6\text{F}_5)_3$ and $[(\text{THF})_3\text{Nd}(\text{SC}_6\text{F}_5)_3]_2$ were also chosen because they only vary in neutral donor used, not metal or chalcogen. In both $(\text{DME})_2\text{Nd}(\text{SC}_6\text{F}_5)_3$ and $[(\text{THF})_3\text{Nd}(\text{SC}_6\text{F}_5)_3]_2$, only the Lewis base solvents contain emission quenching C-H groups. Both of the neutral donor ligands bond to the metal through oxygen atoms, further decreasing any differing crystal field effects that may arise from the polarizability of the atoms bound to the metal. For the QE and radiative lifetime emission comparison, the focus will be on the differences in the number of emission quenching groups around the metal ion. Crystal field effects and structure/bonding/optical property relationships will be discussed further as will a detailed description of the spectroscopic theory and calculations.

$(\text{DME})_2\text{Nd}(\text{SC}_6\text{F}_5)_3$ and $[(\text{THF})_3\text{Nd}(\text{SC}_6\text{F}_5)_3]_2$ show sharp, intense emission bands at 920, 1074, and 1344 nm from the ${}^4\text{F}_{3/2} \rightarrow {}^4\text{I}_{9/2}$, ${}^4\text{F}_{3/2} \rightarrow {}^4\text{I}_{11/2}$, and ${}^4\text{F}_{3/2} \rightarrow {}^4\text{I}_{13/2}$ electronic transitions, respectively.²⁵ Because of the close similarities in the structure of the two molecules, the forbidden nature of the transitions, and because the electronic transitions arise from shielded orbitals, the emission spectra are very similar (Fig 3). Theoretically predicted emission lifetimes for the ${}^4\text{F}_{3/2} \rightarrow {}^4\text{I}_{11/2}$ and ${}^4\text{F}_{3/2} \rightarrow {}^4\text{I}_{13/2}$

transitions were calculated based on the fluorescence decay times and compared to experimental results, and are in agreement with measured values (Figs 18, 19, and 20).

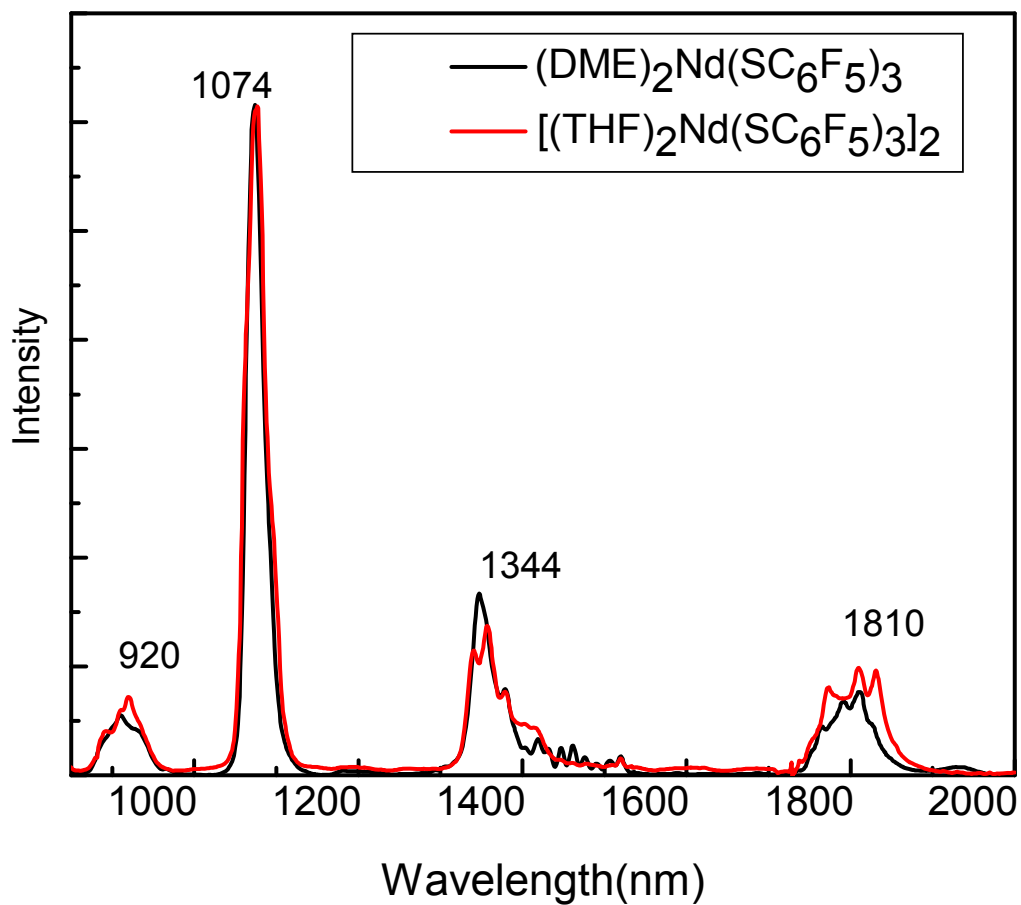


Fig 18. Emission spectra of $(\text{DME})_2\text{Nd}(\text{SC}_6\text{F}_5)_3$ and $[(\text{THF})_2\text{Nd}(\text{SC}_6\text{F}_5)_3]_2$

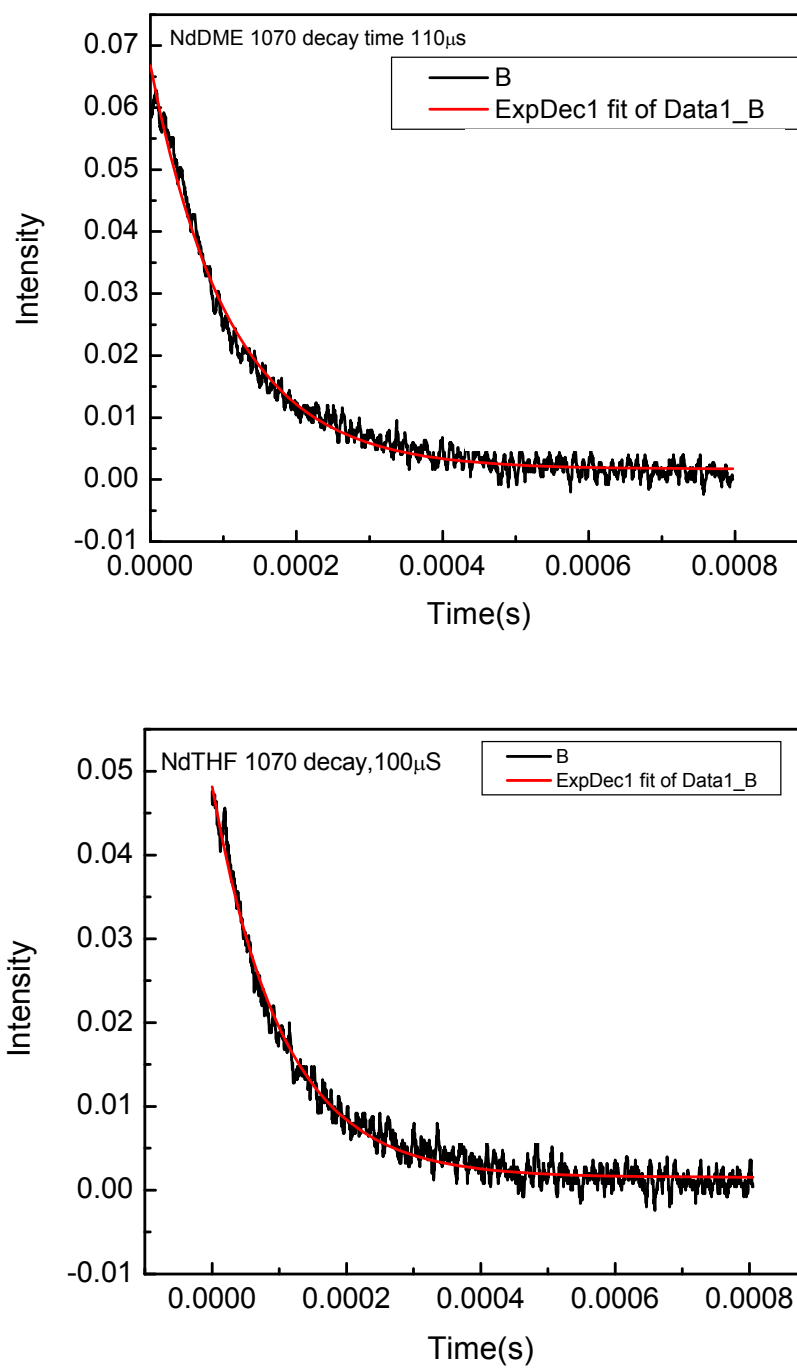


Fig 19. Emission decay curves of $(\text{DME})_2\text{Nd}(\text{SC}_6\text{F}_5)_3$ and $[(\text{THF})_3\text{Nd}(\text{SC}_6\text{F}_5)_3]_2$ for the ${}^4\text{F}_{3/2} \rightarrow {}^4\text{I}_{11/2}$ transition.

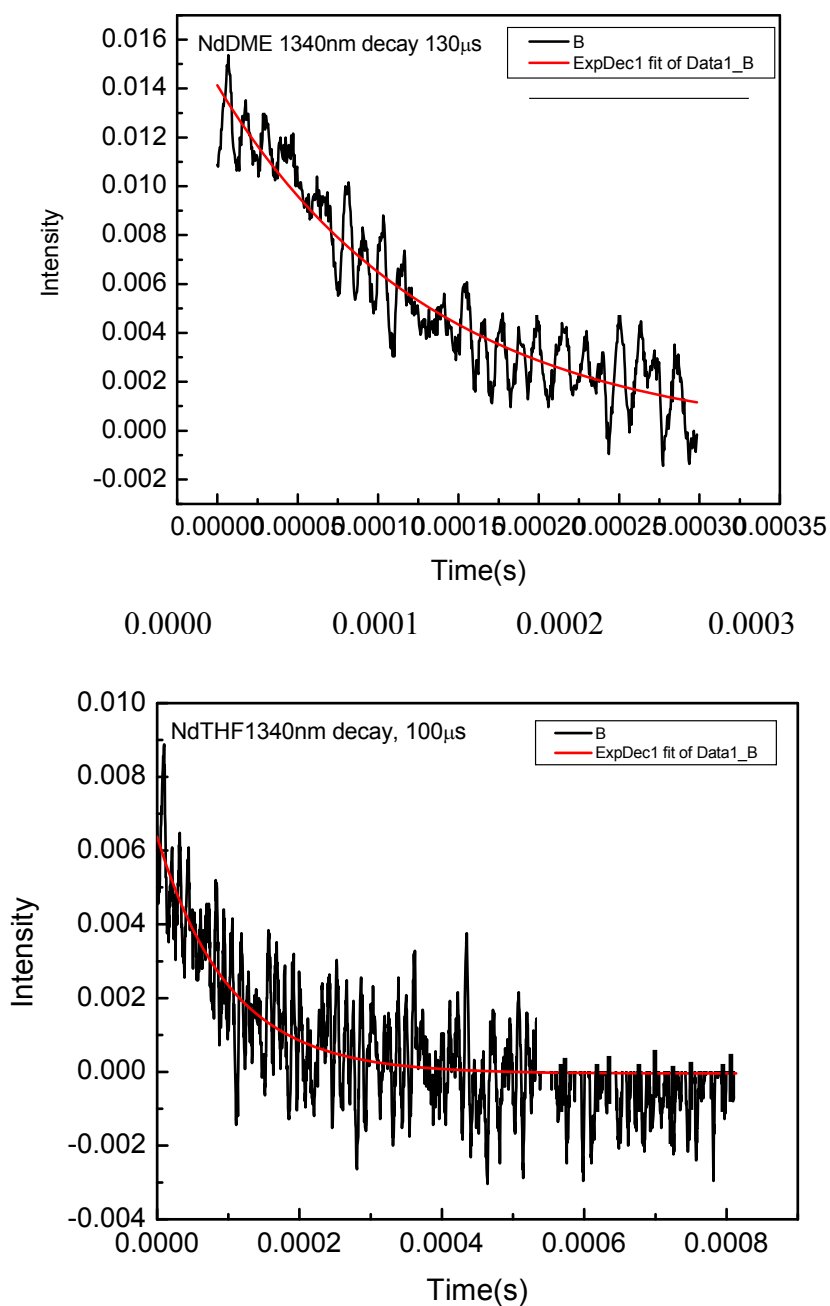


Fig 20. Emission decay curves of $(\text{DME})_2\text{Nd}(\text{SC}_6\text{F}_5)_3$ and $[(\text{THF})_3\text{Nd}(\text{SC}_6\text{F}_5)_3]_2$ for the ${}^4\text{F}_{3/2} \rightarrow {}^4\text{I}_{13/2}$ transition.

The emission properties of $(\text{DME})_2\text{Nd}(\text{SC}_6\text{F}_5)_3$ were compared to the oxyselenido neodymium cluster, $(\text{THF})_8\text{Nd}_8\text{O}_2\text{Se}_2(\text{SePh})_{16}$, because of the longer calculated lifetime for the ${}^4\text{F}_{3/2} \rightarrow {}^4\text{I}_{11/2}$ and ${}^4\text{F}_{3/2} \rightarrow {}^4\text{I}_{13/2}$ transitions in $(\text{DME})_2\text{Nd}(\text{SC}_6\text{F}_5)_3$.²⁶ This longer

lifetime is attributed to a lower number of emission quenching C-H bonds tightly bound to the metal center in $(\text{DME})_2\text{Nd}(\text{SC}_6\text{F}_5)_3$. Greater emission intensity was expected, and found, for the oxo species due to the decrease in the number of emission quenching groups around the metal centers, and the increase in the metal ion concentration of the cluster.

Structure and local environment around the metal have a strong correlation with the optical properties of these materials, and a thorough analysis of these structure/property relationships will help in understanding not only the requirements for improving emission intensities but also the nature of the ligand-metal interactions. It is important to note all structural features of these molecules in order to begin to quantify these relationships. Recall that $(\text{DME})_2\text{Nd}(\text{SC}_6\text{F}_5)_3$ is triclinic, contains an eight coordinate neodymium ion surrounded by three SC_6F_5^- ligands, four oxygen donors (from two chelating neutral DME molecules), and a dative interaction between a fluorine atom of one of the coordinating SC_6F_5^- groups and the Nd^{3+} ion. Pertinent to its photoluminescence properties is the fact that $(\text{DME})_2\text{Nd}(\text{SC}_6\text{F}_5)_3$ has one unique Nd^{3+} ion in the molecule. All metal ions have nearly equivalent environments throughout the crystalline lattice, and the only C-H groups present, are in the DME. The Nd^{3+} ion concentration in $(\text{DME})_2\text{Nd}(\text{SC}_6\text{F}_5)_3$ is calculated to be 12.65×10^{20} ions/cm³.

$(\text{THF})_8\text{Nd}_8\text{O}_2\text{Se}_2(\text{SePh})_{16}$ crystallizes in the higher symmetry P2(1)/c monoclinic space group. The eight unique Nd ions present in the $(\text{THF})_8\text{Nd}_8\text{O}_2\text{Se}_2(\text{SePh})_{16}$ cluster give rise to several unique Nd sites. The first pair of Nd^{3+} ions (Nd2, Nd2A) are eight coordinate, being bound to 4 SeC_6H_5^- (all either μ_2 or μ_3 bridging), 2 $\mu_5\text{-Se}^{2-}$, $\mu_3\text{-O}^{2-}$, and a THF molecule. The second pair (Nd1, Nd1A) are seven coordinate, being bound again

by 4 SeC_6H_5^- (all either μ_2 or μ_3 bridging) and 1 THF, but in place of 1 $\mu_5\text{-Se}^{2-}$ there is now a terminal SeC_6H_5^- , and no coordination to the $\mu_3\text{-O}^{2-}$. The remaining two pairs (Nd3, Nd3A, Nd4, and Nd4A) are seven coordinate and have similar coordination environments, being bound to 4 SeC_6H_5^- (all either μ_2 or μ_3 bridging), 1 $\mu_5\text{-Se}^{2-}$, $\mu_3\text{-O}^{2-}$, and a THF. While Nd3/Nd3A and Nd4/ Nd4A pairs have the same ligand set coordination, they differ in intramolecular bond lengths and bond angles.

$(\text{THF})_8\text{Nd}_8\text{O}_2\text{Se}_2(\text{SePh})_{16}$ has two clusters in the 8341.5\AA^3 unit cell, and the Nd^{3+} ion concentration is calculated to be 19.12×10^{20} ions/ cm^3 . Intramolecular metal-metal distances are important because non radiative excitation migration pathways are sensitive to the local environment of the ions, having an inverse 6th power relationship with donor-acceptor atomic spacing. In $(\text{THF})_8\text{Nd}_8\text{O}_2\text{Se}_2(\text{SePh})_{16}$, all of the Nd-Nd distances are calculated to be between 0.982 and 0.378 nm.

Typical absorption spectra were observed for $(\text{THF})_8\text{Nd}_8\text{O}_2\text{Se}_2(\text{SePh})_{16}$ and $(\text{DME})_2\text{Nd}(\text{SC}_6\text{F}_5)_3$, both showing well defined f-f absorption bands (Fig. 21). The strongest absorption band for both complexes is observed around 580 nm. This band corresponds to a hypersensitive $^4\text{I}_{9/2} - ^4\text{G}_{5/2}$ transition, and as such is not an ideal transition for photon pumping in our PL experiments since it is sensitive to the environment around the metal ion. Furthermore, increasing the stokes shift of the pump energy from the radiative emission energy increases the probability of non radiative energy transfers.

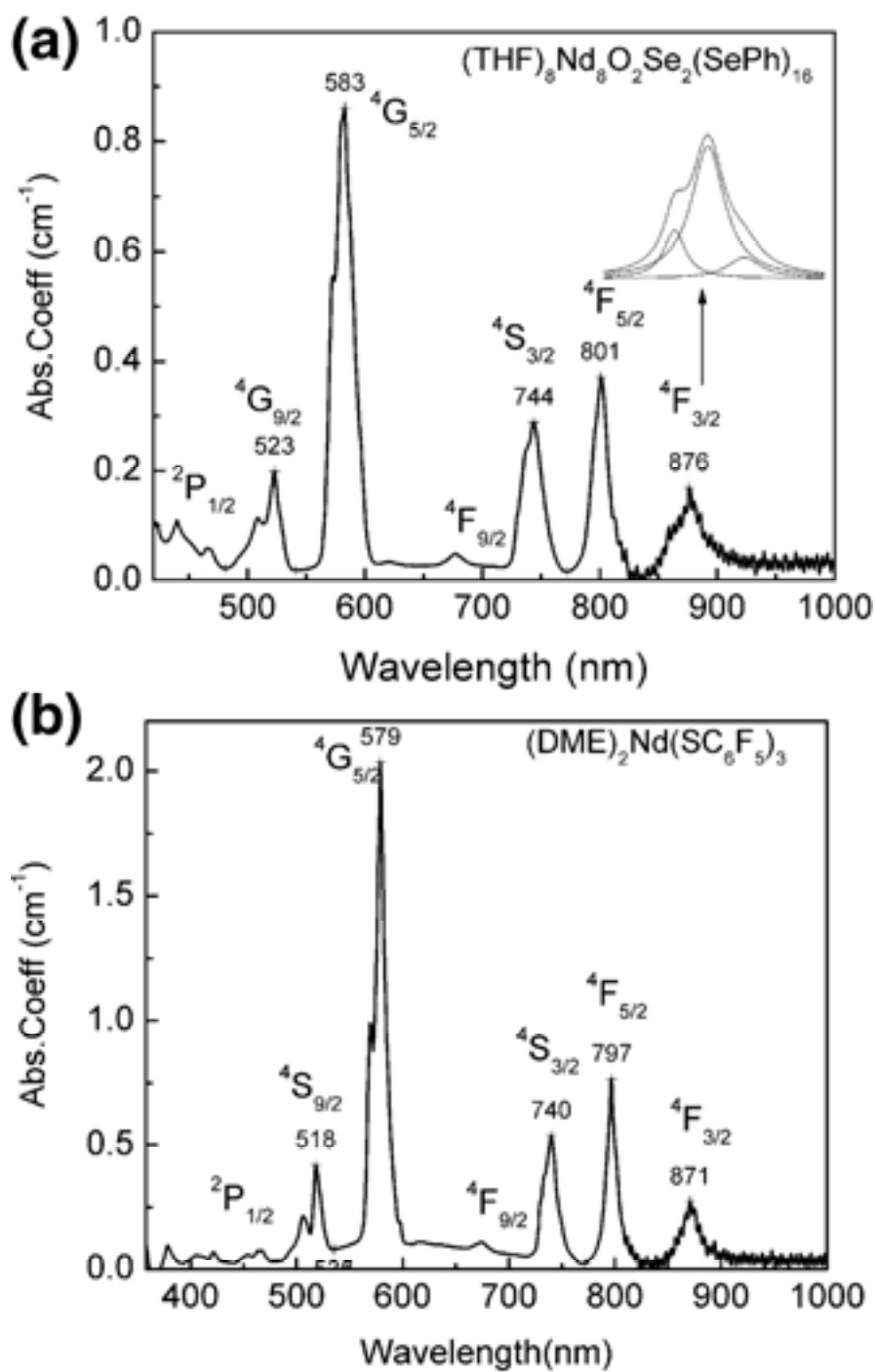


Fig 21. (a) Absorption spectrum for 0.0058 M $(\text{THF})_8\text{Nd}_8\text{O}_2\text{Se}_2(\text{SePh})_{16}$ in THF. The inset shows the deconvolution of the absorption band at 871 nm. (b) Absorption spectrum for 0.0058 M $(\text{DME})_2\text{Nd}(\text{SC}_6\text{F}_5)_3$ in DME. Labeled transitions arise from the $^4\text{I}_{9/2} \text{Nd}^{3+}$ ground state.

When the recorded spectral region containing the absorption band around 876 nm (for $(\text{THF})_8\text{Nd}_8\text{O}_2\text{Se}_2(\text{SePh})_{16}$, corresponding to the $^4\text{F}_{3/2} \rightarrow ^4\text{I}_{9/2}$ transition) was deconvoluted, multiple bands were discovered. The same transition in $(\text{DME})_2\text{Nd}(\text{SC}_6\text{F}_5)_3$ showed only one well defined peak. For a given transition, in the absence of crystal field effects one would expect such a single well defined absorption peak. Splitting of these transitions due to crystal field effects is largely affected by the symmetry of the environment around the metal ion. This is because both the long range and local environments affect the crystal field splitting, but the latter to a greater degree.

In contrast to $(\text{THF})_8\text{Nd}_8\text{O}_2\text{Se}_2(\text{SePh})_{16}$, $(\text{DME})_2\text{Nd}(\text{SC}_6\text{F}_5)_3$ fails to show splitting of the $^4\text{F}_{3/2} \rightarrow ^4\text{I}_{9/2}$ transition. We cannot attribute this effect solely to an asymmetrical environment around a single metal atom because even as a monomeric species, $(\text{DME})_2\text{Nd}(\text{SC}_6\text{F}_5)_3$ contains asymmetry about the metal ion. Nd-S and Nd-O bond lengths, bond angles, and torsion angles vary within one $(\text{DME})_2\text{Nd}(\text{SC}_6\text{F}_5)_3$ molecule. There is also a dative Nd-F interaction from one aromatic group and π - π stacking of the two remaining SC_6F_5 ligands present in this complex. Because crystal field effects are minimized in rare earth coordination environments, it is still likely that the multiple bands in $(\text{THF})_8\text{Nd}_8\text{O}_2\text{Se}_2(\text{SePh})_{16}$ arise from the substantially different local metal ion environments. These changes in local environment can give rise to small differences in the absorption profile for a given transition, even due to relatively small crystal field effects.

We can begin to shed more light on the bonding between metal and ligand by quantifying the changes in optical properties and correlating the results with differing structural features. Spectroscopic calculations begin by numerically integrating the

absorption bands to obtain the experimental oscillator strengths and these experimental values are then fitted with calculated oscillator strength values to obtain three Judd-Ofelt intensity parameters ($\Omega_2, \Omega_4, \Omega_6$). The intensity parameters can be used to evaluate not only the probability that a transition will occur, but also its radiative decay time. Changes in these parameters are due in part to differences in the bonding around the Nd^{3+} ion and its local environment. The calculated values for $(\text{THF})_8\text{Nd}_8\text{O}_2\text{Se}_2(\text{SePh})_{16}$ are $\Omega_2 = 8.00 \pm 0.12 \times 10^{-20} \text{ cm}^2$, $\Omega_4 = 1.50 \pm 0.02 \times 10^{-20} \text{ cm}^2$, and $\Omega_6 = 1.20 \pm 0.01 \times 10^{-20} \text{ cm}^2$. For $(\text{DME})_2\text{Nd}(\text{SC}_6\text{F}_5)_3$, the values are $\Omega_2 = 1.10 \pm 0.01 \times 10^{-20} \text{ cm}^2$, $\Omega_4 = 1.20 \pm 0.01 \times 10^{-20} \text{ cm}^2$, and $\Omega_6 = 1.00 \pm 0.015 \times 10^{-20} \text{ cm}^2$. The Ω_2 parameter, in particular, is strongly correlated with the strength of the crystal field imparted by the ligands around the Nd^{3+} ion, and as such, is related to the degree of covalency in the Nd-L bonds.

As mentioned above, the Judd-Ofelt intensity parameters depend on the chemical environment around the metal ion and on the metal ion itself. The solutions to the equations for these parameters are related to the bonding environment around the metal ion and its asymmetry through the following equations:

$$\Omega_\lambda = \frac{(2\lambda + 1) \sum |A_{SP}|^2 \Xi^2(S, \lambda)}{(2S + 1)}$$

and

$$A_{SP} = \left(\frac{4\pi}{2t + 1} \right)^{1/2} \sum_j \frac{\alpha_j}{R_j^{t+1}} Y_p^t(\theta_j, \phi_j)$$

$A_{S,P}$ is related to the coordination geometry and to the nature of the chemical environment around the Nd^{3+} ion by a dependence upon the non directional polarizability of the atoms at positions around the metal ion. Because of this, any asymmetry around the metal ion is taken into account in the $A_{S,P}$ term, which then directly relates the Judd-Ofelt intensity

parameters to the bonding environment of the metal ion in the complex. The $\Xi(S,\lambda)$ term is directly proportional to the nephelauxetic parameter β (equation below), where v_f and v are the transition energies of the free ion and the ion in the matrix, respectively.

$$\beta = \frac{v_f - v}{v_f}$$

Being directly related to $\Xi(S,\lambda)$, β is also proportional to the degree of covalency between the metal and ligand, and in conjunction with the Judd-Ofelt intensity parameters we can begin to better understand and quantify the metal ligand bonding scheme. An increase in the nephelauxetic parameter is indicative of more covalent metal- ligand interactions in the complex.

Another valuable aspect of the Judd-Ofelt parameter, Ω_2 , is that this parameter is highly dependant upon the hypersensitive transitions in rare earth ions, and another way of accounting for metal-ligand covalency in these species is through calculation of the covalency parameter of these transitions. Hypersensitive transitions, defined by selection rules as having a $\Delta J \geq 2$, are very sensitive to the environment around the metal ion. Small changes in the local environment have much larger effects on these electronic transitions, unlike the Laporte forbidden $\Delta J = 0 f-f$ transitions usually seen in rare earth ions. For Nd^{3+} , the two hypersensitive transitions, $^4I_{9/2} \rightarrow ^4G_{5/2}$ and $^4I_{9/2} \rightarrow ^4F_{7/2}$, have large effects on Ω_2 , and their intensities are directly related to its (Ω_2) value. Through the covalency parameter, I_L/I_S , (where I_L and I_S are the maximum intensity of the long and short wavelength peaks for each of the hypersensitive transitions) we can begin to see how Ω_2 , β , and the I_L/I_S are all interrelated, and how they are useful tools to probe the

bonding in rare earth complexes. For one of these hypersensitive transitions, a red shift of the absorption peak center corresponds to an increase in I_L/I_S , indicating increased metal–ligand bond covalency. This red shift is a consequence of nephelauxetic effects, which arise from ligand-metal charge transfers (LMCT).

By calculating Ω_2 , β , and I_L/I_S , we can now determine the degree of metal–ligand bond covalency. The lower value of Ω_2 in $(DME)_2Nd(SC_6F_5)_3$, when compared to $(THF)_8Nd_8O_2Se_2(SePh)_{16}$, is a result of the bonding interactions between the Nd^{3+} ion and first coordination sphere ligands. Also, the calculated values of β are 8.55×10^{-3} and 1.67×10^{-3} for $(THF)_8Nd_8O_2Se_2(SePh)_{16}$ and $(DME)_2Nd(SC_6F_5)_3$, respectively. In $(DME)_2Nd(SC_6F_5)_3$, the metal ion is only bound to two neutral donor DME, and mono-anionic fluorinated thiolates. In $(THF)_8Nd_8O_2Se_2(SePh)_{16}$, however, the Nd^{3+} ions are bound tightly to oxo and selenido ligands, which will have stronger coulombic interactions. The red shift observed for the two hypersensitive transitions in $(THF)_8Nd_8O_2Se_2(SePh)_{16}$ are in the range 579–583 ($^4I_{9/2} \rightarrow ^4G_{5/2}$) and 733–737 nm ($^4I_{9/2} \rightarrow ^4F_{7/2}$). The increase in the peak wavelength of the hypersensitive transition for $(THF)_8Nd_8O_2Se_2(SePh)_{16}$ reflects a decreasing $4f^n - 4f^{n-1}5d^1$ energy difference. The red shift is also attributed to increasing polarizability of the ligands around the rare earth ions. A selenido ion has higher polarizability than oxo and fluoride ions because of its lower electronegativity. Increased ligand polarizability (“softness”) results in a more diffuse electron density profile, giving rise to a larger metal-ligand orbital overlap (i.e. covalency). Another manifestation of the covalent interaction giving rise to field effects is seen in the line broadening of the emission bands. The splitting of these bands is a direct result of the structure and local environment surrounding the metal ion.

These two systems were studied to explore the nature of the bonding interaction between metal and ligand in lanthanide-chalcogen complexes. Photoluminescence spectroscopy was used to generate well resolved absorption and emission spectra, which were used to calculate various spectroscopic parameters to show the relationship between structure and electronic transitions in such species. Our results show that simple electrostatic models do not take into account all of the interactions taking place in these species and that there is a measurable amount of covalent interactions.

(THF)₈Nd₈O₂Se₂(SePh)₁₆ shows greater crystal field effects when compared to (DME)₂Nd(SC₆F₅)₃. This is in part due to the more complex coordination environment around the Nd³⁺ ions in (THF)₈Nd₈O₂Se₂(SePh)₁₆ leading to increased covalent interactions from more polarizable ligands surrounding the metal ion. While this proves to be a useful study of relative covalent interactions in these species, and certainly gives a more quantified proof of iono-covalent bonding in Ln-E coordination species, DFT calculations remain the definitive analysis for determining orbital contributions to bonding.

With the fundamental significance of these studies established, our parallel goal of understanding and controlling the optical properties of these systems from a purely applications perspective was undertaken. As mentioned, for these materials to become useful in next generation technologies, both photoluminescence quantum efficiency and radiative emission lifetimes need to be controlled, and optimized. The emission spectra of (THF)₈Nd₈O₂Se₂(SePh)₁₆ and (DME)₂Nd(SC₆F₅)₃, after being pumped with 800nm photons, are shown below (Fig 22). In this pumping scheme, the ⁴F_{3/2} state is populated and relaxation to four lower energy states (⁴I_{9/2}, ⁴I_{11/2}, ⁴I_{13/2}, and ⁴I_{15/2}) is monitored. These

transitions correspond to the four characteristic Nd^{3+} NIR emission bands. When choosing pump photon energies, it is important to first choose an energy that matches as closely as possible the energy required to excite the desired transition. This minimizes pump photon loss by competitive absorbers. Also, the chosen excited state must relax predominantly by radiative emission to ensure minimization of cooperative energy transfers.

Once the calculated radiative emission lifetime (τ_{rad}) (for the free ion in the absence of energy transfer mechanisms) and the experimental radiative emission lifetime (τ_{fl}) of the rare earth ion in a matrix (i.e. the coordinated species) are calculated, the quantum efficiency can be determined. The experimental radiative lifetime can be extracted from the measured decay curve (Fig 23) and fitted using a Monte Carlo simulation to ensure the fitting takes into account all of the energy transfer processes available to Nd^{3+} ions at different sites. The ratio of measured lifetime to calculated lifetime will yield the quantum efficiency of the transition. The calculated quantum efficiencies for the $^4\text{F}_{3/2} \rightarrow ^4\text{I}_{11/2}$ ($\sim 1080\text{nm}$) transitions were calculated to be 16 ± 0.2 and $9 \pm 0.1\%$ for $(\text{THF})_8\text{Nd}_8\text{O}_2\text{Se}_2(\text{SePh})_{16}$ and $(\text{DME})_2\text{Nd}(\text{SC}_6\text{F}_5)_3$, respectively. These values were derived from experimental radiative emission lifetimes of $186 \pm 0.9 \mu\text{s}$ for $(\text{THF})_8\text{Nd}_8\text{O}_2\text{Se}_2(\text{SePh})_{16}$ and $110 \pm 0.5 \mu\text{s}$ for $(\text{DME})_2\text{Nd}(\text{SC}_6\text{F}_5)_3$. The calculated radiative emission lifetime is inversely proportional to the linear combination of the Judd-Ofelt intensity parameters Ω_4 and Ω_6 , and is calculated to be $1398 \mu\text{s}$ for $(\text{DME})_2\text{Nd}(\text{SC}_6\text{F}_5)_3$ and $1187 \mu\text{s}$ for $(\text{THF})_8\text{Nd}_8\text{O}_2\text{Se}_2(\text{SePh})_{16}$.

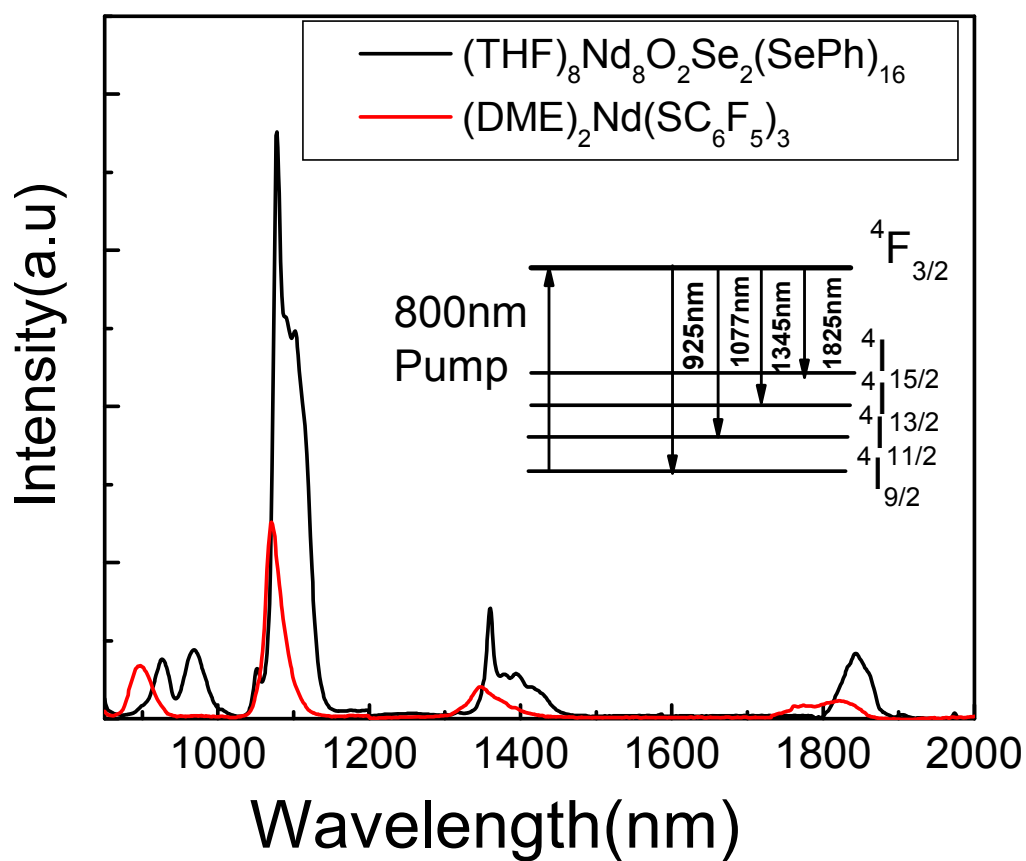


Fig 22. Observed emission bands located at 927, 1078, 1360, and 1843 nm for $(\text{THF})_8\text{Nd}_8\text{O}_2\text{Se}_2(\text{SePh})_{16}$ and 897, 1071, 1347, and 1824 nm for $(\text{DME})_2\text{Nd}(\text{SC}_6\text{F}_5)_3$.

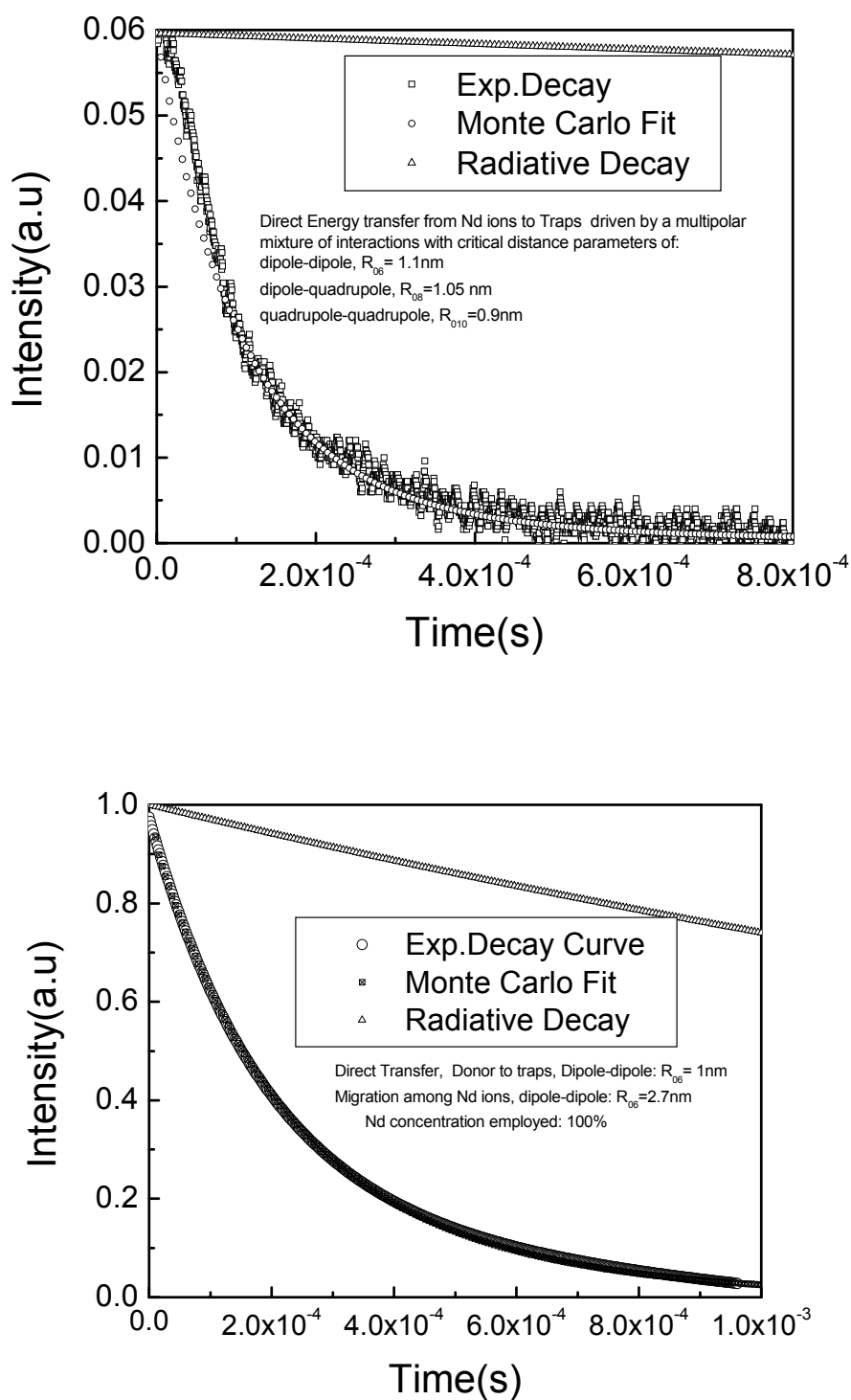


Fig 23. Fluorescence decay of the $^4F_{3/2} \rightarrow ^4I_{11/2}$ transition of Nd^{3+} in $(THF)_8Nd_8O_2Se_2(SePh)_{16}$ (circles) and the corresponding MC fit assuming a dipole-dipole interaction. The upper curve (Triangle) is the radiative decay corresponding to a decay time of $1187 \mu\text{s}$.

At the time of this study, these were by far, the highest reported quantum efficiencies for any molecular neodymium species, and they marked a new path for the realization of utilizing molecular sources as highly luminescent rare earth materials. While these results show a real advancement in the design of highly luminescent species, emission quenching processes are still present as seen by the less than 100% quantum efficiencies. A more detailed discussion of the specific energy transfer mechanisms of these two systems and how they relate to the structure of these species is given in the experimental section of this thesis.

Polymer Studies

The utility of these novel lanthanide chalcogen based molecules in new devices relies on their ability to be soluble in organic matrixes where traditional solid-state lanthanide sources are not. By doping these new molecules into polymer matrixes such as 6F (Hexafluoropropyl derivative) perfluorocyclobutyl (PFCB) polymer, PMMA (Polymethyl methacrylate), or BPVE (biphenol trifluorovinyl ether precursor to the PFCB), the fabrication of novel devices can be realized. Preliminary studies were made using $(\text{DME})_2\text{Nd}(\text{SC}_6\text{F}_5)_3$ as the lanthanide chalcogen species. Initial polymer solutions were made by dissolving the respective powdered polymer (PMMA in this study) in anhydrous toluene at a concentration of 0.1g/mL. Once fully dissolved, composites were generated by adding crystalline $(\text{DME})_2\text{Nd}(\text{SC}_6\text{F}_5)_3$ to the polymer solution at concentrations of 0.01, 0.025, 0.05, and 0.1 mmol Nd/mL polymer solution. Solutions were shaken periodically until all Nd crystals dissolved (~2-3days), after which time each

respective sample was transferred onto a transparent glass slide by means of pipetting, where the slow evaporation of the toluene leaves a hard polymer composite. The purpose of generating increasingly concentrated solutions is to identify the concentration that will yield the highest quantum efficiency before concentration quenching mechanisms degrade optical properties or the material becomes opaque. In this study, concentrations up to 0.1 mmol Nd/mL polymer solution remained optically transparent.

1.5 Conclusions:

From our studies, it is clear that the synthesis of novel lanthanide chalcogen species is useful for both advancing our fundamental knowledge of the bonding in these molecules, as well as for the improvement of optical properties to the extent that real materials can begin to be fabricated for technological applications. Here, a unique series of molecular lanthanide complexes proved effective in extending our understanding of the structural relationships present between metal, ligand, and Lewis base. Most important was the synthesis of mer-octahedral $(\text{THF})_3\text{Er}(\text{SeC}_6\text{F}_5)_3$, which because of its near ideal mer-octahedral geometry, was a suitable model for DFT calculations. DFT studies showed that there is indeed significant orbital overlap contributing to the stability of the lanthanide-ligand bond, quantitatively showing that covalent bonding can have a measurable impact on the structures of lanthanide coordination complexes. The significance of this study is in its confirmation that the inequivalent bond lengths noted in a series of mer-octahedral LnX_3Y_3 compounds result from covalent bonding interactions between ligand based orbitals and the empty Ln 5d orbitals, with no involvement of the Ln 4f orbitals.

The successful isolation of $(L)_x\text{Nd}(\text{SC}_6\text{F}_5)_3$ ($L = \text{THF}, \text{DME}; x = 2, 3$) and $(L)_x\text{Ln}(\text{SeC}_6\text{F}_5)_3$ ($L = \text{THF}, \text{pyr}; \text{Ln} = \text{Nd}, \text{Sm}, \text{Er}, \text{Yb}$) has led to a systematically varied series of species that has allowed us to better understand the correlation of structure with photoluminescence. By comparing $(\text{DME})_2\text{Nd}(\text{SC}_6\text{F}_5)_3$, $(\text{THF})_2\text{Nd}(\text{SC}_6\text{F}_5)_3$, $(\text{THF})_3\text{Nd}(\text{SeC}_6\text{F}_5)_3$, $(\text{THF})_3\text{Nd}(\text{SeC}_6\text{H}_5)_3$, and $(\text{THF})_8\text{Nd}_8\text{O}_2\text{Se}_2(\text{SePh})_{16}$, we have extended our knowledge of how structure affects photoluminescence QEs, shifts in emission energies, and variations in crystal field effects. It was shown that metal ion concentration has the largest impact on increasing the photoluminescent quantum yield in these systems. Having 8 Nd ions/molecule, $(\text{THF})_8\text{Nd}_8\text{O}_2\text{Se}_2(\text{SePh})_{16}$ shows a 7% higher QE than the fluorinated monomer, $(\text{DME})_2\text{Nd}(\text{SC}_6\text{F}_5)_3$. The most optically detrimental structural feature was found to be C-H organic functionalities capable of vibronic coupling with the radiative transitions of the metal ions. This effect was quantified in the 30 μs radiative decay improvement of $(\text{DME})_2\text{Nd}(\text{SC}_6\text{F}_5)_3$ (110 μs) when compared to $(\text{THF})_2\text{Nd}(\text{SC}_6\text{F}_5)_3$ (100 μs).

References

- ¹ Tilley, T.; Andersen, R.; Brock, S.; Zalkin, A. Bis (pentamethylcyclopentadienyl) bis (pyridine) ytterbium(II). *Inorganic Chemistry* **1982**, *21*, 2647.
- ² Berg, D.; Burns, C.; Andersen, R.A.; Zalkin, A. Electron-Transfer Reactions of Divalent Ytterbium Metallocenes. Synthesis of the Series $[(\text{Me}_5\text{C}_5)_2\text{Yb}]_2[\mu_2\text{E}]$ (E = O, S, Se, or Te) and Crystal Structure of $[(\text{Me}_5\text{C}_5)_2\text{Yb}]_2[\mu_2\text{Se}]$. *Organometallics* **1989**, *8*, 1865.
- ³ Brewer, M.; Khasnis, D.; Buretea, M.; Berardini, M.; Emge, T. J.; Brennan, J. G. Pyridine Coordination Complexes of the Divalent Ytterbium Chalcogenolates $\text{Yb}(\text{EPh})_3$ (E = S, Se, Te). *Inorganic Chemistry* **1994**, *33*, 2743.
- ⁴ Lee, J.; Freedman, D.; Melman, J.H.; Brewer, M.; Sun, L.; Emge, T. J.; Long, F.H.; Brennan, J.G. Trivalent Lanthanide Chalcogenolates: $\text{Ln}(\text{SePh})_3$, $\text{Ln}_2(\text{EPh})_6$, $\text{Ln}_4(\text{SPh})_{12}$, and $[\text{Ln}(\text{EPh})_3]_n$ (E = S, Se). How Metal, Chalcogen, and Solvent Influence Structure. *Inorg. Chem.* **1998**, *37*, 2512.
- ⁵ Melman, J.; Emge, T.; Brennan, J. Fluorinated Thiolates of Divalent and Trivalent Lanthanides. Ln-F bonds and the Synthesis of LnF_3 . *Inorganic Chemistry* **2001**, *40*, 1078.
- ⁶ Hasegawa, Y.; Wada, Y.; Yanagida, S. Strategies for the design of luminescent lanthanide(III) complexes and their photonic applications. *J. Photochem. and Photobio. C:Photochemistry Reviews* **2004**, *5*, 183.
- ⁷ Freedman, D.; Emge, T.J.; Brennan, J. $(\text{THF})_8\text{Ln}_8\text{E}_6(\text{EPh})_{12}$ Cluster Reactivity: Systematic Control of Ln, E, EPh, and Neutral Donor Ligands. *Inorg. Chem.* **1999**, *38*, 4400.
- ⁸ Shannon, R.D. Revised Effective Ionic Radii and Systematic Studies of Interatomic Distances in Halides and Chalcogenides. *Acta Cryst* **1976**, *A32*, 751-767.
- ⁹ Spichal, Z.; Necas, M.; Pinkas, J. From parquets to bricks: a series of lanthanide coordination polymers with bis(diphenylphosphino)ethane dioxide. *Inorganic Chemistry* **2005**, *44*, 2074.
- ¹⁰ Evans, W.J.; Rabe, G.W.; Ziller, J.W. Utility of N-Methylimidazole in Isolating Crystalline Lanthanide Iodide and Hydroxide Complexes: Crystallographic Characterization of Octasolvated $[\text{Sm}(\text{N-MeIm})_8]\text{I}_3$ and Polymetallic $[\text{SmI}(\mu\text{-I})(\text{N-MeIm})_3]_2$, $[(\text{N-MeIm})_5\text{Sm}(\mu\text{-OH})]_2\text{I}_4$, and $\{[(\text{N-MeIm})_4\text{Sm}(\mu\text{-OH})]_3(\mu_3\text{-OH})_2\}\text{I}_4$. *Inorganic Chemistry* **1994**, *33*, 3072.
- ¹¹ Daniele, S.; Hubert-Pfalzgraf, L.G.; Perrin, M. Molecular Structures of Volatile Ce(IV) hexafluoroisopropoxide Complexes with TMEDA and Diglyme. CVD Experiments. *Polyhedron* **2002**, *21*, 1985.

-
- ¹² Seigi, S.; Guan, J.; Mfinea, L.A.; Lehn, J.M.; Hoffman, D.M. Chemical Vapor Deposition of Cerium Oxide Films from a Cerium Alkoxide Precursor. *Chem. Mater.* **2004**, *16*, 1667.
- ¹³ Hou, Z.; Kobayashi, K.; Yamazaki, H. Lanthanoid Complexes with Hexamethylphosphoramide (HMPA) Ligand. Preparation and Crystal Structure of Ytterbium Complexes of HMPA, $[\text{Yb}(\text{H}_2\text{O})_5(\text{HMPA})_2]\text{Cl}_3 \cdot \text{H}_2\text{O} \cdot \text{HMPA}$ and $\text{YbCl}_3(\text{HMPA})_3$. *Chem Lett.* **1991**, *20*, 265.
- ¹⁴ Radonovich, L.J.; Glick, M.D. Structure of a six-coordinate rare earth complex. Trichlorotris(hexamethylphosphoramide)praseodymium(III). *Journal of Inorganic and Nuclear Chemistry* **1973**, *35*, 2745.
- ¹⁵ Xing-Wang, Z.; Xing-Fu, L.; Benetollo, F.; Bombieri, G. Crystal structure of a dysprosium trichloride complex with oxygen donor ligands. *Inorganica Chimica Acta* **1987**, *139*, 103.
- ¹⁶ Aspinall, H.C.; Cunningham, S.A.; Maestro, P.; Macaudiere, P. Lanthanide Tris(*tert*-butylthiolates) and the Crystal Structure of $[\text{Yb}(\text{SBU}^t)_2(\mu_2\text{-SBU}^t)(\text{Bipy})]_2$. *Inorg. Chem.* **1998**, *37*, 5396.
- ¹⁷ Deacon, G.B.; Feng, T.; Junk, P.C.; Skelton, B.W.; Sobolev, A.N.; White, A.H. Preparation and X-Ray Crystal Structures of Tetrahydrofuran-Complexed Rare Earth Chlorides - a Structurally Rich Series. *Aust. J. Chem.* **1998**, *51*, 75.
- ¹⁸ Deacon, G.B.; Feng, T.; Junk, P.C.; Meyer, G.; Scott, N.M.; Skelton, B.W.; White, A.H. Structural Variety in Solvated Lanthanoid(III) Halide Complexes. *Aust. J. Chem.* **2000**, *53*, 853.
- ¹⁹ Lee, J.; Brewer, M.; Berardini, M.; Brennan, J. Trivalent Lanthanide Chalcogenolates: Synthesis, Structure, and Thermolysis Chemistry. *Inorg. Chem.* **1995**, *34*, 3215.
- ²⁰ Mashima, K.; Nakayama, Y.; Fukumoto, H.; Kanehisa, N.; Kai, Y.; Nakamura, A. Formation of lanthanoid(II) and lanthanoid(III) thiolate complexes derived from metals and organic disulfides: crystal structures of $[\{\text{Ln}(\text{SAr})(\mu\text{-SAr})(\text{thf})_3\}_2]$ ($\text{Ln} = \text{Sm}, \text{Eu}$), $[\text{Sm}(\text{SAr})_3(\text{py})_2(\text{thf})]$ and $[\text{Yb}(\text{SAr})_3(\text{py})_3]$ ($\text{Ar} = 2,4,6\text{-triisopropylphenyl}$; $\text{py} = \text{pyridine}$). *J. Chem. Soc. Chem. Commun.* **1994**, *21*, 2523.
- ²¹ Norton, K.; Kumar, G.A.; Dilks, J.L.; Emge, T.J.; Riman, R.E.; Brik, M.G.; Brennan, J.G. Lanthanide Compounds with Fluorinated Aryloxide Ligands: Near-Infrared Emission from Nd, Tm, and Er. *Inorg. Chem.* **2009**, *48*, 3573.
- ²² Geissinger, M.; Magull, J. Neue ein- und mehrkernige Komplexe der Lanthanoiden. Zur Reaktion von Ph_2Se_2 mit Ytterbium. *Z. Anorg. Allg. Chem.* **1995**, *621*, 2043.

²³ Melman, J.H. Molecules, clusters, and solid-state materials with lanthanide-sulfur bonds :synthesis, structure, and reactivity. Ph.D. Dissertation, Rutgers the State Univeristy of New Jersey, New Brunswick, NJ, **2004**.

²⁴ Professor, Department of Chemistry and Chemical Biology, Rutgers, the State University of New Jersey.

²⁵ Banerjee, S.; Huebner, L.; Romanelli, M.; Kumar, G.A.; Riman, R.E.; Emge, T.J.; Brennan, J.G. Oxoselenido Clusters of the Lanthanides: Rational Introduction of Oxo Ligands and Near-IR Emission from Nd(III). *J. Am. Chem. Soc.* **2005**, *127*, 15900.

²⁶ Kumar, G.A., Riman, R.E., Diaz-Torres L.A., Banerjee S., Romanelli, M.D., Emge, T.J., Brennan, J.G. "Near Infrared Optical characteristics of Chalcogenide-Bound Nd Organometallic Complexes", *Chem. Mater.* **2007**, *19*, 2937.

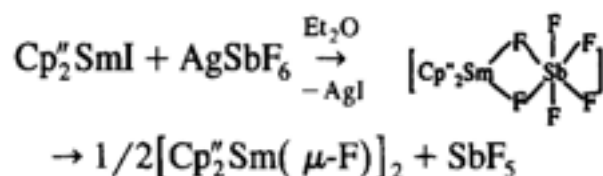
Chapter 2. Lanthanide Fluoride Clusters From C-F Bond Cleavage: An Introduction into Novel Molecular Species Containing Ln-F Bonds

2.1 Introduction

The stability and unique properties of solid-state lanthanide fluorides have made them invaluable materials in many applications. Lanthanide fluorides have found uses as thin-film coatings of optical elements,¹ heavy metal fluoride glasses for optical fibers, and as high-pressure anti-wear lubricants.² The stability of the Ln-F lattice in Ln_xF_y solid-state compounds has slowed the synthesis of novel molecular lanthanide fluoride complexes, and research in this area has remained stagnant over the past decade. Similar to the apprehension given to Ln-E and Ln-O containing molecular complexes, the synthesis of novel Ln-F containing molecules was believed to be an impossible goal. Fluoride containing lanthanide molecules remain to this day elusive species, with almost all of the reported complexes containing bulky cyclopentadienyl ligands. Early work incorporating Ln-F bonds produced very limited results, akin to the early work performed on Ln-E complexes. $\text{Cp}_2\text{Yb}(\mu\text{-F})\text{YbCp}_2$,³ $\text{Cp}_6\text{Yb}_4\text{F}_4$,⁴ $\text{Cp}_6\text{Yb}_5\text{F}_9$,⁵ $\text{Cp}_2\text{YbF}(\text{OEt}_2)$, and $\text{Cp}_2\text{YbF}(\text{THF})$ ⁵ were all prepared from the reaction of divalent organo-lanthanide $\text{Cp}_2\text{Ln}(\text{L})$ ($\text{L} = \text{THF}, \text{Et}_2\text{O}$) species with fluoride sources. Such sources included fluoride salts, a variety of perfluoroolefins including perfluoro-2,4-dimethyl-3-ethylpent-2-ene, perfluoro-2,3-dimethylpent-2-ene, or perfluorocyclohexene.

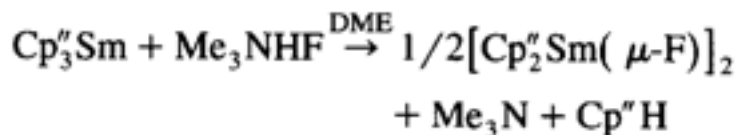
These initial examples of isolable lanthanide molecules containing Ln-F bonds were limited in that they all relied on divalent lanthanide (only Sm, Eu, and Yb) starting materials. Progress was made in 1997 when Xie *et al.* reported the novel synthesis of a

new organolanthanide fluoride, $[\text{Cp}_2''\text{Sm}(\mu\text{-F})]_2$ ($\text{Cp}'' = (\text{Me}_3\text{Si})_2\text{C}_5\text{H}_3$),⁶ according to the following two reaction schemes:



Method 1

In method 1, through the likely intermediate $\text{Cp}_2\text{SmSbF}_6$, fluoride abstraction from the anionic SbF_6^- produced $[\text{Cp}_2''\text{Sm}(\mu\text{-F})]_2$ and neutral SbF_5 .⁶ The energy difference between the Sb-F (96kcal/mol) bond dissociation energy (BDE) and the Sm-F (135kcal/mol) BDE was a key driving force for fluoride abstraction. Method 2 produced $[\text{Cp}_2''\text{Sm}(\mu\text{-F})]_2$ in good yield by the reaction of $\text{Cp}_3''\text{Sm}$ with one equivalent of Me_3NHF in dry 1,2-dimethoxyethane (DME). The main difference in this synthetic method was the use of a direct fluoride source for the incorporation of the fluoride into the resultant lanthanide species.



Method 2

With the exception of these decade old examples, expanding the chemistry of molecular lanthanide fluoride complexes remains a seemingly insurmountable challenge as the stability of the solid-state product is ever present. Progress in this area will likely provide a wealth of information about molecular lanthanide fluoride complexes and result in the discovery of novel species with unique properties.

2.2 DME₃Yb₄F₂O(OCH₂CH₂OCH₃)₂(SeSe)(SC₆F₅)₄•DME : Synthesis, Structure, and Discussion

The new lanthanide-fluoride complex DME₃Yb₄F₂O(OCH₂CH₂OCH₃)₂(SeSe)(SC₆F₅)₄•DME (Yb₄F₂O) was prepared by a fluoride abstraction reaction, without the use of bulky Cp ligands. Yb₄F₂O contains bridging μ_2 -F bonds as well as dative Ln-F interactions. Initially, the goal of this reaction was the synthesis of the heterometallic chalcogenido cluster, (L)_xNd₂Yb₂Se(SeSe)₄(SC₆F₅)₂ (L = pyr, THF, DME). Fitzgerald *et al.* earlier reported the synthesis of (THF)₆Yb₄S(SS)₄(SC₆F₅)₂ and (THF)₆Yb₄Se(SeSe)₄(SC₆F₅)₂ when mixtures of Ln(SC₆F₅)₃ and Ln(EPh)₃ (E = S, Se) react with elemental E.⁷ We sought to prepare a heterometallic derivative to study intramolecular photoluminescent energy transfer mechanisms. After a significant amount of time and work was spent on this area,

efforts to isolate x-ray quality crystals for structural characterization seemed fruitless, with the only isolable species being

$\text{DME}_3\text{Yb}_4\text{F}_2\text{O}(\text{2-methoxy ethoxy})_2(\text{SeSe})(\text{SC}_6\text{F}_5)_4 \cdot \text{DME}$ (Fig 24).

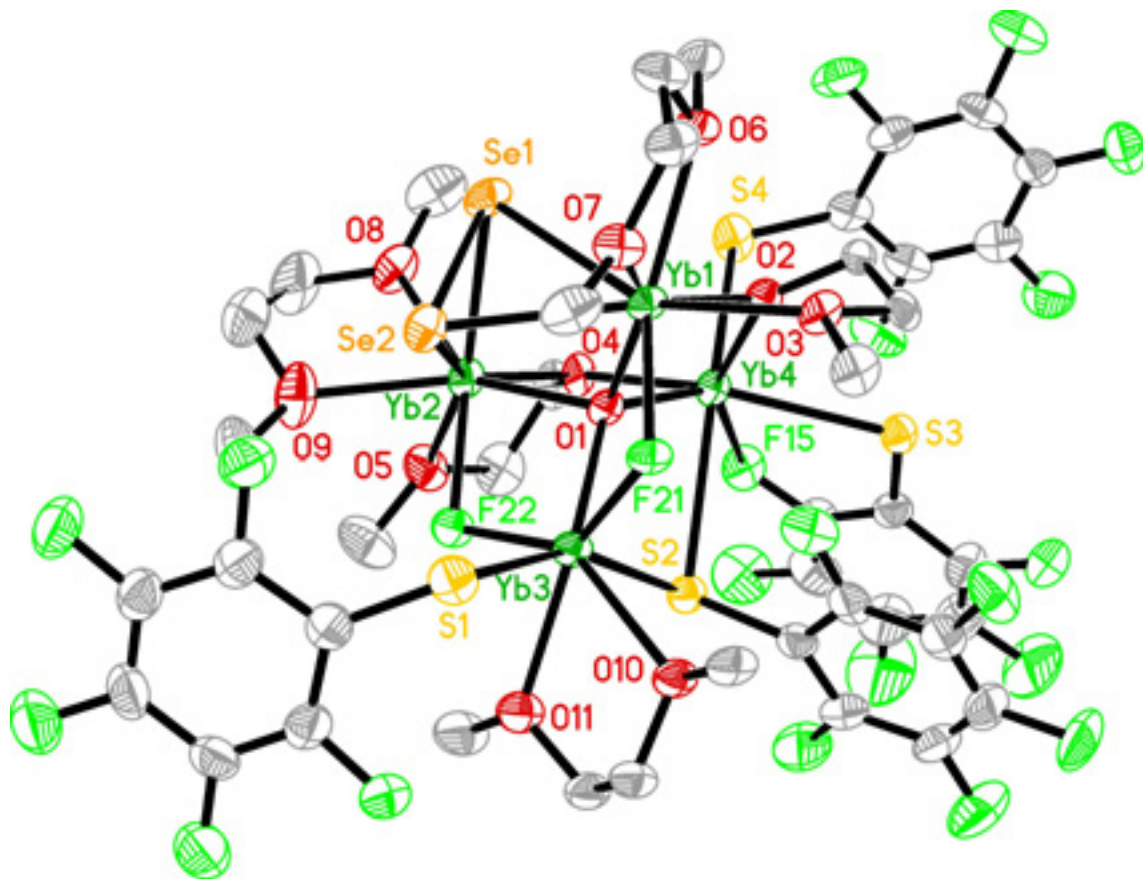


Fig 24. Partially Labeled $\text{DME}_3\text{Yb}_4\text{F}_2\text{O}(\text{OCH}_2\text{CH}_2\text{OCH}_3)_2(\text{SeSe})(\text{SC}_6\text{F}_5)_4 \cdot \text{DME}$ with thermal ellipsoids drawn at 50% probability level.

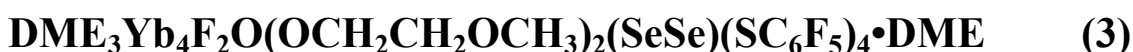
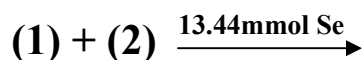
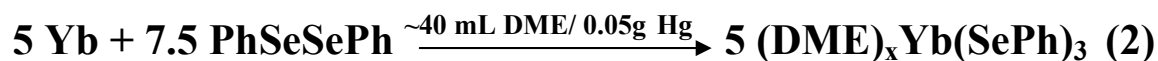
Table 11. Crystal data and structure refinement for

Empirical formula	C ₄₆ H ₅₄ F ₂₂ O ₁₃ S ₄ Se ₂	
	Yb ₄	
Formula weight	2211.21	
Temperature	100(2) K	
Wavelength	0.71073 Å	
Crystal system	Triclinic	
Space group	P-1	
Unit cell dimensions	$a = 13.0151(14)$ Å	$\alpha = 64.062(2)^\circ$.
	$b = 16.4965(17)$ Å	$\beta = 79.378(2)^\circ$.
	$c = 17.3325(18)$ Å	$\gamma = 83.043(2)^\circ$.
Volume	3285.7(6) Å ³	
Z	2	
Density (calculated)	2.235 Mg/m ³	
Final R indices [I>2sigma(I)]	R1 = 0.0590, wR2 = 0.0761	

Table 12. Significant Bond Lengths (Å) and Angles (°) for

Yb(1)-F(21) 2.182(4)	Yb(4)-F(22) 2.154(4)
Yb(4)-F(21) 2.159(4)	Yb(2)-F(22) 2.186(4)
Yb(3)-F(15) 2.571(5)	Yb(2)-Se(1) 2.863(1)
Yb(1)-Se(1) 2.87(1)	Yb(1)-Se(2) 2.934(1)
Yb(2)-O(1) 2.243(5)	Yb(1)-O(1) 2.243(5)
Yb(3)-O(1) 2.159(6)	Yb(4)-O(1) 2.224(5)
Yb(3)-S(2) 2.742(2)	Yb(3)-S(1) 2.757(2)
Yb(3)-S(3) 2.945(2)	

Yb₄F₂O was synthesized according to the following, stepwise reaction scheme:



Yb₄F₂O is a novel lanthanide-fluoride cluster containing bridging Ln-F bonds at the metal's primary coordination sphere. The compound has two eight coordinate metal ions (Yb1, Yb2) and two seven coordinate metal ions (Yb3, Yb4) (Figs. 25 & 26 show the core primary coordination sphere). The most important structural feature of Yb₄F₂O is the μ_2 -F bonds present in the primary coordination sphere of the metal ions. The only fluoride source in this reaction was the (DME)₂Nd(SC₆F₅)₃ molecule which was filtered into the (DME)_xYb(SePh)₃ solution. The fluoride was presumably made available via activation of a C-F bond (~116kcal/mol) of the fluorinated thiolate ligand followed by the formation of the Yb-F bond (~124kcal/mol).

There are two pairs of metal ions (Yb1/Yb4, Yb2/Yb4) that are bridged by oxygen atoms of the OCH₂CH₂OCH₃ ligand (O2, and O4 respectively). This ligand is

with thermal ellipsoids drawn at 50% probability.

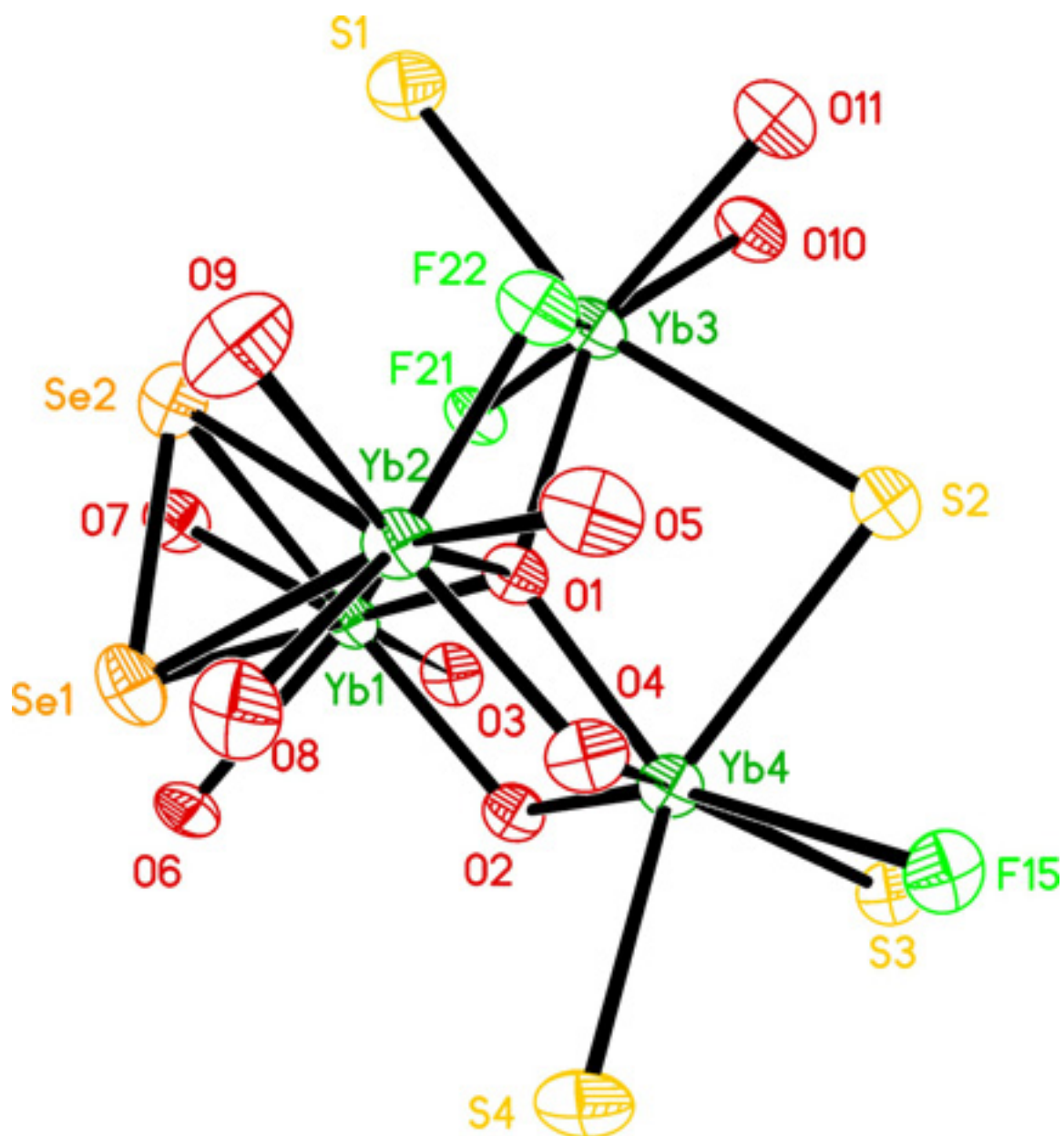


Fig 26. Core Structure: $\text{DME}_3\text{Yb}_4\text{F}_2\text{O}(\text{OCH}_2\text{CH}_2\text{OCH}_3)_2(\text{SeSe})(\text{SC}_6\text{F}_5)_4 \cdot \text{DME}$
with thermal ellipsoids drawn at 50% probability, Rotated 90° with respect to Fig 25.

likely the result of a methoxy carbon-oxygen bond cleavage in DME, resulting in the loss of a methyl group from the parent DME molecule. The two 2-methoxyethoxy ligands present in $\text{Yb}_4\text{F}_2\text{O}$, are both bound to a common Yb atom (Yb4; O2 and O4) through each ligands' methyl cleaved oxygen atom.

The coordination sphere of Yb4 is a crowded site when taking into account the relative positions of the neighboring ligands. Attached to the seven coordinate Yb4 is a bridging thiolate (S2), and two terminal fluorinated thiolates (S3, S4) with the S3 thiolate forming a dative Ln-F bond to Yb4. There is also a centrally located μ_4 -oxo ligand that bridges all four metal ions. The presumed source for the μ_4 -oxo is also the 1,2-dimethoxyethane (DME) solvent. The driving force for the formation of the Ln-O bond is the strength of the coulombic interaction between the electropositive metal and electronegative O^{2-} ion.

Supporting our proposed mechanisms for the formation of the $\text{OCH}_2\text{CH}_2\text{OCH}_3$ ligand and μ_4 -oxygen, is earlier work in 1973 by Britnell *et al.* describing the cleavage of a C-O bond in an ether (DME) by reaction with tungsten(VI) selenide tetrachloride.⁸ This reaction resulted in the same $\text{OCH}_2\text{CH}_2\text{OCH}_3$ ligand found in $\text{Yb}_4\text{F}_2\text{O}$. In a separate publication, Britnell *et al.* reported the oxygen abstraction of DME resulting in available O^{2-} species.⁹ He states that the oxygen was made available from reacting WSeCl_4 with 1,2-dimethoxyethane resulting in oxygen abstraction and formation of a $\text{WSeCl}_4:\text{WOSCl}/\text{DME}$ complex (Fig 27). This is supported in our studies by mass spectrometry data showing the addition of the cleaved CH_3 group to the $\text{C}_6\text{F}_5\text{S}$ anion producing $\text{C}_6\text{F}_5\text{S}-\text{CH}_3$ (peak at 214m/z).

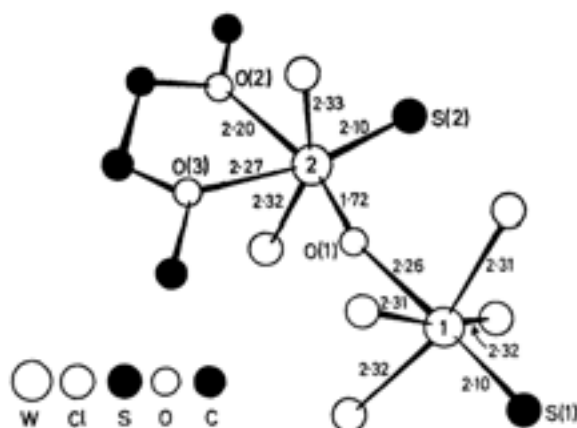


Fig 27. μ_2 -oxo ligand from DME oxygen abstraction producing $\text{WSCl}_4\cdot\text{WOSCl}/\text{DME}$

Further supporting our proposed C-F bond activation mechanism, Koch and Hertwig proposed mechanistic details of lanthanide mediated C-F bond activation by the lanthanide cations Ce^+ and Ho^+ , using quantum chemical calculations. In their study, C-F bond activation was initiated in both CH_3F and $\text{C}_6\text{H}_5\text{F}$.¹⁰ The reaction mechanism for the defluorination (Fig. 28) was mapped by determining all relevant stationary points along the reaction coordinate. This now well established C-F bond activation route by metal cations, including the pertinent Ln ions, substantiates the postulated C-F bond abstraction from the $\text{C}_6\text{F}_5\text{S}$ anion used in our reaction.

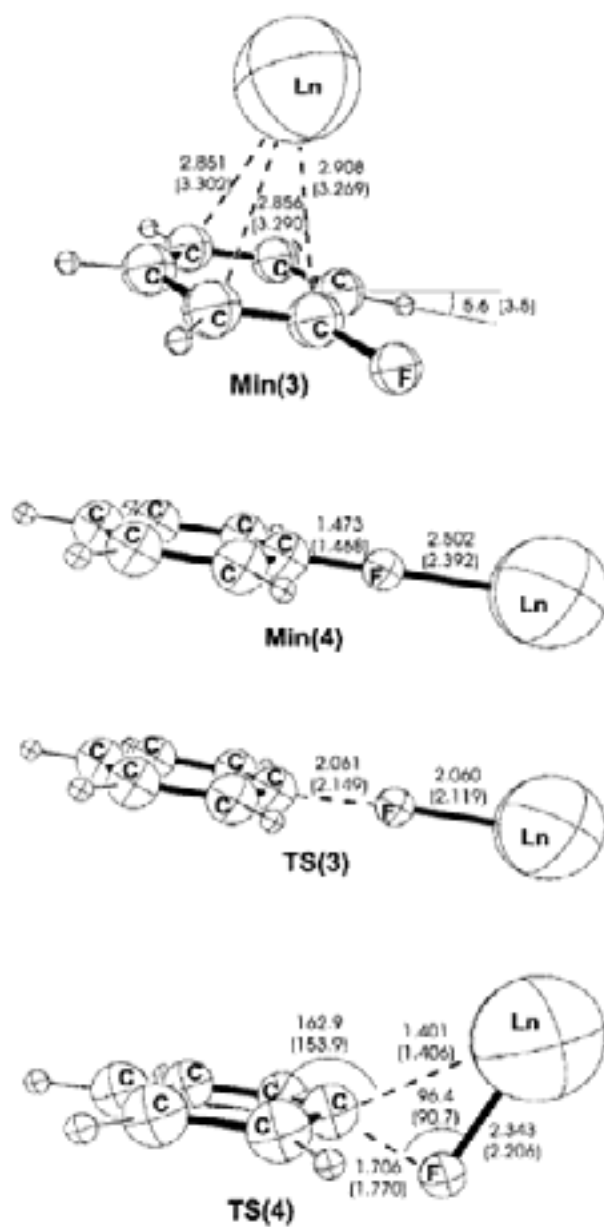


Fig. 28 Ln ion mediated C-F bond activation mechanism for C_6H_5F .

2.3 Conclusions

$\text{Yb}_4\text{F}_2\text{O}$ illustrates the utility of chalcogen based lanthanide complexes in the synthesis of novel rare earth fluoride compounds. Still, more direct and reliable reaction schemes need to be developed for the realization of straightforward methods to produce new Ln-F architectures. It is plausible that C-F and C-O bond activation from SC_6F_5 and DME gave rise to both the fluoride and $\text{OCH}_2\text{CH}_2\text{OCH}_3$ ligands, and that both processes are initiated by the electropositive Yb metal. In many of the past molecular Ln-F examples, divalent Ln complexes were used as precursors to trivalent Ln species with Ln-F connectivities. In our reaction, chalcogenolate ligands were used to stabilize the molecular Ln-F species. Being the first molecular Ln-F species prepared by our group, $\text{Yb}_4\text{F}_2\text{O}$ was the impetus for future work focused on the synthesis of novel Ln-F architectures. Our focus was the incorporation of the fluoride ion into Ln-E architectures using more direct fluoride sources, and the continual improvement of photoluminescence in molecular Ln species.

References

- ¹ Pellicori, S.F.; Colton, E. Fluoride Compounds for IR Coatings. *Thin Solid Films* **1992**, 209, 109.
- ² Lubricant Grade Cerium Fluoride - A new Solid Lubricant Additive for Greases, Pastes and Suspensions, J.M.Dumdum et al., NLGI Spokesman, publ. National Lubrication and Grease Institute, July **1984**, 111.
- ³ Burns, C.J.; Andersen, R.A. Reaction of $(C_5Me_5)_2Yb$ with fluorocarbons: formation of $(C_5Me_5)_4Yb_2(\mu-F)$ by intermolecular C-F activation. *J. Chem. Soc. Chem. Commun.* **1989**, 2, 136.
- ⁴ Burns, C.J.; Berg, D.J.; Andersen, R.A. Preparation and crystal structure of the mixed-valence (YbIII,II) tetranuclear complex, $(Me_5C_5)_6Yb(\mu-F)_4$. *J. Chem. Soc. Chem. Commun.* **1987**, 4, 272.
- ⁵ Watson, P.L.; Tulip, T.H.; Williams, I. Defluorination of perfluoroolefins by divalent lanthanoid reagents: activating carbon-fluorine bonds. *Organometallics* **1990**, 9, 1999.
- ⁶ Xie, Z.; Liu, Z. Synthesis and Crystal Structure of an Organolanthanide Fluoride $[(Me_3Si)_2C_5H_3]_2Sm(\mu-F)_2$. *Journal of Organometallic Chemistry* **1997**, 539, 127.
- ⁷ Fitzgerald, M.; Emge, T.; Brennan, J. Chalcogen-Rich Lanthanide Clusters with Fluorinated Thiolate Ancillary Ligands. *Inorganic Chemistry* **2002**, 41, 3528.
- ⁸ Britnell, D.; Drew, M.G.B.; Fowles, G.W.A.; Rice, D.A. Cleavage of an ether by reaction with tungsten(VI) selenide tetrachloride. *J.C.S. Chem. Comm.* **1973**, 8, 462.
- ⁹ Britnell, D.; Drew, M.G.B.; Fowles, G.W.A.; Rice, D.A. Crystal Structure of a Complex Containing Tungsten(vI) Sulphide Oxide Dichloride. *Inorg. Nuclear Chem. Lett.* **1972**, 9, 415.
- ¹⁰ Hertwig, R.; Koch, W. A Theoretician's View of the C-F Bond Activation Mediated by the Lanthanide Cations Ce^+ and Ho^+ . *Chem. Eur. J.* **1999**, 5, 312.

Chapter 3. Nanosized Molecular Rare-Earth Fluoride Clusters:



3.1 Introduction

Having extended the utility of EPh ligands to the stabilization of novel molecular lanthanide species with Ln-F connectivities, our next goal was to develop a more straightforward approach for the isolation of Ln-F complexes. Many of the details illustrating the background of our Ln-F work, the rather brief and uneventful history of molecular Ln-F species, and the fundamental attributes/detriments inherent in Ln-F chemistry have been discussed in the previous chapter. This chapter presents our advancement of Ln-F chemistry, namely the synthesis of a remarkable series of molecular Ln-F clusters. The PL properties of these clusters are detailed, and highlighted by a calculated 41% QE for the Nd cluster. Correlations between our molecular Ln-F clusters with solid-state LnF₃ are also discussed.

Solid-state LnF₃ based materials are used extensively in optical applications requiring stable, luminescent species.¹⁻⁷ For example, solid-state fluoride glasses doped with lanthanide ions have long been established NIR emission sources. The usefulness of solid-state fluoride hosts in optical applications stems from the structural properties of the fluoride lattice. This is largely due to the low energy phonon environment imparted by the fluoride lattice (Table 13).⁸ This low energy environment reduces the efficiency of non-radiative energy pathways, and increases emission lifetimes. One limitation of solid-state lanthanide sources is their insolubility in all but extreme environments. The development of increasingly soluble Ln_xF_y containing species is necessary then for the

realization of novel optical technologies that will rely on efficient PL from soluble Ln ion sources.⁶⁻¹²

Table 13. Fluorescence Decay Time ($^4F_{3/2} \rightarrow ^4I_{11/2}$) and the Phonon Frequencies of Some Reported Laser Hosts

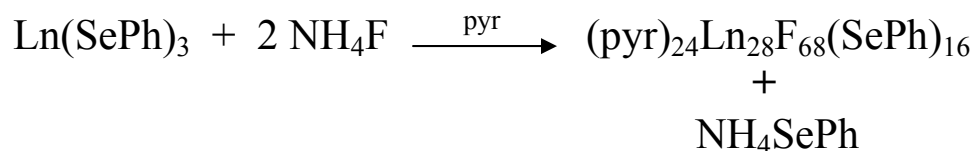
Host Lattice	lifetime (μ s)	phonon frequency (cm^{-1})	Reference
sulfide	110	450–700	1
selenide	410	450–700	1
tellurite	233–313	450–700	2
germanate	406–550	900	1
ZBLAN fluoride glass	540–610	500	1
LaF_3	800	200–400	3-5
yttrium aluminum garnet	250	400	

3.2 $(\text{pyr})_{24}\text{Ln}_{28}\text{F}_{68}(\text{SePh})_{16}$ (Ln = Nd, Pr): Synthesis and Structure

Not all efforts to prepare molecular Ln-F species using straight forward approaches were successful. Experiments combining lanthanide chalcogenolates with direct fluoride sources were explored, and it was expected that these would be metathesis type reactions. It was believed that the exchange of chalcogenolate ligands from lanthanide chalcogenolate complexes with fluoride ions from an ionic fluoride source would lead to the isolation of Ln-F species. Studies were performed using the direct fluoride sources HgF_2 , CsF , $(\text{Me})_4\text{NF}$, and NH_4F . HgF_2 was chosen for its obvious “hard”/“soft” atom mismatch. This was expected to be a reaction in which the fluoride ion would be easily abstracted from the Hg, and the Hg would form $\text{Hg}(\text{EPh})_2$ using the

EPh ligand of the $\text{Ln}(\text{EPh})_3(\text{L})_x$ complex. CsF was chosen since it has the weakest bond of the ionic alkali metal fluorides, and the ammonium fluorides were chosen because their structures are comprised of hydrogen bonds to the fluoride ion. The fluoride sources chosen differ in chemical and physical properties, and all gave distinctly different results. Reactions using HgF_2 produced only oils under all reaction conditions employed. While reactions of CsF with $\text{Ln}(\text{EPh})_3(\text{L})_x$ species did not yield Ln-F species, there was however evidence of fluoride abstraction. When CsF (2mmol) was combined with in situ prepared $\text{Yb}(\text{SePh})_3(\text{DME})_x$ in DME solvent, crystalline $[\text{CsSePh}]_n$ was formed. While this result indicates that fluoride abstraction was successful, there was no evidence of a Ln-F species. For the ammonium fluorides, solutions from $(\text{Me})_4\text{NF}$ reactions did not produce crystalline product, but when NH_4F was used, a novel class of molecular Ln-F clusters was discovered.

The most remarkable advancement in molecular Ln-F chemistry was the synthesis of a molecular cluster, $(\text{pyr})_{24}\text{Ln}_{28}\text{F}_{68}(\text{SePh})_{16}$. $(\text{pyr})_{24}\text{Ln}_{28}\text{F}_{68}(\text{SePh})_{16}$ is isolated as a pyridine adduct and stabilized by our chalcogen based ligand system. Isolation of $(\text{pyr})_{24}\text{Ln}_{28}\text{F}_{68}(\text{SePh})_{16}$ was by the reaction of in-situ prepared $\text{Ln}(\text{SePh})_3$ with the direct fluoride source, NH_4F , according to the following scheme:



The resulting species, $(\text{pyr})_{24}\text{Ln}_{28}\text{F}_{68}(\text{SePh})_{16}$, can be prepared from early lanthanide metals ($\text{Ln} = \text{Ce}, \text{Pr}, \text{Nd}$), and isolation of yields up to 60% have been successful for both Pr and Nd. $(\text{pyr})_{24}\text{Ln}_{28}\text{F}_{68}(\text{SePh})_{16}$ bears structural resemblance to

Fenskian¹³ architectures of high nuclearity Ag and group 12 metal clusters. The reaction yielding $(\text{pyr})_{24}\text{Ln}_{28}\text{F}_{68}(\text{SePh})_{16}$ is significant in that the immediate precipitation of solid-state LnF_3 is arrested, allowing for the formation of structurally complex molecular core/shell clusters.

While most molecular lanthanide species crystallize in either low symmetry triclinic or monoclinic spacegroups, $(\text{pyr})_{24}\text{Ln}_{28}\text{F}_{68}(\text{SePh})_{16}$ crystallizes in the higher symmetry I-42m tetragonal space group. $(\text{pyr})_{24}\text{Ln}_{28}\text{F}_{68}(\text{SePh})_{16}$ has a core/shell structure composed of a metal fluoride core with a shell of selenolate, pyridine, and multidentate fluoride ligands. Fig. 30 shows the structure in its entirety, oriented looking down a fourfold rotoinversion axis. Disorder present at the surface of the cluster can also be seen in this image. The disorder lies in the aromatic rings of several pyridine and selenolate ligands, and is illustrated as intersecting rings with common alpha carbon positions. At its core, $(\text{pyr})_{24}\text{Ln}_{28}\text{F}_{68}(\text{SePh})_{16}$ is comprised of a central set of four 12-coordinate Ln ions encapsulated by six μ_3 and six μ_4 tetrahedral fluoride ions. The next layer consists of twenty four additional lanthanide ions surrounding the inner twelve fluoride ions. At the shell, these twenty four Ln ions are then further connected through an additional 56 μ_2 - μ_4 fluoride ions. Completing the primary coordination sphere of the outer Ln ions are terminal pyridine, and selenolate ligands. Of the sixteen selenolates on the shell, four are μ_3 bridging and related by four fold roto-inversion symmetry. The remaining twelve are also related by roto-inversion symmetry but are bidentate μ_2 ligands. There are twenty four terminal pyridine ligands at the surface of the cluster, and of the fluoride ions at the shell, four are μ_3 bridging and the remaining are μ_2 . Tables 14 and 15 list important

crystal data/structure refinement details as well as important bond lengths and angles for $(\text{pyr})_{24}\text{Ln}_{28}\text{F}_{68}(\text{SePh})_{16}$.

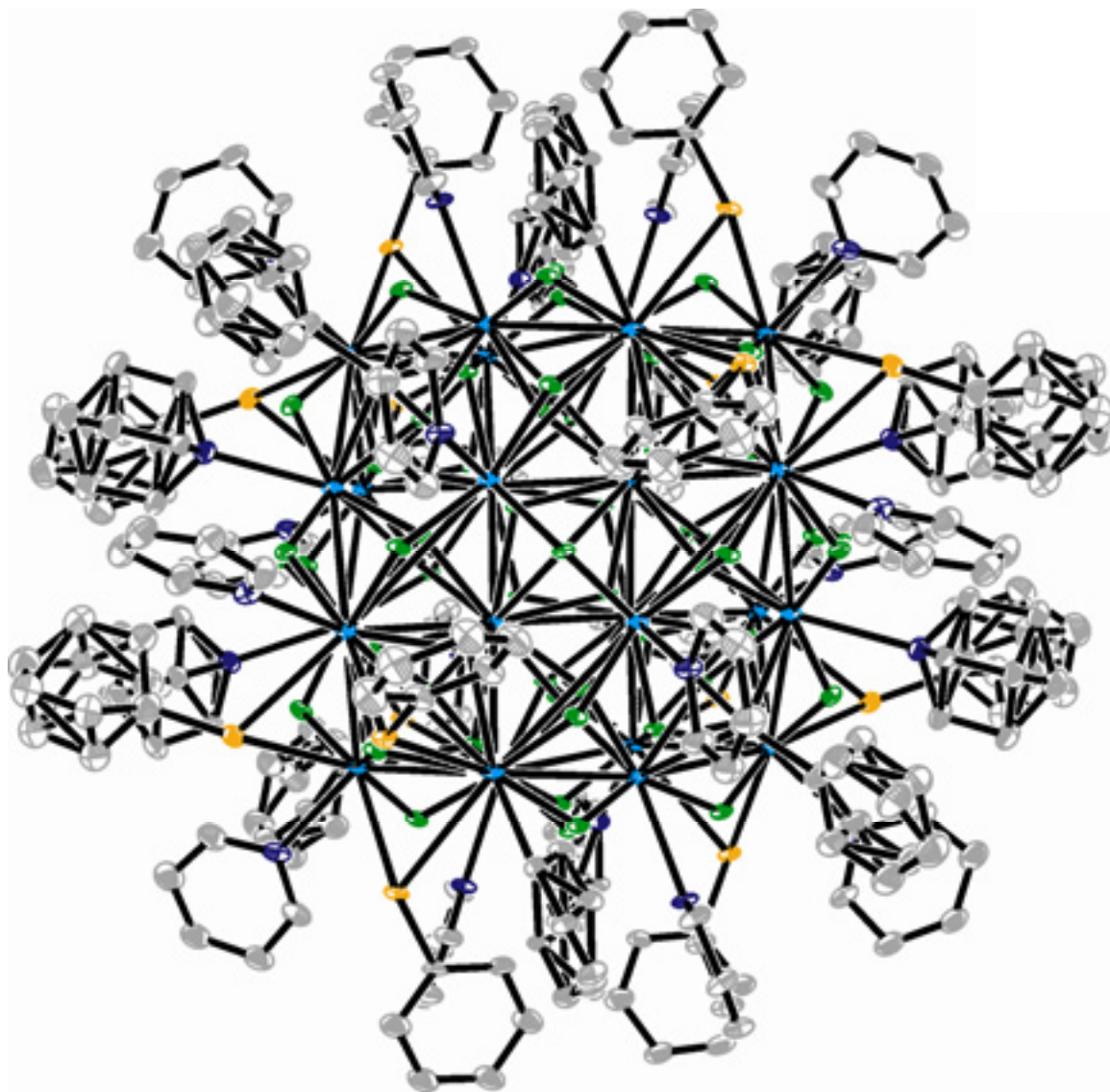


Fig 30. ORTEP of $(\text{pyr})_{24}\text{Ln}_{28}\text{F}_{68}(\text{SePh})_{16}$ ($\text{Ln} = \text{Nd}, \text{Pr}$). All protons have been removed for clarity, and thermal ellipsoids have been drawn at 10% for ease of visualization.

Table 14. Crystal data and structure refinement for (pyr)₂₄Ln₂₈F₆₈(SePh)₁₆ (Ln = Nd, Pr)

	Ln = Nd	Ln = Pr
Empirical formula	C ₃₄₆ H ₃₃₀ F ₆₈ N ₅₀ Nd ₂₈ Se ₁₆	C ₃₄₆ H ₃₃₀ F ₆₈ N ₅₀ Pr ₂₈ Se ₁₆
Formula weight	11782.68	11689.44
Temperature	293(2) K	200(2) K
Wavelength	0.71073 Å	0.71073 Å
Crystal system	Tetragonal	Tetragonal
Space group	I-42m	I-42m
Unit cell dimensions	$a = 23.7770(9)$ Å , $\alpha = 90^\circ$	$a = 23.5934(10)$ Å , $\alpha = 90^\circ$
	$b = 23.7770(9)$ Å , $\beta = 90^\circ$	$b = 23.5934(10)$ Å , $\beta = 90^\circ$
	$c = 39.272(3)$ Å , $\gamma = 90^\circ$	$c = 38.658(3)$ Å , $\gamma = 90^\circ$
Volume	22203(2) Å ³	21519(2) Å ³
Z	2	2
Density (calculated)	1.762 Mg/m ³	1.804 Mg/m ³
Final R indices [I > 2σ(I)]	R1 = 0.0535, wR2 = 0.1197	R1 = 0.0720, wR2 = 0.1751

Table 15. Important Bond Length Ranges (Å) for (pyr)₂₄Ln₂₈F₆₈(SePh)₁₆ (Ln = Nd, Pr)

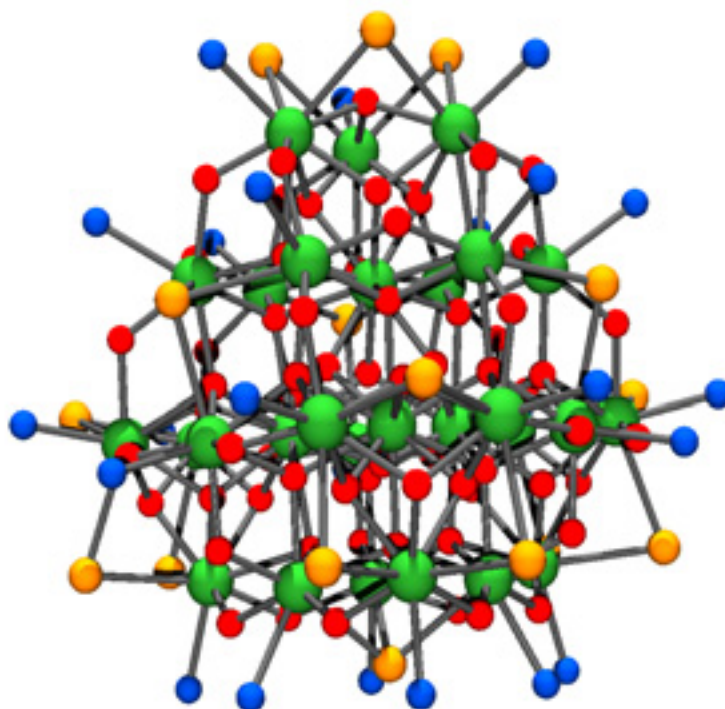
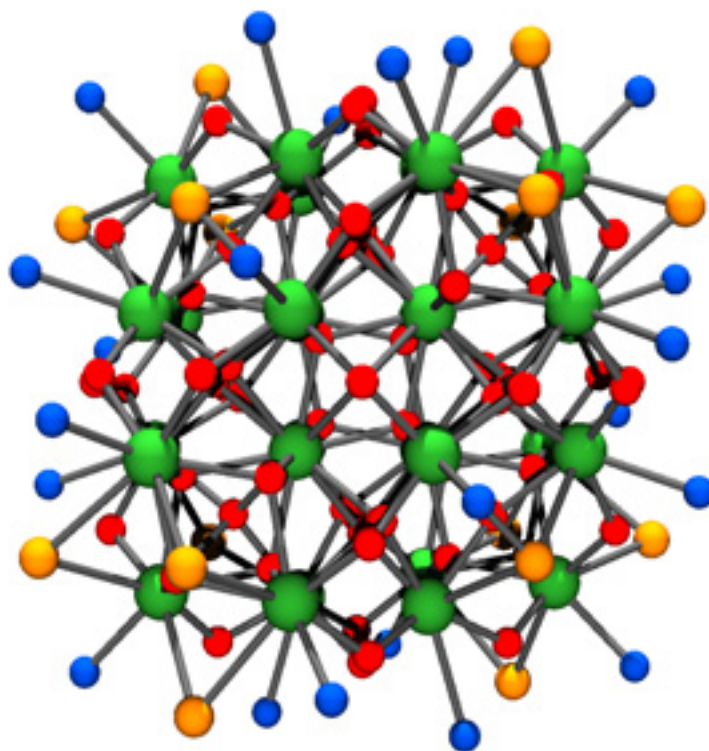
	Nd	Pr
Ln-F	2.26 -2.80 / 2.26 -2.88 Å	
Ln-Se	3.15 -3.18 / 3.13 -3.17 Å	
Ln-N	2.59 -2.72 / 2.57-2.71 Å	

A closer inspection of (pyr)₂₄Ln₂₈F₆₈(SePh)₁₆ reveals more interesting structural features. Foremost are the distinct similarities and differences that the core shares with

solid-state LnF_3 . Having a core comprised of multiple layers of alternating lanthanide and fluoride ions, $(\text{pyr})_{24}\text{Ln}_{28}\text{F}_{68}(\text{SePh})_{16}$ bears a resemblance to bulk LnF_3 . Similar to both molecular $(\text{pyr})_{24}\text{Ln}_{28}\text{F}_{68}(\text{SePh})_{16}$ and solid-state LnF_3 is the presence of pyramidal μ_3 and pseudo tetrahedral μ_4 fluoride ions bound to the Ln ions. There are thirteen crystallographically unique fluoride ions in the asymmetric unit of $(\text{pyr})_{24}\text{Ln}_{28}\text{F}_{68}(\text{SePh})_{16}$, totaling sixty eight after all symmetry equivalents are generated. Of the core fluorides, three have μ_3 -pyramidal geometry with Nd-F-Nd bond angles ranging from 107.9 to 110.7° , and four have μ_4 -tetragonal geometry with average Nd-F-Nd bond angles of 107.63° .

In $(\text{pyr})_{24}\text{Ln}_{28}\text{F}_{68}(\text{SePh})_{16}$, the 4 internal lanthanide ions are 12 coordinate, and the lanthanide ions at the surface of the cluster are either 8 or 9 coordinate. This difference in coordination numbers is because the outermost lanthanide ions are coordinated to bulkier selenolate and pyridine ligands. This increases crowding around the primary coordination sphere and reduces the coordination numbers of these outer metal ions. While many features are similar, the difference in coordination numbers highlights a difference between $(\text{pyr})_{24}\text{Ln}_{28}\text{F}_{68}(\text{SePh})_{16}$ and solid-state NdF_3 . All of the Nd ions in NdF_3 are 10 coordinate and pack into the higher symmetry hexagonal $\text{P6}_3/\text{mcm}$ spacegroup. Furthermore, while LnF_3 is totally insoluble in all but the most extreme environments (i.e. refluxing HF), $(\text{pyr})_{24}\text{Ln}_{28}\text{F}_{68}(\text{SePh})_{16}$ shows limited solubility in polar organic solvents such as pyridine.

The four-fold rotoinversion symmetry present in this cluster can be seen in the POV-Ray image of Figure 31 (Top image, which is looking down any one of the crystallographic axis).



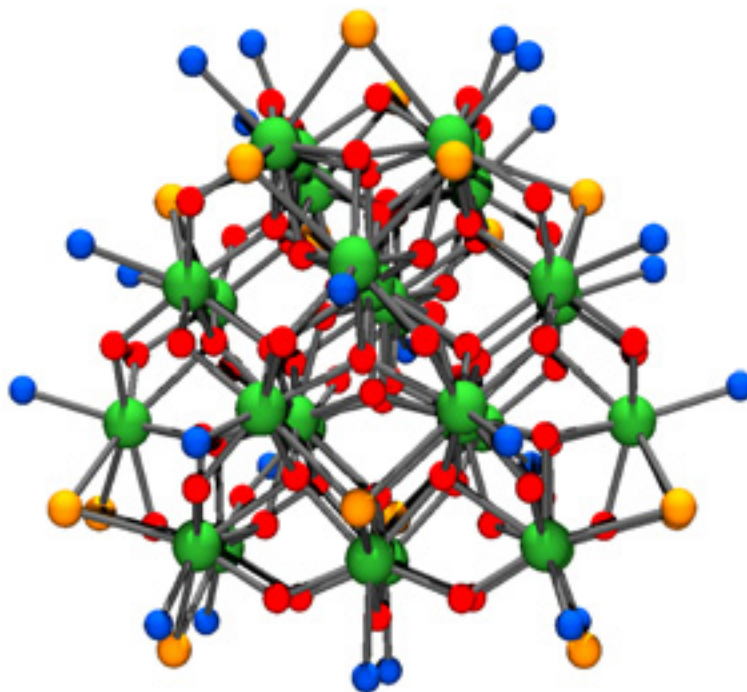


Fig 31. POV-Ray of the fluoride cluster $(\text{pyr})_{24}\text{Ln}_{28}\text{F}_{68}(\text{SePh})_{16}$, with green Ln, red F, blue N (from pyr), yellow Se (from SePh), and the C and H atoms removed for clarity.

The bottom two images of Fig. 31 illustrate additional symmetry present in $(\text{pyr})_{24}\text{Ln}_{28}\text{F}_{68}(\text{SePh})_{16}$ by showing a two fold rotation axis, as well as symmetry generated mirror planes. The alternating layers of lanthanide and fluoride ions are also more easily discernable from the POV-Ray images, and one can more easily see the bulk-like core and encapsulating shell.

The shell is comprised of 16 disordered aryl groups, 8 of which are phenyl rings of selenolate molecules (Se1, Se3, and their symmetry generated equivalents), and 8 of which are pyridine molecules (N2, N5, and their symmetry generated equivalents). The

successful refinement of this structure by single crystal x-ray diffraction was hindered by the disorder present in the atomic positions of these ligands. The disorder in the pyridine resides in the varying atomic positions of the ortho and meta carbon atoms around a single fixed nitrogen position (Fig 32). The disordered pyridines are resolvable and result in two distinct pyridine molecules occupying one site. This is visualized as two rings rotated from each other about the shared para position carbon and nitrogen atoms. For the N2 pyridine, the rings are out of plane by approximately 27° from one another. The disorder about the N5 pyridine is unique in that the para carbons also occupy different atomic coordinates and the two rings are out of plane by nearly 90° . The disorder about the selenolate ligands is similar to that seen in the N2 pyridine in that two resolved phenyl rings are present. Both rings have the same atomic coordinates for the Se, the para carbon, and the carbon bound to the selenium atom. The rings of the Se3 selenolate are out of plane by $\sim 41^\circ$, while the Se1 selenolate disorder gives two distinct rings $\sim 35^\circ$ out of plane.

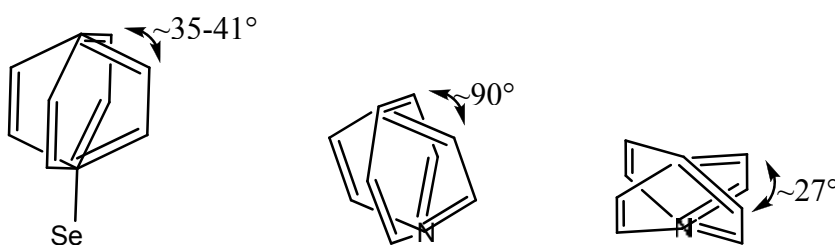


Fig 32. Depiction of different states of disorder about pyridine and selenolate ligands in $(\text{pyr})_{24}\text{Ln}_{28}\text{F}_{68}(\text{SePh})_{16}$

The body centered tetragonal unit cell shows that the packing of $(\text{pyr})_{24}\text{Ln}_{28}\text{F}_{68}(\text{SePh})_{16}$ molecules leaves large voids between the discrete clusters (Fig 33). An increase in the volume of voids in crystalline lattices represents inefficiency in the packing which can lead to instability in the structure. By reducing the rigidity of the lattice, large voids can cause the molecules to collapse into the empty space. This would be seen on a macroscopic level as decomposition of the crystalline product. In many cases, these voids can be occupied by solvent molecules present from the initial reaction conditions.

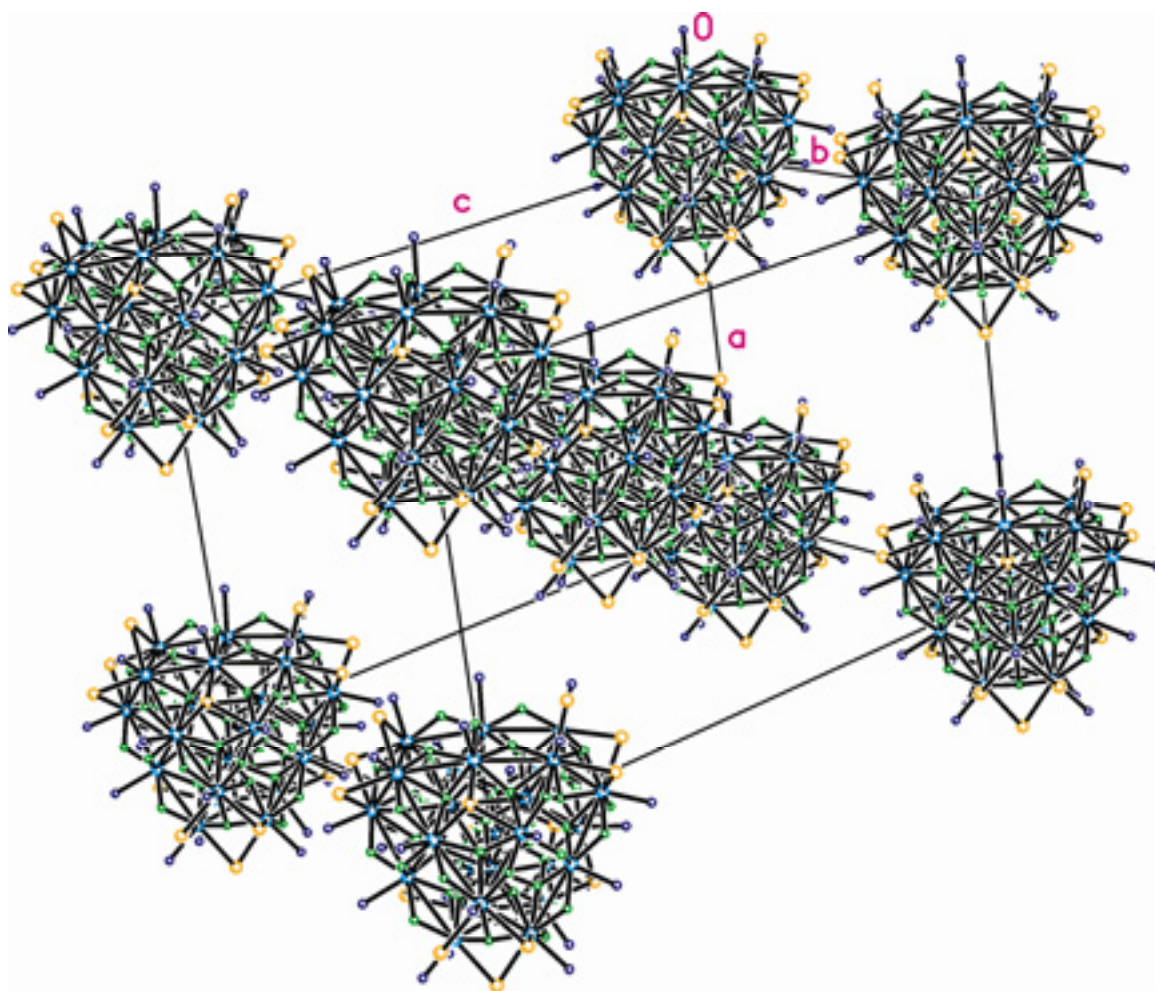


Fig 33. Unit cell packing of $(\text{pyr})_{24}\text{Ln}_{28}\text{F}_{68}(\text{SePh})_{16}$ in I-42m.

Because of this, lattice solvent can increase stability of the solid by adding rigidity to the lattice and reducing the propensity of the molecules to collapse into the voids. It should be noted that not all lattice solvent is beneficial however. Loss of lattice solvent is a common occurrence when crystalline products are removed from their mother liquor. As a result, void space is increased and the crystallinity of the product can be diminished. Total decomposition of the crystalline lattice is not always the result, but even if structure refinement is possible, problems due to disorder of the solvent molecules can arise. The extent to which lattice solvent is present in the isolated species is largely dependant upon the packing of the molecule as well as reaction conditions.

Many of the lanthanide chalcogen species isolated in this research group contain a small number of lattice solvent molecules (typically one or two), and in most instances they are easily refined. $(\text{pyr})_{24}\text{Ln}_{28}\text{F}_{68}(\text{SePh})_{16}$ on the other hand, was found to have 16 lattice pyridines occupying the void space between cluster molecules, and using PLATON,¹⁴ the solvent accessible voids were calculated to be 10085\AA^3 . For many efficiently packed crystal structures, solvent accessible voids will be orders of magnitude smaller than this, but for rigid structures such as zeolites or metal-organic frameworks (MOFs), the loss of lattice solvent can lead to stable species with similarly large void space. Generally, small solvent molecules will have molecular volumes less than 300\AA^3 , with a H_2O molecule being 40\AA^3 and toluene 88\AA^3 .

The solvent excluded volume for a pyridine molecule was calculated to be 66.8\AA^3 . This was done by first using a MM2 molecular mechanics theory calculation to generate an energy minimized structure (Chem3D Pro 11.0),¹⁵ followed by calculation of

the Connolly molecular surface based upon reference MM2 parameters generated from the MM2 output data. According to Connolly, the solvent-excluded volume is equal to the sum of the van der Waals volume and the interstitial volume (Fig 34).¹⁶

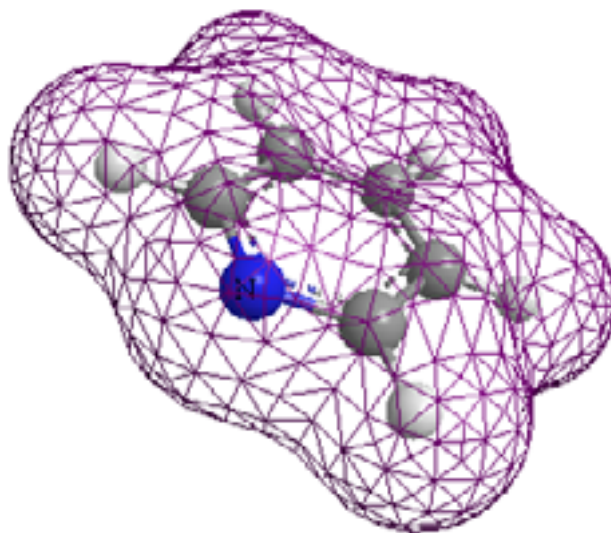


Fig 34. Calculated Connolly surface showing the solvent excluded volume for a pyridine molecule.

There is no straightforward calculation to predict the number of solvent molecules that will fill lattice voids upon crystallization, but taking into account the volume of both the void and solvent molecules as well as intermolecular forces (both attractive and repulsive), one can get a general idea for the maximum number of allowed solvate molecules. While 16 solvate molecules were found in the voids of $(\text{pyr})_{24}\text{Ln}_{28}\text{F}_{68}(\text{SePh})_{16}$, based upon calculated volumes, 6 additional pyridines would have been reasonable.

Of the 16 pyridine molecules present in the unit cell, 12 have a high degree of disorder (Fig 35). The illustrated disorder hindered the successful refinement of this

structure. It was necessary in fact, to impose certain constraints (i.e. DFIX, FLAT, FREE, AFIX 43) during the refinement of this structure to pin down atomic parameters for the convergence of our calculations.

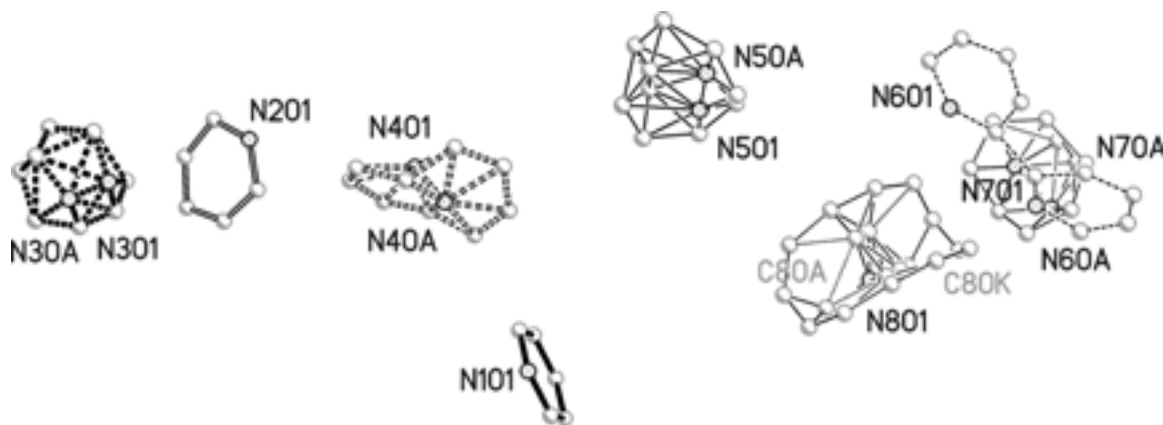


Fig 35. Representation of lattice solvent disorder in $(\text{pyr})_{24}\text{Ln}_{28}\text{F}_{68}(\text{SePh})_{16}$

3.3 $(\text{pyr})_{24}\text{Nd}_{28}\text{F}_{68}(\text{SePh})_{16}$: Photoluminescence

The potential utility of these clusters in optical applications requiring organic based lanthanide sources motivated an evaluation of the cluster's optical properties. Details of the photoluminescence theories and techniques have been discussed in Chapter 1, and the following are the results of photoluminescence studies performed on $(\text{pyr})_{24}\text{Nd}_{28}\text{F}_{68}(\text{SePh})_{16}$. The absorption spectrum of $(\text{pyr})_{24}\text{Nd}_{28}\text{F}_{68}(\text{SePh})_{16}$ (Fig 36) is similar to typical Nd^{3+} electronic transitions in various metal ion environments.¹⁷⁻²⁰ The emission spectrum, obtained by exciting the metastable $^4\text{F}_{5/2}$ level with 800 nm light, is also shown in Figure 36. The $^4\text{F}_{5/2}$ state rapidly relaxes to the emitting $^4\text{F}_{3/2}$ state, giving rise to well defined Nd emission bands. Of the four characteristic Nd^{3+} emission bands, two well resolved transitions were observed at 1076 and 1339 nm, corresponding to the $^4\text{F}_{3/2} \rightarrow ^4\text{I}_{11/2}$ and $^4\text{F}_{3/2} \rightarrow ^4\text{I}_{13/2}$ transitions, respectively. For measurement of the quantum

efficiency of the ${}^4F_{3/2} \rightarrow {}^4I_{11/2}$ transition, the fluorescence decay time (τ_{fl}) was extracted from the measured decay curve, and compared to the calculated decay time (τ_{rad}). For the 1076 nm emission band, the measured decay time was found to be 303 μ s (Fig 37). From both the experimental and calculated decay times,²¹⁻²² the quantum efficiency of this transition was calculated to be a remarkable 41%. While this compares with nearly 100% quantum efficiency for solid-state Nd^{3+} doped fluoride lattices,¹⁻⁵ it is substantially greater than previous QEs reported for molecular Nd sources prepared in our group (i.e. 16% in $(THF)_8Nd_8O_2Se_2(SePh)_{14}$,²³ 12% in $[(pyr)_{18}Nd_{12}O_6Se_4(SePh)_4(SeSePh)_4Hg(SePh)_2]^{2+}$,²⁴ 9% in $(DME)_2Nd(SC_6F_5)_3$,²⁵) and orders of magnitude larger than other molecular lanthanide sources.²⁶⁻³² The 41% quantum efficiency of $(pyr)_{24}Nd_{28}F_{68}(SePh)_{16}$ is the highest reported value for a structurally characterized molecular Nd complex to date.

In terms of optical properties, $(pyr)_{24}Nd_{28}F_{68}(SePh)_{16}$ shows similarities to solid-state NdF_3 . Neither $(pyr)_{24}Nd_{28}F_{68}(SePh)_{16}$ nor NdF_3 emit at 1800nm, which corresponds to the hypersensitive ${}^4F_{3/2} \rightarrow {}^4I_{15/2}$ transition, however, both give strong 1080 and 1300nm emissions. The 41% quantum efficiency is believed to be lower than that found for solid-state species because of non-radiative energy transfer mechanisms; specifically, concentration quenching and the inclusion of emission quenching C-H containing ligands around the metal center. Organo-encapsulated Nd_2O_3 nanoparticle dispersions have displayed higher efficiencies,³³ but because they are still solid-state oxides, their solubility is still limited.

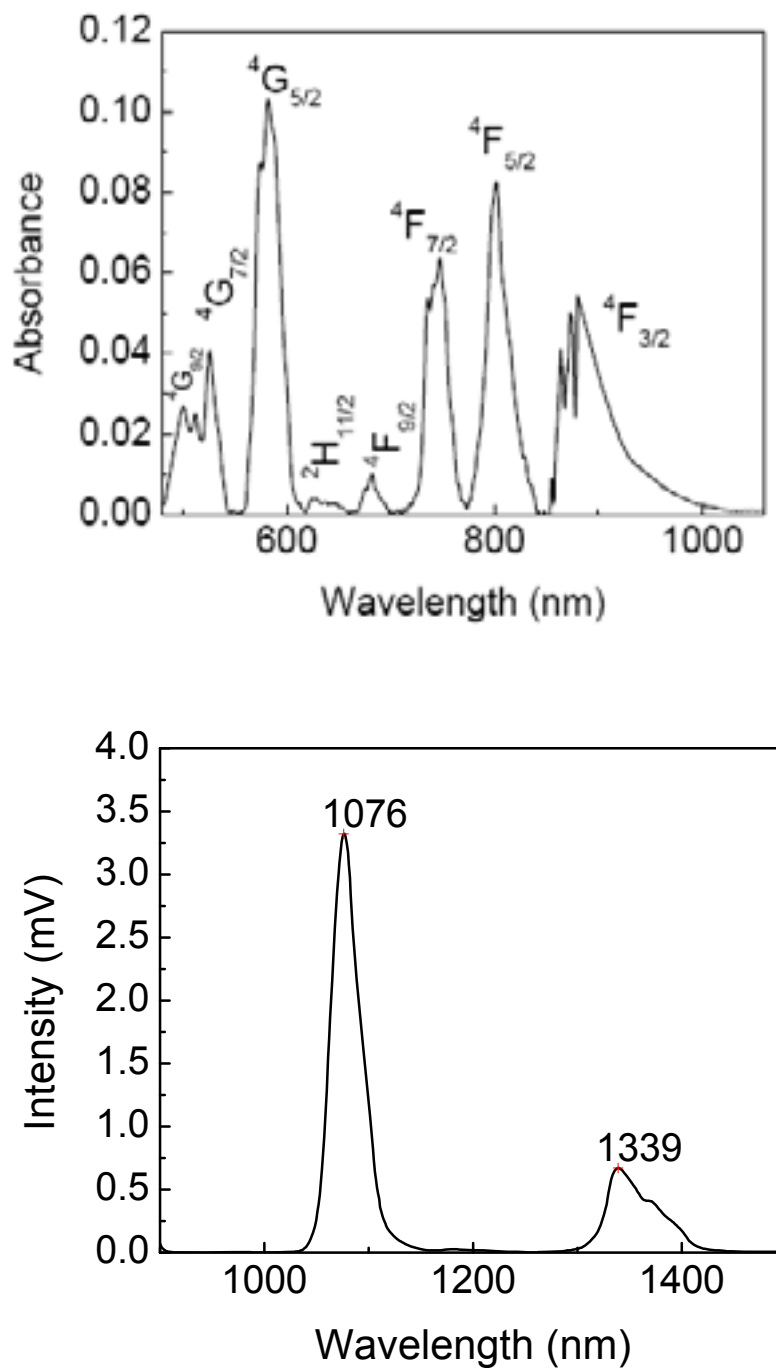
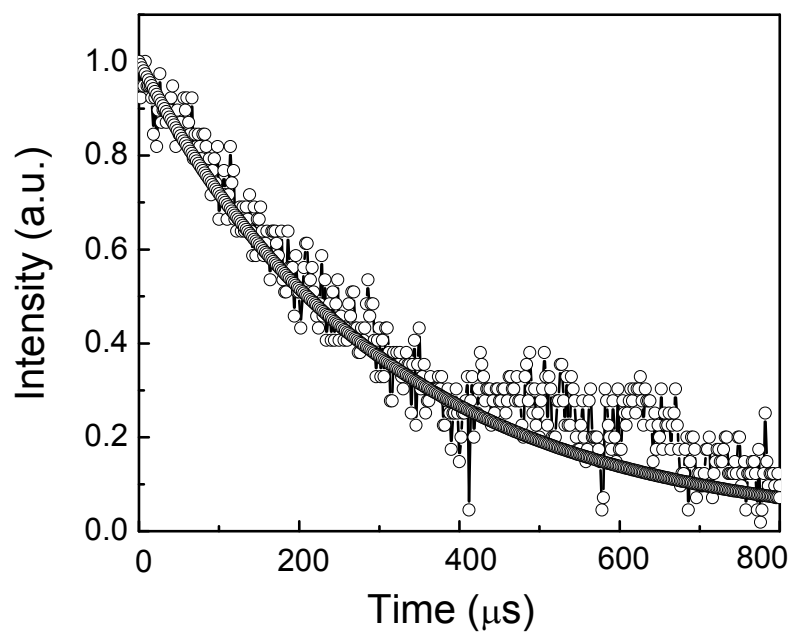


Fig 36. Top: Absorption spectrum of $(\text{pyr})_{24}\text{Nd}_{28}\text{F}_{68}(\text{SePh})_{16}$; Bottom: Emission spectrum of $(\text{pyr})_{24}\text{Nd}_{28}\text{F}_{68}(\text{SePh})_{16}$ pumped with 800 nm light.



Transition from $^4F_{3/2}$ to	Wavelength (nm)	S_{ed} (10^{-20}) (cm^2)	A (s^{-1})	$\Delta\lambda_{eff}$ (nm)	τ_{rad} (μs)	τ_{fl} (μs)	σ_e (10^{-20}) (cm^2)
$^4I_{15/2}$	1843*	0.06356	9.87745		739		
$^4I_{13/2}$	1339	0.48124	191.10702	56			0.56
$^4I_{11/2}$	1076	1.00483	772.164	35		303	1.53
$^4I_{9/2}$	927*	0.25822	379.96976				

Fig 37. Top: Measured decay curve for the $^4F_{3/2} \rightarrow ^4I_{11/2}$ transition; Bottom: spectroscopic details for $(pyr)_{24}Nd_{28}F_{68}(SePh)_{16}$, where $\Delta\lambda_{eff}$ = effective band width at FWHM, τ_{rad} = calculated radiative lifetime, and τ_{fl} = measured radiative lifetime.

3.4 [(pyr)₂₄Ce₂₈F₆₈(SePh)₁₆]³⁺ [Ce₃(SeC₆H₅)₁₀]¹⁻₃ : Synthesis and Structure

When Ln = Ce, the (pyr)₂₄Ln₂₈F₆₈(SePh)₁₆ reaction conditions used for preparation of the Nd and Pr clusters do not produce a single well resolved crystalline product. Following the same reaction used for (pyr)₂₄Nd₂₈F₆₈(SePh)₁₆ and (pyr)₂₄Pr₂₈F₆₈(SePh)₁₆, two distinct single crystal products have been successfully isolated when Ln=Ce. The first product, [(pyr)₂₄Ce₂₈F₆₈(SePh)₁₆]³⁺ [Ce₃(SeC₆H₅)₁₀]¹⁻₃, resembles the expected (pyr)₂₄Ln₂₈F₆₈(SePh)₁₆ cluster, but with distinct differences. The second product, {[pyr(NH₄)]⁺[(pyr)Ce(NH₃)₂(SePh)₄]⁻}₂, is a dimeric species with an altogether novel structure.

Isolated single crystals of [(pyr)₂₄Ce₂₈F₆₈(SePh)₁₆]³⁺ [Ce₃(SeC₆H₅)₁₀]¹⁻₃ have the same thin lathe morphology as the analogous (pyr)₂₄Ln₂₈F₆₈(SePh)₁₆ (Ln = Nd, Pr) species. The discrete cluster (pyr)₂₄Ce₂₈F₆₈(SePh)₁₆ is believed to be isostructural with the Nd₂₈ and Pr₂₈ analogs, but additional parameters are needed to correlate the models properly and to quantitatively confirm the cluster's atomic displacement parameters. Tetragonal constraints were necessary to aid in the structural refinement, and refinement was attempted using several tetragonal systems (I-4, I-4/m, I4/mcm, I-42m, and I4/mmm). The best statistics were found when the I4/mmm spacegroup was used. Still a tetragonal space group, this is different than the I-42m space group of the Nd and Pr analogs.

While the discrete Ce₂₈ cluster may be isostructural to Nd₂₈ and Pr₂₈, the most significant difference in the products is that [(pyr)₂₄Ce₂₈F₆₈(SePh)₁₆]³⁺ [Ce₃(SeC₆H₅)₁₀]¹⁻₃ has disordered trimers located around the Ce₂₈ cluster (Fig. 38). In [(pyr)₂₄Ce₂₈F₆₈(SePh)₁₆]³⁺ [Ce₃(SeC₆H₅)₁₀]¹⁻₃, trimer sites consisting of Ce41 - Ce52 have

been refined having $\frac{1}{4}$ site occupancies, indicating either a four fold disorder about one site, or a two fold disorder about two sites located in respective asymmetric units. For trimers consisting of Ce29 - Ce34 and Ce35 - Ce40, Ce site occupancies are $\frac{1}{2}$, indicating that a two fold disorder is present. The disorder can be properly modeled for the two doubly disordered trimers, but with $\frac{1}{4}$ site occupancies, the Ce41 - Ce52 molecules are still unresolved.

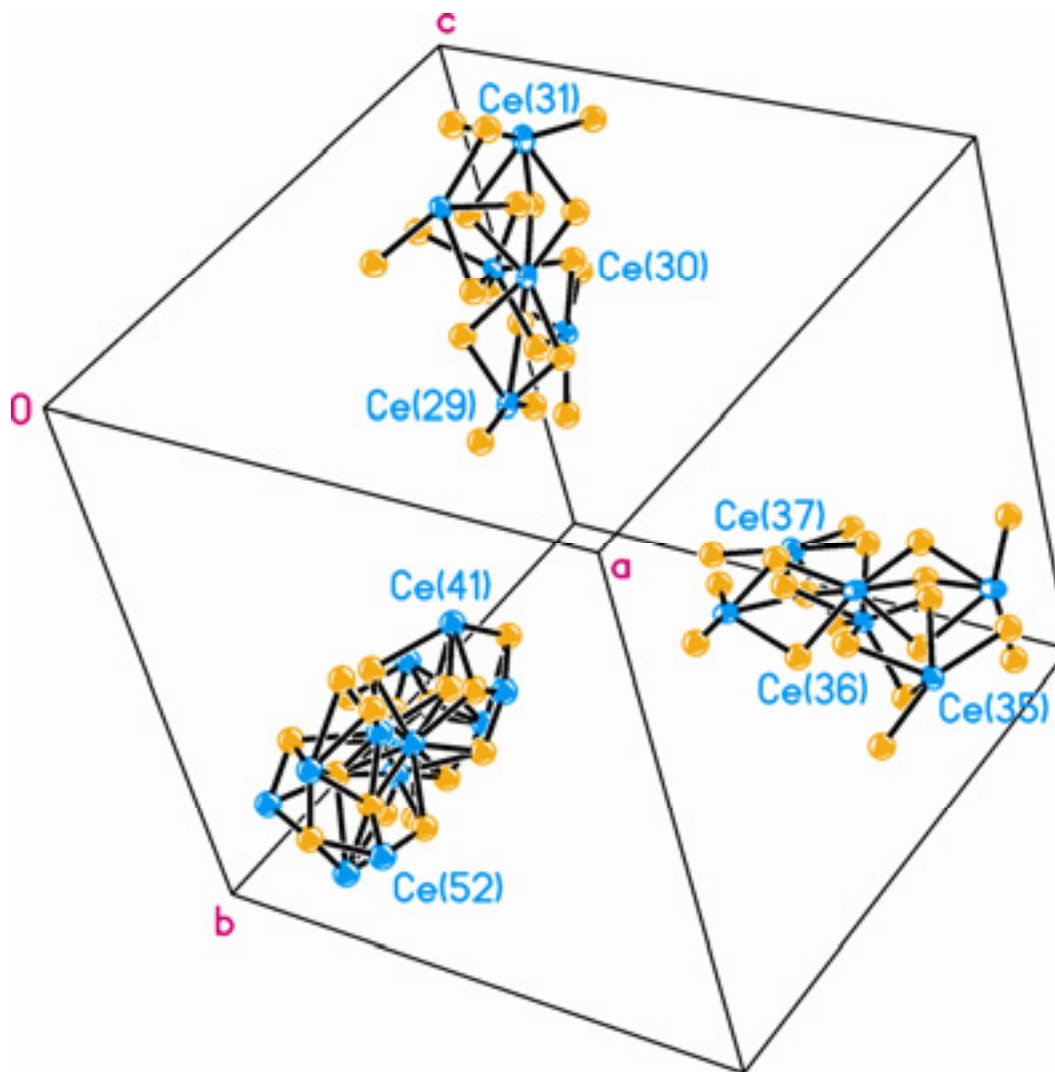


Fig 38. Representation of disordered trimers found in $[(\text{pyr})_{24}\text{Ce}_{28}\text{F}_{68}(\text{SePh})_{16}]^{3+}$



Further distinguishing $[(\text{pyr})_{24}\text{Ce}_{28}\text{F}_{68}(\text{SePh})_{16}]^{3+} [\text{Ce}_3(\text{SeC}_6\text{H}_5)_{10}]^{1-}_3$ from $(\text{pyr})_{24}\text{Ln}_{28}\text{F}_{68}(\text{SePh})_{16}$ ($\text{Ln}=\text{Nd}, \text{Pr}$) is the fact that the overall formula of each trimer is likely $[\text{Ce}_3(\text{SeC}_6\text{H}_5)_{10}]^{1-}$. As such, each trimer would carry a negative charge, and the cluster would be a cationic species with an overall charge of either 3^+ or 4^+ depending on the outcome of the trimer refinement. This is significant in that it would require some of the Ce ions to exist in the Ce^{4+} oxidation state. Initial studies have not shown the presence of Ce^{4+} ions, but further experimentation may prove its existence which could help in understanding the structure and lead to the eventual refinement of the species. While these complications hinder the absolute structure determination of $[(\text{pyr})_{24}\text{Ce}_{28}\text{F}_{68}(\text{SePh})_{16}]^{3+} [\text{Ce}_3(\text{SeC}_6\text{H}_5)_{10}]^{1-}_3$, the current level of refinement clearly show that Ln_{28} clusters can be isolated for the early lanthanide metals (Ce-Nd).

The second isolable product formed from this reaction, $\{[(\text{pyr})(\text{NH}_4)]^+[(\text{pyr})\text{Ce}(\text{NH}_3)_2(\text{SePh})_4]^{-}\}_2$, crystallizes in the triclinic $P\bar{1}$ spacegroup with important crystal structure and refinement details given in Table 16. The myriad lanthanide chalcogenolate products prepared by our group generally lead to neutral species, but as seen in the Ce_{28} cluster, the isolation of ionic products can occur. $\{[(\text{pyr})(\text{NH}_4)]^+[(\text{pyr})\text{Ce}(\text{NH}_3)_2(\text{SePh})_4]^{-}\}_2$ is a rare example where the lanthanide complex acts as the anionic species and is countered by an organic cation. The two Ce ions in this dimer are related by an inversion center, and each Ce ion is eight coordinate. The metal's primary coordination sphere is comprised of two μ_2 -selenenolates, three terminal selenolates, two neutral donor ammonia, and a pyridine. Through dative interactions, there are two ammonium pyridine molecules surrounding the cerium molecule, with interactions occurring between the hydrogen atoms of the ammonia with both the

nitrogen of the pyridine and selenium of two terminal selenolates. Typical N-H bonds are around 1.01 Å and Se-H bonds are around 1.47 Å in selenols. X-ray diffraction results show that the dative hydrogen bonds of the ammonium ion are 2.00 Å from the pyridine nitrogen, 2.71 Å to Se2, and 2.69 to Se4A (Table 17). The terminally bound ammonia molecule (N1) also has a 2.879 Å dative interaction with Se4A, and Ce-N bonds are upwards of 0.1 Å shorter for the ammonia ligand when compared to Ce-N bonds from the pyridine ligand.

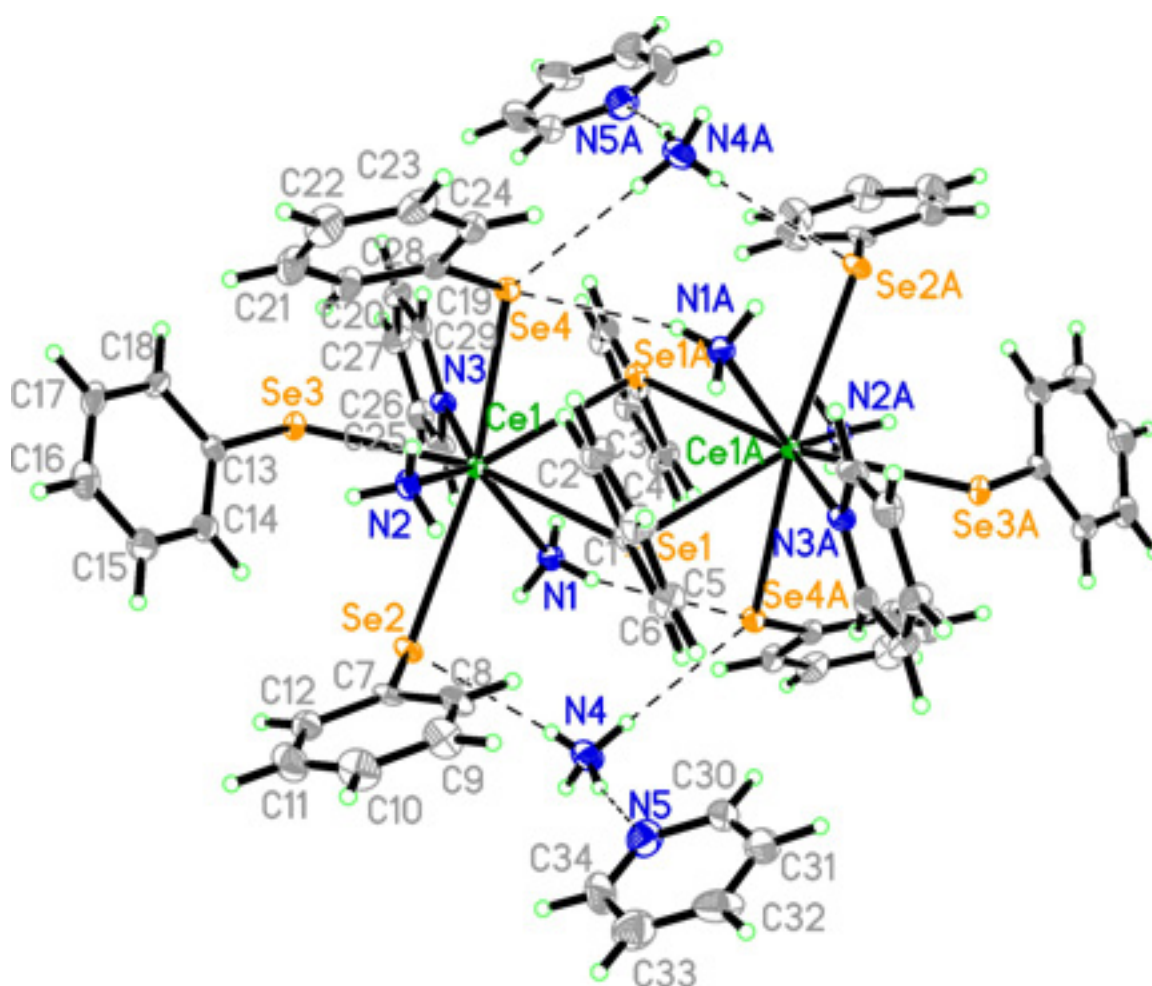
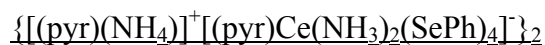


Fig 39. ORTEP of $\{[(\text{pyr})(\text{NH}_4)]^+[(\text{pyr})\text{Ce}(\text{NH}_3)_2(\text{SePh})_4]^- \}_2$, with thermal ellipsoids drawn at 50% probability level.

Table 16. Crystal data and structure refinement for

Identification code	cefseph	
Empirical formula	C ₃₄ H ₄₀ Ce N ₅ Se ₄	
Formula weight	974.67	
Temperature	100(2) K	
Wavelength	0.71073 Å	
Crystal system	Triclinic	
Space group	P-1	
Unit cell dimensions	$a = 10.6175(8)$ Å	$\alpha = 91.075(1)^\circ$
	$b = 14.0064(10)$ Å	$\beta = 107.199(1)^\circ$
	$c = 14.0978(10)$ Å	$\gamma = 111.891(1)^\circ$
Volume	1838.6(2) Å ³	
Z	2	
Density (calculated)	1.761 Mg/m ³	
Final R indices [I > 2σ(I)]	R1 = 0.0492, wR2 = 0.1019	

Table 17. Bond lengths [Å] and angles [°] for $\{[(\text{pyr})(\text{NH}_4)]^+[(\text{pyr})\text{Ce}(\text{NH}_3)_2(\text{SePh})_4]^- \}_2$

Ce(1)-N(1)	2.607(5)	Ce(1)-N(2)	2.614(4)
Ce(1)-N(3)	2.708(4)	Ce(1)-Se(4)	3.0777(6)
Ce(1)-Se(3)	3.0976(6)	Ce(1)-Se(1)	3.1202(6)
Ce(1)-Se(2)	3.1580(6)	Ce(1)-Se(1)A	3.1874(6)

The isolation of $\{[(\text{pyr})(\text{NH}_4)]^+[(\text{pyr})\text{Ce}(\text{NH}_3)_2(\text{SePh})_4]^- \}_2$ and $[(\text{pyr})_{24}\text{Ce}_{28}\text{F}_{68}(\text{SePh})_{16}]^{3+} [\text{Ce}_3(\text{SeC}_6\text{H}_5)_{10}]^{1-}_3$ illustrates that various species are accessible from these relatively straightforward reactions. The use of a direct fluoride source enables the formation of molecular Ln-F species without the need for C-F bond activation, but available counter ions (in this case NH_4^+), can still actively play a role in resultant structures. This is evident in Ln= Ce reactions, where multiple products were isolated. Yields are less than 60% for either product, and powders were often present in large quantities alongside the single crystals.

Powders can result from non-homogeneity in the reaction solution prior to crystallization. This can increase nucleation rates and decrease the growth of larger crystals. It would be advantageous for subsequent analyses if these powders could be identified as single phase crystalline products. Greater yields could be isolated in the powder form, and supplement the low single crystal yields found for $(\text{pyr})_{24}\text{Ln}_{28}\text{F}_{68}(\text{SePh})_{16}$. These powders could be useful for the dissolution of luminescent Ln sources in organic host materials (i.e. polymers) because of their small size and high surface area.

As a feasibility study, powders isolated from a Ce_{28} reaction were analyzed using powder x-ray diffraction. For this powder study, saturation of the solution by vacuum concentration (to dryness) resulted in a faint yellow powder in much larger yields than are normally obtained from typical single crystal crystallization methods (solution layering). The yellow powder contained a very small amount of single crystal Ce_{28} , as identified by XRD. Using the single crystal data previously collected for $[(\text{pyr})(\text{NH}_4)]^+[(\text{pyr})\text{Ce}(\text{NH}_3)_2(\text{SePh})_4]^- \}_2$ and $[(\text{pyr})_{24}\text{Ce}_{28}\text{F}_{68}(\text{SePh})_{16}]^{3+} [\text{Ce}_3(\text{SeC}_6\text{H}_5)_{10}]^{1-}_3$

3, calculated (simulated) powder patterns were generated (Fig 40) using XPREP of the Bruker SAINT software package. Comparison of the calculated powder patterns to those found experimentally will identify which of the expected products are present, their ratio, and possibly additional unidentified products.

While the calculated patterns have many overlapping features, there is discernable data that will help us in identifying different phases present in the experimental powder. Of note is the 10° 2θ region of $[(\text{pyr})_{24}\text{Ce}_{28}\text{F}_{68}(\text{SePh})_{16}]^{3+} [\text{Ce}_3(\text{SeC}_6\text{H}_5)_{10}]^{1-}_3$ where a valley is present at 10° , while $[(\text{pyr})(\text{NH}_4)]^+[(\text{pyr})\text{Ce}(\text{NH}_3)_2(\text{SePh})_4]^-_2$ shows a peak of strong intensity lying just above 10° . Furthermore, unlike the Ce_{28} cluster, the dimer shows several strong intensity peaks between the 13 and 15° 2θ region of the powder pattern. Unfortunately, the patterns calculated using XPREP give very noisy high angle data and also cut off low angle data below $\sim 8^\circ$ due to the beam stop of the instrument used for data collection. This low angle region contains high intensity reflections that are necessary to identify the unknown powder phases.

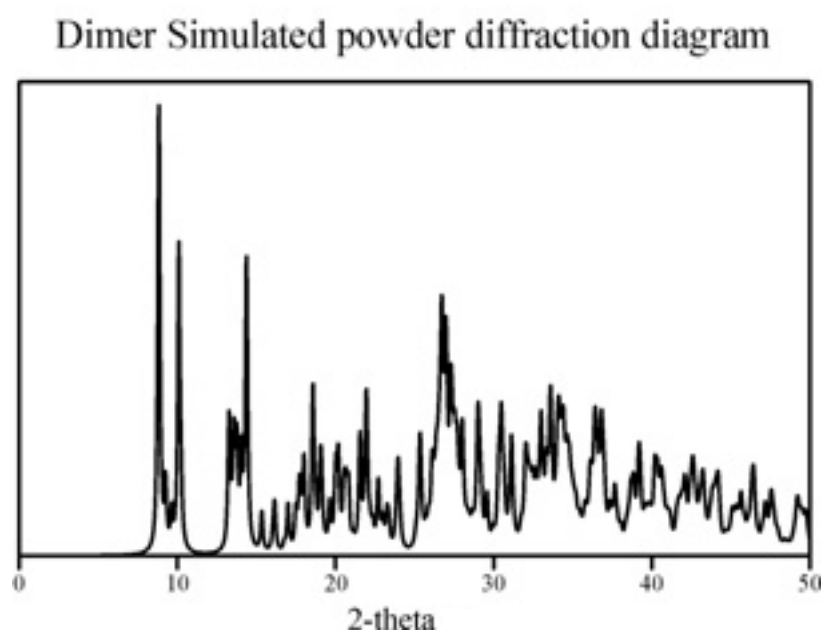
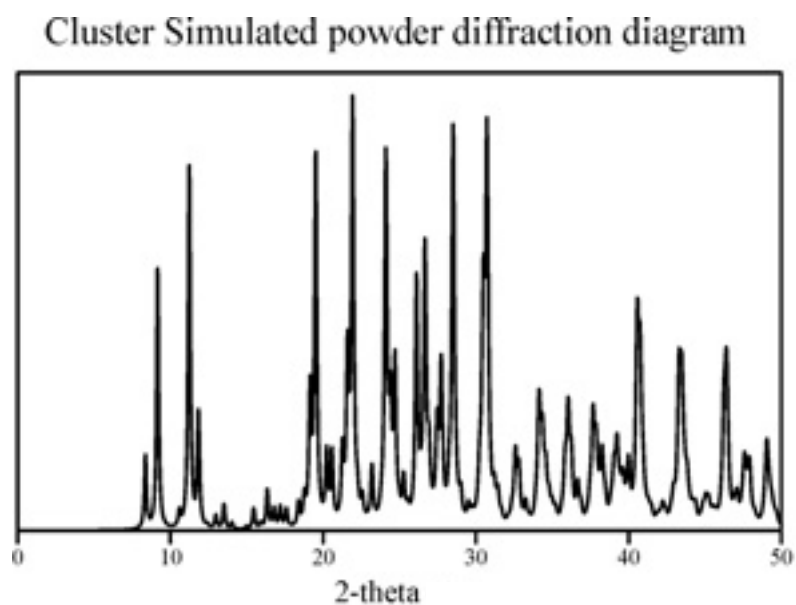


Fig 40. Simulated powder patterns for Ce_{28} and Ce dimer.

After structure refinement is complete and output files are generated, the crystal structure visualization and exploration program, Mercury, can be used to calculate a powder pattern based on the structural information collected on the single crystal (Figs 41 & 42). This calculated pattern includes the low angle data missing from the XPREP generated pattern. Because of the high intensity of the low angle peaks, peak intensity located between 10 - 50° 2θ is attenuated.

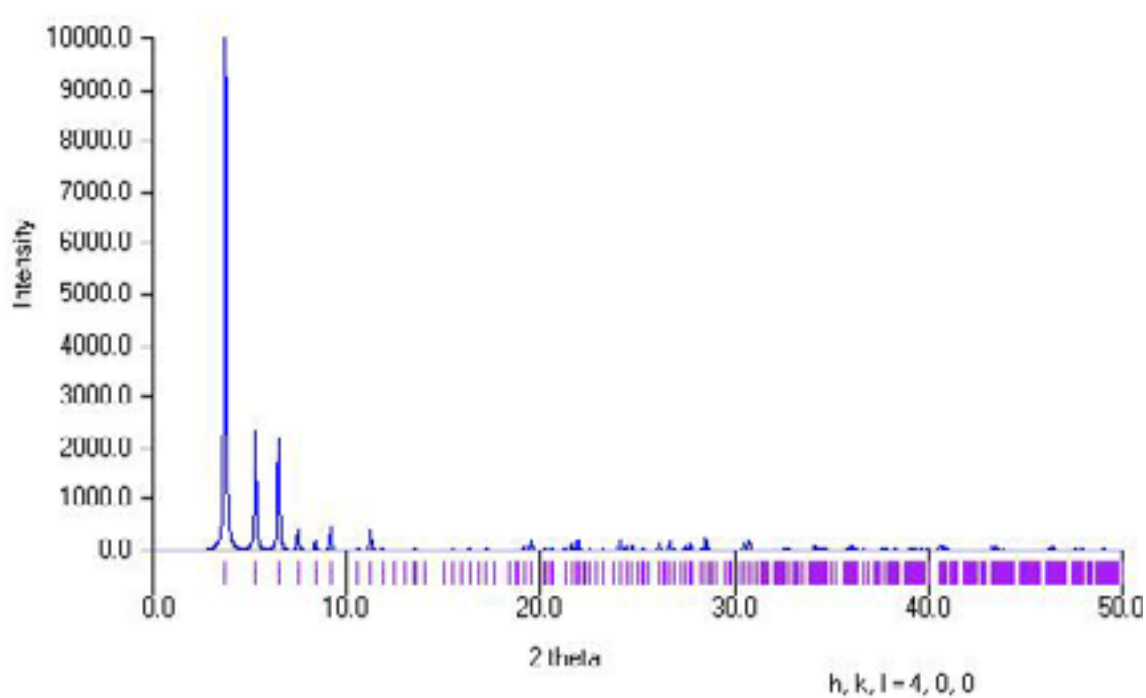


Fig 41. Ce_{28} Cluster : Simulated Powder Pattern for $0 < 2\theta < 50$.

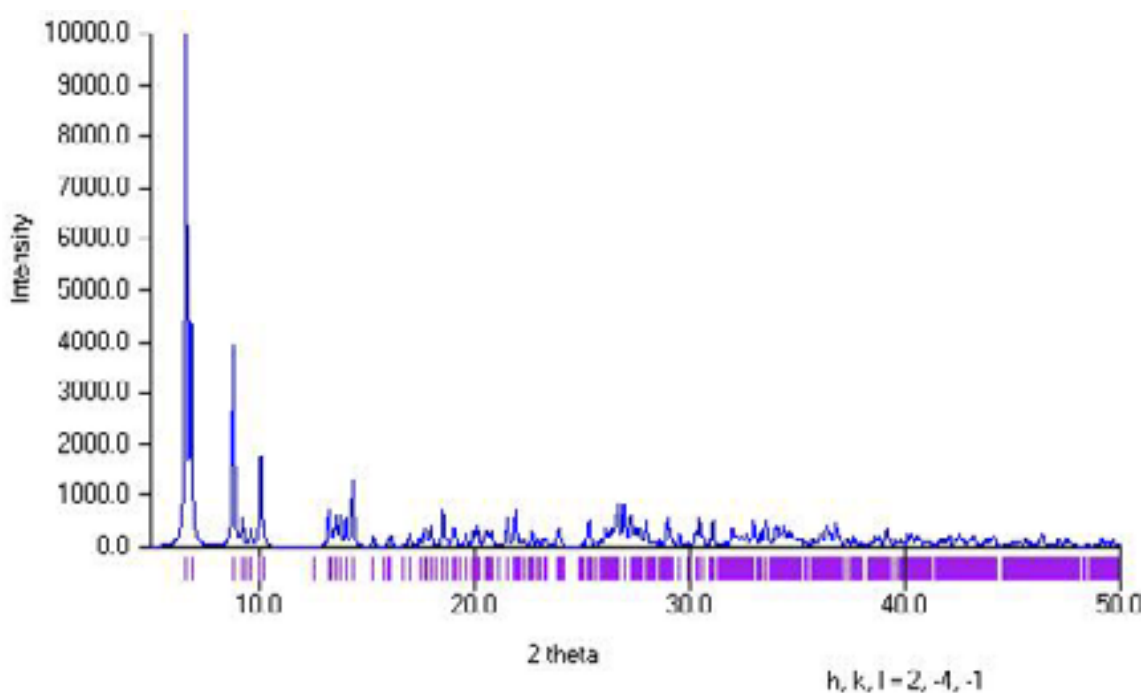


Fig 42. Ce Dimer: Simulated Powder Pattern for $0 < 2\theta < 50$.

From these two patterns, we again see the absence of a peak at 10° for the Cluster and the peaks at $\sim 10^\circ$ and $13\text{-}15^\circ$ for the dimer. There is also a bigger difference in the peaks between the $20\text{-}40^\circ$ regions of the two patterns. In the dimer, we see that the broadened peaks around 27° are much more pronounced than any of the higher angle data in the cluster.

A closer look at the low angle data for both species will resolve the main differences between the two powder patterns. Low angle patterns from $\sim 0\text{-}20^\circ$ 2θ regions are shown below (Figs 43 & 44). The cluster has distinguishing peaks at 3 , 5.25 , and 6.5° 2θ while having minimal intensity in the $14\text{-}15^\circ$ 2θ region. The powder pattern of the dimer shows no peak intensity below 6° 2θ , but several peaks between $13\text{-}15^\circ$ 2θ .

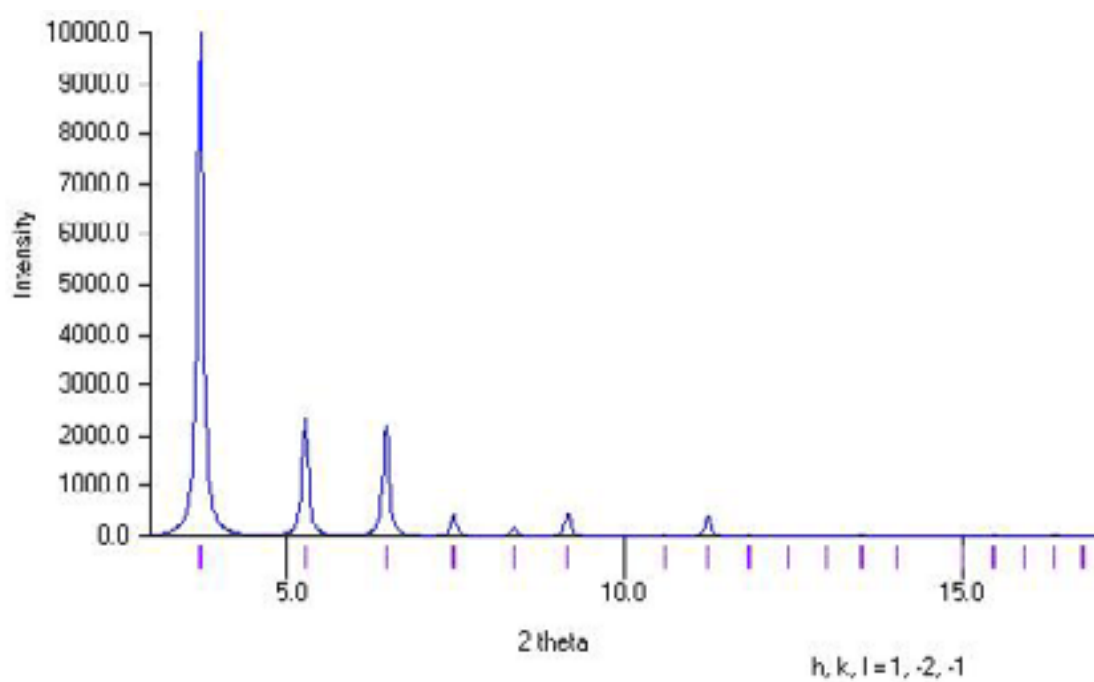


Fig 43. Ce_{28} Cluster : Low Angle Simulated Powder Pattern for $0 < 2\theta < 20$

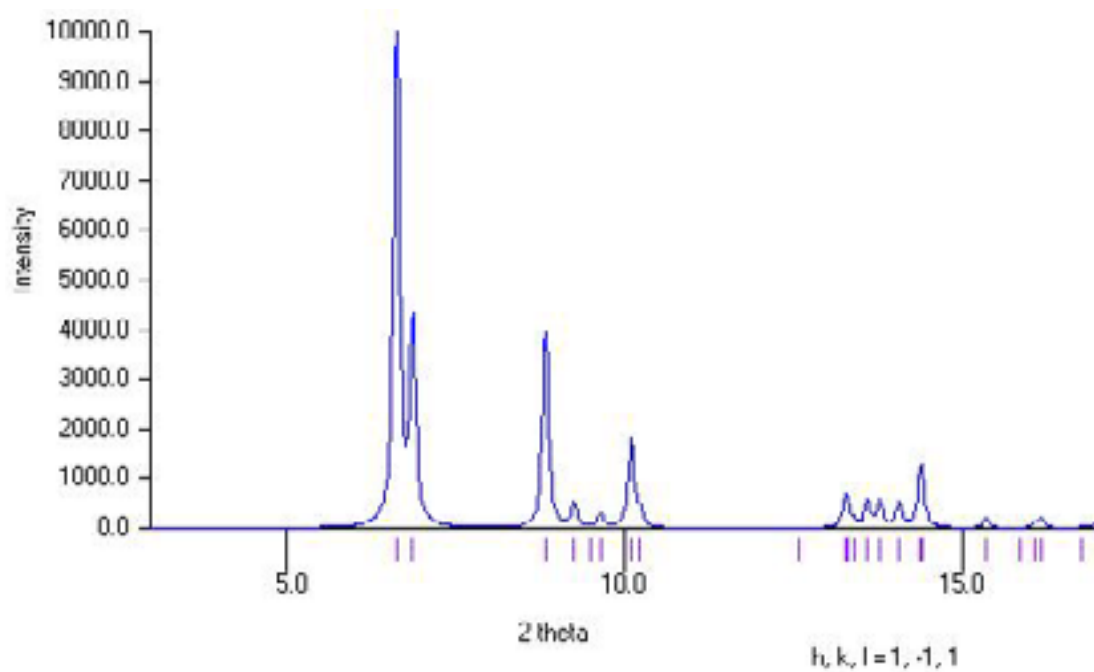


Fig 44. Ce Dimer : Low Angle Simulated Powder Pattern for $0 < 2\theta < 20$

This information is sufficient to qualitatively identify the phases present in our powders. Figure 45 shows the experimental powder pattern obtained through integration of data collected on the Ce powders from our reaction. A HiStar area detector on a rotating anode x-ray generator was used for data collection and a powder pattern was generated by integration of the scattered x-rays with GADDS diffraction software. The data was collected with the powders contained in a 0.7mm quartz capillary. Background subtraction was performed to lessen the effect of air, glass, and solvent scattering.

Identification of the major peaks lead us to believe that the powders are a mixture of both the cluster and dimer phases. Peaks are labeled with their respective HKL values and the phase that is associated with each. All of the major peaks in the 4 - 15° region of the experimental powder pattern are accounted for by comparison with the same regions in the calculated patterns. Being an absorption based measurement, x-ray diffraction allows for the determination of relative ratios of constituent crystalline products in a mixture. This can be done by comparing the relative intensities of the low angle peaks between species. In our experiment, it is believed that the powder is comprised of these two phases, and any other crystalline phase would be present below the ~5% level.

While it is clear that more rigorous crystallization methods are needed to produce phase pure products, this study has shown that examination of powder patterns will be a useful tool for future phase identifications of our rare earth species.

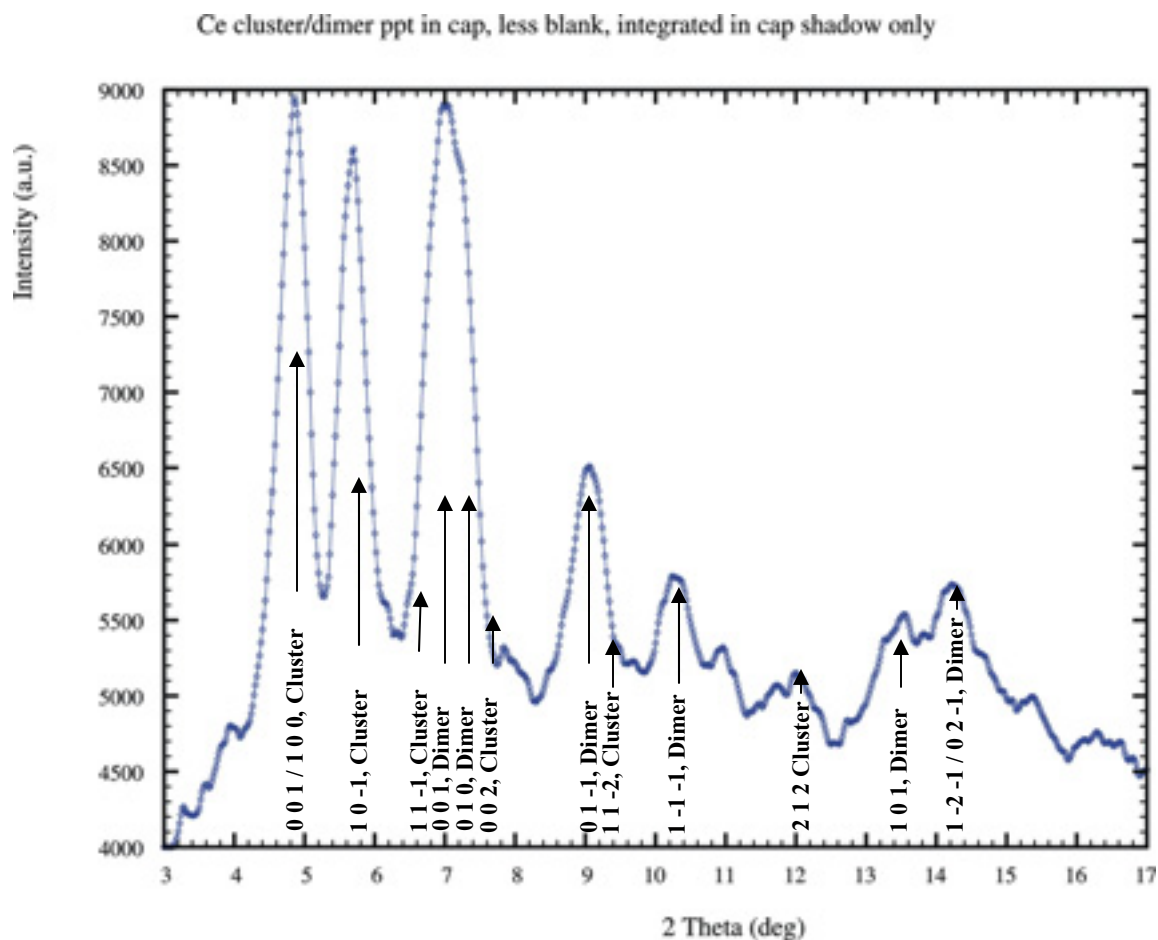


Fig 45. Experimental powder pattern of isolated crystalline powder from Ce_{28} reaction when the homogeneous reaction mixture is brought to dryness via vacuum concentration

Table 18. Highest intensity, low angle diffraction lines for Ce_{28} and Ce dimer.

Ce_{28} Major Diffraction Lines	Ce dimer Major Diffraction Lines
0 0 1	0 0 1
1 0 -1	0 1 0 (close to 0 0 1, forming a doublet)
1 1 -1	0 1 -1

3.5 Conclusions

Because of the background knowledge gained from extensive lanthanide chalcogenolate chemistry, a novel class of lanthanide fluoride molecules have been prepared. Through the reaction of soluble lanthanide chalcogenolates with a direct fluoride source, Ln ions have been found to form molecular core-shell clusters. The successful isolation of these species was realized by utilizing the relative instability of chalcogenolate ligands. The selenolate has sufficient coulombic interaction with the Ln ion to inhibit the disproportionation of $(L)_xLn(SeC_6H_5)_y$ to LnF_3 , but is also “soft” enough to allow fluorination by NH_4F . Because of the enthalpic driving force of the Ln-F bond, initial fluoride ions can effectively displace selenolates from the in-situ metal chalcogenolate. After formation of larger $Ln_xF_y(SePh)_z$ fragments, and the formation of the Ln-F core, crystallization leads to the isolation of the novel core-shell $(pyr)_{24}Ln_{28}F_{68}(SePh)_{16}$ species. Selenolates also act as effective capping agents in these systems because of their ability to bridge metal centers.

$(pyr)_{24}Ln_{28}F_{68}(SePh)_{16}$ are the largest molecular lanthanide cluster compounds reported to date,³⁴ and $(pyr)_{24}Nd_{28}F_{68}(SePh)_{16}$ displays the highest photoluminescence quantum efficiency ever recorded for a molecular Nd source. The high QE is attributed to the bulk-like properties of the fluoride core. Having similarities with both LnF_3 and molecular systems, $(pyr)_{24}Ln_{28}F_{68}(SePh)_{16}$ truly advances the field of lanthanide fluoride chemistry and ultimately, the possibility of soluble lanthanide sources being used in novel technological applications.

References

- ¹ Sudo, S. *Optical Fiber Amplifiers-Materials, Devices, and Applications*; Artech House, Inc.: Norwood, MA, **1997**.
- ² Shen, S.; Jha, A.; Zhang, E.; Wilson, S.J. Compositional effects and spectroscopy of rare earths (Er^{3+} , Tm^{3+} , and Nd^{3+}) in tellurite glasses. *C. R. Chim.* **2002**, *5*, 921.
- ³ Kaminski, A.A. *Crystalline Lasers-Physical Processes and Operating Scheme*; CRC Press: New York, NY, **1996**.
- ⁴ Fan, T.Y.; Kokta, M.R. End-pumped Nd:LaF₃ and Nd:LaMgAl₁₁O₁₉ lasers. *IEEE J. Quantum Electron.* **1989**, *25*, 1845.
- ⁵ Stouwdam, J.W.; van Veggel, F.C. J. M. Near-infrared emission of redispersible Er^{3+} , Nd^{3+} , and Ho^{3+} doped LaF₃ nanoparticles. *Nano Lett.* **2002**, *2*, 733.
- ⁶ Gottmann, J.; Moiseev, L.; Wortmann, D.; Vasilief, I.; Starovoytova, L.; Ganser, D.; Wagner, R. Laser deposition and laser structuring of laser active planar waveguides of Er:ZBLAN, Nd:YAG and Nd:GGG for integrated waveguide lasers *Proc. SPIE* **2007**, *6459*, 10S.
- ⁷ Dekker, R.; Klunder, D.J.W.; Borreman, A.; Diemeer, M.B.J.; Worhoff, K.; Driessen, A.; Stouwdam, J.W.; van Veggel, F.C.J.M. Stimulated emission and optical gain in LaF₃:Nd nanoparticle-doped polymer-based waveguides. *Appl. Phys. Lett.* **2004**, *85*, 6104.
- ⁸ Kumar, G.A.; Chen, C.W.; Ballato, J.; Riman, R.E. Optical Characterization of Infrared Emitting Rare-Earth-Doped Fluoride Nanocrystals and Their Transparent Nanocomposites. *Chem. Mater.* **2007**, *19*, 1523.
- ⁹ Zhang, M.; Shi, S.; Meng, J.; Wang, X.; Fan, H.; Zhu, Y.; Wang, X.; Qian, Y. Preparation and Characterization of Near-Infrared Luminescent Bifunctional Core/Shell Nanocomposites. *J. Phys. Chem. C* **2008**, *112*, 2825.
- ¹⁰ Boyer, J.; Gagnon, J.; Cuccia, L.A.; Capobianco, J.A. Synthesis and Spectroscopic Investigation of NaGdF₄: Ce^{3+} , Tb^{3+} /NaYF₄ Core-shell Nanocrystals. *Chem. Mater.* **2007**, *19*, 3358.
- ¹¹ Mai, H.; Zhang, Y.; Si, R.; Yan, Z.; Sun, L.; You, L.; Yan, C. High-Quality Sodium Rare-Earth Fluoride Nanocrystals: Controlled Synthesis and Optical Properties. *J. Am. Chem. Soc.* **2006**, *128*, 6426.
- ¹² Kumar, G.A.; Ballato, J.; Riman, R.; Snitzer, E. Solution Synthesis and Spectroscopic Characterization of High Er^{3+} Content LaF₃ for Broadband 1.5 μm Amplification. *J. Appl. Phys.* **2004**, *95*, 40.

- ¹³ Dieter Fenske is well known for his work dealing with the isolation of increasingly complex metal clusters of high nuclearity.
- ¹⁴ Spek, A.L. (2008) PLATON, A Multipurpose Crystallographic Tool, Utrecht University, Utrecht, The Netherlands.
- ¹⁵ ©1986 -2006 Cambridgesoft. All rights reserved
- ¹⁶ Connolly, M. L. Computation of Molecular Volume. *J. Am. Chem. Soc.* **1985**, *107*, 1118.
- ¹⁷ Oczko, G. Spectroscopic properties of neodymium monochloroacetate single crystal as an example of complex containing Nd(III) in three different symmetry sites. *J. Alloys Comp.* **2000**, *300*, 414.
- ¹⁸ Lis, S. Applications of spectroscopic methods in studies of polyoxometalates and their complexes with lanthanide(III) ions. *J. Alloys Comp.* **2000**, *300*, 88.
- ¹⁹ Gubina, K. E.; Shatrava, J.A.; Ovchinnikov, V.A.; Amirkhanov, V.M. Spectroscopic characterization of lanthanide complexes with N,N'-tetraethyl-N''-benzoylphosphoryltriamide. Crystal structure of tris(N,N'-tetraethyl-N''-benzoylphosphoryltriamide) cerium(III) trinitrate complex. *Polyhedron* **2000**, *19*, 2203.
- ²⁰ Legendziewicz, J.; Oczko, G.; Wiglusz, R.; Amirkhanov, V. Correlation between spectroscopic characteristics and structure of lanthanide phosphoro-azo derivatives of β -diketones. *J. Alloys Comp.* **2001**, *323*, 792.
- ²¹ Judd, B. R. Optical Absorption Intensities of Rare-Earth Ions. *Phys. Rev B.* **1962**, *127*, 750.
- ²² Ofelt, G. S. Intensities of Crystal Spectra of Rare-Earth Ions. *J. Chem. Phys.* **1962**, *37*, 511.
- ²³ Banerjee, S.; Huebner, L.; Romanelli, M.D.; Kumar, G.A.; Riman, R.E.; Emge, T.J.; Brennan, J.G. Oxoselenido Clusters of the Lanthanides: Rational Introduction of Oxo Ligands and Near-IR Emission from Nd(III). *J. Am. Chem. Soc.* **2005**, *127*, 15900.
- ²⁴ Banerjee, S.; Kumar, G.A.; Riman, R.; Emge, T.J.; Brennan, J. Monodisperse Oxoclusters of the Lanthanides Begin to Resemble Solid-state Materials at Very Small Cluster Sizes: Structure and Near-IR Emission from Nd(III). *J. Amer. Chem. Soc.* **2007**, *129*, 5926.
- ²⁵ Kumar, G.A.; Riman, R.E.; Diaz Torres, L.A.; Banerjee, S.; Romanelli, M.D.; Emge, T.J.; Brennan, J.G. Near Infrared Optical characteristics of Chalcogenide-Bound Nd Organometallic Complexes. *Chem. Mater.* **2007**, *19*, 2937.

- ²⁶ Hasegawa, Y.; Ohkubo, T.; Sogabe, K.; Kawamura, Y.; Wada, Y.; Nakashima, N.; Yanagida, S. Luminescence of Novel Neodymium Sulfonylamine Complexes in Organic Media. *Angew. Chem. Int. Ed.* **2000**, *39*, 357.
- ²⁷ Wolbers, M.P.O.; van Veggel, F. C. J. M.; Hofstraat, J. W.; Geurts, F. A. J.; Reinhoudt, D. N. Luminescence properties of *m*-terphenyl-based Eu^{3+} and Nd^{3+} complexes: visible and near-infrared emission. *J. Chem. Soc. Perkin Trans. 2* **1997**, *11* 2275.
- ²⁸ Wolbers, M. P. O.; van Veggel, F. C. J. M.; Snellink-Ruel, B. H. M.; Hofstraat, J. W.; Geurts, F. A. J.; Reinhoudt, D. N. Photophysical studies of *m*-terphenyl-sensitized visible and near-infrared emission from organic 1:1 lanthanide ion complexes in methanol solutions. *J. Chem. Soc. Perkin Trans. 2* **1998**, *10*, 2141.
- ²⁹ Klink, S. I.; Hebbink, G. A.; Grave, L.; van Veggel, F. C. J. M.; Reinhoudt, D. N.; Slooff, L. H.; Polman, A.; Hofstraat, J. W. Sensitized near-infrared luminescence from polydentate triphenylene-functionalized Nd^{3+} , Yb^{3+} , and Er^{3+} complexes. *J. Appl. Phys.* **1999**, *86*, 1181.
- ³⁰ Hebbink, G. A.; van Veggel, F. C. J. M.; Reinhoudt, D. N. Increased Luminescent Lifetimes of Ln^{3+} Complexes Emitting in the Near-Infrared as a Result of Deuteration. *Eur. J. Org. Chem.* **2001**, 4101.
- ³¹ Hasegawa, Y.; Murakoshi, K.; Wada, Y.; Kim, J. H.; Nakashima, N.; Yamanaka, T.; Yanagida, S. Enhancement of luminescence of Nd^{3+} complexes with deuterated hexafluoroacetylacetonato ligands in organic solvent. *Chem. Phys. Lett.* **1996**, *248*, 8.
- ³² Wada, Y.; Okubo, T.; Ryo, M.; Nakazawa, T.; Hasegawa, Y.; Yanagida, S. High Efficiency Near-IR Emission of Nd(III) Based on Low-Vibrational Environment in Cages of Nanosized Zeolites. *J. Am. Chem. Soc.* **2000**, *122*, 8583.
- ³³ Yu, R.; Yu, K.; Wei, W.; Xu, X.; Qiu, X.; Liu, S.; Huang, W.; Tang, G.; Ford, H.; Peng, B. Nd_2O_3 Nanoparticles Modified with a Silane-Coupling Agent as a Liquid Laser Medium. *Adv. Mater.* **2007**, *19*, 838.
- ³⁴ Romanelli, M.; Kumar, G.A.; Emge, T.J.; Riman, R.E.; Brennan J.G. Intense Near-IR Emission from Nanoscale Lanthanoid Fluoride Clusters. *Angew. Chem. Int. Ed.* **2008**, *47*, 6049.

Chapter 4. Molecular Precursors of II-VI Semiconductors: $(\text{pyr})_x\text{M}(\text{SeC}_6\text{F}_5)_2$ ($\text{M} = \text{Zn}, \text{Cd}$ with $x = 2$; $\text{M} = \text{Hg}$ with $x = 0$)

4.1 Introduction

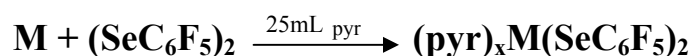
Coordination of metals with anionic ER ligands has been historically significant, with a wealth of novel products isolated using metals from across the periodic table. It is known that significant changes to the structures and properties of metal complexes arise from changing either the chalcogen, or aryl/alkyl substituent of the ligand. Fluorinated ligands, for example, have been shown to impart unique chemical and physical properties to metal compounds. Compared to the hydrocarbon analogs, fluorinated species often have superior solubility in polar solvents, as well as novel structural motifs. These differences can be attributed largely to changes in electronic properties caused by the more electronegative fluorine atoms.

The fluorinated phenoxide ($^-\text{OC}_6\text{F}_5$) has been used extensively throughout the periodic chart in the preparation of metal complexes.⁶⁻¹⁶ The number of reported chalcogenolate coordination complexes declines however, upon descending the group 16 elements. Reports of metal alkyl/aryl-oxides, and alkyl/aryl-thiolates are far more numerous than analogous metal selenolate or tellurolate complexes. Furthermore, reports of fluorinated group 12 metal selenolates are less prevalent than hydrocarbon analogs.¹⁷⁻²⁴ In regards to the chalcogen, this is partially due to the fact that both the fluorinated phenol and thiol are commercially available, allowing for the facile availability and/or synthesis of the respective fluorinated precursor. Fluorinated selenol ($\text{C}_6\text{F}_5\text{SeH}$) on the other hand, is not readily available, making the synthesis of suitable starting materials

more difficult. We began our study using the same $\text{C}_6\text{F}_5\text{SeSeC}_6\text{F}_5$ ligand²⁵ that proved useful for the isolation of novel lanthanide species, and detailed here is the synthesis, characterization, and thermolysis of $\text{M}(\text{SeC}_6\text{F}_5)_2(\text{pyr})_x$ ($\text{M} = \text{Zn, Cd, Hg}$; $x = 0, 2$) species.

4.2 $\text{M}(\text{SeC}_6\text{F}_5)_2(\text{pyr})_2$ ($\text{M} = \text{Zn, Cd}$): Synthesis and Structure

Through the direct reduction of $\text{C}_6\text{F}_5\text{SeSeC}_6\text{F}_5$ by elemental M ($\text{M} = \text{Zn, Cd, Hg}$), the respective metals are oxidized to the 2^+ state in a solution of pyridine. The analogous reactions in less polar solvents (THF, DME) proceed very slowly or not at all, and neither solvent gave isolable single crystal products. When pyridine is used, the metals are quickly brought into solution and crystallization of the respective reactions gave XRD quality single crystals of $(\text{pyr})_x\text{M}(\text{SeC}_6\text{F}_5)_2$ ($x = 0$ for Hg, $x = 2$ for Zn and Cd). The room temperature reactions are straightforward and proceed according to the following:



$(\text{pyr})_2\text{Zn}(\text{SeC}_6\text{F}_5)_2$ is isolated as a four coordinate tetrahedral monomer (Fig 46), and crystallizes in the monoclinic $\text{P2}_1/\text{n}$ space group. The primary coordination sphere consists of two fluorinated selenolate ligands and two neutral donor pyridine molecules, all of which are terminally bound to the metal center. Zn-Se and Zn-N bond lengths are within expected values and typical for similar species.^{17, 26} Important bond distances/angles and crystallographic details are given in tables 19 and 20 below.

Table 19. Crystal data and structure refinement for (pyr)₂Zn(SeC₆F₅)₂

Empirical formula	C ₂₂ H ₁₀ F ₁₀ N ₂ Se ₂ Zn	
Formula weight	715.61	
Temperature	100(2) K	
Wavelength	0.71073 Å	
Crystal system	Monoclinic	
Space group	P2(1)/n	
Unit cell dimensions	$a = 9.3073(5)$ Å	$\alpha = 90.00^\circ$
	$b = 17.0503(9)$ Å	$\beta = 100.020(1)^\circ$
	$c = 14.8291(8)$ Å	$\gamma = 90.00^\circ$
Volume	$2317.4(2)$ Å ³	
Z	4	
Density (calculated)	2.051 Mg/m ³	
Final R indices [$I > 2\sigma(I)$]	R1 = 0.0190, wR2 = 0.0461	

Table 20. Bond Lengths (Å) and Angles (°) for (pyr)₂Zn(SeC₆F₅)₂

Zn1-N1	2.0545(13)	Zn1-N2	2.0599(13)
Zn1-Se1	2.4130(2)	Zn1-Se2	2.4175(3)
N1-Zn1-Se1	111.01(4)	N1-Zn1-Se2	103.74(4)
N2-Zn1-Se1	108.39(4)	N2-Zn1-Se2	110.45(4)
N1-Zn1-N2	105.75(5)	Se1-Zn1-Se2	116.914(9)

(pyr)₂Zn(SeC₆F₅)₂ lacks the *intramolecular* π - π stacking seen in many of the analogous lanthanide complexes. This is likely due to both steric crowding around the small metal ion and directional bonding caused by ligand metal orbital overlap. The ionic radii of a four coordinate Zn²⁺ ion (0.60Å) is considerably smaller than the smallest Ln ion (6-coordinate Yb²⁺ = 1.02Å; 6-coordinate Yb³⁺ = 0.868Å). *Intermolecular* π - π stacking can still be seen between the fluorinated phenyl rings of molecules in adjacent unit cells, however (Fig 47.). The π - π stacking exists between molecules Zn1Q and Zn1O which are located in adjacent unit cells. Z1Q is the equivalent to the Z1P molecule translated one unit in the *a* cell direction. These two molecules are related by an inversion center giving rise to parallel rings with a separation of 3.584Å (calculated from average intermolecular C-C distances).

The Cd analog crystallizes from the same reaction conditions used for the preparation of (pyr)₂Zn(SeC₆F₅)₂. For the Cd reaction however, two isolable products are possible. The first is monomeric (pyr)₂Cd(SeC₆F₅)₂, and the second is dimeric [(pyr)Cd(SeC₆F₅)₂]₂. (pyr)₂Cd(SeC₆F₅)₂ crystallizes in the P2₁/c monoclinic space group and like (pyr)₂Zn(SeC₆F₅)₂, has a tetrahedral coordination environment (Important crystallographic details and bond information are given in tables 21 and 22).

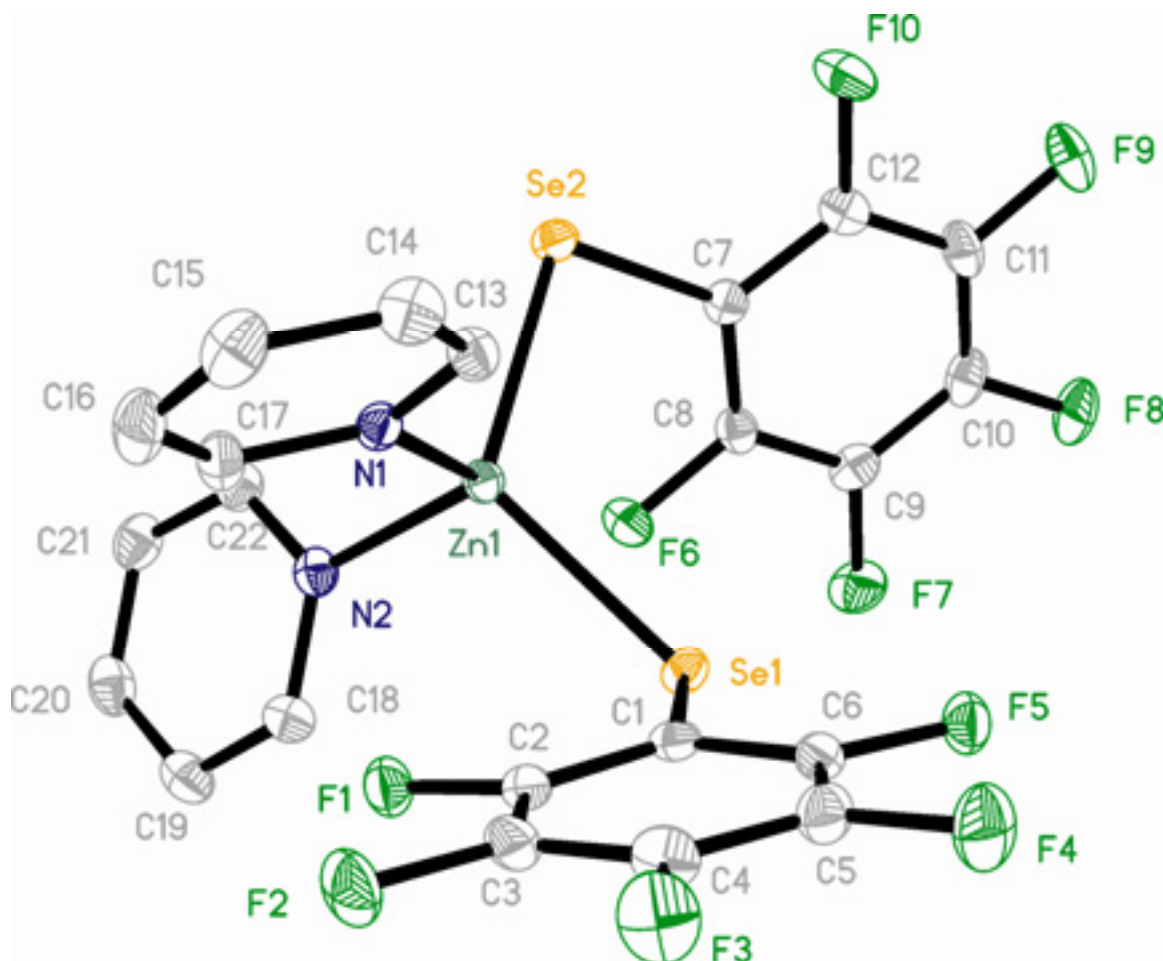


Fig 46. ORTEP of $(\text{pyr})_2\text{Zn}(\text{SeC}_6\text{F}_5)_2$ with thermal ellipsoids drawn at 50% probability level. Hydrogen atoms have been removed for clarity.

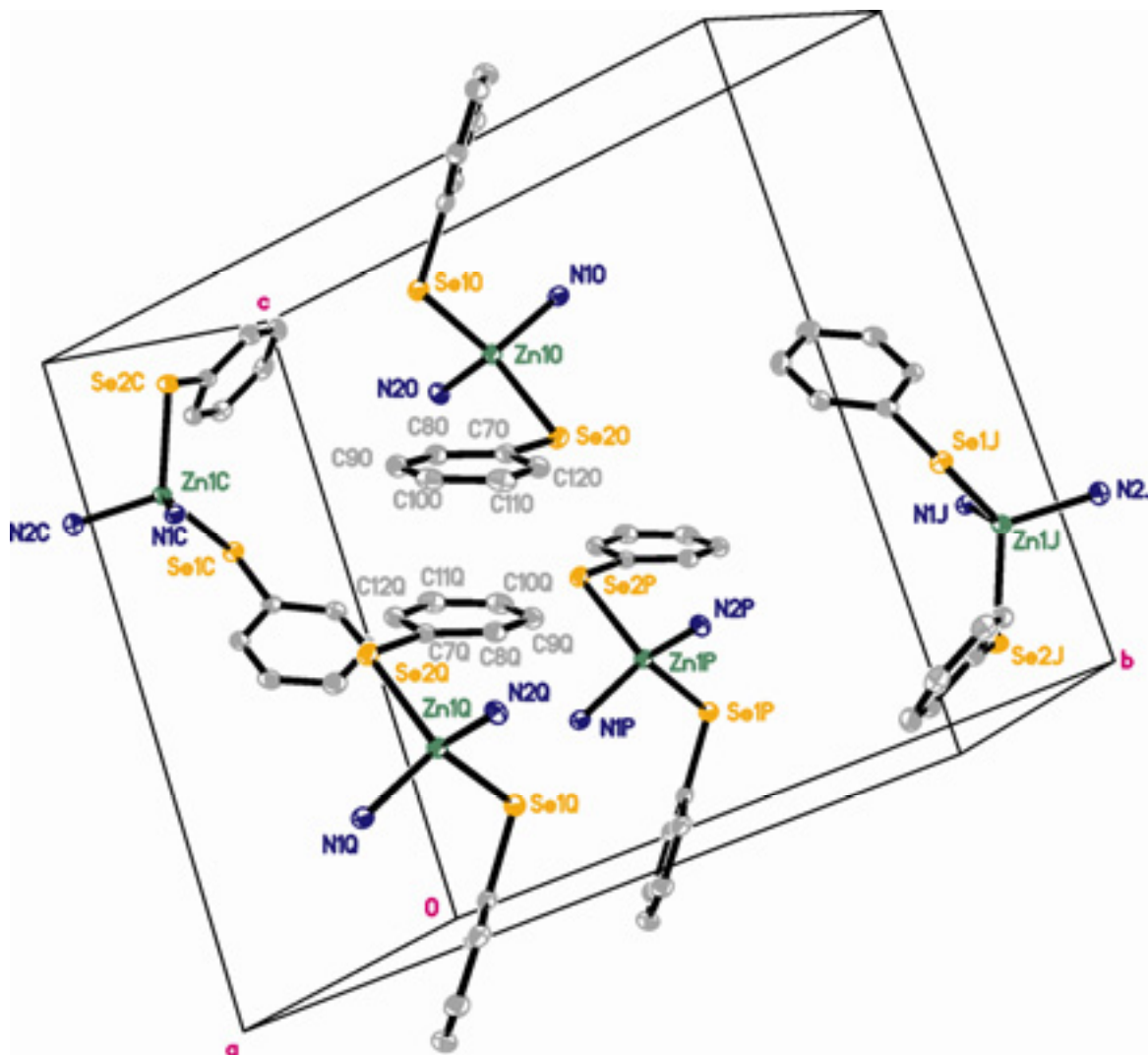


Fig 47. ORTEP of $(\text{pyr})_2\text{Zn}(\text{SeC}_6\text{F}_5)_2$ unit cell packing with thermal ellipsoids drawn at 50% probability. Protons and carbon atoms of pyridine molecules, as well as fluorine atoms have been removed for clarity.

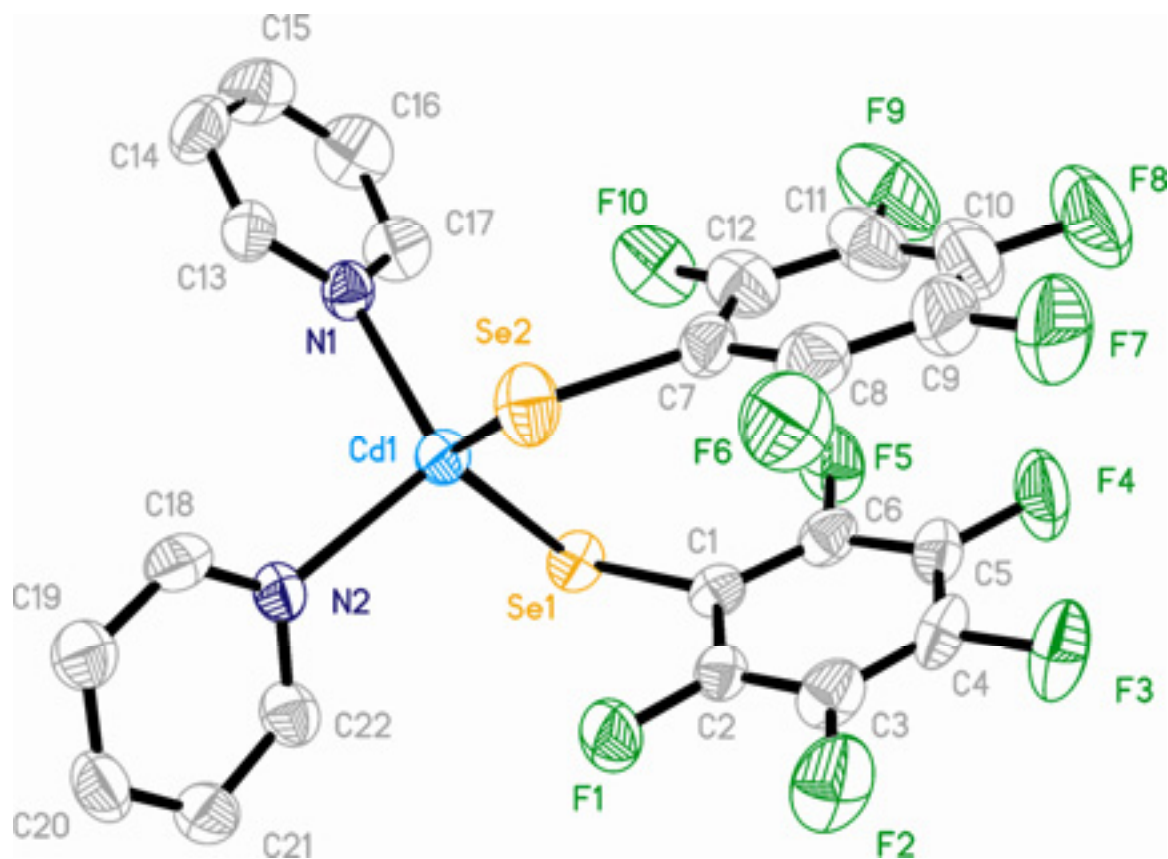


Fig 48. ORTEP of $(\text{pyr})_2\text{Cd}(\text{SeC}_6\text{F}_5)_2$ with thermal ellipsoids drawn at 50% probability level.

Table 21. Crystal data and structure refinement for (pyr)₂Cd(SeC₆F₅)₂

Empirical formula	C ₂₂ H ₁₀ Cd F ₁₀ N ₂ Se ₂	
Formula weight	762.64	
Temperature	200(2) K	
Wavelength	0.71073 Å	
Crystal system	Monoclinic	
Space group	P2(1)/c	
Unit cell dimensions	$a = 9.086(3)$ Å	$\alpha = 90.00^\circ$
	$b = 23.255(7)$ Å	$\beta = 109.276(6)^\circ$
	$c = 12.034(4)$ Å	$\gamma = 90.00^\circ$
Volume	2400.3(12) Å ³	
Z	4	
Density (calculated)	2.110 Mg/m ³	
Final R indices [I > 2σ(I)]	R ₁ = 0.0438, wR ₂ = 0.0842	

Table 22. Bond Lengths (Å) and Angles (°) for (pyr)₂Cd(SeC₆F₅)₂

Cd1-N1	2.286(5)	Cd1-N2	2.289(4)
Cd1-Se1	2.5645(9)	Cd1-Se2	2.5958(10)
N1-Cd1-N2	105.77(18)	N1-Cd1-Se1	110.49(13)
N2-Cd1-Se1	109.88(12)	N1-Cd1-Se2	111.32(11)
N2-Cd1-Se2	95.07(13)	Se1-Cd1-Se2	122.15(3)

While there are many similarities between the monomers, $(\text{pyr})_2\text{Cd}(\text{SeC}_6\text{F}_5)_2$ differs from $(\text{pyr})_2\text{Zn}(\text{SeC}_6\text{F}_5)_2$ in that $(\text{pyr})_2\text{Cd}(\text{SeC}_6\text{F}_5)_2$ contains *intramolecular* π - π stacking in addition to the *intermolecular* π - π stacking seen in $(\text{pyr})_2\text{Zn}(\text{SeC}_6\text{F}_5)_2$. The *intramolecular* π - π stacking involves the Se1 and Se2 selenolate rings, with ring separations of 3.677 Å (calculated from average intermolecular C-C distances). The ability of this species to exhibit this conjugated π - π stacking is likely due to the longer Cd-Se bond distances decreasing steric repulsion around the primary coordination sphere. Average Cd-Se bonds are 0.165 Å longer than the analogous Zn-Se bonds.

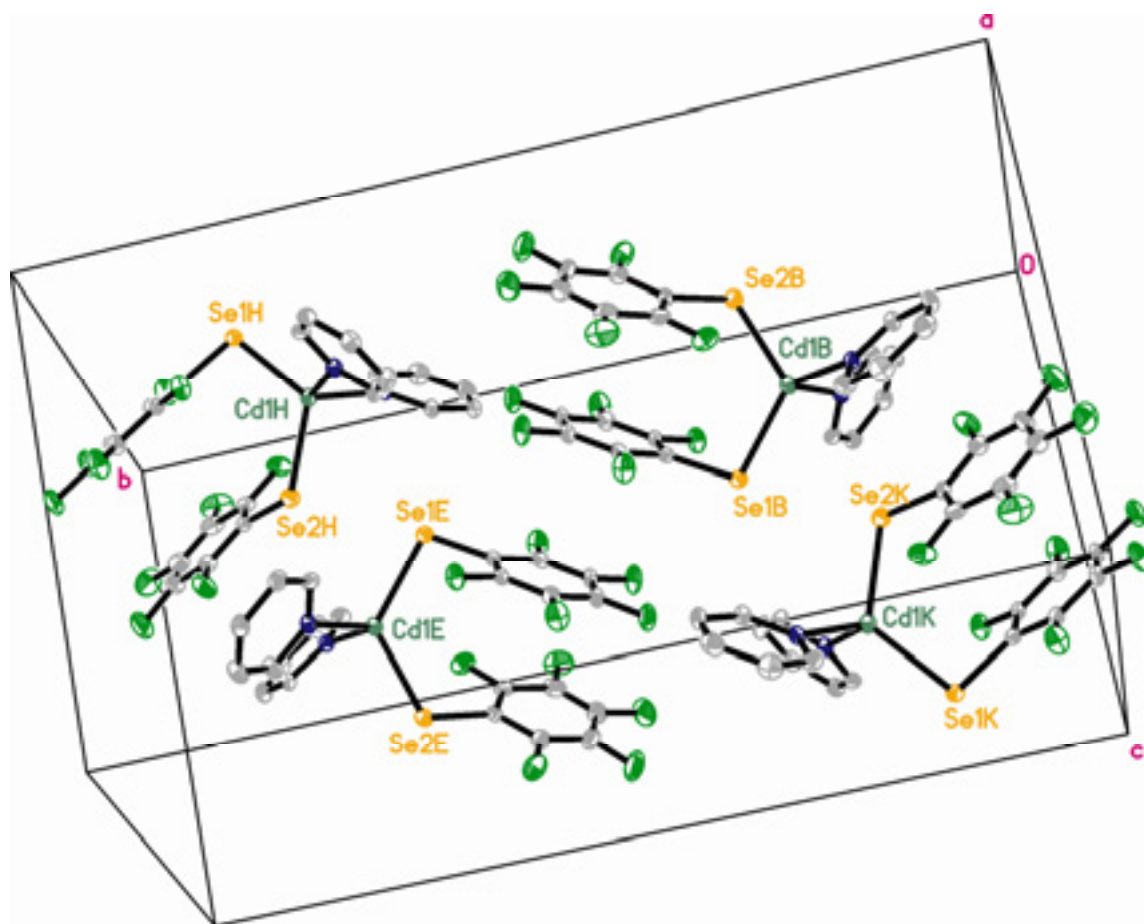


Fig 49. ORTEP of $(\text{pyr})_2\text{Cd}(\text{SeC}_6\text{F}_5)_2$ unit cell with thermal ellipsoids drawn at 50% probability level. Hydrogen atoms have been removed for clarity.

The *intermolecular* π - π stacking can also be seen in the packing diagram of $(\text{pyr})_2\text{Cd}(\text{SeC}_6\text{F}_5)_2$ (Fig 49). The unit cell consists of 4 monomers, two of which ($\text{Cd1E}/\text{Cd1B}$) are related by an inversion center which aligns the rings bound to the Se1 atoms of the respective molecules. The *intermolecular* ring separation is 3.764 Å, which is 0.087 Å longer than the *intramolecular* stacking separation (calculated from average intermolecular C-C distances). The larger ring-ring separation is likely due to steric crowding of the four molecules in the unit cell. This is likely a result of the four molecules not participating in the intermolecular π - π interactions ($\text{Cd1K}/\text{Cd1H}$) increasing steric repulsions between the four molecules. Nearly isostructural, the crystallographic packing motifs illustrate the crystallographic differences between the Cd and Zn analogs.

The second isolable product from this reaction, $[(\text{pyr})\text{Cd}(\text{SeC}_6\text{F}_5)_2]_2$, is structurally similar to $(\text{pyr})_2\text{Cd}(\text{SeC}_6\text{F}_5)_2$ in that it has a pseudo tetrahedral coordination environment. $[(\text{pyr})\text{Cd}(\text{SeC}_6\text{F}_5)_2]_2$ also exhibits intramolecular π - π stacking (Fig. 50). L-Cd-L (L= Se or N) bond angles are all between 94 and 122° (Table 24), which are in the same range as those in $(\text{pyr})_2\text{Cd}(\text{SeC}_6\text{F}_5)_2$. Also similar to $(\text{pyr})_2\text{Cd}(\text{SeC}_6\text{F}_5)_2$ are average π - π ring separations of 3.58 Å (average C-C distances).

While there are similarities between $[(\text{pyr})\text{Cd}(\text{SeC}_6\text{F}_5)_2]_2$ and $(\text{pyr})_2\text{Cd}(\text{SeC}_6\text{F}_5)_2$, distinct differences can be seen. Formation of the dimeric species can be rationalized as two monomers coming together with the concomitant bridging of selenolate molecules between metal centers and the displacement of one pyridine molecule from each metal. The selenolates have been shown to effectively compete for access to the metal center,

and have sufficient electron density to bridge metals in a μ_2 fashion. In addition to containing bridging selenolates and having only one bound neutral donor, $[\text{Cd}(\text{SeC}_6\text{F}_5)_2(\text{pyr})_2]_2$ differs from $(\text{pyr})_2\text{Cd}(\text{SeC}_6\text{F}_5)_2$ in that there exists a dative 2.948 \AA Cd-F interaction (Cd1-F6) not seen in the monomer.

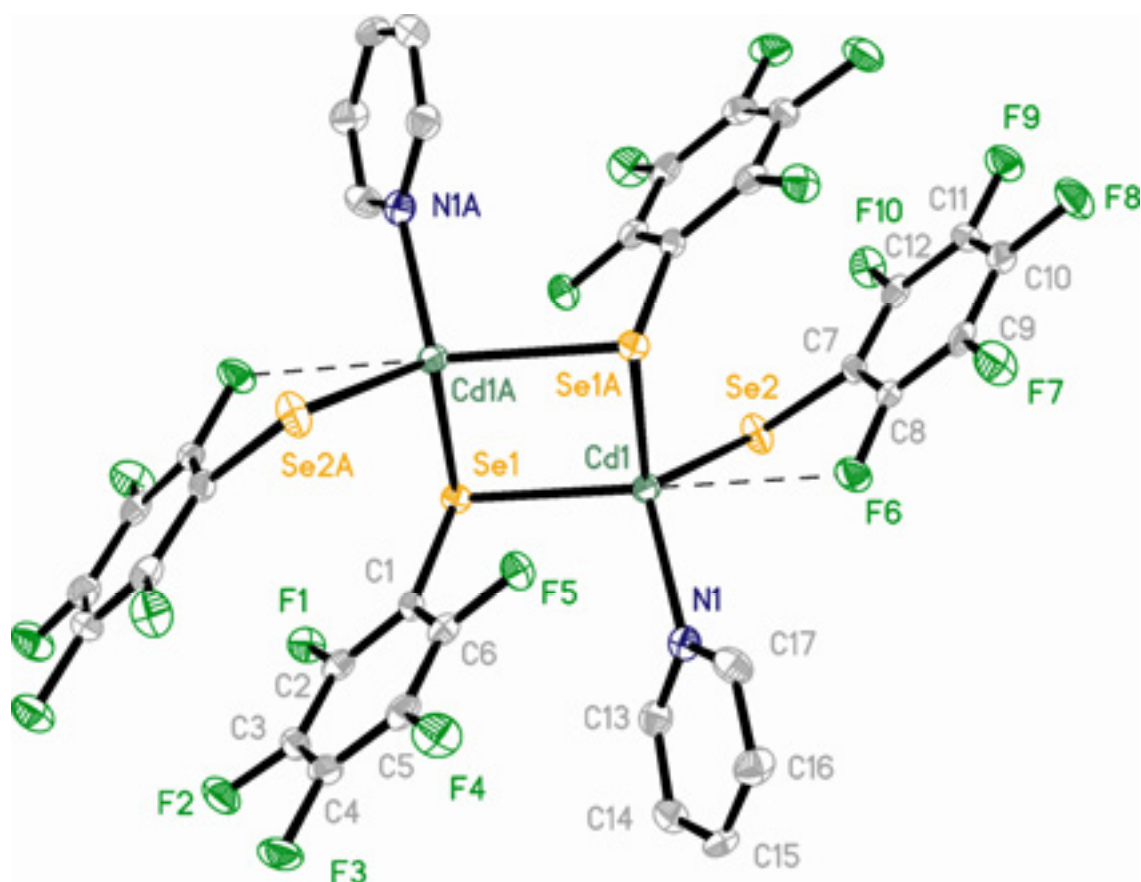


Fig 50. ORTEP of $[(\text{pyr})\text{Cd}(\text{SeC}_6\text{F}_5)_2]_2$ unit cell with thermal ellipsoids drawn at 50% probability level. Hydrogen atoms have been removed for clarity.

Table 23. Crystal data and structure refinement for [(pyr)Cd(SeC₆F₅)₂]₂

Empirical formula	C ₃₄ H ₁₀ Cd ₂ F ₂₀ N ₂ Se ₄	
Formula weight	920.84	
Temperature	200(2) K	
Wavelength	0.71073 Å	
Crystal system	Monoclinic	
Space group	P2(1)/c	
Unit cell dimensions	$a = 13.268(4)$ Å	$\alpha = 90.00^\circ$
	$b = 8.123(2)$ Å	$\beta = 109.424(6)^\circ$
	$c = 18.397(5)$ Å	$\gamma = 90.00^\circ$
Volume	1869.8(9) Å ³	
Z	2	
Density (calculated)	1.636 Mg/m ³	
Final R indices [I > 2σ(I)]	R1 = 0.0381, wR2 0.0799	

Table 24. Bond Lengths (Å) and Angles (°) for [(pyr)Cd(SeC₆F₅)₂]₂

Cd1-N1	2.274	Cd1-Se1A	2.6869(10)
Cd1-Se1	2.7059(9)	Cd1-Se2	2.5806(9)
N1-Cd1-Se2	111.57(13)N1	Cd1-Se1A	102.55(13)
Se2-Cd1-Se1	122.04(3)	N1-Cd1-Se1	114.90(13)
Se2-Cd1-Se1A	110.51(3)	Se1-Cd1-Se1A	94.40(3)

4.3 3D+1 Modulated $\text{Hg}(\text{SeC}_6\text{F}_5)_2$: Synthesis and Structure

In contrast to the analogous Zn and Cd reactions, Hg reduces $(\text{SeC}_6\text{F}_5)_2$ in pyridine to give unsolvated $\text{Hg}(\text{SeC}_6\text{F}_5)_2$. $\text{Hg}(\text{SeC}_6\text{F}_5)_2$ is a near linear monomeric species bound only by two terminal selenolate ligands. Typical bond distances and angles are given in table 24, and are within expected values for Hg-Se bonds. At first glance $\text{Hg}(\text{SeC}_6\text{F}_5)_2$ is a typical 2-coordinate linear Hg complex, but a closer look at its crystallographic details reveals an intricate, 3D+1 modulated structure. This molecule crystallizes in the $\text{P}i(\alpha\beta\gamma)0$ space group with 3D+1 dimensionality and with near commensurate modulation wave vector $q=[-0.1292a^*, 0.3391b^*, 0.3296c^*]$. This structural modulation hindered the refinement of this structure. The daunting task of elucidating the modulated structure and its refinement was performed by Thomas J. Emge (Dept. of Chemistry and Chemical Biology, Rutgers University, New Brunswick), and is described herein.

In essence, the long range order of this molecule is perturbed by a structural modulation that propagates along a vector (q-vector) not parallel to the unit cell axis. The modulated structure is characterized by large displacements of the Hg atom from its average position as well as rotation and translation of the SeC_6F_5 groups about their center of mass. The addition of this modulation severely complicates refinement of the atomic positions in the unit cell. To begin refinement of this structure, a top down approach is used in which a super cell is first identified by imposing constraints to pin down the modulation. Figure 51 shows ORTEPs for the respective $\text{Hg}(\text{SeC}_6\text{F}_5)_2$ molecules of the long range supercell. In this figure, the modulation is compressed so as

to superimpose the 9 unique monomers present in the supercell. The superimposed images show the degree of modulation present in the system.

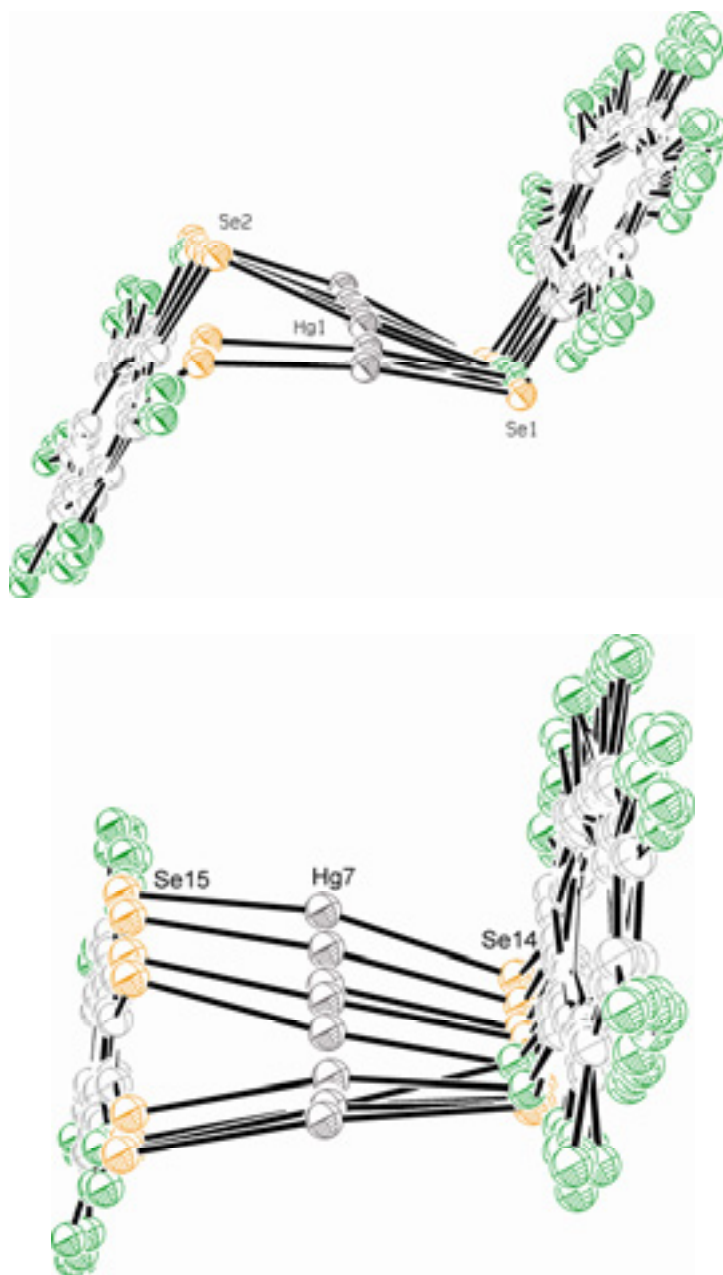


Fig 51. Top: ORTEP of $\text{Hg}(\text{SeC}_6\text{F}_5)_2$ oriented with the Se-C bond in the plane of the paper. Bottom: ORTEP of $\text{Hg}(\text{SeC}_6\text{F}_5)_2$ oriented with the Se-C bond pointing out of the plane of the paper. Both have thermal ellipsoids drawn at 50% probability.

Across the nine unique molecules, one can see the deviation from linearity along the modulated atomic positions of each molecule. Viewed nearly orthogonal to one another, the two illustrations above (Fig 51) show deviations in not only the linearity of the Se-Hg-Se bonds along several directions, but also in the Hg-Se-C bond angles and Hg-Se-C-C torsion angles. It is these deviations that define the modulation and complicate refinement of the structure.

If the nine molecules present in the super cell are illustrated propagating (Fig 52) along the modulation vector as they do in the crystal (rather than compressed as in Figure 51, which was for illustrative purposes only), one can see the changes in the bonding environment that exist for each molecule. Figure 52 (Top Image) shows that the selenolates of the Hg1 molecule are almost perfectly trans to each other, with one pointing into the plane of the paper and the other pointing out. Modulation can be seen in the linearity of the Se-Hg-Se bonds, and a trend in the deviation of this parameter can be seen propagating across the series (Table 25). Approaching the center of the modulated series, the deviation from linearity (180°) in the Se-Hg-Se bonds increases until a maximum deviation is reached for Hg4. The same trend is seen in the second Hg5 – Hg9 row, but with exceptions, namely because Se-Hg7-Se has the greatest deviation at 166.13° .

Table 25. Se-Hg-Se bond angles ($^\circ$) for molecules Hg1 – Hg9

Molecule	Se-Hg-Se angle	Molecule	Se-Hg-Se angle
Hg1	178.76	Hg5	171.88
Hg2	174.53	Hg6	170.03
Hg3	166.81	Hg7	166.13
Hg4	166.97	Hg8	173.45
		Hg9	180.00

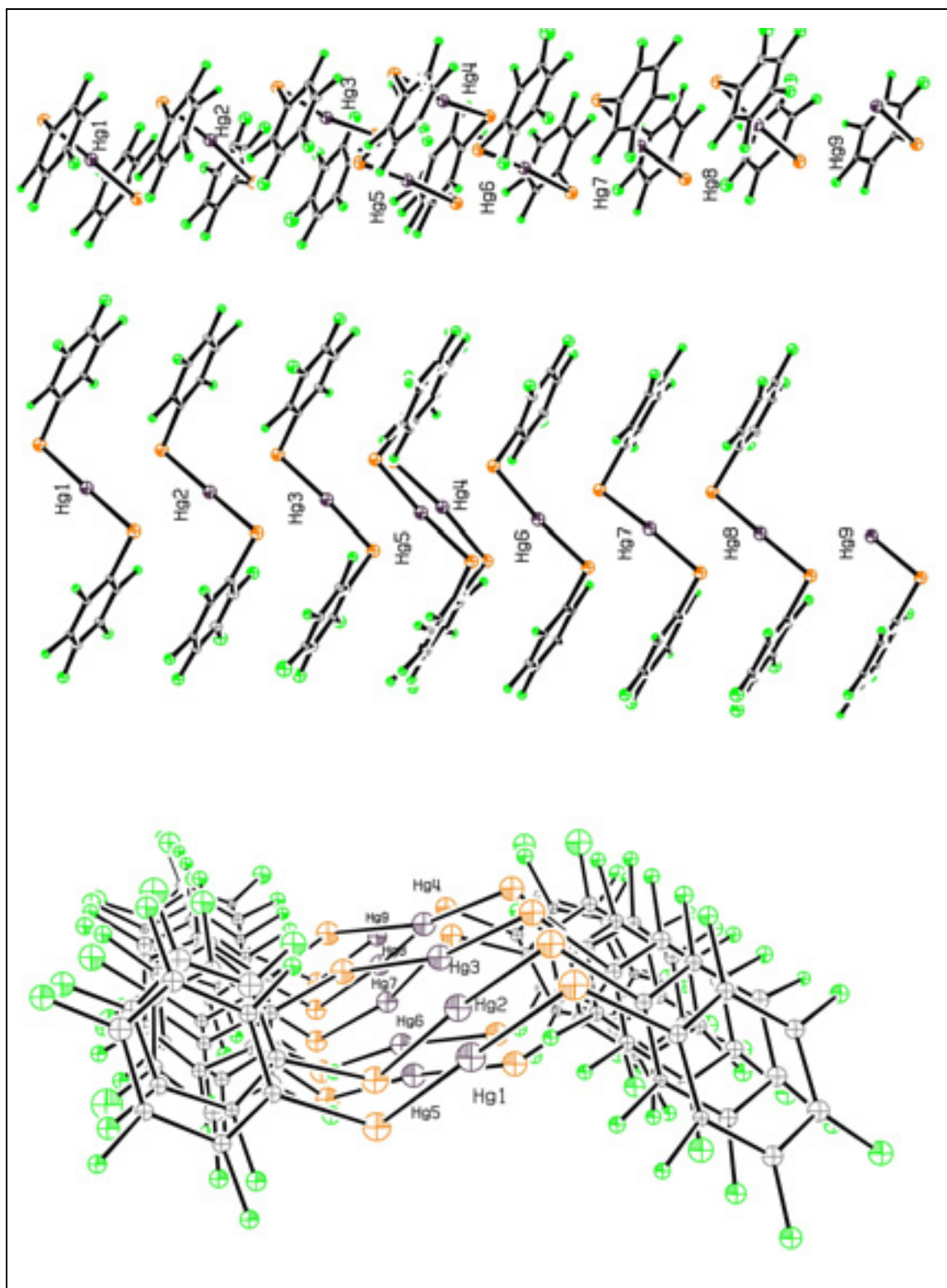


Fig 52. ORTEP of modulated $\text{Hg}(\text{SeC}_6\text{F}_5)_2$ super cell viewed perpendicular to the 100, 010, and 001 direction (respectively, from top to bottom).

In addition, if $\text{Hg}(\text{SeC}_6\text{F}_5)_2$ were a linear molecule having perfectly trans selenolate ligands, the C-Hg-C (The carbon atom is the carbon bound to the selenium) angle would be 180° . Changes in this angle allow us to quantify the deviation from ideality (180°) that one would expect for a perfectly trans molecule. If we consider the nine $\text{Hg}(\text{SeC}_6\text{F}_5)_2$ molecules as one complete cycle of the modulation, after which it begins again with Hg1, a trend in the deviations of the C-Hg-C angle is noticed. Modulation in the C-Hg-C angle begins at Hg1 where the C-Hg-C bond angle is 175.32° . As the super cell is traversed, deviations in this angle increase until a maximum deviation of 146.09° at Hg4 is reached. At this point the deviation decreases back to a perfectly trans molecule at Hg9 (C-Hg-C angle of 180.00°). Table 26 lists the C-Hg-C bond angles for $\text{Hg}(\text{SeC}_6\text{F}_5)_2$.

Table 26. C-Hg-C Bond Angles ($^\circ$) for molecules Hg1 – Hg9

Molecule	C-Hg-C angle	Molecule	C-Hg-C angle
Hg1	175.32	Hg5	149.85
Hg2	164.31	Hg6	151.48
Hg3	155.84	Hg7	158.82
Hg4	146.09	Hg8	169.74
		Hg9	180.00

$\text{Hg}(\text{SeC}_6\text{F}_5)_2$ also has a unique packing motif that is best described as sheets of 2D propagating 1D modulated molecules. These sheets are a consequence of associative interactions between Hg atoms from one molecule with selenium atoms of a neighboring molecule. The layers propagate along the 001 axis with the selenolates of one layer's molecules pointing towards the Hg atoms of a neighboring layer's molecules. These long

range dative interactions are also seen in the analogous non fluorinated $\text{Hg}(\text{SeC}_6\text{H}_5)_2$ species, where dative Hg-Se interactions between neighboring molecules are between 3.4-3.6 Å.²⁷ In $\text{Hg}(\text{SeC}_6\text{F}_5)_2$, these interactions are between 2.78 and 3.33 Å, the relationships the resultant structure has with the ligand's electronic properties, the crystallographic packing, and the modulation in this molecule. Table 27 shows additional similarities and differences between $\text{Hg}(\text{SeC}_6\text{F}_5)_2$ and $\text{Hg}(\text{SeC}_6\text{H}_5)_2$.

Table 27. Comparison of key features between $\text{Hg}(\text{SeC}_6\text{F}_5)_2$ and $\text{Hg}(\text{SeC}_6\text{H}_5)_2$

	$\text{Hg}(\text{SeC}_6\text{F}_5)_2$	$\text{Hg}(\text{SeC}_6\text{H}_5)_2$
Molecules in asymmetric unit	9	$\frac{1}{2}$
Space Group, Dimensionality	$\text{P}\bar{1}(\alpha\beta\gamma)0$, 3D+1	$\text{P}\bar{1}$, 3D
Intramolecular Hg-Se Bond length(s)	2.437-2.509 Å	2.471 Å
Hg-Se Bond angle(s)	166.13-180.0°	178.0°

4.4 Thermolysis Reactions

The feasibility of these $(\text{pyr})_2\text{M}(\text{SeC}_6\text{F}_5)$ species to be used as molecular precursors in the deposition of solid-state II-VI products was tested by thermolysis reactions. General reactions that lead to the isolation of crystalline II-VI materials can be performed by heating the crystalline $(\text{pyr})_2\text{M}(\text{SeC}_6\text{F}_5)$ under low pressures. For our experiments, samples of the respective metal selenolates (~20mg) were sealed in quartz tubes under vacuum and placed in the center of the hot zone of a horizontal tube furnace. The quartz reaction tube extended out of the furnace's alumina tube where a cold zone was generated by immersing its end in a liquid nitrogen bath for the duration of the experiment. This cold zone was used for the deposition of any sublimation products or

volatile materials generated via the high temp/low pressure reaction. The reactions followed the general temperature profile:

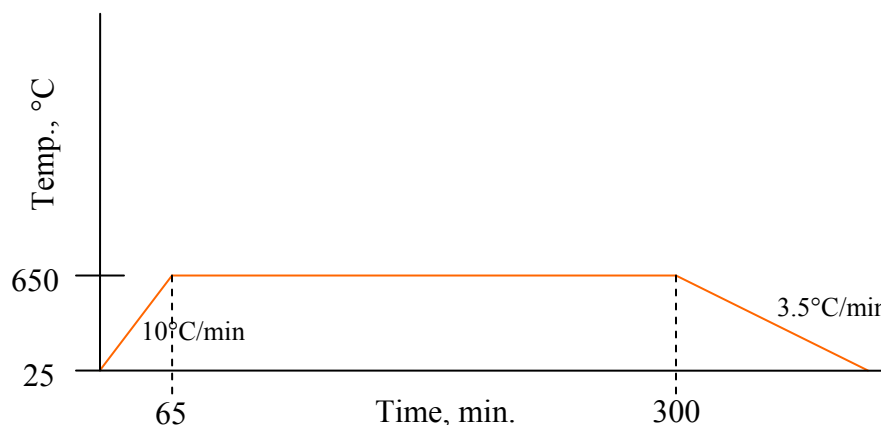


Fig 53. Thermolysis temperature profile

Thermolysis reactions for all three metal precursors gave similar results, but each had distinct differences. Powder products for each reaction were analyzed using a HiStar multiwire area detector (Bruker-AXS) on a 3-kW FR571 rotating anode x-ray generator (Nonius) with graphite monochromatized fine focus Cu radiation. For the reaction of $(\text{pyr})_2\text{Zn}(\text{SeC}_6\text{F}_5)_2$, a fine black powder deposited on the inner walls of the reaction tube where the sample was held. Cubic ZnSe was the only crystalline phase identified in the black powder (referencing 2003 JCPDS Card number 88-2345).²⁸ A yellow sublimation product was found at the cold region of the quartz tube. The yellow polycrystalline material was identified as $\text{Se}(\text{C}_6\text{F}_5)_2$ by GC-MS analysis.

The analogous reaction with $(\text{pyr})_2\text{Cd}(\text{SeC}_6\text{F}_5)_2$ was similar in that it produced a dark powder that was formed near the location that the sample was initially held. The

dark powder product was found to be a mixture of hexagonal CdSe (referencing 2003 JCPDS Card number 77-0021)²⁹ and an unidentified amorphous component. There was also a yellow crystalline sublimation product at the cold end of the quartz tube. Quality single crystals of the sublimation product were present, and allowed for single crystal XRD analysis. The yellow crystals were found to be $\text{Se}_2(\text{C}_6\text{F}_5)_2$ by XRD.

$\text{Hg}(\text{SeC}_6\text{F}_5)_2$ thermolysis reactions resulted in a dark powder product, but unlike the Zn and Cd reactions, this product formed at the region where the quartz tube exited the alumina tube. Cubic HgSe was the only crystalline phase identified in the powder (referencing 2003 JCPDS Card number 65-4590).³⁰ Sublimed $\text{Se}(\text{C}_6\text{F}_5)_2$ was again found at the cold region of the quartz tube.

4.5 Conclusions

The successful isolation of novel $\text{M}(\text{SeC}_6\text{F}_5)_2$ species has been achieved by the reductive cleavage of perfluoro-dipenyldiselenide in pyridine. This series of Group 12 metal complexes is one of the first reports of Group 12 fluorinated selenolates. $(\text{pyr})_2\text{Zn}(\text{SeC}_6\text{F}_5)_2$ and $(\text{pyr})_2\text{Cd}(\text{SeC}_6\text{F}_5)_2$ are structurally similar, illustrating their common chemistry. In all cases, the metals are divalent and bound by two anionic ligands to give neutral molecular species. While the Cd and Zn species are tetrahedrally bound with two coordinated pyridine molecules, the Hg complex reveals a nearly linear coordination complex with a highly disordered 3D+1 modulated structure. While only intermolecular π - π stacking is present in both $(\text{pyr})_2\text{Zn}(\text{SeC}_6\text{F}_5)_2$ and $(\text{pyr})_2\text{Cd}(\text{SeC}_6\text{F}_5)_2$, only $(\text{pyr})_2\text{Cd}(\text{SeC}_6\text{F}_5)_2$ has intramolecular stacking.

Thermolysis of the Zn, Cd, and Hg complexes led to the straightforward isolation of crystalline MSe products. While metal chalcogenolates have long been identified as suitable precursors to metal chalcogenides,³¹⁻³³ this study illustrates the utility of novel group 12 fluorinated selenolates in the isolation of solid-state ME.

4.6 References

- ¹ Brewer, M.; Khasnis, D.; Buretea, M.; Berardini, M.; Emge, T.J.; Brennan, J.G. Pyridine Coordination Complexes of the Divalent Ytterbium Chalcogenolates Yb(EPh)₂ (E = S, Se, Te). *Inorg. Chem.* **1994**, *33*, 2743.
- ² Berg, D.; Burns, C.J.; Andersen, R.A.; Zalkin, A. Electron-transfer reactions of divalent ytterbium metallocenes. Synthesis of the series [(Me₅C₅)₂Yb]₂[μ-E] (E = oxygen, sulfur, selenium, or tellurium) and crystal structure of [(Me₅C₅)₂Yb]₂[μ-Se]. *Organometallics* **1989**, *8*, 1865.
- ³ Lee J.; Freedman D.; Melman J.H.; Brewer M.; Sun L.; Emge T.J.; Long F.H.; Brennan J.G. Trivalent Lanthanide Chalcogenolates: Ln(SePh)₃, Ln₂(EPh)₆, Ln₄(SPh)₁₂, and [Ln(EPh)₃]_n (E = S, Se). How Metal, Chalcogen, and Solvent Influence Structure. *Inorg. Chem.* **1998**, *37*, 2512.
- ⁴ Tilley, T.D.; Andersen, R.A.; Spencer, B.; Zalkin, A. Crystal structure of bis(pentamethylcyclopentadienyl)bis(pyridine)ytterbium(II). *Inorg. Chem.* **1982**, *21*, 2647.
- ⁵ Banerjee, S.; Huebner, L.; Romanelli, M.; Kumar, G.A.; Riman, R.E.; Emge, T.J.; Brennan, J.G. Oxoselenido Clusters of the Lanthanides: Rational Introduction of Oxo Ligands and Near-IR Emission from Nd(III). *J. Am. Chem. Soc.* **2005**, *127*, 15900.
- ⁶ Britovsek, G. J. P.; Ugoletti, J.; White, A. J. P. From B(C₆F₅)₃ to B(OC₆F₅)₃: Synthesis of (C₆F₅)₂BOC₆F₅ and C₆F₅B(OC₆F₅)₂ and Their Relative Lewis Acidity. *Organometallics* **2005**, *24*, 1685.
- ⁷ Metz, M. V.; Sun, Y.; Stern, C. L.; Marks, T. J. Weakly Coordinating Al-, Nb-, Ta-, Y-, and La-Based Perfluoroaryloxymetalate Anions as Cocatalyst Components for Single-Site Olefin Polymerization. *Organometallics* **2002**, *21*, 3691.
- ⁸ Jolas, J. L.; Hoppe, S.; Whitmire, K. H. Oligomerization and Oxide Formation in Bismuth Aryloxides: Synthesis, Characterization, and Structures of [NaBi(OC₆F₅)₄(THF)]_∞ and Na₄Bi₂(μ₆-O)(OC₆F₅)₈(THF)₄. *Inorg. Chem.* **1997**, *36*, 3335.
- ⁹ Jones, C. M.; Burkart, M. D.; Bachman, R. E.; Serra, D. L.; Hwu, S. J.; Whitmire, K. H. Hypervalent bismuth alkoxide dimer complexes: syntheses, structures, and thermal decompositions of [Bi(OCH(CF₃)₂)₂(μ-OCH(CF₃)₂)(THF)]₂ and [Bi(OC₆F₅)₂(μ-OC₆F₅)X_n]₂·zY (X = Y = C₇H₈, n = 1, z = 1 or 2; X = THF, Y = C₆H₁₄, n = 2, z = 0 or 1). *Inorg. Chem.* **1993**, *32*, 5136.
- ¹⁰ Tremblay, T. L.; Ewart, S. W.; Sarsfield, M. J.; Baird, M. C. Solution structures and exchange phenomena of the new alkene polymerization initiators (η-C₅Me₅)TiMe(E)(μ-Me)B(C₆F₅)₃ (E = C₆F₅, OC₆F₅) and [(η-C₅Me₅)Ti(OC₆F₅)₂][BMe(C₆F₅)₃]. *Chem. Commun.* **1997**, *9*, 831.

- ¹¹ Campbell, C.; Bott, S. G.; Larsen, R.; Van Der Sluys, W. G. Preparation of Titanium Fluoroalkoxides by Alcoholysis of Titanium Alkoxides. *Inorg. Chem.* **1994**, 33, 4950.
- ¹² Amor, J. I.; Burton, N. C.; Cuenca, T.; Gomez-Sal, P.; Royo, P. Synthesis and characterization of new alkoxide and aryloxy derivatives of titanium and zirconium. X-ray molecular structure. *J. Organomet. Chem.* **1995**, 485, 153.
- ¹³ Abbott, R. G.; Cotton, F. A.; Falvello, L. R. Multiply bonded dimetal fluoroalkoxides. Pentafluorophenoxides of dimolybdenum and ditungsten. *Inorg. Chem.* **1990**, 29, 514.
- ¹⁴ Dilworth, J. R.; Gibson, V. C.; Redshaw, C.; White, A. J. P.; Williams, D. J. Molybdenum and tungsten mono-isodiazene complexes with alkyl ligands as ring-opening metathesis polymerisation precatalysts. Crystal and molecular structures of $[\text{Mo}(\text{CH}_2\text{CMe}_2\text{Ph})_3(\text{NNPh}_2)(\text{OC}_6\text{F}_5)]$, $[\text{W}(\text{CH}_2\text{SiMe}_3)_3(\text{NNPh}_2)(\text{OC}_6\text{F}_5)]$ and $[\text{WCl}_2(\text{NNPh}_2)(\text{OC}_6\text{F}_5)_2(\text{thf})]$. *J. Chem. Soc., Dalton Trans.: Inorg. Chem.* **1999**, 16, 2701.
- ¹⁵ Kim, M.; Zakharov, L. N.; Rheingold, A. L.; Doerrer, L. H. Synthesis and structural characterization of Groups 10 and 11 mononuclear fluoroaryloxy complexes. *Polyhedron* **2005**, 24, 1803.
- ¹⁶ Buzzeo, M. C.; Iqbal, A. H.; Long, C. M.; Millar, D.; Patel, S.; Pellow, M. A.; Saddoughi, S. A.; Smenton, A. L.; Turner, J. F. C.; Wadhawan, J. D.; Compton, R. G.; Golen, J. A.; Rheingold, A. L.; Doerrer, L. H. Homoleptic Cobalt and Copper Phenolate $\text{A}_2[\text{M}(\text{OAr})_4]$ Compounds: The Effect of Phenoxide Fluorination. *Inorg. Chem.* **2004**, 43, 7709.
- ¹⁷ Malik, M.; Azad, M.M.; O'Brien, P. Chalcogenolato-di-thiocarbamate-complexes of zinc: The X-ray single crystal structures of pyridine adducts. *Polyhedron* **1999**, 18, 1259.
- ¹⁸ Casagrandea, G.A.; Lang, E.S.; Manzoni de Oliveira, G.; Hörnera, M.; Broch, F. Dealing with 1,3-bis(4-nitrophenyl)triazene as intermediary ligand in the synthesis of polymeric $(\mu\text{-Se})\text{Hg}$ -clusters: One-pot synthetic procedures and X-ray structural characterization of $[(\text{PhSe})_7\text{Hg}_4\text{BrPy}]_n$. *Inorganica Chimica Acta* **2007**, 360, 1776.
- ¹⁹ Arnold, A.P.; Canty, A.J.; Skelton, B.W.; White, A.H. Mercury(II) selenolates. Crystal structures of polymeric $\text{Hg}(\text{SeMe})_2$ and the tetrameric pyridinates $[\{\text{HgCl}(\text{py})(\text{SeEt})\}_4]$ and $[\{\text{HgCl}(\text{py})_{0.5}(\text{SeBut})\}_4]$. *J. Chem. Soc., Dalton Trans.* **1982**, 3, 607.
- ²⁰ Subramanian, R.; Givindaswamy, N.; Santos, R.A. Single-Crystal, Solid-State, and Solution ^{113}Cd and ^{77}Se NMR and X-ray Single-Crystal Study of a $[\text{Cd}(\text{SeR})_2(\text{N-donor})_2]$ Complex. *Inorg. Chem.* **1998**, 37, 4929.
- ²¹ Secondo, P.M.; Land, J.M.; Baughman, R.G.; Collier, H.L. Polymeric octahedral and monomeric tetrahedral Group 12 pseudohalogeno (NCX^-) : $\text{X}=\text{O}, \text{S}, \text{Se}$ complexes of 4-(N,N-dimethylamino)pyridine. *Inorg. Chem. Acta* **2000**, 309, 13.

- ²² Cheng, Y.; Emge, T.J.; Brennan, J.G. Polymeric Cd(Se-2-NC₅H₄)₂ and Square Planar Hg(Se-2-NC₅H₄)₂: Volatile CVD Precursors to II-VI Semiconductors. *Inorg. Chem.* **1994**, *33*, 3711.
- ²³ Davidson, J. L.; Holz, B.; Leverd, P. C.; Lindsell, W. E.; Simpson, N. J. Reactions of monocyclopentadienyl complexes of molybdenum and tungsten with derivatives of phenols and pentafluorobenzeneselenol. *J. Chem. Soc., Dalton Trans.* **1994**, *24*, 3527.
- ²⁴ Kostiner, E.; Reddy, M. L. N.; Urch, D. S.; Massey, A. G. Perfluorophenyl derivatives of the elements XX. Some reactions of the bis(pentafluorophenyl)dichalcogenides. *J. Organomet. Chem.* **1968**, *15*, 383.
- ²⁵ Klapötke, T. M.; Krumm, B.; Polborn K. Synthesis, Chemistry, and Characterization of Perfluoroaromatic Selenium Derivatives. *Eur. J. Inorg. Chem.* **1999**, *8*, 1359.
- ²⁶ DeGroot M.W.; Corrigan, J.F. Coordination Complexes of Zinc with Reactive ESiMe₃ (E = S, Se, Te) Ligands. *Organometallics* **2005**, *24*, 3378.
- ²⁷ Lang, E.S.; Dias M.M.; Abram U.; Vazquez-Lopez E.M. Benzeneselenolates of Mercury(II). Crystal and Molecular Structures of [Hg(SePh)₂] and (Bu₄N)[Hg(SePh)₃]. *Anorg. Allg. Chem.* **2000**, *626*, 784.
- ²⁸ Lao, P.D.; Guo, Y.; Siu, G.G.; Shen, S. C. Optical-phonon behavior in Zn_{1-x}Mn_xSe: Zinc-blende and wurtzite structures. **1993**, *Phys. Rev. B.*, *48*, 11701.
- ²⁹ Freeman, D.K.; Mair, S.L.; Barnea, Z. The structure and Bijvoet ratios of cadmium selenide. *Acta Cryst.* **1977**, *A33*, 355.
- ³⁰ V. Leute, V.; Plate, H. *Ber. Bunsenges. Phys. Chem.* **1989**, *93*, 757.
- ³¹ Rao, C. N. R.; Gopalakrishnan, J. *New Directions in Solid State Chemistry*, Cambridge University Press: Cambridge, UK, **1986**, 116.
- ³² Jensen, J. A.; Gozum, J. E.; Pollina, D. M.; Girolami, G. S. Titanium, zirconium, and hafnium tetrahydroborates as "tailored" CVD precursors for metal diboride thin films. *J. Am. Chem. Soc.* **1988**, *110*, 1643.
- ³³ Brennan, J.G.; Siegrist, T.; Carroll, P. J.; Stuczynski, S. M.; Reynders, P.; Brus, L.E.; Steigerwald, M. L. Bulk and nanostructure Group II-VI compounds from molecular organometallic precursors. *Chem. Mater.* **1990**, *2*, 403.

Experimental

General Procedures:

All syntheses were carried out under high purity nitrogen (WELCO Praxair) using conventional drybox or Schlenk techniques. Solvents (Aldrich) were purified with a dual column Solv-Tek Solvent Purification System. Lanthanide metals, Hg metal, and Zn metal were purchased from Strem. Cd metal was purchased from J.T. Baker, and HSC_6F_5 was purchased from Aldrich. PhSeSePh was purchased from Acros and recrystallized from hexanes. $\text{Hg}(\text{SC}_6\text{F}_5)_2$ and $(\text{SeC}_6\text{F}_5)_2$ were prepared according to the literature procedures.^{1,2} Melting points were taken in sealed capillaries and are uncorrected. IR spectra were taken on a Thermo Nicolet Avatar 360 FTIR spectrometer and were recorded from 4000 to 600 cm^{-1} as a Nujol mull on NaCl plates, or from 4000 to 400 cm^{-1} using CsI plates. Electronic spectra were recorded on a Varian DMS 100S spectrometer with the samples in a 0.10 cm quartz cell attached to a Teflon stopcock. Single crystal XRD data were collected on a Bruker Smart APEX CCD diffractometer with graphite monochromatized Mo $K\alpha$ radiation ($\lambda = 0.71073 \text{ \AA}$). All crystals were immersed in Paratone oil and examined at low temperature, except for crystals of Nd_{28} which were loaded in 1.0 mm glass capillaries at room temperature. The data were corrected for Lorentz effects, polarization, and absorption. The latter by a multi-scan (SADABS)³ method. The structure was solved by direct methods (SHELXS86).⁴ All non-hydrogen atoms were refined (SHELXL97)⁵ based upon F_{obs}^2 . All hydrogen atom coordinates were calculated with idealized geometries (SHELXL97). Scattering factors (f_o , f' , f'') are as described in SHELXL97. Powder diffraction spectra were obtained from Bruker AXS D8 Advance diffractometer using Cu $K\alpha$ radiation. Elemental analyses were performed

by Quantitative Technologies, Inc. (Whitehouse Station, NJ). Absorption measurements were carried out with crystalline powder dissolved in THF using a double beam spectrophotometer (Perkin-Elmer Lambda 9, Wellesley, MA) in a 1 cm cuvette using THF as the reference solvent. The emission spectra of the crystalline samples were recorded by exciting the samples with the 800 nm band of a titanium-sapphire laser (Coherent, Inc., Santa Clara, CA) in the 90°-excitation geometry. The emission from the sample was focused onto a 0.55 m monochromator (Jobin Yvon, Triax 550, Edison, NJ) and detected by a thermoelectrically cooled InGaAs detector. The signal was intensified with a lock-in amplifier (SR 850 DSP, Stanford Research System, Sunnyvale, CA) and processed with a computer controlled by the Spectramax commercial software (GRAMS 32, Galactic Corp., Salem, NH). To measure the decay time, the laser beam was modulated by a chopper and the signal was collected on a digital oscilloscope (model 54520A, 500 MHz, Hewlett-Packard, Palo Alto, CA). The spectroscopic measurements and calculations were performed by Dr. Ajith Kumar and Dr. R. Riman from the Materials Science and Engineering Department at Rutgers University. XRD was performed by Dr. Thomas J. Emge from the Department of Chemistry and Chemical Biology at Rutgers University.

Computational Details (DFT) for $\text{Er}(\text{SeC}_6\text{F}_5)_3(\text{THF})_3$ and $(\text{THF})_3\text{Yb}(\text{SC}_6\text{F}_5)_3$

Courtesy of Karsten Krogh-Jespersen,⁶ electronic structure calculations have been carried out at the DFT⁷ level of theory with the PBE⁸ combination of exchange and correlation functionals. The SDD model MWB57 and MWB59 quasi-relativistic effective core potentials (ECPs) and corresponding valence basis sets [5s4p3d] were used to replace the inner electrons of Er and Yb,⁹ respectively. Inner-shell electrons on S and Se

atoms were also replaced by an SDD model ECP (MWB10 and MWB28, respectively)¹⁰ and, in addition to the standard [2s3p] valence basis set appropriate for these ECPs, each S or Se atom received a single set of d-type polarization functions (exponent = 0.496(S), 0.363(Se))¹¹. Oxygen atoms carried a Dunning-Huzinaga [3s,2p] basis set augmented by a set of polarization functions (exponent = 0.85) and a set of diffuse p-functions (exponent = 0.059)¹²; all C, F and H atoms carried valence double zeta quality Dunning-Huzinaga basis sets ([3s,2p] for C and F; [2s] for H)⁷. These choices of functionals, ECPs and basis sets from our basic computational model and entail 632 basis functions in calculations on the molecular compounds (THF)₃Er(SeC₆F₅)₃ and (THF)₃Yb(SC₆F₅)₃. Selected calculations were made modified basis sets as described in the text. Geometries were fully optimized on the potential energy surfaces and characterized further by normal mode analysis. Electronic population and bonding analyses were made within the NBO framework.¹³⁻¹⁵ All computational work was performed using the GAUSSIAN03¹⁶ software package.

Synthesis of (DME)₂Nd(SC₆F₅)₃:

Nd (0.144 g, 1.00 mmol) and Hg(SC₆F₅)₂ (0.895 g, 1.50 mmol) were combined in DME (ca. 20mL), and the mixture was stirred until the metal flakes were completely consumed and elemental mercury was visible in the bottom of the flask (overnight). The pale blue/green solution was filtered away from the mercury (0.247 g, 82%), and layered with hexane (ca. 20 mL) to give pale blue crystals (0.920g, 96%) which turn red at 140 °C and melt at 145°C. IR: 2949 (s), 2926 (s), 2844 (s), 2725 (w), 2394 (w), 2345 (w), 1883 (w), 1707 (w), 1619 (m), 1568 (w), 1508 (s), 1461 (s), 1380 (s), 1257 (m), 1187 (w), 1082 (m), 1030 (s), 960 (s), 866 (s), 721 (w) cm⁻¹. UVvis: This compound gives no

optical absorption maximum between 250 – 800nm. Anal.Calcd for $C_{26}H_{20}F_{15}NdO_4S_3$: C, 33.9; H, 2.2. Found: C, 34.7; H, 2.55.

Synthesis of $[(THF)_3Nd(SC_6F_5)_3]_2$:

Nd (0.144 g, 1.00 mmol) and $Hg(SC_6F_5)_2$ (0.895 g, 1.50 mmol) were combined in THF (ca. 20mL), and the mixture was stirred until the metal flakes were completely consumed and elemental mercury was visible in the bottom of the flask (overnight). The pale blue/green solution was filtered away from the mercury, and layered with hexane (ca. 20 mL) to give pale blue crystals (0.862, 90%) which turn an opaque white at 200 °C, melt at 250-255 °C and turn red at 255 °C. IR: 2923 (s), 2724 (w), 2357 (w), 1987 (w), 1709 (w), 1666 (w), 1622 (m), 1571 (w), 1463 (s), 1378 (s), 1264 (m), 1173 (m), 1121 (m), 1071 (s), 1007 (s), 971 (s), 916 (m), 857 (s), 722 (m), 665 (m) cm^{-1} . UVvis: The compound shows an optical absorption maximum at 591 nm in THF. Anal. Calcd for $C_{30}H_{24}F_{15}NdO_3S_3$: C, 37.6; H, 2.5. Found: C, 35.1; H, 2.97.

Synthesis of $DME_3Yb_4F_2O(OCH_2CH_2OCH_3)_2(SeSe)(SC_6F_5)_4 \cdot DME$:

Nd (0.144g, 1mmol) and $Hg(SC_6F_5)_2$ (0.895g, 1.5mmol) were combined in DME (~25ml) and the solution was stirred until all metal was consumed (2 days). In parallel, Yb (0.865g, 5mmol), $(SeC_6H_5)_2$ (2.339g, 7.5mmol), and Hg (0.05g) were combined in DME and the solution was stirred until all Yb metal was consumed. The pale blue Nd solution was then filtered into the as prepared orange/brown Yb solution. After 5 days stirring, the resultant solution is a dark orange/brown with a large amount of off white precipitate present. Se powder (1.061g, 13.44mmol) was added to the solution and

stirring continued. After 1.5 weeks, the dark brown solution is filtered and Layered 1:1 with hexanes. The filtered solution is a deep red color with a yellow hue. After 4 months, a small cluster of crystals were found and identified as the title complex by XRD. Alternatively, good yields of the title compound were produced by transferring the solution to a -50°C freezer 6 weeks after being layered 1:1 with hexanes, and being held at -50°C for 1 month.

Synthesis of $(C_5H_5N)_{36}Pr_{28}F_{68}(SePh)_{16} \cdot 16(C_5H_5N)$:

Pr (0.141 g, 1.00 mmol), $Se_2(C_6H_5)_2$ (0.468 g, 1.50 mmol), and Mercury (ca. 25 mg) were combined in Pyridine (ca. 35mL). The mixture was stirred at room temperature until the metal powder was completely consumed (~1 day). To the pale yellow/green solution, NH_4F was added (0.740 g, 2.00 mmol) and again the solution was stirred. After ~1 week the solution was filtered, concentrated to ca. 15mL and held at -5°C for one day, affording small colorless lathes (range of mg corresponding to the range in yields; (42-84 mg, 10-22%). Single crystals of $(C_5H_5N)_{36}Pr_{28}F_{68}(SePh)_{16} \cdot 16(C_5H_5N)$ turn orange at 77°C and melt completely at 195°C. IR: 2949 (s), 2904 (s), 2847 (s), 2716 (w), 2671 (w), 2357 (w), 2328 (w), 1597 (w), 1568 (w), 1458 (s), 1376 (s), 1299 (w), 1217 (w), 1148 (w), 1070 (w), 1033 (w), 739 (m), 702 (m) cm^{-1} . UVvis: This compound gives an optical absorption maximum at 359nm. Anal Calcd. for $C_{346}H_{330}F_{68}N_{50}Se_{16}Pr_{28}$: C, 35.3(26.9); H, 2.84(2.19); N, 5.99(3.48) (values in parentheses are with loss of lattice solvent). Found: C, 28.4; H, 2.71; N, 3.49.

Synthesis of $(\text{C}_5\text{H}_5\text{N})_{36}\text{Nd}_{28}\text{F}_{68}(\text{SePh})_{16} \cdot 16(\text{C}_5\text{H}_5\text{N})$:

Nd (0.144 g, 1.00 mmol), $\text{Se}_2(\text{C}_6\text{H}_5)_2$ (0.468 g, 1.50 mmol), and Mercury (ca. 28 mg) were combined in Pyridine (ca. 35mL). The mixture was stirred at room temperature until the metal flakes were completely consumed (~2 days). To the pale blue/green solution, NH_4F was added (0.740 mg, 2.00 mmol) and again the solution was stirred. After a minimum of 2 weeks, the solution turned brown/orange at which time it was filtered and crystallized one of two ways. The first method is concentration of the filtered solution to ~20 mL followed by layering with Hexanes in a 1:1 ratio. This method gives larger almost block-like yellow lathes in low yields (7-15%). The second crystallization method is more direct and involves concentrating the filtered solution to ~15 mL and cooling at -5°C for one day, affording smaller colorless lathes also in poor yields (42-84 mg, 9-20%). The latter crystallization method proved necessary to obtain single crystals of XRD quality for absolute structure determination while the former produced crystals with lattice defects allowing only for the determination of the unit cell. Single crystals of $(\text{C}_5\text{H}_5\text{N})_{36}\text{Nd}_{28}\text{F}_{68}(\text{SePh})_{16} \cdot 16(\text{C}_5\text{H}_5\text{N})$ begin to melt at 200°C , turn black at 233°C and melt completely at 305°C . IR: 2953 (s), 2917 (s), 2847 (s), 2725 (w), 2663 (w), 2361 (w), 2336 (w), 11593 (w), 1568 (w), 1458 (m), 1376 (m), 1298 (w), 1143 (w), 1070 (w), 730 (m), 690 (m) cm^{-1} . Anal Calcd. For $\text{C}_{346}\text{H}_{330}\text{F}_{68}\text{N}_{50}\text{Se}_{16}\text{Nd}_{28}$: C, 35.2(26.6); H, 2.82(2.17); N, 5.94(3.45). Found: C, 34.0; H, 2.45; N, 3.45. (values in parentheses are with loss of lattice solvent).

Synthesis of $[(\text{pyr})_{24}\text{Ce}_{28}\text{F}_{68}(\text{SePh})_{16}]^{3+} [\text{Ce}_3(\text{SeC}_6\text{H}_5)_{10}]^{1-}_3$:

Ce(1.00 mmol), $\text{Se}_2(\text{C}_6\text{H}_5)_2$ (1.50 mmol), and Mercury (ca. 25 mg) were combined in Pyridine (ca. 35mL). The mixture was stirred at room temperature until the metal powder was completely consumed (~1 day). To the pale yellow solution, NH_4F was added (2.00 mmol) and again the solution was stirred. After ~2 weeks the solution was filtered, concentrated to ca. 15mL and held at -5°C for one day, affording small colorless lathes in poor yields (<15%).

Synthesis of $(\text{pyr})_2\text{Zn}(\text{SeC}_6\text{F}_5)_2$:

Zn (0.065 g, 0.993 mmol), Hg (0.020g, 0.099 mmol) and $\text{Se}_2(\text{C}_6\text{F}_5)_2$ (0.492 g, 1.00 mmol) were combined in pyridine (ca. 25 mL), and the mixture was stirred at room temperature for 10 days. The solution was filtered, concentrated to ~5 mL, and held at -5°C to give near colorless lathes (0.604 g, 85 % yield) that begin to melt at 154°C and melt completely at 163°C . IR: 2921 (s), 2717 (w), 2357(w), 1605 (m), 1507 (m), 1462 (s), 1372 (s), 1217 (w), 1070 (m), 964 (m), 813(m), 718 (m), 637 (w), 420 (w) cm^{-1} . UVvis: This compound gives a broad optical absorption maximum at 477 nm. Anal. Calcd for $\text{C}_{22}\text{H}_{10}\text{N}_2\text{F}_{10}\text{ZnSe}_2$: C, 36.9; H, 1.40; N, 3.91. Found: C, 36.7; H, 1.42; N, 3.90. ^1H NMR (399.89 MHz, acetone- d_6 ; δ , ppm): 8.76-8.78 (dd), 8.17-8.28 (tt), 7.74-7.77 (dt). ^{19}F NMR (376.22 MHz, acetone- d_6 ; δ , ppm): -121.08 - -121.18 (dd, 2F), -158.50 - -158.6 (t, 1F), -160.94 - -161.10 (tt, 2F). ^{77}Se NMR (76.28 MHz, pyridine- d_5 ; δ , ppm) 476.6 (s) (vs PhSeSePh at 468.0 ppm as an external standard). ESI-MS: m/z 738 (MNa^+), m/z 494 ($\text{F}_5\text{C}_6\text{Se-SeC}_6\text{F}_5^+$), m/z 247 (SeC_6F_5^+).

Synthesis of (pyr)₂Cd(SeC₆F₅)₂:

Cd (0.056 g, 0.498 mmol) and Se₂(C₆F₅)₂ (0.245 g, 0.498 mmol) were combined in pyridine (ca. 25 mL), and the mixture was stirred at room temperature for one week. The solution was filtered, concentrated to ~5 mL, and held at -5 °C to give colorless plates (0.239 g, 63 % yield), that begin to melt at 150 °C and melt completely at 175°C. IR: 2900 (s), 1602 (m), 1510 (m), 1504 (m), 1462 (s), 1459 (s), 1376 (s), 1264 (w), 1037 (w), 1010 (w), 814(m), 693 (m), 629 (w), 463 (w) cm⁻¹. This compound gives no absorption maximum between 320 – 800 nm. Anal. Calcd for C₂₂H₁₀N₂F₁₀CdSe₂: C, 34.6; H, 1.32; N, 3.67. Found: C, 34.5; H, 1.51; N, 3.54. ¹H NMR (499.77 MHz, DMSO-d₆; δ, ppm): 8.64-8.62 (m), 7.46-7.43 (tt), 7.32-7.18 (m). ¹⁹F NMR (470.25 MHz, DMSO-d₆; δ, ppm): -124.62 - -124.66 (d, 2F), -163.37 - -163.46 (t, 1F), -165.16 - -165.26 (t, 2F).

Synthesis of Hg(SeC₆F₅)₂:

Hg (0.100 g, 0.498 mmol) and Se₂(C₆F₅)₂ (0.245 g, 0.497 mmol) were combined in Pyridine (ca. 25 mL), and the mixture was stirred at room temperature for one week. The solution was filtered, and brought to dryness. The solid was washed with hexanes, re-dissolved in ~8 mL toluene, and heated to 60°C for 30 minutes before cooling back to room temperature. The solution was then held at -5°C for 1 week to give colorless needles (0.215 g, 62% yield) that melt at 115°C. IR: 2850 (s), 1598 (m), 1505 (m), 1499 (m), 1458 (s), 1455 (s), 1372 (s), 1040 (w), 1001 (w), 812(m), 682 (m), 631 (w), 457 (w) cm⁻¹. This compound gives no optical absorption maximum between 320 – 800nm. Anal.

Calcd for $C_{12}F_{10}HgSe_2$: C, 20.8; Found: C, 20.3. ^{19}F NMR (470.25 MHz, DMSO- d_6 ; δ , ppm): -125.15 - -125.28 (dd, 2F), -158.05 - -158.14 (t, 1F), -162.89 - -163.02(m, 2F).

Thermolysis of $Hg(SeC_6F_5)_2$, $(pyr)_2Cd(SeC_6F_5)_2$, and $(pyr)_2Zn(SeC_6F_5)_2$:

20mg of $(pyr)_2Zn(SeC_6F_5)_2$ was placed in a quartz thermolysis tube that was sealed under vacuum, and the sample end was placed into a model 847 Lindberg tube furnace. The “cold” end of the quartz tube was held at -196 °C by means of immersing it in liquid nitrogen. The sample was heated to 650 °C at a ramp rate of 10°C/min, then held at 650°C for 5 h at which time it was cooled to 25°C at a rate of 3.5°C/min. The black powder that was formed at the sample end of the quartz tube was identified as cubic ZnSe (2003 JCPDS Card number 88-2345). A volatile, polycrystalline thermolysis product was found at the cold region of the quartz tube, and was identified as $Se(C_6F_5)_2$ with GC-MS.

10mg of $(pyr)_2Cd(SeC_6F_5)_2$ was placed in a quartz thermolysis tube, sealed under vacuum, and the sample end was placed into a model 847 Lindberg tube furnace. The “cold” end of the glass tube was held at -196 °C by means of immersing it in liquid nitrogen. The sample was heated to 650 °C at a ramp rate of 10°C/min, then held at 650°C for 133minutes at which time it was cooled to 25°C at a rate of 5°C/min. The dark powder that was formed was found to be a mixture of hexagonal CdSe (2003 JCPDS Card number 77-0021) and an amorphous component, possibly Cd(s). The volatile product, a yellow crystalline material, was found to be $Se_2(C_6F_5)_2$ by single crystal XRD, and its melting point of 61°C matches well with that of the starting ligand $Se_2(C_6F_5)_2$, M.P. = 59-60°C).

10mg of $\text{Hg}(\text{SeC}_6\text{F}_5)_2$ was placed in a quartz thermolysis tube, sealed under vacuum, and the sample end was placed into a model 847 Lindberg tube furnace. The “cold” end of the glass tube was held at $-196\text{ }^\circ\text{C}$ by means of immersing it in liquid nitrogen. The sample was heated to $650\text{ }^\circ\text{C}$ at a ramp rate of $10^\circ\text{C}/\text{min}$, then held at 650°C for 5 h at which time it was cooled to 25°C at a rate of $3.5^\circ\text{C}/\text{min}$. The resultant dark powder formed upon deposition at the region of the tube furnace where the quartz sample tube exited the alumina furnace tube. The powder was identified as cubic HgSe by XRPD (2003 JCPDS Card number 65-4590), and the volatile product was identified as $\text{Se}(\text{C}_6\text{F}_5)_2$.

Synthesis of $(\text{THF})_3\text{Sm}(\text{SeC}_6\text{F}_5)_3$:

Sm (0.075 g, 0.500 mmol), $(\text{SeC}_6\text{F}_5)_2$ (0.369 g, 0.750 mmol), and Mercury (0.028g) were combined in THF (ca. 20mL). The mixture was stirred until the metal flakes were completely consumed (5 days). The pale yellow/orange solution was filtered, and concentrated to ~5ml. After being held at room temperature for 1 day, the solution was cooled at -5°C for one day and then layered with hexanes (ca. 15 mL) to give small crystalline rods. After 6 days, a final yield of pale orange rods (~0.331g, ~60%) was collected. The crystals begin to melt at $125\text{ }^\circ\text{C}$ and at $131\text{ }^\circ\text{C}$ give a red liquid. IR: 2974 (s), 2876 (s), 1699 (w), 1634 (m), 1614 (m), 1548 (w), 1503 (s), 1470 (s), 1258 (m), 1074 (s), 1001 (s), 960 (s), 911 (s), 858 (s), 809 (s), 661 (m), 612 (w), 494 (w) cm^{-1} . UVvis: This compound shows no optical absorption maxima between 350–800 nm. Anal.Calcd for $\text{C}_{30}\text{H}_{24}\text{F}_{15}\text{O}_3\text{Se}_3\text{Sm}$: C, 32.61; H, 2.19. Found: C, 31.66; H, 2.24.

Synthesis of (THF)₃Er(SeC₆F₅)₃:

Er (0.084 g, 0.500mmol), (SeC₆F₅)₂ (0.369 g, 0.750 mmol) and Mercury (0.026g) were combined in THF (ca. 20mL), and the mixture was stirred until the metal flakes were completely consumed (8 days). The pale pink solution was filtered, and concentrated to ~5ml. The solution was held at -5°C for two days, brought up to room temperature, and layered 2:1 with hexanes to give a good yield (~0.421g, ~75%) of pale pink lathes which melt at 153 °C. IR: 2958 (s), 1634 (w), 1605 (w), 1531 (w), 1507 (s), 1474 (s), 1254 (m), 1070 (s), 960 (s), 809 (s), 669 (m), 604 (w), cm⁻¹. UVvis: For a 0.104M THF solution with a 1mm path length, this compound gives absorption maxima at 655(2.04 L·mol⁻¹·cm⁻¹), 547(1.29 L·mol⁻¹·cm⁻¹), 523(27.21 L·mol⁻¹·cm⁻¹), 490(3.31 L·mol⁻¹·cm⁻¹), 453 (2.99 L·mol⁻¹·cm⁻¹), 409(8.62 L·mol⁻¹·cm⁻¹), and 380(75.24 L·mol⁻¹·cm⁻¹) nm, with molar absorptivity given in parenthesis. These absorption peaks correspond to the ⁴F_{9/2}, ⁴S_{3/2}, ²H_{11/2}, ⁴F_{7/2}, ⁴F_{5/2,3/2}, ²G_{9/2}, and ⁴G_{11/2} transitions typically seen from the ⁴I_{15/2} ground state of Er³⁺ (Fig 56). Anal.Calcd for C₃₀ H₂₄ F₁₅ O₃ Se₃ Er: C, 32.12; H, 2.16. Found: C, 31.63; H, 1.97.

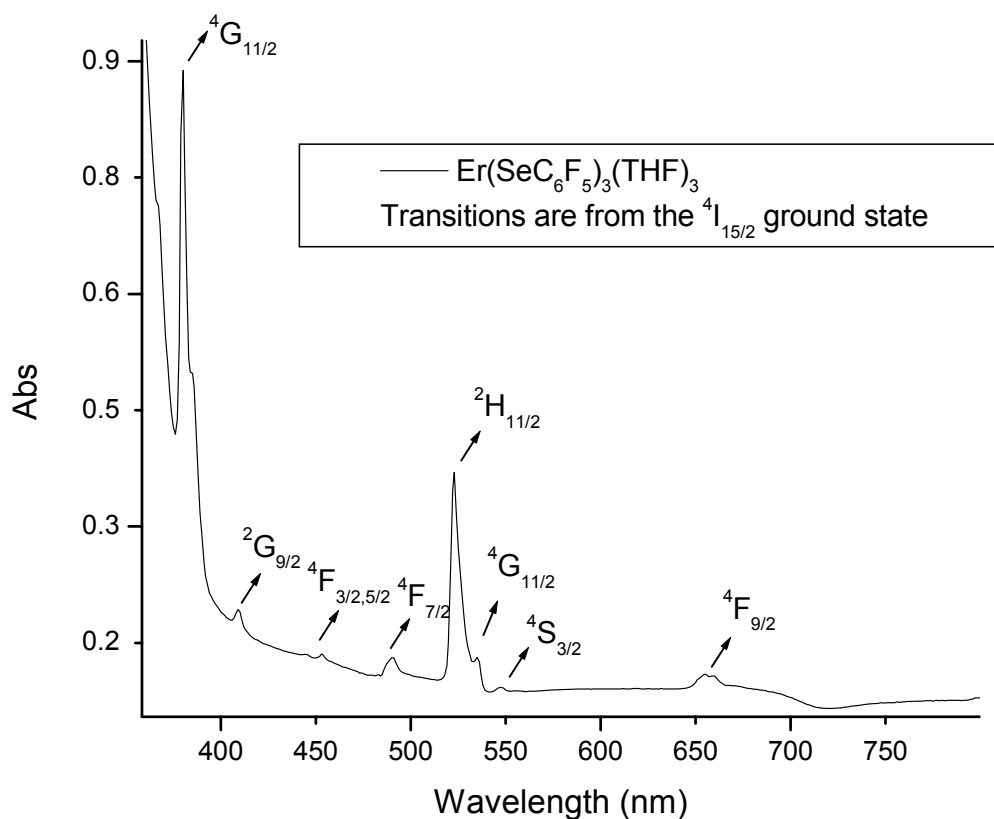


Fig 56. Visible Absorption spectrum for $\text{Er}(\text{SeC}_6\text{F}_5)_3(\text{THF})_3$

Synthesis of $(\text{THF})_3\text{Nd}(\text{SeC}_6\text{F}_5)_3$:

Nd (0.064 g, 0.444mmol), $(\text{SeC}_6\text{F}_5)_2$ (0.328 g, 0.666 mmol) and Mercury (0.030g) were combined in THF (ca. 30mL), and the mixture was stirred until the metal flakes were completely consumed (4 days). The pale blue/green solution was filtered, concentrated to ~5ml, and held at -30°C overnight. The solution was then brought up to room temperature, and layered 2:1 with hexanes to give a good yield (~0.312g, ~64%) of pale blue lathes which begin to melt at 147°C and melt completely at 153°C . IR: 2954 (s), 2898(s), 1634 (w), 1609 (w), 1503 (s), 1474 (s), 1258 (s), 1074 (s), 1012(s), 964 (s),

813 (s), 665 (m), 608 (w), and 465 (w) cm^{-1} . UVvis: For a 0.172M THF solution with a 1mm path length, this compound gives absorption maxima at 884(3.70 $\text{L}\cdot\text{mol}^{-1}\cdot\text{cm}^{-1}$), 809(9.77 $\text{L}\cdot\text{mol}^{-1}\cdot\text{cm}^{-1}$), 752(6.56 $\text{L}\cdot\text{mol}^{-1}\cdot\text{cm}^{-1}$), 685(0.511 $\text{L}\cdot\text{mol}^{-1}\cdot\text{cm}^{-1}$), 592(46.7 $\text{L}\cdot\text{mol}^{-1}\cdot\text{cm}^{-1}$), 531(7.87 $\text{L}\cdot\text{mol}^{-1}\cdot\text{cm}^{-1}$), and 519(3.24 $\text{L}\cdot\text{mol}^{-1}\cdot\text{cm}^{-1}$)nm, with molar absorptivity given in parenthesis. These absorption peaks correspond to the $^4\text{F}_{3/2}$, $^4\text{F}_{5/2}$, $^4\text{S}_{3/2}$, $^4\text{F}_{9/2}$, $^4\text{G}_{5/2}$, $^4\text{G}_{7/2}$ and $^4\text{G}_{9/2}$ transitions typically seen from the $^4\text{I}_{9/2}$ ground state of Nd^{3+} (Fig 57).
 Anal.Calcd for $\text{C}_{30}\text{H}_{24}\text{F}_{15}\text{O}_3\text{Se}_3\text{Nd}$: C, 32.79; H, 2.20. Found: C, 32.08; H, 1.99.

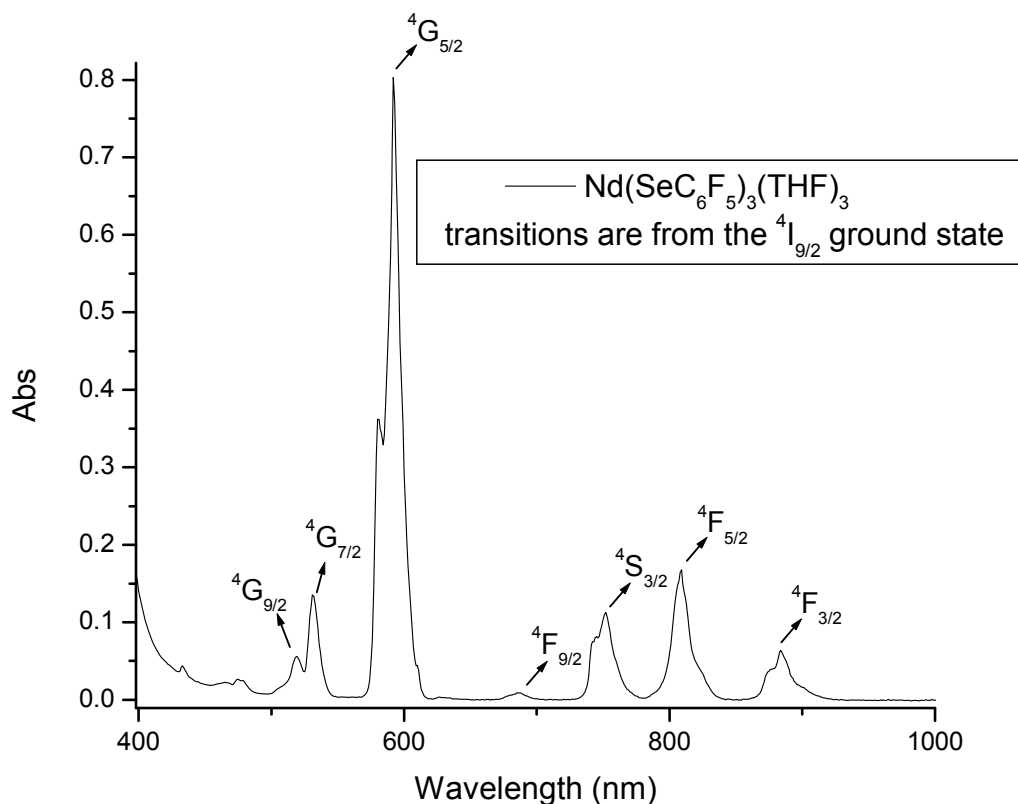


Fig 57. Visible Absorption spectrum for $\text{Nd}(\text{SeC}_6\text{F}_5)_3(\text{THF})_3$

Synthesis of (pyr)₄Yb(SeC₆F₅)₃·pyr:

Yb (0.086 g, 0.500 mmol), (SeC₆F₅)₂ (0.369g, 0.750 mmol) and Mercury (0.025g) were combined in pyridine (ca. 25mL), and the mixture was stirred until the metal flakes were completely consumed (2 days). The deep red solution was filtered, concentrated to ~5ml, and layered 3:1 with hexanes to give a good yield (~0.588g, ~90%) of deep red rods which begin to melt at 98°C and completely melt at 122°C. IR: 3068 (m), 2966 (m), 2872 (m), 1634 (w), 1601 (m), 1495 (s), 1470 (s), 1622 (m), 1571 (w), 1463 (s), 1378 (s), 1264 (m), 1173 (m), 1121 (m), 1071 (s), 1007 (s), 1442 (m), 1262(w), 1217(w), 1078(m), 968 (s), 813 (m), 751 (w), 694 (w), and 416 (w) cm⁻¹. UVvis: This compound shows a broad absorption maximum at 480 nm in pyridine. Anal.Calcd for C₄₃ H₂₅ F₁₅ N₅ Se₃ Yb: C, 38.39; H, 1.79; N, 4.97. Found: C, 38.39; H, 1.92; N, 5.17.

Synthesis of [(CH₃)₄N]⁺[SeC₆H₅]⁻:

In an attempt to synthesize a (C₅H₅N)₃₆Ce₂₈F₆₈(SePh)₁₆·26(C₅H₅N) analog to the previously isolable Ln₂₈ clusters, [(CH₃)₄N]⁺[SeC₆H₅]⁻ was obtained by combining Ce (0.140 g, 1.00mmol), Se₂(C₆H₅)₂ (0.468 g, 1.50 mmol), and Mercury (ca. 25 mg) in Pyridine (ca. 20mL). The mixture was stirred at room temperature until the metal powder was completely consumed (~2 days). To the olive green solution with fine grey powder, [(CH₃)₄N]F was added (74 mg, 2.0 mmol) and again the solution was stirred. After 2 weeks the lime green solution with grey powder was filtered as a yellow solution, and layered 1:1 with hexanes. After ~3 weeks, the reaction afforded colorless rods determined to be the title salt by XRD (Fig 58).



Fig 58. Wire Frame Illustration of isolated $[(\text{CH}_3)_4\text{N}]^+[\text{SeC}_6\text{H}_5]^-$

Synthesis of $[\text{Nd}_6\text{O}_2(\text{Se})_4(\text{SeC}_6\text{F}_5)_6(\text{THF})_{10}][\text{Hg}(\text{SeC}_6\text{F}_5)_2]_2 \cdot 2\text{THF}$:

In an attempt to isolate $(\text{THF})_3\text{Nd}(\text{SeC}_6\text{F}_5)_3$, Nd (0.064 g, 0.444mmol), $(\text{SeC}_6\text{F}_5)_2$ (0.328 g, 0.666 mmol) and Mercury (0.030g) were combined in THF (ca. 30mL). The mixture was stirred until the metal flakes were completely consumed (4 days). The dark green solution was filtered, and mixed dropwise with hexanes until precipitate began to form. The saturated solution was filtered a second time, and held at -30°C for 5 days after which a crystalline powder was present. From this powder, single crystals of the title compound were recrystallized (Fig 59).

Synthesis of $[\text{Nd}_3(\text{SePh})_9(\text{THF})_4]_n \cdot 2.5\text{THF}$:

In an attempt to synthesize $(\text{C}_5\text{H}_5\text{N})_{36}\text{Nd}_{28}\text{F}_{68}(\text{SePh})_{16}\cdot 26(\text{C}_5\text{H}_5\text{N})$ using NdF_3 as the fluoride source, Nd (0.144 g, 1.00 mmol), $\text{Se}_2(\text{C}_6\text{H}_5)_2$ (0.468 g, 1.50 mmol), and Mercury (ca. 20 mg) were combined in THF (ca. 30mL). The mixture was stirred at room temperature until the metal flakes were completely consumed (1 day). To the pale blue/green solution, white crystalline NdF_3 was added, and after one day a fine grey powder was present in the blue/green solution. After one month, the precipitate remained, and when settled, the solution was an emerald green. The solution was filtered and layered 1:1 with hexanes to afford colorless crystals of the title compound (Figs 60 & 61).

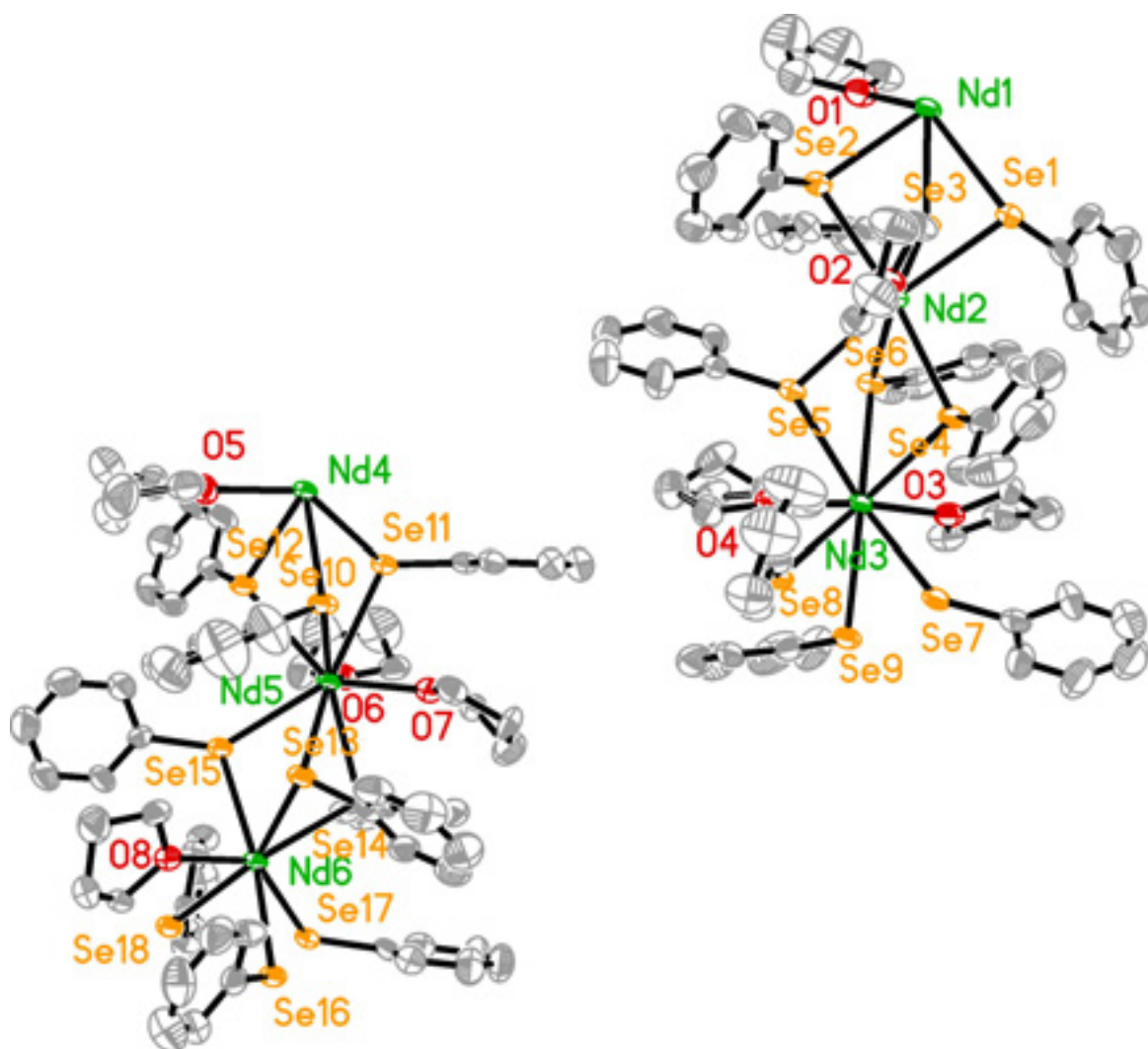


Fig 60. ORTEP of $[\text{Nd}_3(\text{SePh})_9(\text{THF})_4]_n \cdot 2.5\text{THF}$.

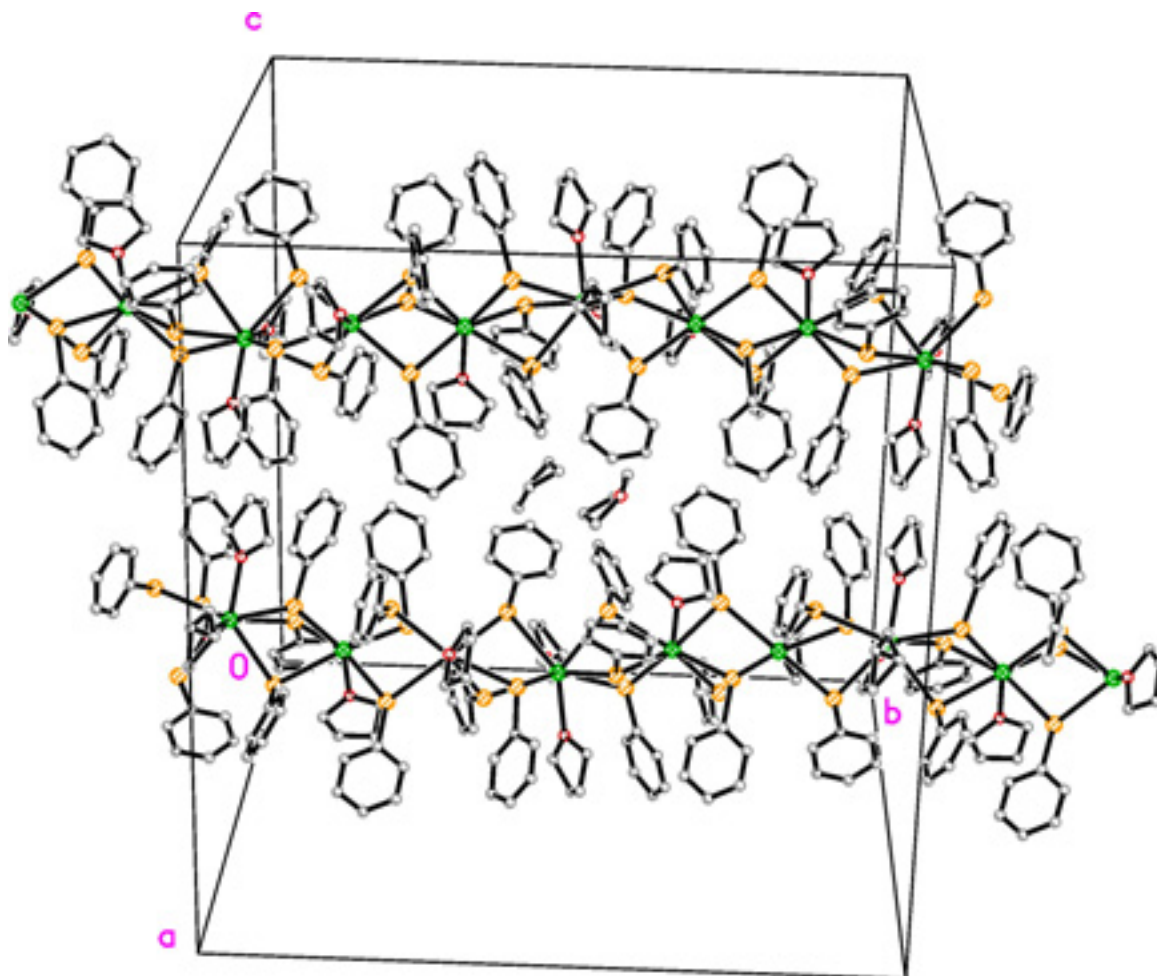


Fig 61. ORTEP of $[\text{Nd}_3(\text{SePh})_9(\text{THF})_4]_n \cdot 2.5\text{THF}$ unit cell packing.

Attempted Synthesis of diamagnetic $(\text{THF})_{36}\text{La}_{28}\text{F}_{68}(\text{SePh})_{16} \cdot 26(\text{C}_5\text{H}_5\text{N})$

La (0.139 g, 1.00 mmol), $\text{Se}_2(\text{C}_6\text{H}_5)_2$ (0.468 g, 1.50 mmol), and Mercury (ca. 25 mg) were combined in Pyridine (ca. 30mL). The mixture was stirred at room temperature until the metal powder was completely consumed (~4 days), after which NH_4F was added. After five months, the pale green solution continued to have a large amount of light grey precipitate present, so it was filtered and concentrated to ~8ml. After being held at -30°C for one week, the solution was concentrated to dryness and powder XRD

was performed on the solute. The resultant diffraction pattern was compared to a generated powder pattern of a representative Ln_{28} cluster (Fig 62). Results were inconclusive.

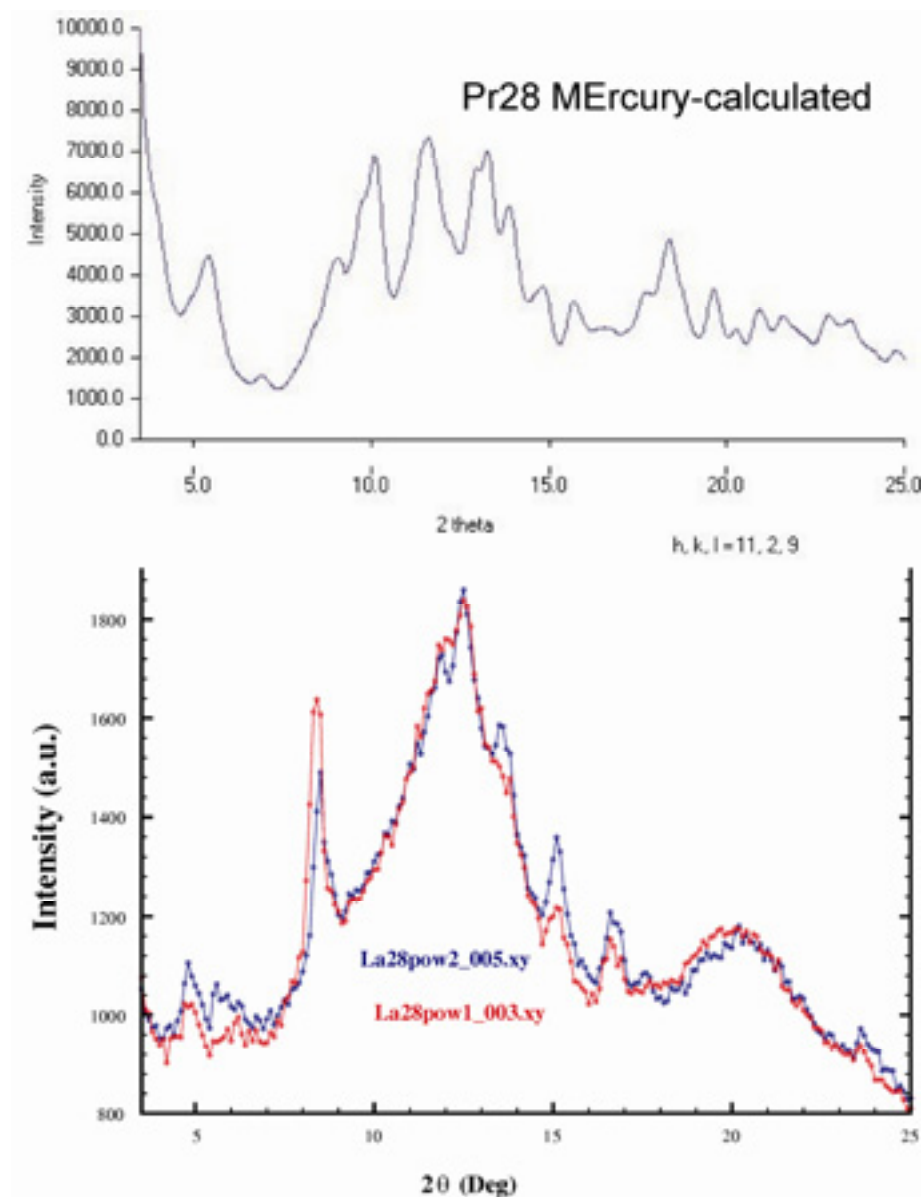


Fig 63. Comparison of calculated powder pattern for $(\text{THF})_{36}\text{Pr}_{28}\text{F}_{68}(\text{SePh})_{16} \cdot 26(\text{C}_5\text{H}_5\text{N})$ with experimental powder pattern of $(\text{THF})_{36}\text{La}_{28}\text{F}_{68}(\text{SePh})_{16} \cdot 26(\text{C}_5\text{H}_5\text{N})$ reaction product.

Synthesis of $[\text{NdI}_2(\text{pyr})_4]^+[(\text{NH}_4)\text{I}_2(\text{pyr})_4]^-$

Nd (0.144g, 1.00 mmol), I_2 (0.380g, 1.50 mmol), and Hg (0.025g) were combined in pyr (ca. 50mL), and the mixture was stirred until the metal flakes were completely consumed and elemental mercury was visible in the bottom of the flask (overnight). To the orange/red solution, NH_4F (0.074g) was added. After 5 days, the solution was near colourless with a light brown precipitate present. Stirring continued for 3 months, filtered, and concentrated to 30ml. The solution was cooled to -5°C , and after a month gave a poor yield of small colorless lathes of the title compound.

Reaction of $\text{Eu}(\text{SePh})_2/\text{NH}_4\text{F}/\text{pyr}/\text{Hg}$:

Eu (1mmol), $(\text{SePh})_2$ (1mmol), and Hg (0.025g) were combined in pyr (~30ml). The solution was orange after 1 day with all metal dissolved. NH_4F was added, and after 3 days, the solution turned a pale yellow/brown color with a fine powder present. After 3 days, the solution was filtered and layered 1:1 with hexanes, but afforded no crystalline product.

Reaction of $\text{Nd}(\text{SePh})_3(\text{L})_x$ with HgF_2 (L =pyr, THF, or DME):

To a blue/green solution of $\text{Nd}(\text{SePh})_3(\text{L})_x$ (1mmol), HgF_2 either (1mmol or 0.5mmol) was added and the solution was stirred for 1 month. After one week, all of the respective solutions formed yellow oils. The solutions were filtered and layered 1:1 with hexanes. Only orange/yellow oils were present in these reactions.

Reactions of $\text{Ln}(\text{EPh})_x(\text{L})_y/\text{CsF}$ ($\text{L}=\text{Ce}$, Nd , or Yb ; $\text{E} = \text{Se}$ or S ; $\text{L} = \text{THF}$, DME , or Pyr):

In situ prepared $\text{Ln}(\text{EPh})_x(\text{L})_y$ (1mmol) was prepared for the respective metal complexes. After all metals were dissolved in their respective solutions, CsF (2mmol) was added to each. The only noticeable change for any of the reactions was that for all, the solutions lost color intensity after addition of the CsF and a light colored precipitate formed. The only crystalline product isolated, $[\text{CsSePh}]_n$, was when $\text{Ln} = \text{Yb}$, $\text{E} = \text{Se}$, $x=3$, and $\text{L} = \text{DME}$.

Synthesis of $[\text{CsSePh}]_n$ 2D Polymer

In an attempt to use CsF as a direct fluoride source, the title compound was prepared. Yb (1mmol), $(\text{SePh})_2$ (1.5mmol), and Hg (0.025g) were combined in DME . After all metal was in solution, CsF (2 mmol) was added to the red solution. After 1 week, the solution turns pale yellow, with off-white precipitate present in large quantities. After sitting for three months, the unfiltered solution has colourless lathes present. XRD determined these lathes to be $[\text{CsSePh}]_n$ (Fig 64).

Reaction of $\text{Ce}/(\text{Me})_4\text{NF}/\text{SePh}/\text{pyr}$:

Ce (1mmol), $(\text{SePh})_2$ (1.5mmol), and Hg (0.025g) were combined in pyridine. The solution was stirred until all metal was consumed (2 days). $(\text{Me})_4\text{NF}$ (2 mmol) was added to the olive green solution, After 2 weeks, the solution was a lime green color with grey precipitate. The solution was filtered, and layered 1:1 with hexanes. A poor yield of color rods were identified as $[(\text{Ph})_2\text{Se}]^-[(\text{Me})_4\text{N}]^+$.

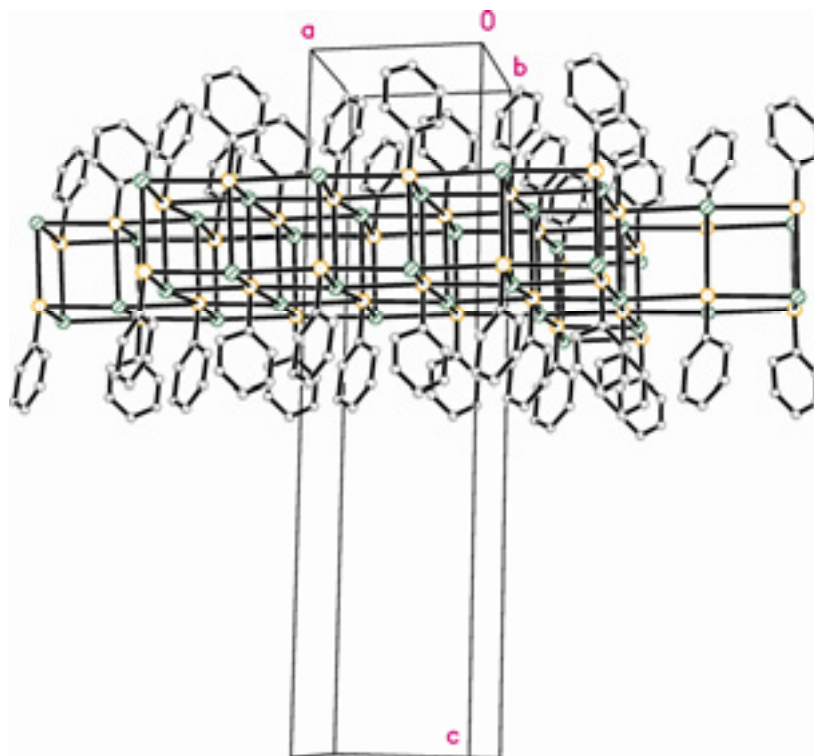


Fig 64. ORTEP of $[\text{CsSePh}]_n$ unit cell.

Reaction of CeF_3/pyr :

To see if pyr is able to disrupt the LnF_3 lattice, CeF_3 (1mmol) was added to ~30ml pyr and the solution was stirred. After heating for 2 days at 100°C , the solution was filtered and concentrated to dryness. There was unidentified precipitate present, but in very small yield.

Reaction of $\text{Ce}(\text{SePh})_3/\text{CeF}_3/\text{pyr}/\text{Hg}$:

Ce (1mmol), $(\text{SePh})_2$ (1.5mmol), and Hg (0.025g) were combined and the reaction was stirred until all metal was in solution (3 days). CeF_3 was added to the olive green solution, and after 1 week, the solution turned a yellow green, and had fine grey

precipitate present. The white powder of CeF_3 was not seen. The solution was filtered, and layered 1:1 with hexanes, but afforded no crystalline product.

Reaction of $\text{Nd}(\text{SePh})_3/\text{NdF}_3/\text{L}/\text{Hg}$ (L=THF, DME, or pyr):

Nd (1mmol), $(\text{SePh})_2$ (1.5mmol), and Hg (0.025g) were combined and the reaction was stirred until all metal was in solution (3 days), after which NdF_3 (1.4mmol) was added. In THF and pyr, the blue/green colored solutions did not change color, but there was a fine grey precipitate present after 3 days. In DME, after one month, the settled solution was a brown/orange color with a fine grey precipitate present. All three reactions were filtered and layered 1:1 with hexanes. Only when L=THF was $[\text{Nd}_3(\text{SePh})_9(\text{THF})_5]_n$ isolated.

Reaction of $\text{Nd}(\text{TePh})_3/\text{NdF}_3/\text{Pyr}/\text{Hg}$:

Nd (1mmol), $(\text{TePh})_2$ (1.5mmol), and Hg (0.025g) were combined and the reaction was stirred until all metal was in solution (~2weeks), after which NdF_3 (1.4mmol) was added. The solution was a deep red color with fine grey precipitate. The solution was filtered after 9 days, and layered 1:1 with hexanes. After 3 months, the solution had crystalline material and was held at -5°C for 2 months, after which unidentified colourless lathes were present.

Reaction of $\text{Nd}(\text{SPh})_3/\text{NdF}_3/\text{L}/\text{Hg}$ (L=THF,DME, or pyr)

Nd (1mmol), $(\text{SPh})_2$ (1.5mmol), and Hg (0.025g) were combined, and the reaction was stirred until all metal was in solution (3 days), after which NdF_3 (1.4mmol) was

added. When $L = \text{DME}$, the solution was near colourless after 1 week, with a large amount of grey precipitate. The solution was heated to $\sim 50^\circ\text{C}$ for 5 days with no change in the solution color. The solution was filtered, and layered 1:1 with hexanes, but only gave an unidentified pale blue suspension. When $L = \text{THF}$ or pyr , the solutions were both dark blue/green in color after 1 week, with a fine grey precipitate present. Respective reactions were filtered and layered 1:1 with hexanes, but did not give single crystal products.

Reaction of $\text{Sm}/\text{SePh}/\text{NH}_4\text{F}/\text{pyr}$:

Sm (1mmol), $(\text{SePh})_2$ (1.5mmol), NH_4F (2mmol), and Hg (0.025g) were combined and stirring begun. After 4 days the solution was yellow with undissolved NH_4F . After 1 month, the orange solution was filtered and layered 1:1 with hexanes, but afforded no crystalline product.

Reaction of $\text{Sm}_8\text{Se}_6(\text{SePh})_{12}(\text{pyr})_x/\text{NH}_4\text{F}$:

Sm (1mmol), $(\text{SePh})_2$ (1.5mmol), and Hg (0.025g) were combined in pyridine ($\sim 30\text{ml}$) and the reaction was stirred. After 1 day the solution turned orange and the metal was consumed. Elemental Se (0.625mmol) was added. After two weeks, the dark orange solution contained a large amount of dark precipitate. This solution was filtered, concentrated, and cooled but gave no single crystal product.

Experimental References:

- ¹ Peach, M.E. Some reactions of pentafluorothiophenol. Preparation of some pentafluorophenylthio metal derivatives. *Can. J. Chem.* **1968**, *46*, 2699.
- ² Klapötke, T.M., Krumm, B., Polborn, K. Synthesis, Chemistry, and Characterization of Perfluoroaromatic Selenium Derivatives. *Eur. J. Inorg. Chem.* **1999**, *8*, 1359.
- ³ Bruker-ASX. SADABS, Bruker Nonius area detector scaling and absorption correction, v2.05, Bruker-AXS Inc., Madison, Wisconsin, 2003.
- ⁴ Sheldrick, G. M. SHELXS86, Program for the Solution of Crystal Structures, University of Göttingen, Germany, **1986**.
- ⁵ Sheldrick, G. M. SHELXL97, Program for Crystal Structure Refinement, University of Göttingen, Germany, **1997**.
- ⁶ Dept. of Chemistry and Chemical Biology, Rutgers University, New Brunswick. Email: kroghjes@rci.rutgers.edu
- ⁷ Parr, R. G., Yang, W. *Density-Functional Theory of Atoms and Molecules*; University Press: Oxford, **1989**.
- ⁸ Perdew, J. P., Burke, K., Ernzerhof, M. Generalized Gradient Approximation Made Simple. *Phys Rev. Lett.* **1996**, *77*, 3865.
- ⁹ Dolg, M., Stoll, H., Savin, A., Preuss, H. Energy-adjusted pseudopotentials for rare earth elements. *Theor. Chim. Acta* **1989**, *75*, 173.; Dolg, M., Stoll, H., Preuss, H. A combination of quasirelativistic pseudopotential and ligand field calculations for lanthanoid compounds. *Theor. Chim. Acta* **1993**, *85*, 441.
- ¹⁰ Bergner, A., Dolg, M., Kuechle, W., Stoll, H., Preuss, H. Ab initio energy-adjusted pseudopotentials for elements of groups 13 through 17. *Mol. Phys.*, **1993**, *80*, 1431.
- ¹¹ Check, C. E., Faust, T. O., Bailey, J. M., Wright, B. J., Gilbert, T. M., Sunderlin, I. S. Addition of polarization and diffuse functions to the LANL2DZ basis set for p-block elements. *J. Phys. Chem. A*, **2001**, *105*, 8111.
- ¹² Dunning, T. H.; Hay, P. J. In *Modern Theoretical Chemistry, Vol. 3*; Schaefer, H. F., III, Ed.; Plenum: New York, 1976; pp 1-28.
- ¹⁴ Reed, A. E., Curtiss, L. A., Weinhold, F. Intermolecular Interactions from a Natural Bond Orbital, Donor-Acceptor Viewpoint. *Chem. Rev.* **1988**, *88*, 899.
- ¹⁵ Glendening, E. D., Badenhoop, J. K., Reed, A. J., Carpenter, J. E., Weinhold, F., NBO 4.0, Theoretical Chemistry Institute, University of Wisconsin, Madison, Wisconsin, **1996**.

¹⁶ Gaussian 03, Revision E.01, Frisch, M. J., Trucks, G. W., Schlegel, H. B., Scuseria, G. E., Robb, M. A., Cheeseman, J. R., Montgomery, Jr., J. A., Vreven, T., Kudin, K. N., Burant, J. C., Millam, J. M., Iyengar, S. S., Tomasi, J., Barone, V., Mennucci, B., Cossi, M., Scalmani, G., Rega, N., Petersson, G. A., Nakatsuji, H., Hada, M., Ehara, M., Toyota, K., Fukuda, R., Hasegawa, J., Ishida, M., Nakajima, T., Honda, Y., Kitao, O., Nakai, H., Klene, M., Li, X., Knox, J. E., Hratchian, H. P., Cross, J. B., Bakken, V., Adamo, C., Jaramillo, J., Gomperts, R., Stratmann, R. E., Yazyev, O., Austin, A. J., Cammi, R., Pomelli, C., Ochterski, J. W., Ayala, P. Y., Morokuma, K., Voth, G. A., Salvador, P., Dannenberg, J. J., Zakrzewski, V. G., Dapprich, S., Daniels, A. D., Strain, M. C., Farkas, O., Malick, D. K., Rabuck, A. D., Raghavachari, K., Foresman, J. B., Ortiz, J. V., Cui, Q., Baboul, A. G., Clifford, S., Cioslowski, J., Stefanov, B. B., Liu, G., Liashenko, A., Piskorz, P., Komaromi, I., Martin, R. L., Fox, D. J., Keith, T., Al-Laham, M. A., Peng, C. Y., Nanayakkara, A., Challacombe, M., Gill, P. M. W., Johnson, B., Chen, W., Wong, M. W., Gonzalez, C., and Pople, J. A., Gaussian, Inc., Wallingford CT, **2004**.

Vita:

Michael Romanelli

Education

- Ph.D., Chemistry, Rutgers, the State University of New Jersey, 2010
Adviser: Professor John Brennan
Thesis Title: Molecular Lanthanide Fluorides: Photoluminescence from Novel Architectures
- B.S., Chemistry, Rowan University, Glassboro NJ, 2004

Publications

- Krogh-Jespersen, K., **Romanelli, M.D.**, Emge T.J., Brennan, J.G. Covalent Bonding and the Trans Influence in Lanthanide Compounds. *Inorganic Chemistry*, submitted for publication.
- **Romanelli, M.**, Kumar, G.A., R. E. Riman, T. J. Emge, and J. G. Brennan “Highly Emissive Nanoscale Lanthanide Fluoride Clusters”, *Angew. Chem. Int. Ed.* **2008**, 47, 6049.
- **Romanelli, Michael D.**, Emge, Thomas J., Brennan, John G., “Tetrakis(1,2-dimethoxyethane- μ_2 O,O')ytterbium(II) bis(μ_2 -phenylselenolato- μ_2 Se:Se)bis[bis(phenylselenolato- μ Se)mercurate(II)]”, *Acta Cryst, Section E.* **2008**, E64(8), m987-m988, m987/1-m987/13.
- G. A. Kumar R. E. Riman, L.A. Diaz Torres, S. Banerjee, **M. D. Romanelli**, T. J. Emge, J. G. Brennan, “Near Infrared Optical characteristics of Chalcogenide-Bound Nd Organometallic Complexes”, *Chem. Mater.* **2007**, 19, 2937.
- S. Banerjee, L. Huebner., **M. D. Romanelli**, G.A. Kumar, R.E. Riman, T. J. Emge, and J. G. Brennan, “Oxoselenido Clusters of the Lanthanides: Rational Introduction of Oxo Ligands and Near-IR Emission from Nd(III)”, *J. Am. Chem. Soc.* **2005**, 127, 15900.